



**HAL**  
open science

# Adaptive scanning and 3D motion artefact compensation in optical coherence tomography

Nahashon Osinde

► **To cite this version:**

Nahashon Osinde. Adaptive scanning and 3D motion artefact compensation in optical coherence tomography. Automatic Control Engineering. Université Bourgogne Franche-Comté, 2024. English. NNT : 2024UBFCD003 . tel-04795423

**HAL Id: tel-04795423**

**<https://theses.hal.science/tel-04795423v1>**

Submitted on 21 Nov 2024

**HAL** is a multi-disciplinary open access archive for the deposit and dissemination of scientific research documents, whether they are published or not. The documents may come from teaching and research institutions in France or abroad, or from public or private research centers.

L'archive ouverte pluridisciplinaire **HAL**, est destinée au dépôt et à la diffusion de documents scientifiques de niveau recherche, publiés ou non, émanant des établissements d'enseignement et de recherche français ou étrangers, des laboratoires publics ou privés.

THÈSE DE DOCTORAT DE L'ÉTABLISSEMENT  
UNIVERSITÉ BOURGOGNE FRANCHE-COMTÉ  
PRÉPARÉE À L'UNIVERSITÉ DE FRANCHE-COMTÉ  
ET L'INSTITUT FEMTO-ST

ÉCOLE DOCTORALE N° 37  
SCIENCES POUR L'INGÉNIEUR ET MICROTECHNIQUES

Doctorat d'automatique

PAR

Nahashon Onchong'a OSINDE

**Balayage adaptatif et compensation  
des artefacts de mouvement 3D en  
tomographie par cohérence optique**

Thèse présentée et soutenue publiquement à Besançon, en 22 Mars 2024

Composition du Jury :

Pascal VASSEUR	Professeur, Université de Picardie Jules Verne, France	Président
Maciej SZKULMOWSKI	Associate Professor (Dr Hab.), Nicolaus Copernicus University, Poland	Rapporteur
Omar AIT-AIDER	Maître de Conférences (HDR), Université Clermont Auvergne, France	Rapporteur
Christophe GORECKI	Directeur de Recherche, ICTER, Poland	Examineur
Michalina GORA	Chargée de Recherche, Centre Wyss de Bio et Neuroingénierie, Suisse	Examinatrice
Nicolas ANDREFF	Professeur, Université de Franche-Comté, France	Directeur de thèse





DOCTORAL THESIS OF THE UNIVERSITY OF  
BOURGOGNE FRANCHE-COMTÉ PREPARED AT  
UNIVERSITY OF FRANCHE-COMTÉ AND  
FEMTO-ST INSTITUTE

DOCTORAL SCHOOL N° 37  
ENGINEERING SCIENCES AND MICROTECHNOLOGIES

Doctorate in Automatics

BY

Nahashon Onchong'a OSINDE

**Adaptive scanning and 3D motion  
artefact compensation in optical  
coherence tomography**

Thesis presented and defended publicly at Besançon, on 22<sup>nd</sup> March 2024

Composition of Jury :

Pascal VASSEUR	Professor, University of Picardie Jules Verne, France	President
Maciej SZKULMOWSKI	Associate Professor (Dr Hab.), Nicolaus Copernicus University, Poland	Reviewer
Omar AIT-AIDER	Associate Professor (HDR), University of Clermont Auvergne, France	Reviewer
Christophe GORECKI	Research director, ICTER, Poland	Examiner
Michalina GORA	Research manager, Wyss Center for Bio and Neuro Engineering, Switzerland	Examiner
Nicolas ANDREFF	Professor, University of Franche-Comté, France	Thesis director



*To my late mother, Hellen Kwamboka, and my late grandfather, Sir Charles Maisiba, for the wisdom and indefatigability they instilled in me.*



## Acknowledgements

The PhD journey is a blend of challenges and rewards, marked by the inevitable ups and downs. It is, therefore, not a solitary path, and I extend my gratitude to all who have crossed paths with me, offering unwavering support and assistance.

First and foremost, I express my gratitude to God for granting me the health and strength to navigate the complexities of these years pursuing a PhD.

I express sincere appreciation to my thesis advisor, Prof. Nicolas Andreff, for providing me with the opportunity to undertake a PhD under his guidance. His invaluable lessons, both scientifically and career-wise, have left a lasting impact. Thanks also to Prof. Jean Bosco for the academic advice as well as the encouragement to pursue further studies.

I extend my gratitude to the esteemed jury members, Dr. Maciej Szkulmowski (Dr Hab.), Dr. Omar Ait-Aider (HDR), Prof. Pascal Vasseur, Dr. Michalina Gora, and Prof. Christophe Gorecki for graciously agreeing to assess and provide criticisms on this research work.

Appreciation is also due to those who've been close to me during this journey; Mayra Yucely, Morris Mwangi, Alice Wanjiku, Timothy Tonui, Peter Rono, Rodgers Langat, Gloria Adegue, Clement Ndiritu, Michael Gichane, Edwin Nyoni, Simon Ndung'u, Elijah Ithatwa, Stephen Gitau, Lemmy Kagwithi, Simon Kigo, Rodgers Oloo, Washington Wambugu, Victor Langat, Japheth Too, Paul Morogo, John Karumba, Lee Nduati, Peter Kirumba, Claire Muthui, Keziah Kariuki, Eunice Kaara, Audrey Nzilani, Wanjiru Kaburu, Joy Waithira, Ria Talukder, Adriá Grabulosa, Mateo, Irina, Daniel Garzon, Jinlong Kang, Meesam Naqvi, Spiro Dourbaly, Ralf Hannouch, Belal Ahmad, Jiawei Yi, Nelson Cisneros, Kejun Hu, Liseth Pasaguay, Nwafor Chibundo, Ivan Kepseu, Nemer Issa, Fernando Eleazar, Lavinia Lanting, the entire Seventh Day Adventist church of Besançon, and others. Your encouragement and shared adventures during leisure moments have meant the world to me.

I acknowledge the AS2M department, Prof. Yann Le Gorrec, Isabelle, Estelle and my fellow colleagues in the department for their warm welcome and persistent support throughout my PhD journey. I also extend my thanks to the doctoral school and Alika Rossetti for the administrative assistance throughout my doctorate studies.

Heartfelt thanks go to my family for their financial and emotional support during my studies. During the toughest days, I always found comfort in knowing that I could rely on you. Special thanks to my father, Evans Maisiba, for providing valuable advice, and to Dr. Stella Kerongo, Isabella Maisiba, Joyce Maisiba, Dr. Angela, Teresa, Joyce Kadenge, Gladys and grandma Jerusa for their emotional support and encouragement. Thanks to James Maisiba, Gilbert Maisiba, and Tom Maisiba for inspiring me to always strive harder. Thanks to Mercy, Benson, Del

‘Kizo’, Sharon, Britney and Barbra for their consistent support and never failing to reach out. Also, a thank you to Dr. Nancy, Marrion ‘Tichi’, Irene, Ezekiel ‘Babu’, Mark ‘Pastor’, Lilian ‘Shoti’, Pauline, Mocheche, Ruth, and Emily for standing by me. Gratitude also goes to the Otworu family, Matara family, Nyakundi family, Kerubo family, Ryro family, Mokaya family, Nyamamba family, Mageto family and Bagwasi family for their support. Thanks also to Caren Nyakoni, Damaris Nyakoni, Grace Nyakoni, Pauline Nyakoni, James Nyakoni, Naomi, Elvin and grandpa Chris Nyakoni for the support and guidance. Appreciation also to the Miranyi family, Carol Muthui and Tahei Nakata.

To all those I haven’t explicitly mentioned but have contributed to my journey in various ways, I extend a big thank you. Asanteni sana!

Nahashon Onchong’ a Osinde  
April 19<sup>th</sup>, 2024, Besançon, France

*“Keep in mind how fast things pass by and are gone—those that are now, and those to come. Existence flows past us like a river: the “what” is in constant flux, the “why” has a thousand variations. Nothing is stable, not even what’s right here. The infinity of past and future gapes before us—a chasm whose depths we cannot see”*

*Marcus Aurelius*

# Table of contents

<b>Acknowledgements</b> .....	iii
<b>Table of contents</b> .....	v
<b>List of Figures</b> .....	ix
<b>List of Tables</b> .....	xvii
<b>List of abbreviations and acronyms</b> .....	xxi
<b>General introduction</b> .....	1
<b>1 Introduction and motivation for optical coherence tomography</b> .....	5
<b>1.1 Medical diagnosis</b> .....	6
1.1.1 Physical biopsy .....	6
1.1.2 Optical biopsy .....	7
<b>1.2 Introduction to optical coherence tomography</b> .....	9
1.2.1 OCT working principle.....	9
1.2.2 Comparison of OCT with other medical imaging modalities.....	11
1.2.3 Claimed advantages of OCT.....	12
<b>1.3 Background of OCT technology</b> .....	13
1.3.1 Time domain OCT (TD-OCT) .....	13
1.3.2 Fourier domain OCT (FD-OCT).....	14
<b>1.4 Development of OCT technology</b> .....	18
1.4.1 Fundamental research in OCT.....	18
1.4.2 OCT adaptation to medical needs.....	21
1.4.3 OCT and robotics .....	24
<b>1.5 Improvement of OCT data acquisition</b> .....	27
1.5.1 Architectural improvements .....	27
1.5.2 Improvement by anticipation of data processing .....	30



1.6	Conclusion.....	31
<b>2</b>	<b>Multi-criteria assessment of optical coherence tomography using non-raster trajectories .....</b>	<b>33</b>
2.1	Background and motivation .....	35
2.1.1	Contributions of this chapter .....	36
2.2	OCT scan trajectories .....	38
2.2.1	Raster scan trajectory .....	38
2.2.2	Other scan families: non-raster scan trajectories.....	39
2.3	Qualitative analysis.....	42
2.3.1	Fast preview .....	42
2.3.2	Geometric smoothness of the scan trajectory .....	43
2.3.3	Connection with compressed sensing .....	44
2.3.4	Waveforms, velocity, and acceleration profiles of scan trajectories .....	45
2.3.5	Conclusion of qualitative analysis .....	45
2.4	Novel criteria for quantitative assessment of OCT scan trajectories .....	47
2.4.1	Exploitation vs exploration (local vs global quality)..	47
2.4.2	Smoothness of the scan trajectory.....	48
2.4.3	Spatial resolution of the scan trajectories .....	50
2.4.4	Conclusion of quantitative analysis .....	51
2.5	Experimental assessment of OCT volumes .....	52
2.5.1	Experimental set-up .....	52
2.5.2	OCT volume file format.....	52
2.5.3	OCT volume similarity assessment to ground truth ..	53
2.5.4	Exploitation vs exploration.....	55
2.5.5	Progressivity (fast preview) of the scan resolution ...	56
2.5.6	Time analysis of the scan trajectories.....	58
2.5.7	Summary of scan trajectories assessment.....	59
2.6	Conclusion.....	60
<b>3</b>	<b>Optical coherence tomography adaptive scanning ..</b>	<b>61</b>
3.1	Adaptive scanning .....	62
3.1.1	Existing works on adaptive scanning .....	64
3.1.2	Contributions of this chapter .....	66

---

<b>3.2</b>	<b>Adaptive scanning protocol</b> .....	67
3.2.1	Conceptual description of adaptive scanning .....	67
3.2.2	Technical description of adaptive scanning .....	71
<b>3.3</b>	<b>Numerical (simulation) validation of adaptive scanning</b> .....	82
3.3.1	Simulation of volumetric OCT data of a tissue sample containing a tumour. ....	82
3.3.2	Simulation of adaptive scanning. ....	86
<b>3.4</b>	<b>Experimental validation of adaptive scanning</b> .....	89
3.4.1	Experimental set-up procedure. ....	90
3.4.2	Experimental adaptive scanning .....	92
3.4.3	Discussion of the simulation and experimental results of adaptive scanning .....	98
<b>3.5</b>	<b>Conclusion</b> . ....	99
<b>4</b>	<b>Exploitation of motion artefacts in optical coherence tomography</b> .....	101
<b>4.1</b>	<b>Motion artefacts</b> . ....	102
4.1.1	Motion artefacts/rolling shutter in cameras .....	104
4.1.2	Motion artefacts in optical coherence tomography ...	105
4.1.3	Contributions of this chapter .....	106
<b>4.2</b>	<b>State of the art in motion artefacts compensation of optical coherence tomography data</b> . ....	107
4.2.1	Intra-processing methods. ....	107
4.2.2	Post-processing methods .....	110
<b>4.3</b>	<b>Modelling of motion artefacts in optical coherence tomography</b> . ....	111
4.3.1	Mathematical formalisation of motion artefacts in OCT. ....	112
4.3.2	Simulation of OCT volumes with motion artefacts ...	114
4.3.3	Experimental validation. ....	117
<b>4.4</b>	<b>Proposed method for estimating 3D motion from an OCT volume with motion artefacts</b> .....	120
4.4.1	Numerical (simulation) validation .....	123
4.4.2	Experimental validation. ....	130
<b>4.5</b>	<b>3D Shape and motion estimation from a single unknown OCT volume obtained using a non-raster scan trajectory</b> . ....	134

---

4.5.1	Motion artefacts in optical coherence tomography during raster and non-raster scanning . . . . .	134
4.5.2	The rosette scan trajectory and its peculiarities . . . . .	138
4.5.3	Proposed shape and motion estimation method from a single OCT volume . . . . .	139
4.5.4	Numerical (simulation) validation . . . . .	143
4.5.5	Experimental validation . . . . .	148
4.6	<b>Motion artefacts during adaptive scanning in OCT</b> . . . . .	152
4.7	<b>Conclusion</b> . . . . .	152
	<b>General conclusions and perspectives</b> . . . . .	155
<b>A</b>	<b>The Frenet-Serret frame</b> . . . . .	161
A.1	Description of the Frenet-Serret frame . . . . .	162
A.2	Predicting an $(n + 1)$ curve position using the Frenet-Serret frame . . . . .	163
<b>B</b>	<b>Some pseudocodes to mentioned algorithms in the thesis</b> . . . . .	169
B.1	Tumour boundary estimation . . . . .	170
B.2	Shape and motion estimation from a single OCT volume obtained using the rosette scan trajectory . . . . .	171
<b>C</b>	<b>PointPCA similarity error computation</b> . . . . .	173
	<b>Bibliography</b> . . . . .	179

# List of Figures

1	Stomach cancer stages [Byakodi 23].....	1
2	Colorectal cancer development and treatment.....	2
1.1	Physical biopsy procedure of the gut [MedlinePlus 21]. ....	6
1.2	Optical coherence tomography working principle illustration. ....	9
1.3	A-scan (1D), B-scan (2D) and C-scan (3D) images obtained using OCT [Fujimoto 15].....	10
1.4	OCT C-scan schematic. ....	11
1.5	Comparison of endoscopy, confocal microscopy, ultrasound and OCT in resolution and image penetration, adapted from [Fujimoto 15]. ...	12
1.6	(a) Adenocarcinoma OCT image and (b) its corresponding histology image [Kang 15]. ....	12
1.7	Time domain OCT schematic. ....	13
1.8	Spectral-domain OCT schematic. ....	15
1.9	Mirror artefact in spectral-domain OCT [Fujimoto 15].....	15
1.10	Swept-source OCT schematic. ....	16
1.11	B-scan images of (a) time domain, (b) spectral-domain, and (c) swept-source OCT of normal macula in the eye [Bhende 17].....	17
1.12	Polarization-sensitive OCT schematic. BS - beam splitter, QWP - quarter-wave plate, PBS - polarizing beam splitter, v - vertical, h - horizontal. ....	18
1.13	Doppler optical coherence tomography measures the axial velocity component $v_{  }$ . The yellow line represents the OCT beam [Leitgeb 14]. 19	
1.14	Surgical forceps with a common path OCT system for axial ranging using A-scans only [Cheon 15].....	21
1.15	Commercial MIOCT systems. (A) Zeiss RESCAN 700. (B) Haag- Streit Surgical iOCT. (C) Leica Microsystems Biotigen EnFocus. Red arrows denote the location of the OCT scanners [Carrasco-Zevallos 17]. 22	

---

1.16	(a) Tethered capsule endomicroscope, (b) schematic of the procedure of tethered capsule endomicroscopy, (c-f) esophagus images obtained using the tethered capsule endomicroscope utilising OCT [Gora 16]. . . . .	23
1.17	Schematic diagram of the coaxial setup of the OCT system and the CO <sub>2</sub> laser with overlapping working spaces [Zhang 14]. . . . .	24
1.18	Cooperative robotic system consisting of a custom OCT probe and a drug delivery channel [Ahronovich 23]. . . . .	25
1.19	Image sequence showing the 3D positioning task achievement. (a) shows the desired pose, (b) the initial pose, (c)-(e) represents intermediate pose acquired during the positioning task and (f), the reached pose [Dahroug 20]. . . . .	26
1.20	Adaptive optics components and configuration, adapted from [Krawitz 16]. . . . .	28
1.21	Electrothermal mirror: (a) schematic and (b) microphotograph of a MEMS scanner assembled on top of a Mirau interferometer [Gorecki 21]. . . . .	29
2.1	(a) OCT volume (C-scan) of a biological sample (head of a bee) obtained using the conventional raster scan trajectory, (b) photo of the bee-head as well as sequential B-scans on the $x - y$ plane. . . . .	35
2.2	(a) 2D scanning system with two galvanometer scanners with perpendicular axis (GS X for the fast axis scan and GS Y for the slow axis scan), (b) raster scan trajectory in the $x - y$ plane. Adapted from [Duma 19]. . . . .	35
2.3	Illustration of the scan trajectory based on the raster (a) and bi-directional raster (b) as they evolve with time. . . . .	38
2.4	(a) 3D view of a free-form B-scan of a smooth trajectory, (b) Unwrapped B-scan. . . . .	39
2.5	(a) Top view of a free-form smooth trajectory, (b) Segmented free-form smooth trajectory, (c) Unwrapped and digitized B-scan illustrating A-scans and voxels. . . . .	39
2.6	Spiral scan trajectory at different time intervals. (a) At time $t \in [0, T/4]$ . (b) At time $t \in [0, T/2]$ . (c) At time $t \in [0, 3T/4]$ . (d) At time $t \in [0, T]$ . T is the period of scanning. . . . .	40
2.7	Lissajous scan trajectory at different time intervals. (a) At time $t \in [0, T/4]$ . (b) At time $t \in [0, T/2]$ . (c) At time $t \in [0, 3T/4]$ . (d) At time $t \in [0, T]$ . T is the period of scanning. . . . .	41
2.8	Rosette scan trajectory at different time intervals. (a) At time $t \in [0, T/4]$ . (b) At time $t \in [0, T/2]$ . (c) At time $t \in [0, 3T/4]$ . (d) At time $t \in [0, T]$ . T is the period of scanning. . . . .	42

---

---

2.9	Illustration of data distribution (coherence) for the paradigm of compressed sensing. (a) raster scan trajectory, (b) CLV spiral scan trajectory, (c) Lissajous scan trajectory, (d) rosette scan trajectory. ....	44
2.10	Exploitation/exploration ratio of scan trajectories (blue region - exploration, red region - exploitation). (a) raster, $\lambda = 0.30$ , (b) CAV spiral, $\lambda = 0.54$ , (c) CLV spiral, $\lambda = 0.30$ , (d) Lissajous, $\lambda = 0.14$ , (e) rosette, $\lambda = 0.37$ . ....	48
2.11	Mean and maximum values of velocity, acceleration and jerk for the scan trajectories in the $x - axis$ . ....	49
2.12	Mean and maximum values of velocity, acceleration and jerk for the scan trajectories in the $y - axis$ . ....	49
2.13	Mean and maximum values of velocity, acceleration and jerk for the scan trajectories in the resulting motion due to both the $x$ and $y - axis$ . ....	50
2.14	Delaunay triangulation of several scan trajectories. (a) raster scan trajectory, (b) CAV spiral scan trajectory, (c) CLV spiral scan trajectory, (d) Lissajous scan trajectory, (e) rosette scan trajectory. 50	
2.15	Histogram of the Delaunay triangles area of several scan trajectories. (a) raster scan trajectory, (b) CAV spiral scan trajectory, (c) CLV spiral scan trajectory, (d) Lissajous scan trajectory, (e) rosette scan trajectory. ....	51
2.16	Illustration of the experimental set-up used to validate the qualitative and quantitative analysis (the end effector of the parallel robot serves as the stationary platform). ....	52
2.17	(a) Biological sample (bee-head), (b) Sectional view of the 3D OCT volume, (c) 3D OCT point cloud volume of the biological sample. ...	53
2.18	PointPCA architecture [Alexiou 21]. ....	54
2.19	Similarity scores of OCT volumes obtained from scan trajectories when compared to the ground truth. ....	55
2.20	Exploitation/exploration similarity scores of scan trajectories. ....	56
2.21	Mean similarity score on progressive scanning for different experimental configurations. ....	58
2.22	Time taken by different scan trajectories to obtain A-scans. The time taken using non-raster trajectories is almost equal, therefore the curves overlap each other. ....	58
2.23	Individual radar plots for each scan trajectory and a combined radar plot comprising all the trajectories for more variability analysis of the multi-criteria assessment. ....	59

---

3.1	Using microstructural contrast, tumour tissue (an allotransplanted mammary adenocarcinoma) can be differentiated from surrounding host subcutaneous and muscle tissues in a dorsal skin-fold chamber model. By defining the tumour margins, the three-dimensional tumour volume can be calculated. Transverse extent is $5mm$ ( $x$ -axis) and $4.4mm$ ( $y$ -axis) [Vakoc 09].....	63
3.2	Probabilistic adaptive scanning approach. (a), a subset of the selected scan positions from previous acquisition and (b), an optimised raster scan trajectory designed to acquire data only at those positions [Draelos 22]. .....	64
3.3	(a) Local raster scanning of a DNA strand using an AFM [Andersson 05], (b) Andersson's scanning algorithm with smooth trajectory and contour prediction [Zhang 15]. .....	65
3.4	Proposed scan trajectory for atomic force microscope (AFM) data acquisition for biological samples in [Zhang 15]. .....	66
3.5	Adaptive scanning process. ....	67
3.6	Surgeon tracing a tumour boundary on the large intestine on a tablet [Dalle 23]. .....	68
3.7	2D tumour manual delineation [Janowczyk 16, Janowczyk 17]. .....	69
3.8	Sinusoidal scan trajectory following the 2D tumour boundary.....	70
3.9	(a) 2D tumour boundary, (b) Sinusoidal scan trajectory following the 2D tumour boundary. ....	70
3.10	Illustration of the Frenet-Serret frame on a 2D tumour boundary. ...	71
3.11	OCT image (B-scan) examples of normal fibrous stroma and invasive ductal carcinoma, scale bar: $250\mu m$ [Yao 17]. .....	72
3.12	Healthy and cancerous OCT B-scan images [Luo 19a]. .....	73
3.13	(a) 3D view of a free-form B-scan of a smooth trajectory, (b) Unwrapped B-scan. ....	74
3.14	(a) Top view of a free-form smooth trajectory, (b) Segmented free-form smooth trajectory, (c) Unwrapped and digitized B-scan illustrating A-scans and voxels. ....	74
3.15	Detection of individual healthy and tumour A-scan positions using k-means clustering. ....	75
3.16	Tumour boundary estimation. ....	76
3.17	Illustration of the tumour boundary evolution considering previous positions on the tumour boundary. ....	77
3.18	Illustration of the heading angle estimation.....	78

---

3.19	Curvature estimation parameters based on Heron's formula. . . . .	78
3.20	Tumour boundary prediction. . . . .	79
3.21	Section of an adaptive scan trajectory. . . . .	80
3.22	Adaptive scanning flowchart. . . . .	81
3.23	Illustration of sections in a simulated A-scan. . . . .	82
3.24	Healthy and cancerous OCT A-scan data. . . . .	83
3.25	Distribution of healthy and tumour boundary scan positions. . . . .	84
3.26	Simulated OCT point cloud volumes of a tissue sample. . . . .	85
3.27	B-scan of the simulated OCT point cloud volumes in Figure 3.26 of a tissue sample at $y = 0$ . . . . .	85
3.28	Standard deviation of A-scan intensity values. . . . .	85
3.29	Adaptive scan trajectory using simulated data in an ideal scenario. . .	86
3.30	Simulated OCT point cloud volumes obtained using an adaptive scan trajectory in an ideal scenario. . . . .	87
3.31	Adaptive scan trajectory using simulated data in a realistic like sce- nario. . . . .	88
3.32	Detected tumour boundary after first loop of adaptive scanning. . . . .	88
3.33	Simulated OCT point cloud volume obtained using an adaptive scan trajectory in a realistic like scenario. . . . .	89
3.34	Healthy and tumour regions delineated using k-means clustering. . . . .	89
3.35	Illustration of the experimental set-up used to validate the adaptive scanning protocol. . . . .	90
3.36	Gelatine sheets used to prepare the tissue phantom. . . . .	91
3.37	Illustration of the tumour-like structure used. . . . .	91
3.38	Illustration of the cylindrical structure used. . . . .	91
3.39	Gelatine tissue phantom with tumour-like structures. . . . .	92
3.40	Photo of the samples with an initial boundary drawn on it. . . . .	93
3.41	Plot of the surgeon's boundary and the corresponding planned scan trajectory. . . . .	94
3.42	Adaptive scanning on experimental OCT data. . . . .	94
3.43	Detected tumour boundary after first loop of adaptive scanning. . . . .	95
3.44	Experimental point cloud volume of the tumour boundary. . . . .	95
3.45	Experimental full point cloud OCT volumes. . . . .	96
3.46	Healthy and tumour regions delineated using k-means clustering. . . . .	96

---



3.47	Healthy and tumour regions delineated using k-means clustering.....	97
4.1	A photo from an iPhone 3GS camera acquired during fast motion [Forssén 10]. The pole holding the signs is slanted instead of being straight.....	102
4.2	Motion artefacts due to relative motion during image acquisition. ...	102
4.3	Motion artefacts from medical images.....	103
4.4	Example of motion artefacts in a raster-scanned 3D OCT volume. The volume consists of 400 by 400 A-Scans sampled over 6mm by 6mm centred on the optic nerve head. (a) <i>En face</i> fundus projection of the volume. The dotted red line marks the fast scan direction of the volume. The black arrows indicate motion artefacts caused by transverse eye motion that create discontinuities in the vessel pattern. (b) Central slice of the volume along the slow scan direction (blue line in a). Axial motion leads to a wavy deformation of the retina in axial direction (green curve). (c) Central slice of the volume along the fast scan direction (orange line in a). The spatial structure of the retina remains intact along the fast scan direction [Kraus Martin 15]. ....	103
4.5	Image acquisition process in (a), CCD and (b), CMOS sensor [Cho 07].	104
4.6	Rolling shutter effect in cameras [Cho 07]. ....	105
4.7	Motion artefacts of a bee-head due to motion in the $x - axis$ during OCT volume data acquisition. ....	106
4.8	Eye motion compensation for OCT imaging with tracking SLO [Vienola 12].	109
4.9	Schematic of a distorted OCT volume due to motion during data acquisition. ....	112
4.10	Schematic of the OCT and object frames.....	114
4.11	OCT point cloud volume of a stationary bee-head.....	114
4.12	Illustration of the experimental setup used to execute motions during OCT volume data acquisition. ....	117
4.13	Illustration of the proposed motion estimation process knowing the OCT volume reference shape.....	121
4.14	Algorithm to estimate the linear ( $V$ ) and angular velocity ( $\Omega$ ) in addition to the pose ${}^{oct}T_{B(t_0)}$ .....	122
4.15	OCT point cloud volume of a stationary bee-head.....	124
4.16	Optimisation errors .....	128

---

4.17	Initial vs final (after optimisation) PointPCA error.....	129
4.18	OCT point cloud volume of a stationary bee-head.....	130
4.19	Initial vs final (after optimisation) PointPCA error.....	133
4.20	Illustration of the rosette scan pattern; (a) Three successive petals of the pattern depicted by different colours, (b) Concentric circles crossing the intersections - the intersections are shown by $\times$ and the edge points by $*$ [Nikooienejad 19].....	138
4.21	OCT point cloud volume obtained using the rosette scan trajectory. .	139
4.22	Rosette distorted OCT sub-volumes. (Magenta points - first repeated sub-volume, yellow points - second repeated sub-volume.....	141
4.23	Extraction of two sub-volumes from one static OCT volume.....	141
4.24	Illustration of the proposed method to estimate the distortion motion from one OCT volume. ....	142
4.25	Optimisation errors. ....	147
4.26	Initial vs final (after optimisation) PointPCA error.....	148
4.27	Initial vs final (after optimisation) PointPCA error.....	151
5.1	Examples of modulated Lissajous scan trajectories [Sun 21]. ....	158
A.1	A space curve; the vectors $\mathbf{t}$ , $\mathbf{n}$ , and $\mathbf{b}$ ; and the osculating plane spanned by $\mathbf{t}$ and $\mathbf{n}$ .....	162
A.2	Section of a scan trajectory. ....	163
C.1	PointPCA architecture [Alexiou 21].....	174



---

# List of Tables

1.1	Comparison of time domain, spectral-domain, and swept-source optical coherence tomography [Bernardes 12, Bhende 17].....	17
2.1	Waveforms, velocity and acceleration profiles of scan trajectories. The double horizontal line in the second row separates figures of the raster scan trajectory with the non-raster scan trajectories (blue plot - $x$ - axis, red plot - $y$ - axis).....	46
2.2	Time-lapse sequence of scanning a biological sample (bee-head) with different scan trajectories. ....	57
3.1	A-scan design in a healthy tissue region. ....	83
3.2	A-scan design in a tumorous tissue region. ....	83
4.1	Motion artefacts due to translatory motions (blue points - motion-free volume, red points - motion-distorted volume). ....	115
4.2	Motion artefacts due to rotary and compound motions (blue points - motion-free volume, red points - motion-distorted volume).....	116
4.3	Comparison study between some simulated data and experimental data (blue points - simulated motion-distorted volume, red points - experimentally motion-distorted volume). The units for the linear velocities, $V$ , are in $mm/s$ and angular velocities, $\Omega$ , are in $1e - 2rad/s$ .....	119
4.4	Results from a few motion estimation runs (blue points - reference volume, red points - motion-distorted volume, green points - corrected volume). The units for the linear velocities, $V$ , are in $mm/s$ and angular velocities, $\Omega$ , are in $1e - 2rad/s$ .....	126
4.5	Results from a few motion estimation runs (blue points - reference volume, red points - motion-distorted volume, green points - corrected volume). The units for the linear velocities, $V$ , are in $mm/s$ and angular velocities, $\Omega$ , are in $1e - 2rad/s$ . ....	127
4.6	Numerical simulation errors.....	129

4.7	Results from the motion estimation process using experimental data (blue points - reference volume, red points - motion-distorted volume, green points - corrected volume). The units for the linear velocities, $V$ , are in $mm/s$ and angular velocities, $\Omega$ , are in $1e-2rad/s$ .	131
4.8	Results from the motion estimation process using experimental data (blue points - reference volume, red points - motion-distorted volume, green points - corrected volume). The units for the linear velocities, $V$ , are in $mm/s$ and angular velocities, $\Omega$ , are in $1e-2rad/s$ .	132
4.9	Motion artefact effects on volumes obtained using the raster and non-raster scan trajectories. The units for the linear velocities, $V$ , are in $mm/s$ and angular velocities, $\Omega$ , are in $1e-2rad/s$ .	135
4.10	Motion artefact effects on volumes obtained using the raster, Lissajous and continuous angular velocity (CAV) spiral scan trajectories. The units for the linear velocities, $V$ , are in $mm/s$ and angular velocities, $\Omega$ , are in $1e-2rad/s$ .	136
4.11	Motion artefact effects on volumes obtained using the raster and rosette scan trajectories. The units for the linear velocities, $V$ , are in $mm/s$ and angular velocities, $\Omega$ , are in $1e-2rad/s$ .	137
4.12	Two sub-volumes extracted from one motion-free OCT volume.	140
4.13	Two sub-volumes extracted from one motion-distorted OCT volume. The units for the linear velocities, $V$ , are in $mm/s$ and angular velocities, $\Omega$ , are in $1e-2rad/s$ .	140
4.14	Results from a few motion estimation runs from a single distorted OCT volume (blue points - motion-free volume, red points - motion-distorted volume, green points - corrected volume). The units for the linear velocities, $V$ , are in $mm/s$ and angular velocities, $\Omega$ , are in $1e-2rad/s$ .	145
4.15	Results from a few motion estimation runs from a single distorted OCT volume (blue points - motion-free volume, red points - motion-distorted volume, green points - corrected volume). The units for the linear velocities, $V$ , are in $mm/s$ and angular velocities, $\Omega$ , are in $1e-2rad/s$ .	146
4.16	Results from a few motion estimation runs from a single distorted OCT volume using experimental data (blue points - motion-free volume, red points - motion-distorted volume, green points - corrected volume). The units for the linear velocities, $V$ , are in $mm/s$ and angular velocities, $\Omega$ , are in $1e-2rad/s$ .	149

4.17	Results from a few motion estimation runs from a single distorted OCT volume using experimental data ( <b>blue points</b> - motion-free volume, <b>red points</b> - motion-distorted volume, <b>green points</b> - corrected volume). The units for the linear velocities, $V$ , are in $mm/s$ and angular velocities, $\Omega$ , are in $1e - 2rad/s$ .....	150
C.1	Definition of geometric and textural descriptors.....	175



## List of abbreviations and acronyms

<b>AFM</b>	Atomic force microscopy
<b>AMD</b>	Age-related macular degeneration
<b>AO</b>	Adaptive optics
<b>AO-OCT</b>	Adaptive optics optical coherence tomography
<b>AO-SLO</b>	Adaptive optics scanning laser ophthalmoscope
<b>API</b>	Application programming interface
<b>BS</b>	Beam splitter
<b>CAV</b>	Constant angular velocity
<b>CCD</b>	Charge coupled device
<b>CMOS</b>	Complementary-metal-oxide-semiconductor
<b>CLV</b>	Constant linear velocity
<b>DICOM</b>	Digital Imaging and Communications in Medicine
<b>DOCT</b>	Doppler optical coherence tomography
<b>DOF</b>	Degree of freedom
<b>FDA</b>	Food and drug administration
<b>FD-OCT</b>	Fourier domain optical coherence tomography
<b>FOV</b>	Field of view
<b>FPGA</b>	Field programmable graphics array
<b>ga</b>	Genetic algorithm
<b>GPU</b>	Graphical processing unit
<b>GS</b>	Galvanometer scanner
<b>HHOCT</b>	Hand-held optical coherence tomography
<b>iOCT</b>	Intra-operative optical coherence tomography
<b>LED</b>	Light emitting diode
<b>MEMS</b>	Micro-electromechanical system
<b>MINC</b>	Medical Image NetCDF
<b>MIOCT</b>	Microscope-integrated optical coherence tomography
<b>MOS</b>	Mean opinion score
<b>MRI</b>	Magnetic resonance imaging
<b>NA</b>	Numerical aperture
<b>NAFLD</b>	Non-alcoholic fatty liver disease
<b>NIFTI</b>	Neuroimaging Informatics Technology Initiative
<b>OCT</b>	Optical coherence tomography
<b>OFDI</b>	Optical frequency domain interferometry
<b>OS</b>	Operating system
<b>PBS</b>	Polarizing beam splitter
<b>PCA</b>	Principal component analysis
<b>PSNR</b>	Peak signal to noise ratio



<b>PS-OCT</b>	Polarization-sensitive optical coherence tomography
<b>PVA-C</b>	Polyvinyl alcohol cryogel
<b>QWP</b>	Quarter-wave plate
<b>RAM</b>	Random access memory
<b>RD</b>	Radial distance
<b>RGB</b>	Red, Green, Blue
<b>RMSE</b>	Root mean square error
<b>RS</b>	Rolling shutter
<b>SD-OCT</b>	Spectral-domain optical coherence tomography
<b>SE(3)</b>	Special Euclidean group in 3 dimensions
<b>SLO</b>	Scanning laser ophthalmoscope
<b>SNR</b>	Signal to noise ratio
<b>SOCT</b>	Spectroscopic optical coherence tomography
<b>SPM</b>	Scanning probe microscopy
<b>SSD</b>	Sum of squared differences
<b>SSIM</b>	Structural similarity index method
<b>SS-OCT</b>	Swept-source optical coherence tomography
<b>TCE</b>	Tethered capsule endomicroscopy
<b>TD</b>	Tangential distance
<b>TD-OCT</b>	Time domain optical coherence tomography
<b>TSLO</b>	Tracking scanning laser ophthalmoscope
<b>VEGFR2</b>	Vascular endothelial growth factor receptor 2
<b>AS2M</b>	Automation and MicroMechatronics Systems
<b>FEMTO-ST</b>	Franche-Comté Electronique, Mécanique, Thermique et Optique - Sciences et Technologies
<b>INSERM</b>	Institut national de la santé et de la recherche médicale

# General introduction

## Context

The incidence of cancer is on the rise in the European Union (EU), with a reported 2.7 million new cases in 2022 and an estimated 1.3 million deaths in 2022 [ECIS 23]. This represents a 2.3% increase in new cases and a 2.4% increase in deaths compared to 2020 statistics. These alarming figures necessitate strategic interventions by governments. In France, the National Cancer Strategy 2021-2030 reflects ambitious objectives aimed at improving cancer prevention and care. The goal of this strategy launched in February 2021 is to reduce the number of avoidable cancers by 60,000 per year. It is structured around four key priorities: i) improving prevention and an uptake of screening tests; ii) improving the quality of life of cancer patients; iii) increasing cancer survival among adults and children, particularly for cancers with low prognosis; and iv) ensuring that all population groups can benefit equally from progress in cancer care [OECD 23].

To tailor effective treatment plans for cancer, doctors must determine the stage of cancer. Staging provides information about the tumour location, size, lymph node involvement and metastasis (spread of cancer cells to different parts of the body). Considering gastrointestinal cancer such as in the stomach, Figure 1 illustrates the various stages.

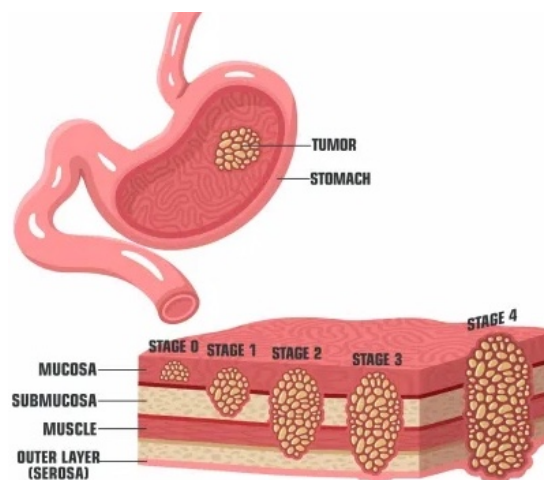


Figure 1 – Stomach cancer stages [Byakodi 23].

In the initial stage (0), cancer cells develop within the mucosa (innermost layer on the stomach wall). At this stage it is difficult to carry out diagnosis. As cancer progresses, it infiltrates the submucosa, muscle, subserosa and serosa layers. By stage 4, the cancer has permeated all stomach layers and started to spread to distant parts of the body along with the area around the stomach. At this stage,

the cancer has developed to a great extent making the success of treatment difficult. Taking an example of colorectal cancer development as highlighted in Figure 2, if cancer is detected in the first 2 stages, the patient has a 90% chance of survival since it is quite easy to eliminate the small polyps by classical surgery. However, when cancer is diagnosed in later stages, the chances of survival dramatically decreases to 20% [Krepelkova 19]. This substantively ignites the need for **early cancer detection**.

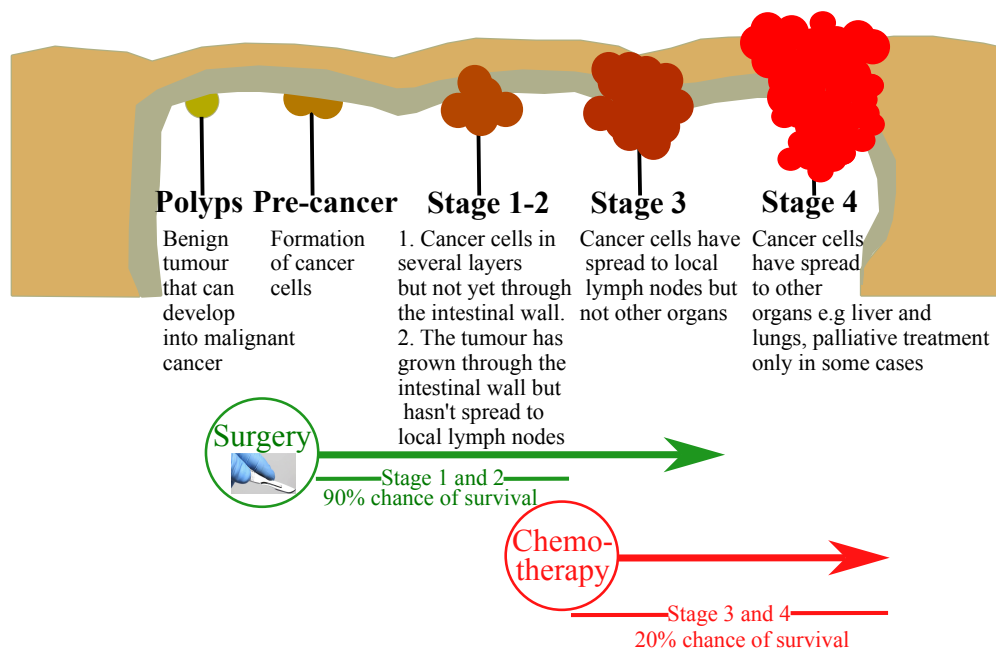


Figure 2 – Colorectal cancer development and treatment.

Determining the stage of cancer in the gastrointestinal tract usually involves an endoscopic procedure where the doctor checks for suspicious signs of cancer. If there are suspicious signs, the doctor takes a sliver of tissue and sends it to the lab for histopathological analysis. This procedure of tissue extraction from the body for histopathology analysis is referred to as physical biopsy. In as much as physical biopsy is useful during cancer diagnosis, it presents challenges such as possible contamination of nearby tissues with cancer cells, as well as potential side effects of surgery. An alternative procedure that mitigates these limitations of physical biopsy is **optical biopsy**. This is whereby, instead of extracting tissue samples from the body, this concept relies on an imaging modality that takes multiple images as well as 3-dimensional (3D) volumes which provide micro-structural information to the doctor to determine a diagnosis. Among the existing and investigated techniques, optical coherence tomography (OCT) is a valuable imaging modality that acquires *in situ* high-resolution, cross-sectional and volumetric micro-structural information of the tissue sample being imaged and provides it to the medical professional for diagnosis. Moreover, with the advent of intracorporeal robotics and OCT miniaturisation, it is now within reach to embed a tiny OCT probe on a robot-assisted endoscope. In the 30 years of OCT existence, it is

now the gold standard in ophthalmology diagnosis and finds applications in other medical fields especially oncology. OCT is particularly useful in oncology since it is able to facilitate **early cancer detection** as well as **optical biopsy**.

The volumetric data provided by OCT, which allows for the determination of the localisation and dimensions of structures beneath a biological tissue surface, is obtained through a mechanical scan of the tissue surface by a light beam that delivers interferometric information along the tissue depth. Due to the mechanical scan, acquisition frequency and spatial resolution are antagonistic characteristics (increasing the acquisition frequency decreases the spatial resolution of the data obtained, and vice versa). Moreover, the mechanical scan induces a rolling shutter acquisition mode that produces geometric artefacts due to the relative motion between the imaged tissue and the OCT probe, as was also observed in high-speed vision. In light of this, the research objectives in this thesis are all aimed at improvement of OCT while dealing with the optical and mechanical constraints.

The work in this thesis was carried out at the department of Automation and MicroMechatronics Systems (AS2M) of FEMTO-ST<sup>1</sup> institute. It was part of the INSERM<sup>2</sup> ROBOT project (Robotics and Optical coherence tomography for optical BiOpsy in the digestive Tract), which focused on the use of OCT in an intracorporeal setting. Additionally, it was part of the image-guided surgery research axis from the Grand Prix Scientifique 2018, Fondation Charles Defforey, Institut de France. This thesis consists of 5 chapters: an introductory chapter on OCT, three chapters detailing the scientific and technical contributions, and a chapter summarising the conclusions and offering perspectives on this research.

### Scientific and technical contributions/thesis outline

The first chapter provides background information on OCT technology and its development. It also discusses the current state of the art in OCT and various techniques for improving data acquisition.

The second chapter details a **multi-criteria methodology** for assessing OCT. This chapter introduces various non-raster trajectories and proposes novel criteria for evaluating these scan trajectories, along with the volumetric data obtained. The novel criteria includes; **exploitation/exploration ratio** of the OCT data obtained, **smoothness** of the scan trajectory, and **fast preview** of the acquired OCT data, in addition to conventional criteria; **time** and quality (expressed as **volume similarity** rather than slice-by-slice image quality). The set of criteria proposed will be useful in assessing OCT scan trajectories for optimisation in various applications such as robot assisted *in vivo* optical biopsy. It is shown that the rate of data acquisition is improved without degrading the OCT volume quality by scanning using non-raster trajectories (they are fast, smooth, and make the galvanometer scanners have less wear and tear). In particular, the rosette scan trajectory, which was the preferred non-raster trajectory, provided the best performing scores globally.

---

1. Franche-Comté Electronique, Mécanique, Thermique et Optique - Sciences et Technologies  
2. Institut national de la santé et de la recherche médicale

In the third chapter, the concept of **adaptive scanning** is investigated both conceptually and technically. To increase the OCT volumetric acquisition rate, existing techniques (such as compressed sensing and optimisation of scan trajectories) aim to reduce the amount of the data acquired by scanning fewer positions optimally throughout the field of view, resulting in less time used to obtain the data. Despite an improvement in the data acquisition rate, these techniques are open-loop processes, as no use is made of the data previously scanned during the scanning process (the scan trajectories are designed offline prior to OCT scanning). In this research objective, the aim is to propose a **closed-loop capable method**, where a subset of previously acquired data is analysed and used to **predict** the next scan positions that should be scanned (replanning the scan trajectory online). By executing this process, the **amount of OCT data** acquired can be **significantly reduced** (and consequently the time), while still extracting as much useful information as possible. This method is referred to as adaptive scanning, and its effectiveness is demonstrated through simulation and experimental validation.

The fourth chapter highlights the final contribution of this thesis, which deals with the **compensation of 3D motion artefacts in OCT** volumes. In the realm of medical imaging, motion artefacts can arise from both voluntary and involuntary patient movements during the image acquisition process. Involuntary movements, like respiration, and voluntary actions due to patient discomfort (such as being instructed to remain perfectly still or hold one's breath) manifest as artefacts in the captured images. These artefacts can significantly degrade image quality and impede accurate interpretation, resulting in inaccurate diagnoses by medical professionals. In the context of 2D and particularly 3D data acquisition using OCT, motion is a critical issue that introduces geometric artefacts in the data. Therefore, it is essential to develop techniques that measure or correct for object motion in OCT data. In this chapter, a novel numerical method that leverages OCT motion artefacts to **estimate the motion** (linear and angular velocity) from a prior known shape that caused the artefacts, drawing inspiration from robotic and computer vision concepts, is proposed. These estimated velocities are then utilised to compensate for the artefacts, opening the way to robot-assisted motion tracking and, consequently, image stabilisation during robot-assisted surgery. Of particular interest, is the novel methodology in which the relative motion causing distortions in an OCT volume during data acquisition is estimated **without prior knowledge of the shape**, using only **one OCT volume** obtained by the rosette non-raster trajectory. This represents an improvement, eliminating the need to obtain two consecutive OCT volumes to estimate the **shape and motion** in motion-distorted volumes. These developments open up new avenues for research in motion artefact compensation in OCT imaging.

In the final chapter, a summary of conclusions as well as future perspectives are outlined.

---

---

# Chapter 1

## Introduction and motivation for optical coherence tomography

---

<b>1.1</b>	<b>Medical diagnosis</b> .....	6
1.1.1	Physical biopsy .....	6
1.1.2	Optical biopsy .....	7
<b>1.2</b>	<b>Introduction to optical coherence tomography</b> .....	9
1.2.1	OCT working principle .....	9
1.2.2	Comparison of OCT with other medical imaging modalities .....	11
1.2.3	Claimed advantages of OCT .....	12
<b>1.3</b>	<b>Background of OCT technology</b> .....	13
1.3.1	Time domain OCT (TD-OCT) .....	13
1.3.2	Fourier domain OCT (FD-OCT) .....	14
<b>1.4</b>	<b>Development of OCT technology</b> .....	18
1.4.1	Fundamental research in OCT .....	18
1.4.2	OCT adaptation to medical needs .....	21
1.4.3	OCT and robotics .....	24
<b>1.5</b>	<b>Improvement of OCT data acquisition</b> .....	27
1.5.1	Architectural improvements .....	27
1.5.2	Improvement by anticipation of data processing .....	30
<b>1.6</b>	<b>Conclusion</b> .....	31

## 1.1 MEDICAL DIAGNOSIS

Medical diagnosis is the process of determining the underlying cause of a patient's symptoms and condition. This process is critical to the provision of appropriate and effective treatment by a doctor to the patient and it typically involves a combination of assessment, testing and analysis. In medical diagnosis, identification of pathologies such as early abnormal changes (neoplasia) in the mucosa region of a tissue requires technologies that resolve clinically relevant tissue microstructure [Tearney 97]. The testing phase of medical diagnosis includes laboratory tests, imaging studies and other specialised diagnostic procedures. Laboratory analysis necessitates methods such as physical biopsy (also referred to as conventional biopsy) and optical biopsy.

### 1.1.1 Physical biopsy

Physical biopsy is a medical process that involves the extraction of a small tissue sample from a part of the body to determine the presence or extent of a disease as shown in Figure 1.1.

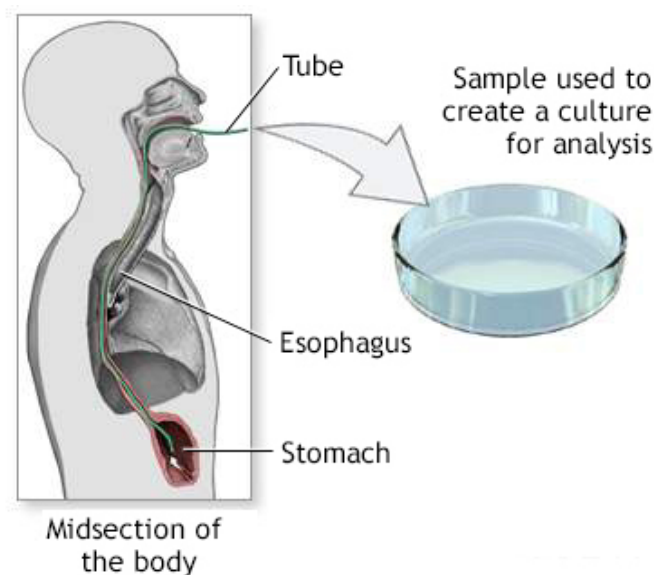


Figure 1.1 – Physical biopsy procedure of the gut [MedlinePlus 21].

The tissue sample could be removed using a needle or surgically removed as a suspicious nodule/lump [Meek 20]. The extracted tissue sample is then examined by a pathologist either chemically or under a microscope. Biopsies are normally conducted so that the surgeon can have insight on the presence of cancer, infections, autoimmune disorders or inflammatory conditions. In as much as a physical biopsy is essential for the medical professional to reach an informed diagnosis of a medical condition, there exists possible complications and limitations [Abhishek 15].



### 1.1.1.a Limitations of physical biopsy

The first major limitation of physical biopsy is the invasiveness of the procedure. Most biopsies require the use of a local or general anaesthesia and involve some level of discomfort or pain to the patient. Moreover, this surgical procedure could expose the patient to accidental contamination of nearby tissues by spreading cancerous cells (when tumour/needle seeding occurs), excessive bleeding and other associated complications such as accidental damage to nearby tissues or organs such as the bowel during abdominal biopsy or the lung parenchyma during lung biopsy [ASCO 21, Temilola 19]. In some cases, the biopsied site may become sore or bruised and may take several weeks to fully heal and/or cause physical changes to the body. For example, a needle biopsy may leave a small scar at the biopsy site and a surgical biopsy may leave a larger scar that is more noticeable. This presents a concern for patients who are worried about the appearance of their body. Another limitation of physical biopsy is the cost and time associated with the procedure. Physical biopsies can be expensive if they are done on an outpatient basis or require a hospital stay. In addition, the results of a biopsy may take several days or even weeks to be returned, which can be frustrating for patients who are anxious to receive a diagnosis and begin treatment. Furthermore, physical biopsies are not always the most accurate or reliable method for diagnosing certain medical conditions such as liver disease diagnosis, specifically, non-alcoholic fatty liver disease (NAFLD). Liver physical biopsy only samples a small portion of the liver which may not be representative of the entire organ. As a result, alternative diagnostic methods such as using imaging modalities as well as blood tests to detect specific biomarkers are preferred [Cheung 18]. In some cases, the tissue sample obtained using needle biopsies might not be sufficient, necessitating the biopsy to be repeated making it more uncomfortable for the patient. Less invasive biopsies such as breast biopsies might be unable to provide sufficient information on the extent or presence of a disease and if the diagnosis is still inconclusive after a technically successful procedure, surgical biopsy is required to be performed [RadiologyInfo 22]. Additionally, the biopsy procedure itself may damage or alter the tissue such that it affects the accuracy of the results.

While physical biopsy is a useful and a necessary tool in medical diagnosis, the presented possible limitations are important considerations for patients and healthcare providers. There exists optical biopsy which addresses some of the limitations of physical biopsy.

### 1.1.2 Optical biopsy

Optical biopsy is a medical procedure whereby a medical diagnosis modality uses the properties of light or other forms of electromagnetic radiation to acquire and examine tissue microstructure with the objective of performing instant medical diagnosis or pathology without tissue removal from the body. Instead of physically extracting the tissue sample and performing histological or cytological analysis, images are taken at a micrometer resolution in a minimally invasive ap-



proach [Brezinski 97]. This is particularly important when physical biopsy can be challenging or highly risky (such as biopsy of the eye). Imaging modalities that are used to perform optical biopsies include optical coherence tomography (OCT), fluorescence endoscopy, confocal microscopy, ultrasound imaging, molecular imaging, Raman spectroscopy, etc [Wang 04, Alfano 13].

#### 1.1.2.a Characteristics of optical biopsy that mitigate the limitations of physical biopsy

Optical biopsy solves most of the potential complications and limitations of physical biopsy. First and foremost, optical biopsy is minimally invasive. In some diagnostic cases such as in ophthalmology and in dermatology optical biopsy is non-invasive since insertion of instruments or probes into the organ is not required. During optical biopsy, multiple images can be taken several times without causing potential harm to the patient. This makes the process much less uncomfortable for the patient and eliminates the risk of tissue contamination by cancer cells, infection, and other possible complications associated with surgery such as excessive bleeding or perforation of body organs. In many cases, optical biopsy can be performed on an outpatient basis making it faster and more convenient than physical biopsy. Most optical biopsies could be completed in a matter of minutes and the results available in real time or within a few hours as compared to physical biopsies which could take days. Optical biopsy also has the potential to be less damaging to the body. This can be beneficial for patients who are concerned about the appearance of their body or who may have a limited number of tissue samples that can be safely removed. In addition, optical biopsy has the likelihood of being more accurate and reliable than physical biopsy in some cases such as liver disease diagnosis [Ren 09]. In another example, optical biopsy techniques such as fluorescence-guided surgery and OCT-guided surgery can visualise cancerous tissue during surgery which allows the surgeons to remove it accurately and completely [Lopater 16, Wang 17]. This could improve the chances of successful treatment by enabling precise targeting of suspicious lesions thereby reducing the risk of recurrence.

Among the optical biopsy techniques that have been mentioned, optical coherence tomography (OCT) has certain advantages that make it attractive such as micrometer resolution allowing to have detailed images at the cellular level and its minimally invasiveness. OCT will therefore be the main focus of this research and will be explored further.

## 1.2 INTRODUCTION TO OPTICAL COHERENCE TOMOGRAPHY

For the past three decades, OCT has been a significant tool in carrying out minimally invasive biopsies. OCT is an optical diagnostic imaging modality that utilises low-coherence interferometry to obtain high-resolution, cross-sectional and volumetric images of internal tissue micro-structure in the micrometer resolution range by measuring echoes of backscattered light [Drexler 10, Bille 19]. The conceptualisation of visualising inside biological tissues using echoes of light was proposed by Michel Duguay at AT&T Bell laboratories in 1971 [Duguay 71a, Duguay 71b]. Duguay used an ultrafast laser activated optical Kerr shutter to create photographs of propagating light pulses using high speed photography. Duguay demonstrated the concept of ‘gated picture ranging’ by placing the AT&T logo behind a scattering screen and partially recovering the image by gating out unwanted scattered light. He suggested that one could ‘see inside’ biological tissues, a concept remarkably close to OCT. Using OCT, pathological analysis of tissues can be done *in situ* with resolutions of  $1 - 15\mu\text{m}$ , which is one to two orders of magnitude finer than conventional ultrasound. These distinct features make OCT a powerful imaging modality having applications spanning several clinical specialities as well as fundamental scientific and biological research [Fujimoto 15].

### 1.2.1 OCT working principle

The basic setup of OCT includes a low-coherence near infrared light source (usually a super-luminescent diode), which directs light through a beam splitter and a scanning mechanism to the tissue being examined as shown in Figure 1.2.

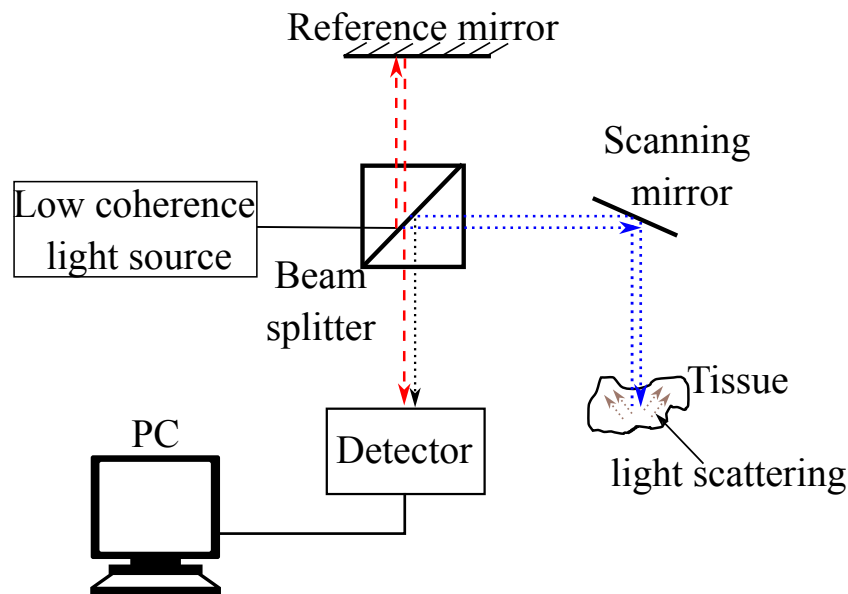


Figure 1.2 – Optical coherence tomography working principle illustration.

A low coherent light is a type of light with a broad range of wavelengths and lacking a stable phase relationship between the photons emitted, often produced by a non-laser light source such as a light emitting diode (LED) or thermal source. The light travels to the beam splitter where it is split into two with one half directed to the tissue sample via a scanning mechanism, and the other half to a reference arm of known length having a mirror at the end. The light perfectly reflects on the mirror while it interacts differently with (biological) samples. The light is scattered as it crosses the non-uniformly oriented tissue. A small part of this light is reflected back towards the beam splitter while the scattered light is lost. The backscattered light from the tissue sample and reference arm are then recombined and collected by a detector. The detector measures the intensity of the backscattered light and the time delay between the light being emitted and the light being received, which is proportional to the distance that the light travelled through the tissue. By carrying out a Fourier transform, this measurement of the back-reflected light versus depth results in a one-dimensional (1D) axial scan (depth scan or A-scan). When the incident optical beam is transversely scanned and sequential axial measurements of the echo time delay performed, a cross-sectional image of the tissue is obtained in grey-scale or false-color shades representing the different levels of light intensity (optical backscattering) through the tissue. The two-dimensional (2D) image from OCT is referred to as a B-scan. Three-dimensional (3D) volumetric data sets are obtained by acquiring sequential cross-sectional images through raster or any other 2D pattern scanning of the incident optical beam at different transverse positions [Pan 20]. The volumetric image obtained contains comprehensive structural information about the tissue sample. The 3D image is referred to as a C-scan. In Figure 1.3 tomographic data in 1D, 2D and 3D are shown.

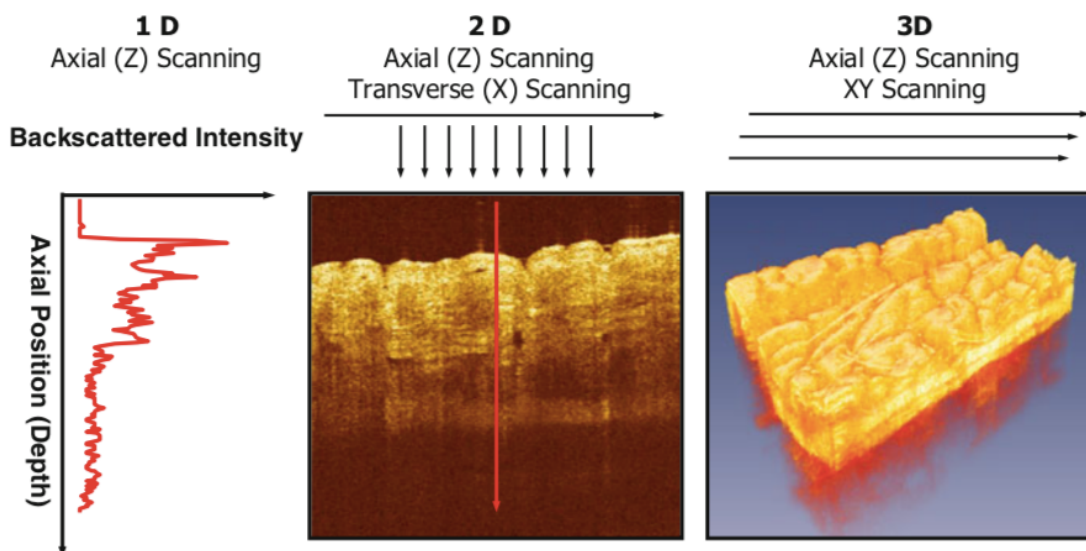


Figure 1.3 – A-scan (1D), B-scan (2D) and C-scan (3D) images obtained using OCT [Fujimoto 15].

Additionally, Figure 1.4 presents a schematic representation of the C-scan, depicting a voxel - a singular element characterised by  $x$ ,  $y$ , and  $z$  coordinates, along with an intensity value. A voxel constitutes an individual unit within an OCT volume once acquired and digitised.

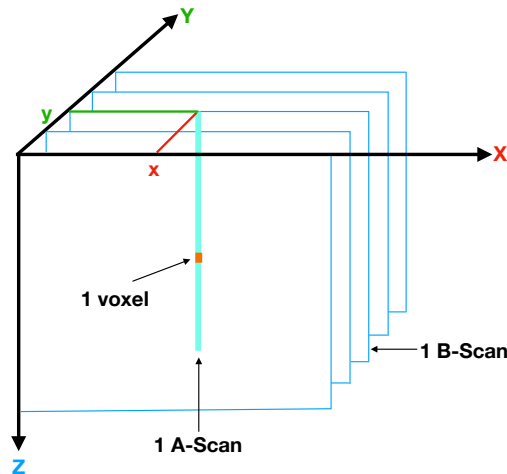


Figure 1.4 – OCT C-scan schematic.

### 1.2.2 Comparison of OCT with other medical imaging modalities

OCT has common features with other medical imaging modalities such as ultrasound imaging and microscopy. OCT imaging is analogous to ultrasound imaging with the exception that instead of using sound waves, light is used. In ultrasound imaging, acquiring the A-scan is referred to as A-mode scanning and the resulting profile referred to as the amplitude scan. In addition, cross-sectional imaging is referred to as B-mode imaging and the resulting image called the brightness scan [Bille 19]. In Figure 1.5, endoscopy, ultrasound, OCT and confocal microscopy imaging are compared in terms of image penetration and resolution. Endoscopy can't 'see' through the tissue and only gives surface level information. Nonetheless, this information can give an observation on the inflammation induced by a tumour, probing the doctor to use other techniques. Ultrasound obtains data at deeper imaging depths, however at a limited resolution. To obtain finer resolution, higher sound frequencies could be used but image penetration would be decreased since the ultrasound attenuation would have been increased. Confocal microscopy has sub-micron resolution, however, its imaging depth is limited to only a few hundred microns in most tissues [Fujimoto 15].

Therefore, OCT falls at an 'optimal position' between imaging depth and resolution when compared to ultrasound and confocal microscopy. OCT enables the doctor to observe tumours that are about 1 – 3mm deep in the tissue with a resolution ranging from 1 to 15 $\mu$ m (about the size of a cell). As compared to other

imaging modalities such as X-ray or computed tomography (CT), OCT does not use ionizing radiation and therefore doesn't increase the risk of cancer or other radiation-induced effects.

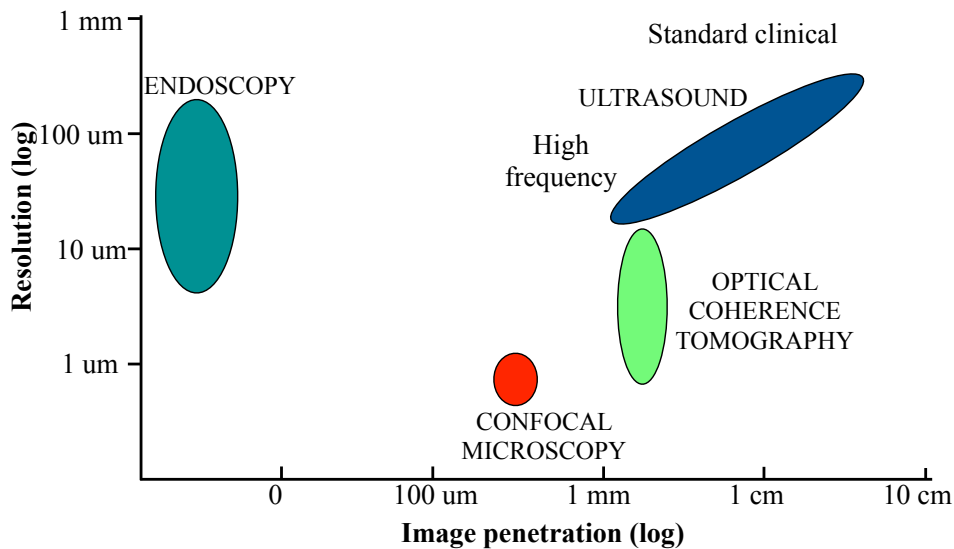


Figure 1.5 – Comparison of endoscopy, confocal microscopy, ultrasound and OCT in resolution and image penetration, adapted from [Fujimoto 15].

In addition, OCT images show good correlation with architectural morphology of histological images as shown in Figure 1.6.

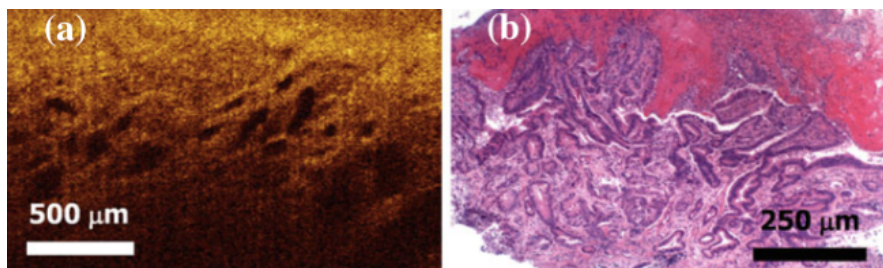


Figure 1.6 – (a) Adenocarcinoma OCT image and (b) its corresponding histology image [Kang 15].

The major limitation of OCT is that it has a limited imaging depth and is typically only useful for imaging shallow tissue structures. Light from OCT is highly scattered and absorbed as it penetrates deeper into the tissue limiting the depth to about 1 – 3mm. As a result, OCT is best suited for imaging structures that are located close to the surface of the tissue.

### 1.2.3 Claimed advantages of OCT

A major advantage of OCT is its high resolution ranging from 1 – 15μm. OCT uses light waves to create detailed images of the body at a cellular level, which allows healthcare providers to see abnormalities within the tissue that may not

be visible using other imaging techniques [Brezinski 97, Lopater 16, Manen 18, Samel 19]. This can be particularly useful for identifying early stage cancers or other abnormalities that may be difficult to detect using other methods. Another advantage of OCT technology is that it is minimally invasive or even non-invasive in some cases [Vakoc 12, Kaur 20]. This makes the procedure much more comfortable for the patient and eliminates the risk of contamination, infection or other complications associated with surgical procedures. In addition, OCT is less expensive than many other imaging techniques, as it does not require the use of more expensive equipment or specialised training to operate. This can be a significant advantage for patients who are concerned about the cost of medical care. Finally, OCT has the potential to be more accurate and reliable than many other imaging techniques, as it provides detailed images of the body at a cellular level. This can improve the chances of a correct diagnosis and the success of treatment [Vakoc 12, Fujimoto 16, Wang 17, Kaur 20].

### 1.3 BACKGROUND OF OCT TECHNOLOGY

OCT technology is categorised into two main families: time domain OCT (TD-OCT) and Fourier domain OCT (FD-OCT), which are subsequently detailed.

#### 1.3.1 Time domain OCT (TD-OCT)

TD-OCT was the first implementation of OCT and its schematic is shown in Figure 1.7.

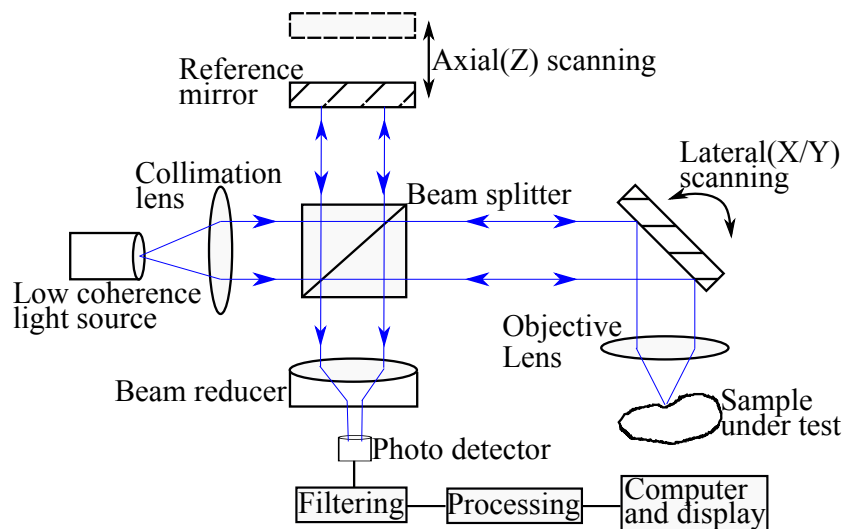


Figure 1.7 – Time domain OCT schematic.

For TD-OCT, the mirror in the reference arm is mechanically moved and the echo time delay measured so as to give the reflectance profile of the sample. TD-OCT is a low speed scanning mechanism since the scan speed is dependent on the



mechanical cycle time of the moving reference mirror. Indeed, moving the axial reference mirror limits the scanning speed to a few thousand A-scans per second leading to a low frame rate and resolution [Aumman 19].

### 1.3.2 Fourier domain OCT (FD-OCT)

Noisy images and the slow data acquisition resulting from TD-OCT impacted the adoption of OCT, and FD-OCT was developed to mitigate the drawbacks of TD-OCT by achieving faster speeds, higher signal-to-noise ratio and detection sensitivity [Aumman 19]. The confirmation of FD-OCT sensitivity advantage over time domain technologies enabled the development of real-time B-Scan imaging to near real-time volumetric imaging while preserving OCT unique features in medical diagnosis [Choma 03, Leitgeb 03]. FD-OCT offers a more efficient implementation of low-coherence interferometry principles by utilising spectral information in the generation of A-scans. Moreover, the stationary reference arm enables an interference spectrum to be obtained which allows for simultaneous measurement of all echo time delays (simultaneous sampling of multiple depth locations). This feature reduces the acquisition time of OCT data. By performing an inverse Fourier transform on the interference signal, the depth profile of the image is then obtained [Chinn 97, Golubovic 97, de Boer 03, Szkulmowski 05]. In spite of the higher resolution and frame rate, FD-OCT requires higher computational resources, including a faster processor and higher-capacity RAM than TD-OCT [Haydar 20]. FD-OCT was further subdivided into two methods for acquiring spectral information from the interferometric signal: spectral-domain OCT (SD-OCT) and swept-source OCT (SS-OCT). Both SD-OCT and SS-OCT involve the recording of an interference spectrum (spectral interferogram), from which the A-scan is computed through Fourier transformation. These methods have introduced significant advancements and additional features to the field of OCT.

#### 1.3.2.a Spectral-domain OCT (SD-OCT)

For SD-OCT, a broad bandwidth light source is used and detection of the interference spectrum from the interferometer is done using a spectrometer as can be seen in Figure 1.8. Despite SD-OCT having high imaging speed advantages, it has unique artefacts that are not present in TD-OCT. SD-OCT is subject to mirror/inverted image artefacts when the sample is positioned incorrectly. A-scans are obtained by SD-OCT detection through Fourier transforming the interference spectrum of backscattered light from a sample with light from a reference path delay which determines a ‘zero delay’. Standard SD-OCT detection machines are unable to distinguish between positive and negative time delays as compared to the zero delay. Therefore, if the sample is exactly at the reference zero delay position or if features cross this zero delay, then the OCT image appears folded about this zero delay producing a ‘mirror’ artefact as seen in Figure 1.9. In other words, the magnitude of the Fourier transform is symmetric for positive or negative values, making it unable to distinguish between positive and negative time delays.

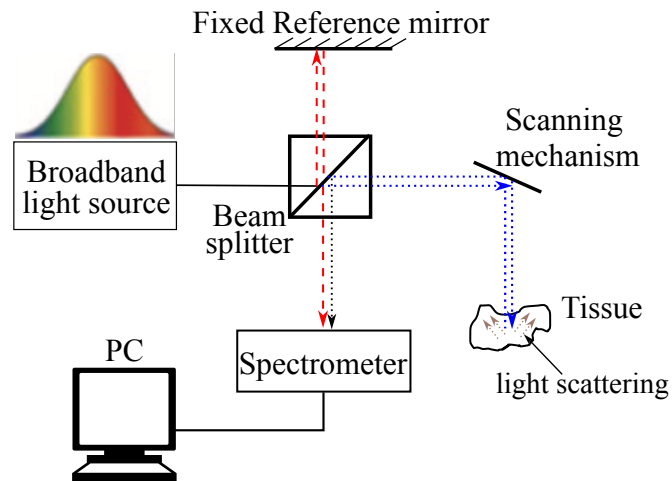


Figure 1.8 – Spectral-domain OCT schematic.

Furthermore, in spectral-domain detection, the detection sensitivity varies with the measurement range. It is most sensitive to echoes near the zero delay position, gradually decreasing as the distance from the zero delay increases [Fujimoto 15].

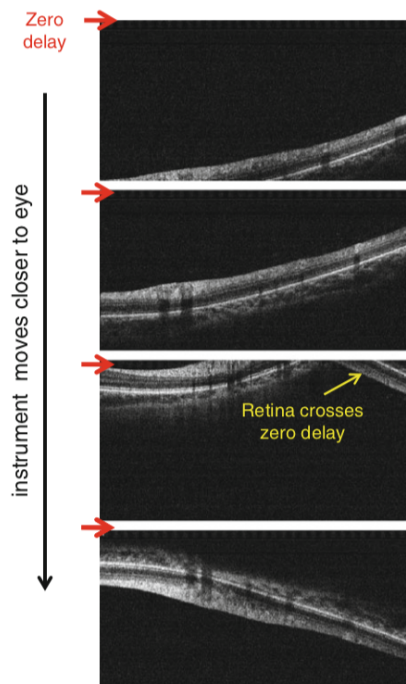


Figure 1.9 – Mirror artefact in spectral-domain OCT [Fujimoto 15].

### 1.3.2.b Swept-source OCT (SS-OCT)

SS-OCT, also referred to as optical frequency domain interferometry (OFDI), utilises a similar optical configuration to TD-OCT. However, instead of a broadband light source, SS-OCT employs an optical source that rapidly sweeps a narrow



line-width across a wide range of wavelengths. Within a single sweep, the interferometric signal is sequentially detected for each wavelength component by a high-speed photodetector. This process yields a spectral interferogram similar to the one observed in SD-OCT. The schematic of SS-OCT is given in Figure 1.10.

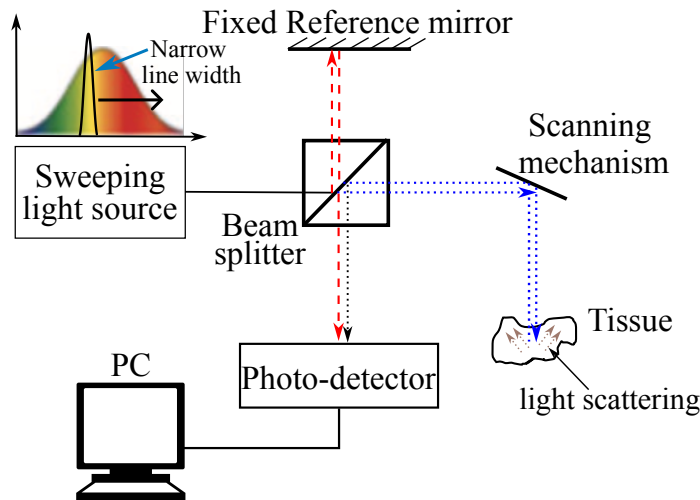


Figure 1.10 – Swept-source OCT schematic.

### 1.3.2.c Comparison of spectral-domain OCT and swept-source OCT

These two different techniques of Fourier domain detection have the following distinguishing characteristics [Tsai 14, Bhende 17]:

#### SS-OCT

- Improved sensitivity since there is no spectrometer loss and the photodetector used for detection is more sensitive than cameras.
- Improved system dynamic range because it uses high speed and low noise photo detectors and higher bit depth acquisition systems.
- Can provide a very large number of axial samples as determined by the speed of data acquisition systems.
- Well suited for applications requiring the fastest possible imaging speeds at wavelengths of  $1.3\mu m$  and  $1\mu m$ .

#### SD-OCT

- Provides a crucial resolution advantage ( $< 3\mu m$ ) over SS-OCT since it uses a light source with a broader selection of operation wavelength and bandwidth.

Acquisition speed in SD-OCT is limited by the line-scan rate whereas in SS-OCT, it is limited by the sweep rate of the swept-source and subsequent analog to digital conversion. Therefore, for applications where slower speeds are acceptable, but axial resolution is of critical importance, such as retinal imaging, SD-OCT remains the dominant technology.

### 1.3.2.d Comparison of time domain, spectral-domain, and swept-source optical coherence tomography

In Table 1.1, a comparison summary of the three OCT technologies is given. It is also shown in Figure 1.11, the improvement in quality of OCT images from time domain to Fourier domain i.e., spectral-domain OCT and swept-source OCT.

Table 1.1 – Comparison of time domain, spectral-domain, and swept-source optical coherence tomography [Bernardes 12, Bhende 17].

	<b>Time domain OCT</b>	<b>Spectral-domain OCT</b>	<b>Swept-source OCT</b>
<b>Data acquisition</b>	Superluminescent diode (810 nm) single photon detector, moving axial mirror.	Superluminescent broadband diode source (840 nm), array of detectors, fixed axial mirror.	Swept-source tunable laser (1050 nm), single detector, fixed axial mirror.
<b>Scanning speed</b>	400 A-scans per second	27,000 - 70,000 A-scans per second	100,000 - 400,000 A-scans per second
<b>Axial resolution</b>	10 - 15 $\mu\text{m}$	5 - 7 $\mu\text{m}$	5 $\mu\text{m}$
<b>Transverse resolution</b>	20 - 25 $\mu\text{m}$	3 - 20 $\mu\text{m}$	5 - 20 $\mu\text{m}$

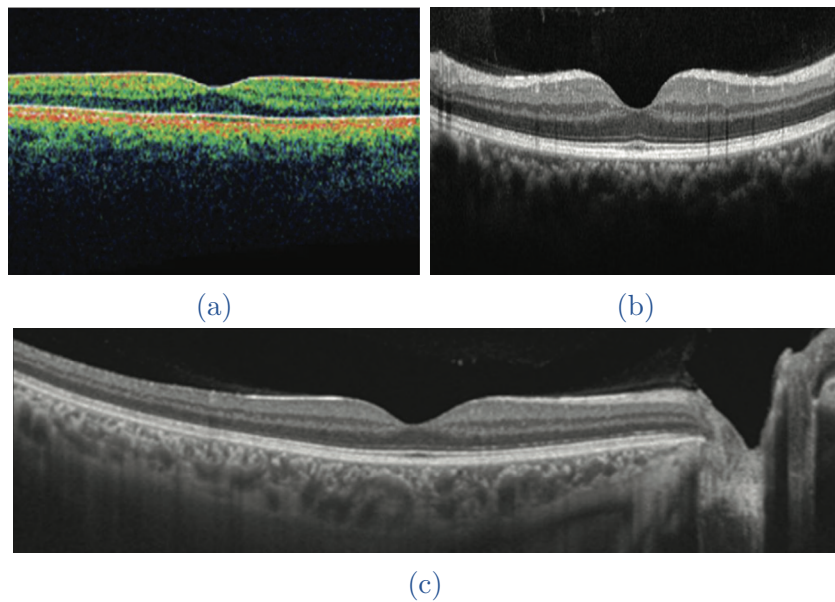


Figure 1.11 – B-scan images of (a) time domain, (b) spectral-domain, and (c) swept-source OCT of normal macula in the eye [Bhende 17].

## 1.4 DEVELOPMENT OF OCT TECHNOLOGY

In the late 1990's, potential use of OCT in surgical interventions was first conducted [Brezinski 97]. The results indicated that intra-operative OCT (iOCT) could have substantial benefits as compared to other imaging modalities not only because it had better resolution but also because OCT was based on optical communication technology that could be readily integrated into conventional surgical instruments and microscopes. With the widespread revolution of FD-OCT of the early 2000's, several key technological developments enabled the introduction of OCT into the operating suite i.e., handheld OCT probes [Boppart 97, Radhakrishnan 01], microscope-integrated OCT [Boppart 98, Lankenau 07, Tao 10] and OCT guided laser surgery [Boppart 99, Palanker 10]. As a result, there was an increase in OCT commercialisation and adoption in clinical diagnosis especially in ophthalmology, gastroenterology, oncology, and cardiology [Manen 18, Tsai 14]. Presently, OCT is the gold standard of care in ophthalmology.

### 1.4.1 Fundamental research in OCT

In this subsection, a few examples of variations in OCT technology aimed at enhancing imaging are discussed.

#### 1.4.1.a Polarization-sensitive optical coherence tomography (PS-OCT)

Polarization-sensitive OCT (PS-OCT) is a variation of OCT that utilises the information carried by polarized light to create images and obtain additional information on the tissue [Pircher 11, De Boer 17, Baumann 17, Martin 22]. Figure 1.12 shows a schematic of PS-OCT.

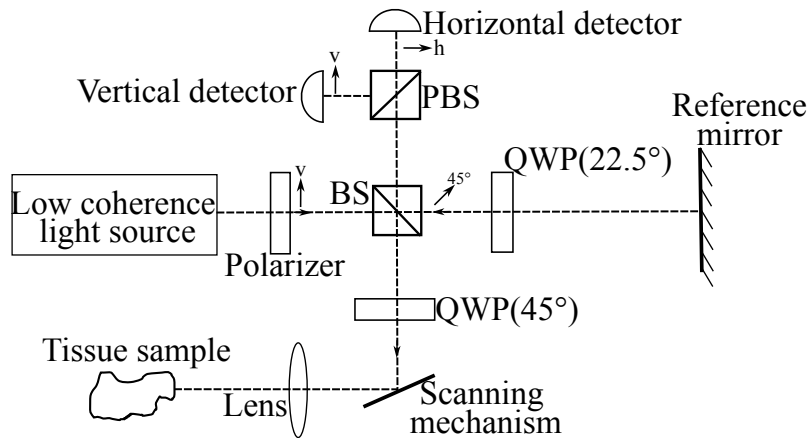


Figure 1.12 – Polarization-sensitive OCT schematic. BS - beam splitter, QWP - quarter-wave plate, PBS - polarizing beam splitter, v - vertical, h - horizontal.

In Figure 1.12, light from the OCT light source (swept laser source or broad-band light source) is vertically linearly polarized by a polarizer before entering a Michelson interferometer. The incoming light is then split into a sample beam and

a reference beam by the polarization insensitive beam splitter (BS). In the reference arm, the light travels through a quarter-wave plate (QWP) oriented at  $22.5^\circ$  to the vertical. This orientation ensures that the light becomes linearly polarized with a polarization plane of  $45^\circ$  with respect to the incident light, having traversed the QWP twice. This configuration provides equal reference light intensity in both detection channels. In the sample arm, the light passes through a QWP oriented at  $45^\circ$ , resulting in circularly polarized light incident on the sample, which enables retardation measurements independent of the sample axis orientation. This setup ensures that the measured polarization parameters are independent of the birefringent axis orientation of the sample. The light backscattered from the sample is generally in an elliptical polarization state as it enters the detection arm of the interferometer. In the detection arm, the interfering reference and sample beams are separated into horizontal ( $x$ ) and vertical ( $y$ ) polarization states by the polarizing beam splitter (PBS), and their corresponding interference signals, recorded by the photodetectors [Pircher 11, De Boer 17].

Not only does PS-OCT provide information on tissue microstructure, but is also used to detect changes in the birefringence (splitting of a light wave into two unequally reflected or transmitted waves by an optically anisotropic medium) of the tissue, which can be used to identify certain types of tissue structure, such as nerve fibers. This added information gives rise to better tumour detection on OCT images. It has been shown by Hariri *et al.*, that PS-OCT has the potential to distinguish between lung tumor and fibrosis [Hariri 13]. Kiseleva *et al.* also utilised PS-OCT in the diagnosis of mucosal pathologies in *in-vivo* human bladders [Kiseleva 15].

#### 1.4.1.b Doppler optical coherence tomography (DOCT)

Doppler optical coherence tomography (DOCT) is a non-invasive imaging technique that combines the principles of OCT with the Doppler effect to measure blood flow [Fercher 95] as shown in Figure 1.13.

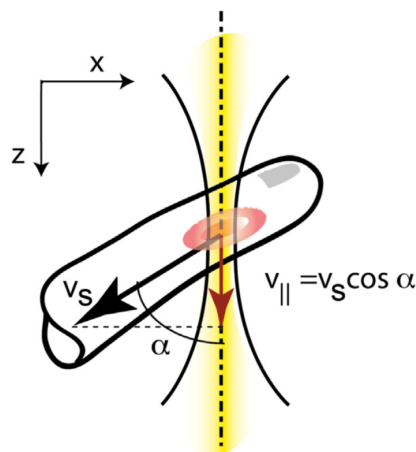


Figure 1.13 – Doppler optical coherence tomography measures the axial velocity component  $v_{||}$ . The yellow line represents the OCT beam [Leitgeb 14].

The Doppler effect is a phenomenon that occurs when a source of light is moving relative to an observer. It causes a shift in the frequency of the light, which can be used to measure the velocity of moving particles, such as blood cells. DOCT uses a laser light source to illuminate the tissue and a detector to detect the backscattered light. The backscattered light is split into two paths: a reference path and a sample path. The reference path is used to obtain a high-resolution image of the tissue, while the sample path is used to measure the Doppler shift in the frequency of the light. The Doppler shift is proportional to the velocity of the moving particles in the tissue such as blood cells. DOCT can be used to measure blood flow in various organs and tissues, including the eye, heart, brain, and skin. In ophthalmology, DOCT can be used to measure blood flow in the retina and choroid, which is important for the diagnosis and management of retinal diseases such as diabetic retinopathy and age-related macular degeneration (AMD). In cardiology, DOCT can be used to measure blood flow in the coronary artery, which is important for the diagnosis and management of coronary artery disease. In neurology, DOCT can be used to measure blood flow in the brain, which is important for the diagnosis and management of cerebrovascular diseases such as stroke [Fujimoto 03]. One of the advantages of DOCT is its ability to measure blood flow in real-time, which allows for dynamic monitoring of the blood flow in the tissue. Additionally, DOCT has high spatial resolution, which allows for detailed imaging of the microvasculature in the tissue. DOCT also has high sensitivity and specificity, which allows for the accurate measurement of blood flow [Huang 14]. However, DOCT has a limited penetration depth and it may not be able to measure blood flow deep inside the tissue [Zhu 18].

### 1.4.1.c Spectroscopic optical coherence tomography (SOCT)

Spectroscopic OCT is a non-invasive imaging technique that combines the principles of OCT with spectroscopy to obtain both structural and molecular information from biological tissues [Morgner 00]. In addition, SOCT is also used to obtain information about the various biomolecules in biological tissues such as lipids, water, haemoglobin, collagen and elastin. In dermatology, SOCT has been used to measure the concentration of melanin and haemoglobin in the skin, which is important for the diagnosis and management of pigmented skin lesions such as melanoma [Soundararajan 19]. In ophthalmology, SOCT can be used to measure the thickness of the retinal nerve fibre layer, which is important for the diagnosis and management of glaucoma. In cardiology, SOCT can be used to measure the concentration of lipids and collagen in the coronary artery, which is important for the diagnosis and management of atherosclerosis [Nam 18]. An advantage of SOCT is its ability to obtain both structural and molecular information from biological tissues. Additionally, SOCT has high spatial resolution and high sensitivity, which allows for detailed imaging of the microstructure and biomolecules in the tissue. However, SOCT has a limited penetration depth and it may not be able to obtain information from deep inside the tissue. SOCT also has a high cost of instrumentation and complex data analysis [Fujimoto 03, Nam 18].

### 1.4.2 OCT adaptation to medical needs

In this sub-section, a few adaptations of OCT technology for medical purposes will be discussed.

#### 1.4.2.a Hand-held optical coherence tomography (HHOCT)

For patients under anaesthesia who are unable to maintain the required posture during medical imaging using conventional table-top OCTs, Hand-held OCT (HHOCT) probes have proven to be extremely valuable [Swanson 93]. The first HHOCT probe which used a piezoelectric cantilever for the translation of a light-delivering fibre and scan a focused beam across a sample was reported by Boppart *et al.* [Boppart 97]. However, this fibre based system had a limited field of view and the image acquisition rate was slow as compared to the conventional galvanometer approach. When galvanometer scanners were incorporated, the image acquisition rate increased at the cost of the weight and size of the scanner. Miniaturisation approaches [Tanguy 20] then led to the use of micro-electromechanical system (MEMS) devices which resulted in significantly smaller, lighter and more compact HHOCT probes [Lu 14, LaRocca 16].

Conventional OCT scanners have a limitation on the depth of penetration the light can bypass. Needle-based OCT probes can bypass opacities and highly light attenuating tissue to facilitate deep tissue imaging in turbid media [Boppart 97, Liang 11]. In ophthalmic surgery, needle-based probes which are small enough to be inserted into the surgical ports at the pars-plana have been used to bypass the optics of the microscope and patient. The success of HHOCT has inspired the integration of 1D and 2D OCT imaging into surgical instruments to ensure alignment of images with the instrument tip and provide a level of feedback control during surgical procedures [Balicki 09, Song 13]. The Kang group at John Hopkins University demonstrated that A-scans could be acquired adjacent to the tooltip by mounting a fibre-optic common-path OCT probe along or within the shafts of forceps and needles for vitreoretinal surgery as shown in Figure 1.14 [Cheon 15].

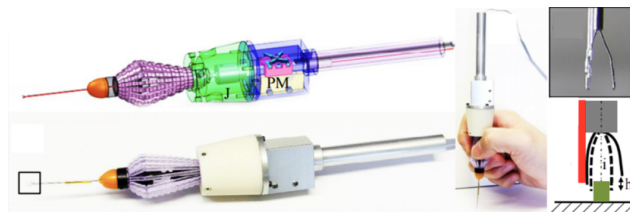


Figure 1.14 – Surgical forceps with a common path OCT system for axial ranging using A-scans only [Cheon 15].

#### 1.4.2.b Microscope-integrated optical coherence tomography (MIOCT)

HHOCT has a limitation of introducing imaging surgical pauses (brief period of less than one minute in which operating-room activity pauses immediately before incision). The positioning angle of HHOCT might not be optimal for the



surgeon conducting the surgery necessitating the help of an assistant to hold the OCT device during the operation. A potential solution is to integrate the OCT sample arm into the operating microscope required for microsurgeries such as ophthalmic surgery and neurosurgery. This design called microscope integrated OCT (MIOCT) enhances the surgeon's workflow by allowing live OCT imaging during surgery and facilitates faster decision making during surgeries.

Nonetheless, this approach presents a problem; integrating the OCT and microscope after the objective reduces the microscope working distance, potentially obstructing the surgical workflow. A solution that has been implemented [Lankenau 07, Tao 10] is the coupling of the two modalities prior to the microscope objective at the expense of degrading OCT optical performance. Examples of commercialised MIOCT designs that have already received FDA 510(k) clearance are given in Figure 1.15. They include;

- Zeiss RESCAN 700 for human ocular surgery. This system houses a permanently integrated OCT scanner coupled directly prior to the microscope objective and was FDA cleared in 2014 [Zeiss 14].
- iOCT Camera system for human ocular surgery commercialised by Haag-Streit Surgical. This system uses a modular OCT scanner attached to the camera port of the microscope and was FDA cleared in 2015 [Surgical 15].
- Leica Microsystems EnFocus for human ocular surgery. This system uses a modular OCT scanner attached prior to the objective and was FDA cleared in 2015 [Microsystems 15].

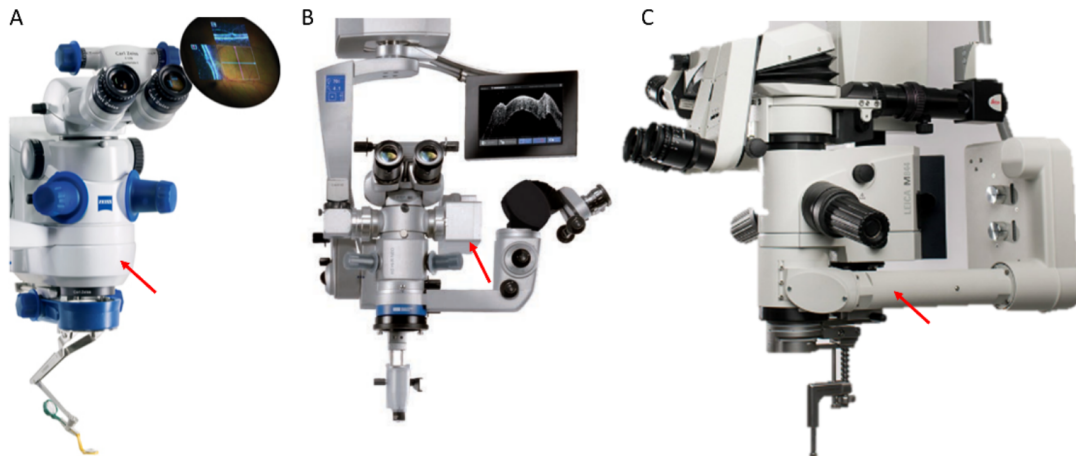


Figure 1.15 – Commercial MIOCT systems. (A) Zeiss RESCAN 700. (B) Haag-Streit Surgical iOCT. (C) Leica Microsystems Bioptigen EnFocus. Red arrows denote the location of the OCT scanners [Carrasco-Zevallos 17].

#### 1.4.2.c Endomicroscopy using optical coherence tomography

In [Gora 13a, Gora 13b], enhanced imaging of the upper gastrointestinal tract was achieved by utilizing a swallowable tethered capsule implemented with OCT technology as shown in Figure 1.16b. Tethered capsule endomicroscopy (TCE)

offers three-dimensional microscopic information throughout the entire esophagus, making it valuable for studying various disorders such as Barrett's esophagus without the need for sedation. The TCE capsule, an opto-mechatronic engineered pill measuring  $1\text{mm}$  by  $24\text{mm}$  as shown in Figure 1.16a, is tethered to a distal end via a string-like structure. Once ingested by the patient, the TCE capsule acquires OCT images while traversing the esophagus through peristalsis. In a standard imaging session lasting about 5 minutes, the entire esophagus undergoes multiple OCT imaging scans as illustrated in Figure 1.16 c-f. After completing OCT image acquisition, the capsule is guided upward through the esophagus using the tether. The retrieved capsule is then sterilised for re-use, significantly minimising utilisation costs. Recent clinical experiences with tethered capsule endomicroscopy involving 26 subjects, including 10 patients with Barrett's esophagus, revealed that only two healthy volunteers faced difficulty swallowing the capsule, and five patients experienced a mild gag reflex. Impressively, high-quality images covering over 50% of the esophageal circumference were obtained in 93.7% of frames for subjects without hiatal hernia and 89% for patients with hiatal hernia. Advancements in tethered capsule endomicroscopy technology were demonstrated in swine models, incorporating an integrated micro-motor and linear translation mechanism within the capsule to facilitate the visualisation of high-quality *en face* views of the epithelium [Liang 15].

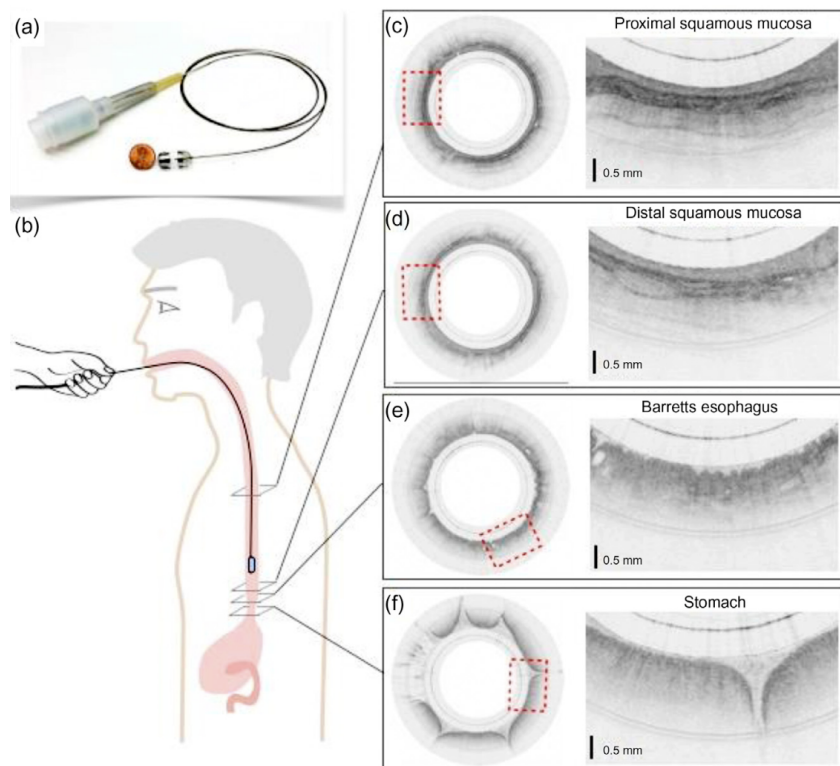


Figure 1.16 – (a) Tethered capsule endomicroscope, (b) schematic of the procedure of tethered capsule endomicroscopy, (c-f) esophagus images obtained using the tethered capsule endomicroscope utilising OCT [Gora 16].



### 1.4.3 OCT and robotics

#### 1.4.3.a Optical coherence tomography guided laser surgery

OCT guidance and monitoring of laser surgery was first explored in the late 1990s and later studies have shown the feasibility of OCT in monitoring structural alteration after prostate tissue ablation *in vivo* [Boppart 01] and laser treatment of laryngeal carcinoma surgery [Shakhov 01]. The integration of OCT into laser surgical systems improves the lateral and depth positioning of laser ablation [Li 14]. In [Zhang 14], Zhang *et al.* demonstrated a closed-loop control of a short-pulsed CO<sub>2</sub> laser with tunable pulse durations (20s to 100s) and energies ranging from 4.2 mJ to 28.5 mJ per pulse to perform laser cochleostomy under the the monitoring of an OCT system, achieving a foresighted detection of the bone-endosteum-perilymph boundary several hundred micrometers before its exposure. The setup of the OCT system and CO<sub>2</sub> laser is schematically illustrated in Figure 1.17. A preliminary *ex vivo* evaluation on fresh porcine cochleae showed that the ablation process terminated automatically when the thickness of the residual tissue layer uniformly reached a predefined value. This resulted in the shape of the resulting channel bottom converging to the natural curvature of the endosteal layer without causing injury to the critical structure. The potential of OCT to guide the laser ablation process by detecting the position of the subsurface critical structure before its exposure, allowing for a more precise and atraumatic surgical approach to the human cochlea was demonstrated.

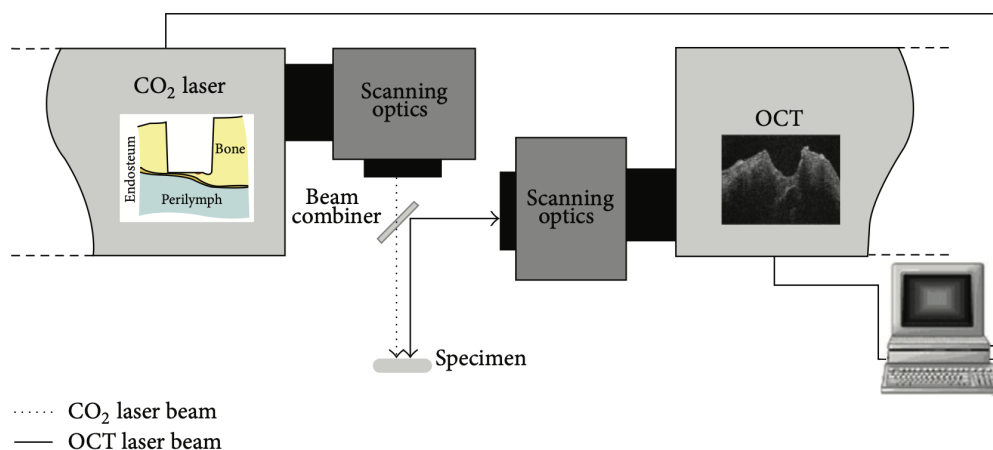


Figure 1.17 – Schematic diagram of the coaxial setup of the OCT system and the CO<sub>2</sub> laser with overlapping working spaces [Zhang 14].

#### 1.4.3.b Optical coherence tomography-assisted robotic medical procedures

The coupling of OCT into surgical systems as described with MIOCT has facilitated the exploration of OCT-assisted robotic surgery. This introduced the driving of robotic platforms that position surgical instruments using OCT image-based feedback with improved precision as compared to manual surgery [Yu 13, Yu 15].

In [Baran 17], OCT images were used to provide medical information as well as guide surgical devices. An image-guided closed loop controller was proposed to perform an inplane positioning task of a concentric tube robot with respect to a biological sample. In [Ahronovich 23], Ahronovich *et al.* proposed a novel approach for localised drug delivery in the eye using OCT B-scan images in conjunction with a serial robot arm for cooperative manipulation. The cooperative robotic system is illustrated in Figure 1.18. This system comprises a distal micro-manipulator, which serves as a handheld tool for OCT-assisted injection, and is connected to a 6 degree of freedom (DOF) serial robot arm to enable cooperative manipulation. By including B-scan OCT imaging, specific target regions for drug delivery are identified, and the robot control is adjusted accordingly; the admittance gains, which determine the robot response to external forces, are manually set and regulated in proportion to the distance between the injection needle and the target location using OCT feedback. This approach provides proximity-aware assistance to the user, facilitating finer motion control and enhancing safety by restricting robot movements when in close proximity to the target injection site. The experimental results demonstrated the feasibility of safe needle injection through constrained cooperative control motions of the serial robot. This innovative system has the potential to enhance precision and accuracy in localised drug delivery procedures, opening up new possibilities for ocular treatments.

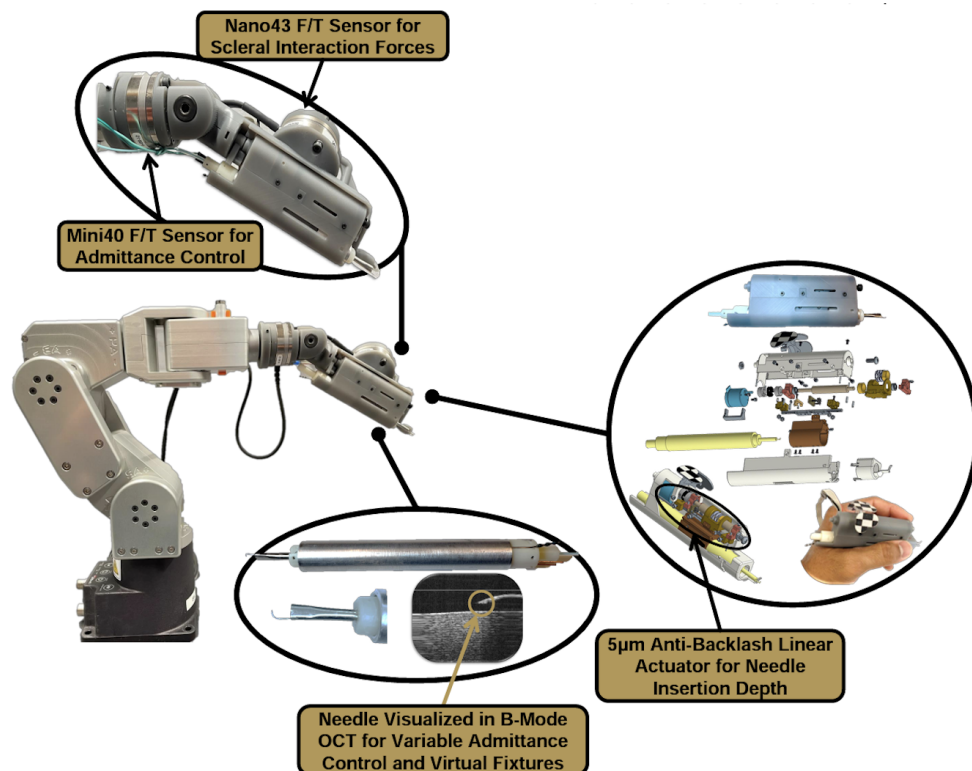


Figure 1.18 – Cooperative robotic system consisting of a custom OCT probe and a drug delivery channel [Ahronovich 23].

## 1.4.3.c Visual servoing using optical coherence tomography

During optical biopsies, the surgeon would like to monitor the progression (shape, texture, size) of treatment of a tumour or abnormality in the body. This necessitates capturing the volumetric image at precisely the same initial location during each visit. Ourak *et al.* [Ourak 16] developed a system that combines a camera and an OCT system to perform 6 degrees of freedom visual servoing for automatic and repeated optical biopsies based on wavelets coefficients. The system setup allowed for simultaneous imaging of the tissue surface by the camera and the subsurface structures by the OCT. The visual information from the image obtained from the camera and the B-scan obtained from the OCT device were used to control the position and orientation of a parallel robot end-effector. The system represented a promising approach for performing automatic and repetitive optical biopsies by combining the advantages of both the camera and OCT images. While Ourak *et al.* used B-scan images from the OCT device, Dahroug *et al.* [Dahroug 20] improved further the technique by using C-scans (volumetric OCT data) as an input signal to the visual servoing controller as depicted in Figure 1.19.

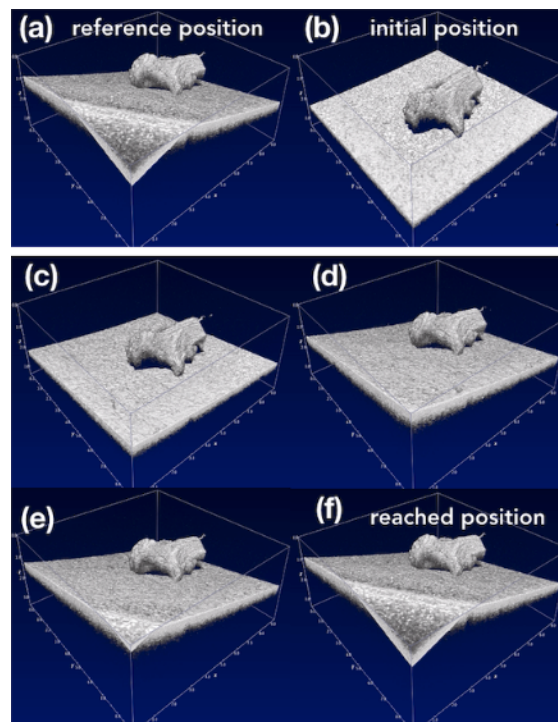


Figure 1.19 – Image sequence showing the 3D positioning task achievement. (a) shows the desired pose, (b) the initial pose, (c)-(e) represents intermediate pose acquired during the positioning task and (f), the reached pose [Dahroug 20].

The OCT device was used as a sensor to control robot motion by estimating the 3D pose of the sample from the C-scan image using principal component analysis (PCA). PCA is a mathematical technique that is used to reduce the dimensionality of the data and extract relevant features from the OCT volumetric

image for visual servoing. The experimental results showed a positioning accuracy of  $0.052 \pm 0.03mm$  (mean error  $\pm$  standard deviation) for linear errors and  $0.41 \pm 0.16^\circ$  for angular ones over a  $8 \times 9 \times 3.5mm^3$  workspace.

In [Zhang 21], Zhang *et al.* developed a system that uses image guidance to control the position and movement of an endoscopic robot for OCT path scanning. The proposed visual control strategy was achieved by using an image feedback from both a monocular endoscopic camera (eye-to-hand) and an OCT probe (eye in hand). The OCT device was used to acquire images of the subsurface structures in the tissue while the camera acquired planar images of the tissue surface. The image-guided control algorithm used the information from the camera images to control the position and movement of the endoscopic robot and ensured that the OCT probe is properly positioned to acquire high-quality images. The system used an image-based visual servoing approach which used the images from the camera to compute the control command to be applied to the robot. The method was tested on simulated and real scenarios and the results showed that the image-based visual servoing approach was able to accurately control the position and movement of the endoscopic robot and improve the quality of the acquired OCT images by providing more detailed information about the tissue subsurface structures.

## 1.5 IMPROVEMENT OF OCT DATA ACQUISITION

Despite the advantages of OCT, 3D data acquisition is time-consuming. For instance, acquiring a volume of  $10 \times 10 \times 3.5mm^3$  using a standard SD-OCT system, such as the Telesto II 1325nm from Thorlabs, requires more than 1 minute and 10 GBs of RAM for a preview of a 3D volumetric image with micrometer resolution ( $5.5\mu m$  and  $7\mu m$  for axial and lateral resolution respectively). Firstly, during data acquisition, the object needs to be scanned, and then the data undergoes image processing for visualisation. For volumetric visualisation, huge amounts of data are processed compared to when 2D data is acquired. Secondly, the scanning speed is limited by mechanical constraints such as the kinematics and mechanical bandwidth inherent in the scanner. Therefore, the quality and rate of data acquisition can be increased by: i), developing better scanners through architectural improvements or, ii), improving the data processing steps through hardware improvements such as using GPUs or software improvements such as compressed sensing.

### 1.5.1 Architectural improvements

#### 1.5.1.a Optics improvements

##### Adaptive optics

Adaptive optics (AO) is a technique used to enhance the resolution of an optical imaging device by actively correcting static and dynamic aberrations in the optical system [Bille 19]. In retinal imaging, the diffraction-limited optical resolution is

primarily determined by the numerical aperture of the human eye. The numerical aperture is constrained by the given focal length of the eye and the maximum pupil diameter which can be dilated to approximately  $8\text{mm}$ , resulting in a numerical aperture (NA) of around 0.24. Hence, theoretically, a resolution of approximately  $2\mu\text{m}$  can be achieved at a wavelength of  $840\text{nm}$ . However, in practice, the optical resolution is compromised when the pupil is dilated, as the optical aberrations of the human eye increase significantly with pupil diameter. This decrease in optical performance outweighs the potential benefits of a higher NA [Bille 19].

Adaptive optics utilises an adaptive optical component such as a deformable mirror. The precise deformation of the mirror enables to compensate for distortions caused by light scattering in tissue, refractions, and aberrations, thereby, enhancing the quality of OCT images [Carroll 05]. A schematic of adaptive optics is depicted in Figure 1.20. In the field of ophthalmology, AO-OCT has proven to be highly effective in improving the visualisation of retinal structures, including individual cells and capillaries [Godara 10]. Furthermore, AO-OCT has demonstrated its utility in enhancing imaging of the cornea, lens, and anterior chamber of the eye [Akyol 21, Jayabalan 19]. In addition, AO-OCT has found success in endoscopic OCT, where it corrects for aberrations originating from the distal optics of the endoscope. This correction enables high-resolution and high-contrast imaging of deep tissue structures, particularly valuable in gastroenterology and urology applications. By reducing the effects of tissue scattering, adaptive optics can also enhance the penetration depth of OCT, making it advantageous for imaging highly scattering tissues such as the skin, oral mucosa, and breast tissue. Additionally, the integration of adaptive optics with other techniques like polarimetry and full-field OCT allows for the extraction of additional information from tissue samples [Pircher 17]. The integration of adaptive optics into optical coherence tomography has proven to be a transformative advancement, revolutionising image quality, resolution, and contrast.

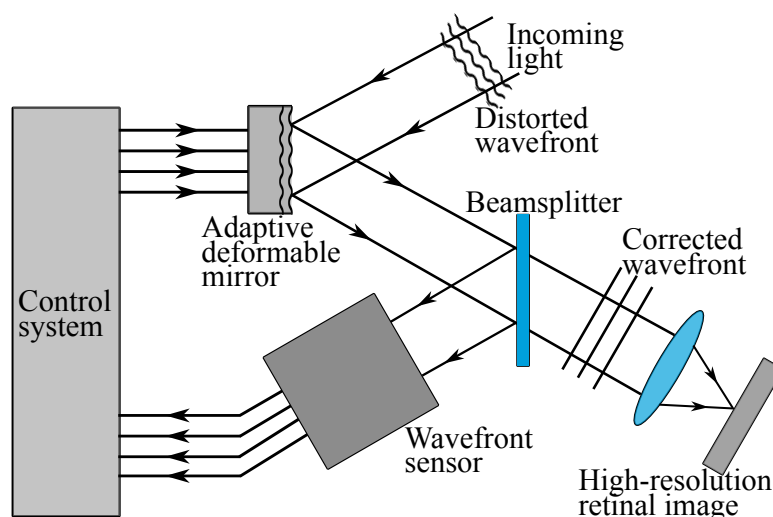


Figure 1.20 – Adaptive optics components and configuration, adapted from [Krawitz 16].

## 1.5.1.b Opto-mechatronic improvement

## Galvanometer and micro-electromechanical systems (MEMS) scanning mechanisms

The galvanometer scanner (GS) is the conventional device for implementing the scanning function in OCT systems [Carrasco-Zevallos 17]. A galvanometer scanner is a type of mirror that is capable of rotating rapidly and precisely in two dimensions [Duma 15]. This allows the OCT device to scan the tissue in a raster pattern illuminating different locations and collecting backscattered light at each location. A galvanometer scanner has a high scanning and rotation speed which allows the OCT system to acquire images quickly. A limitation of the galvanometer scanner is that aberrations can be introduced in the image due to the non-uniformity of the mirror surface. Noise can also be introduced in the image due to the mechanical vibrations of the scanner. The galvanometer scanner is also bulky which adds up to the overall weight of the OCT system. To overcome these limitations, researchers proposed the use of adaptive optics to improve the efficiency of scanning in OCT. Another proposal was the replacement of the bulky galvanometer scanner with a micro-electromechanical system (MEMS) scanner [McCormick 06, Strathman 15, Gorecki 21]. An electrothermal MEMS scanning mechanism is shown in Figure 1.21. MEMS scanners are much faster than the galvanometer scanner since they can be actuated at high frequencies. This is beneficial in high-speed imaging or wide-field imaging where high temporal resolution is required. MEMS scanners also offer a higher accuracy and stability. This is due to the fact that, they are much smaller and have a lower mass than galvanometer scanners resulting in a lower inertia (consequently low power consumption) and more precise movement. Another advantage of MEMS scanners is that they are more compact and lightweight making them suitable for portable or handheld devices [Sun 11]. This is particularly beneficial in applications such as endoscopic or laparoscopic imaging where the size and weight of the device is an important factor [Huang 14, Hwang 17, Tanguy 20].

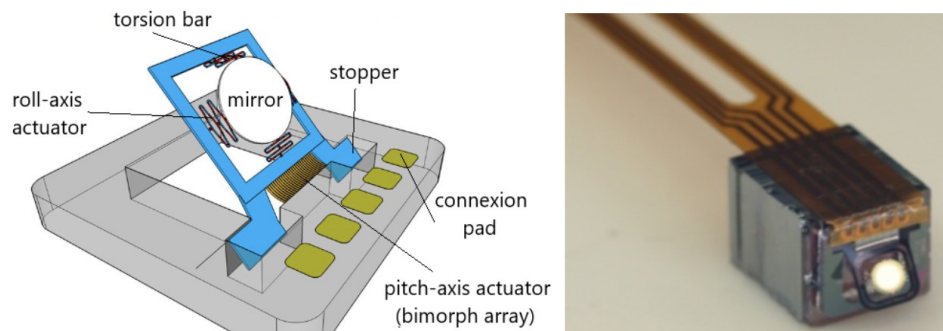


Figure 1.21 – Electrothermal mirror: (a) schematic and (b) microphotograph of a MEMS scanner assembled on top of a Mirau interferometer [Gorecki 21].



## 1.5.2 Improvement by anticipation of data processing

In this sub-section, the focus is on employing strategies prior to data acquisition in anticipation of processing to enhance the quality of the obtained OCT data.

### Compressed sensing

FD-OCT was developed as an improvement to TD-OCT and is characterised by a high speed scanning mechanism and better resolution [Wang 15]. Despite this superiority, FD-OCT has some challenges in its use in medical applications. The required time to acquire, process, transfer and store 3D volumetric data is highly problematic. It needs a faster processor and requires more time. FD-OCT also requires the use of high performance array detectors such as CCD (charge coupled device) to discretise and digitise the spectral interferograms at high resolution and frame rate [Choma 03]. The use of such sensors substantially increases the computation cost as well as the monetary cost of the FD-OCT system. To overcome these challenges when volumetric data is obtained using OCT, the acquisition rate can be efficiently increased through under-sampling. Implementing under-sampling, the amount of measurement data acquired is reduced with the aim of retaining the final quality of the OCT volume while at the same time significantly reducing the data acquisition time [Haydar 20, Luo 19b]. This scheme, referred to as compressed sensing, was developed by Donoho in 2006 [Donoho 06]. Compressed sensing is a mathematical technique applied in signal processing to efficiently acquire and reconstruct a signal by finding solutions to under-determined linear systems [Maass Marco 17]. It is based on the paradigm that through optimisation, a signal can be recovered by exploiting its sparsity and using fewer samples at a sub-Nyquist rate. Recovery of the signal is dependent on the signal being sparse and the sampling data being incoherent (i.e., randomly or at least non-uniformly distributed).

Haydar *et al.* investigated and successfully applied compressed sensing on a commercial FD-OCT system [Haydar 20]. The galvanometer mirrors equipping the OCT system were directly controlled to acquire a limited number of A-scans. The OCT volume was then able to be recovered with experimental results showing promising performance in terms of quality of the reconstructed volumetric images when compared to ground truth data. Researchers in Shanghai Jiao Tong University also used ‘sparse sampling’ to significantly acquire fewer 2D images and then applied compressive sensing algorithms to supply missing data and reconstruct the images. They confirmed that effective volumetric OCT imaging can be done with 40% less experimental data [Wang 18]. Implementing compressed sensing to OCT volume acquisition, results in obtaining fewer A-scans, which reduces the acquisition time and required volume processing energy (energy required to discard unwanted data) [Haydar 20]. Then the question would arise: how do we find a good balance between compression rate and reconstruction? Higher compression

rates increases reconstruction time but decreases the quality of the image/volume. Lower compression rates, on the other hand, increases the raw quality of the image/volume at the expense of acquisition time.

#### Modification of scan trajectories

The conventional scan trajectory used in OCT devices is the raster trajectory which involves scanning a single line of light across the tissue and then moving to the next line in a top-to-bottom sequential fashion. Raster scanning is widely adopted due to its simplicity; however, it suffers from drawbacks such as relatively slow imaging speed and the introduction of distortions in the OCT image [Bazaei 12, Sang 16, Carrasco-Zevallos 18]. To address these limitations, non-raster scan trajectories could be used. These alternative scan trajectories do not adhere to a regular grid pattern and can be optimised to better suit the characteristics of the object being scanned. Examples of non-raster scan trajectories include the spiral, Lissajous, radial, and rosette trajectories, among others. Each of these trajectories has its own set of unique advantages and disadvantages regarding OCT data acquisition. Nonetheless, there is currently no standardised criteria developed in the literature to assess these scan trajectories, as well as the quality of the volumetric OCT data obtained through their implementation in data acquisition. Moreover, these non-raster scan trajectories can be further enhanced to selectively acquire informative data in the field of view.

#### Compensation of motion artefacts

During the process of medical imaging for tissues within the human body, involuntary physiological phenomena like breathing can cause tissue movement, resulting in the introduction of motion artefacts. Neglecting to account for tissue motion during data acquisition or image processing can lead to a degradation in image quality, potentially leading to inaccurate medical diagnoses [Walther 08]. In the context of OCT, when acquiring 2D and 3D data, motion becomes a critical issue that needs to be addressed. Motion artefacts are inherent in OCT imaging due to the underlying principles of data acquisition (one-dimensional data sequentially captured over a period of time), in addition to potential motion of the imaged object in various physiological scenarios. Consequently, it is crucial to develop techniques that can measure or correct for object motion in OCT data [Kraus Martin 15].

## 1.6 CONCLUSION

In this chapter, the working principle and an overview of the application of optical coherence tomography (OCT) have been discussed, recent technological advancements and potential approaches to enhance OCT data acquisition has also been presented. OCT data acquisition can be improved through architectural



modifications or by employing improvement strategies in anticipation of data processing. For this PhD research, the focus is on leveraging improvement strategies in anticipation of data processing as the preferred approach to enhance OCT performance. Subsequent chapters will delve deeper into these methods and investigate their efficacy in improving OCT data acquisition. Firstly, to fully take advantage of implementing non-raster trajectories in OCT data acquisition, the following research objectives will be pursued:

- ✓ Development of a criteria to assess the performance of different scan trajectories in OCT data acquisition. This assessment will aid in comparing and selecting the most suitable scan trajectory for specific imaging scenarios.
- ✓ Development of an adaptive scanning protocol that focuses on acquiring data only from informative regions. This protocol aims to optimise the data acquisition process by selectively capturing relevant information in the field of view.

And to enhance the overall quality and reliability of the obtained OCT data to facilitate more accurate interpretations more so in medical settings, the final research objective will focus on:

- ✓ Presentation of a motion artefact compensation method, which addresses the challenges posed by motion-induced distortions in OCT imaging.

The ultimate goal of these objectives is to advance optical coherence tomography and reinforce its capabilities for various clinical applications.

---

## Chapter 2

# Multi-criteria assessment of optical coherence tomography using non-raster trajectories

---

<b>2.1</b>	<b>Background and motivation</b> . . . . .	35
2.1.1	Contributions of this chapter . . . . .	36
<b>2.2</b>	<b>OCT scan trajectories</b> . . . . .	38
2.2.1	Raster scan trajectory . . . . .	38
2.2.2	Other scan families: non-raster scan trajectories . . . . .	39
<b>2.3</b>	<b>Qualitative analysis</b> . . . . .	42
2.3.1	Fast preview . . . . .	42
2.3.2	Geometric smoothness of the scan trajectory . . . . .	43
2.3.3	Connection with compressed sensing . . . . .	44
2.3.4	Waveforms, velocity, and acceleration profiles of scan trajectories . . . . .	45
2.3.5	Conclusion of qualitative analysis . . . . .	45
<b>2.4</b>	<b>Novel criteria for quantitative assessment of OCT scan trajectories</b> . . . . .	47
2.4.1	Exploitation vs exploration (local vs global quality) . . . . .	47
2.4.2	Smoothness of the scan trajectory . . . . .	48
2.4.3	Spatial resolution of the scan trajectories . . . . .	50
2.4.4	Conclusion of quantitative analysis . . . . .	51
<b>2.5</b>	<b>Experimental assessment of OCT volumes</b> . . . . .	52
2.5.1	Experimental set-up . . . . .	52
2.5.2	OCT volume file format . . . . .	52
2.5.3	OCT volume similarity assessment to ground truth . . . . .	53
2.5.4	Exploitation vs exploration . . . . .	55
2.5.5	Progressivity (fast preview) of the scan resolution. . . . .	56
2.5.6	Time analysis of the scan trajectories . . . . .	58
2.5.7	Summary of scan trajectories assessment . . . . .	59

**2.6 Conclusion** ..... 60

## 2.1 BACKGROUND AND MOTIVATION

In conventional OCT scanning, 3D datasets are acquired using a raster trajectory where one lateral axis of the galvanometer scanner (GS) is made to follow a saw-tooth signal while the other axis follows a ramp or staircase set point [Duma 15, Pan 20]. OCT volumetric scan data is then acquired in sequential B-scans from top to bottom having uniformly spaced A-scans and resulting in a rectangular scan area in the  $x - y$  plane as shown in Figure 2.1b.

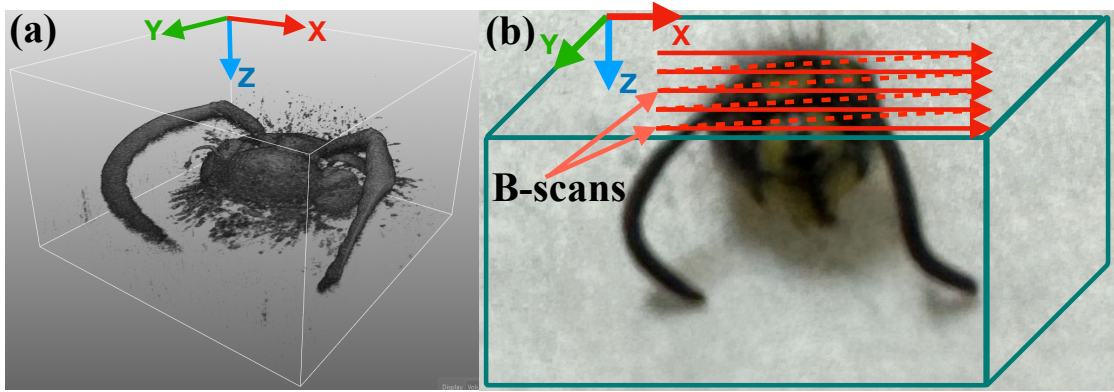


Figure 2.1 – (a) OCT volume (C-scan) of a biological sample (head of a bee) obtained using the conventional raster scan trajectory, (b) photo of the bee-head as well as sequential B-scans on the  $x - y$  plane.

The actuation mechanism and mechanical bandwidth of the galvanometer scanner plays a role in the data acquisition time. Raster scanning necessitates the galvanometer scanner to have lateral (fast) and vertical (slow) scanning frequencies, which results in higher driving voltages due to high accelerations and lowers the mechanical stability of the scanner [Gorecki 21]. Figure 2.2 illustrates a 2D scanning system with two galvanometer scanners.

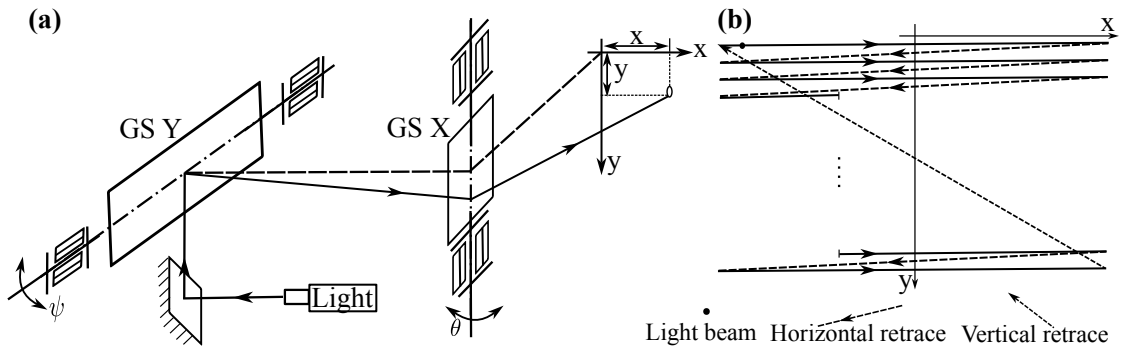


Figure 2.2 – (a) 2D scanning system with two galvanometer scanners with perpendicular axis (GS X for the fast axis scan and GS Y for the slow axis scan), (b) raster scan trajectory in the  $x - y$  plane. Adapted from [Duma 19].

The raster scan trajectory has long acquisition times since it scans blankly while changing direction in each B-scan from top to bottom, resulting in reduced data acquisition efficiency [Carrasco-Zevallos 18, Sang 16]. To increase the imaging rate, improved mechanical designs have been proposed [Kenton 11, Maroufi 15] as well as advanced controllers implemented to push the limits of those designs [Yong 12b, Rana 12, Tang 21]. Despite these improvements, the raster trajectory still suffers from speed limitations. This is because the raster trajectory requires relatively higher accelerations as compared to other scanning trajectories [Nikooienejad 19]. An alternative approach to increase the OCT data acquisition rate is through modifying the software used. This approach has the benefit that it can be implemented on any OCT device without making any major modifications on the hardware. One such method is through modifying the raster trajectory commonly used in acquiring OCT data into a non-raster trajectory. Non-raster trajectories have superior optical sampling uniformity and eliminate the need for B-scan and inter-volume acquisition dead times required in raster scanning [Carrasco-Zevallos 18, Tanguy 20].

### 2.1.1 Contributions of this chapter

In recent years, there has been an increasing interest in developing new strategies for OCT to improve image quality, reduce acquisition time and increase the field of view. These strategies include altering the scan trajectory from raster to non-raster scan trajectories as well as compressed sensing to acquire data sparsely and perform reconstruction of the image [Tanguy 20, Park 14, Welge 13]. However, at the time of this research there is no standardised criteria to be used in evaluating the scan trajectory used as well as the quality of OCT volumetric data obtained by employing these different strategies. Furthermore, there is limited analysis of full OCT volumes obtained using non-raster scan trajectories. Most of the existing assessment has been done on volume slices rather than on full volumes. The contributions of this chapter all aim at providing to new and expert OCT users, a multi-criteria assessment tool to be used in assessing several families of scan trajectories in addition to the OCT volumetric point cloud data of static objects obtained using these trajectories. A particular scan trajectory can then be selected by the user depending on their use-case application. The OCT data quality assessment is done using the PointPCA [Alexiou 21] similarity index which is suited to work directly on volumetric data as opposed to slices (this makes up one of the technical contribution). The quality of the OCT volume should be sufficient as well as the data acquisition rate to be fast enough for real-time visualisation especially when miniaturised OCT probes are mounted on a robotic endoscope [Strathman 15, Mora 20, Zhang 21]. Acquisition time is of course highly dependent on the volume of the object scanned and the hardware characteristics of the scanner. For a given volume and scanner, the acquisition time also depends on three so far under-looked criteria that have been made explicit in this chapter and that are related to the scan trajectory.

The first novel criterion is the smoothness of the scan trajectory. Ideally, the scan trajectory should have a constant velocity. Indeed, non-constant velocities result in higher acceleration and jerk. This thereby increases the mechanical wear and tear of the scanner as well as the energy consumption, which should be avoided both for economic and environmental reasons. High accelerations of the scanner also result in potential degradation of the image quality depending on the geometric distribution of the high and low velocities over the field of view. This concern yields our proposal for a second novel criterion.

Images are normally represented in a rectangular shape, but the human eye has a circular field of view with a central zone of highly accurate attention, and a peripheral zone having less accuracy but sensitive to the appearance of new objects in the scene [Hans 11]. The eye's mobility allows one to change their focus of attention. Following this bio-inspiration, it is proposed to assess separately the image quality in the central zone of the OCT field of view (named the exploitation zone) and the quality in the periphery (the exploration zone). This yields our exploitation/exploration ratio criterion which is particularly useful in robot-assisted endoscopic OCT probe for intracorporeal optical biopsy. Indeed, the OCT probe location can be adjusted through robot control to a line of sight having more useful information (exploitable region) for better data acquisition efficiency. Moreover, this opens up the possibility of simplifying the creation of large mosaics (combining several smaller images to form a larger one) since the explored zone provides a sparse dataset that overlaps with the neighbouring exploitation zone.

Last but not least, the perceived frame rate is more relevant to a user than the actual acquisition frequency. Old television sets used interlaced images to reach the  $25Hz$  human visual frequency whereas the progressive (raster) display on the screen by the cathode ray tube was twice slower. Less old displays of high-resolution images on the Web also used a fast preview mode where a low-resolution image is first shown and its fine details and quality improved as the image is being downloaded to the display. Similarly, in the clinical case of optical biopsy, the doctor would gain time when searching for a lesion in a tissue if he/she can reject rapidly (at first glance) a healthy current region in the exploitation zone while staying longer in a suspicious zone to get more details. Also, since OCT is inherently a progressive process with unavoidable time delays (and thus image distortion), a scan trajectory with a fast preview would likely deliver less distorted (or more frequently updated) images/volumes. Therefore, it is essential to assess image/volume quality with respect to scan progression forming the progressivity criterion.

By providing a standardised framework for evaluating different scan strategies, the proposed criteria will enable researchers and non-expert users alike to compare and optimise different OCT systems for various applications. Thus, to allow for a better comparison between scan trajectories used in OCT data acquisition, it is proposed to present the performance of the trajectories against the mentioned criteria on a radar plot rather than try to come up with a unique score. Finally, through extensive experimental analysis, it is confirmed that faster data acquisition

while maintaining a good enough quality score is possible using non-raster scan trajectories. It is also revealed that the rosette scan trajectory has a better trade-off in satisfying the selected criteria.

## 2.2 OCT SCAN TRAJECTORIES

A scan trajectory is a continuous function of time with values in  $\mathbb{R}^2$  which determine the path (geometric trace) traced in a 2D Cartesian plane:

$$C : [0, T] \rightarrow \mathbb{R}^2$$

$$C \mapsto \begin{bmatrix} x(t) \\ y(t) \end{bmatrix} \quad (2.1)$$

where  $T$  is the duration and  $x(t)$  and  $y(t)$  are the A-scan positions in the  $x$  – axis and  $y$  – axis respectively. In this section, the raster and non-raster scan trajectories used to acquire OCT data will be discussed.

### 2.2.1 Raster scan trajectory

For OCT, the conventional scan trajectory used is the raster as shown in Figure 2.3a. The resolution is the ratio of the scan length to the number of scan points per line. To improve upon the data acquisition efficiency of the conventional raster trajectory, a bi-directional raster trajectory that eliminates the blank interval during which no data is collected was developed [Carrasco-Zevallos 18]. The A-scan position distribution remains the same as the conventional raster, but the trajectory evolution with time differs, as shown in Figure 2.3b. OCT data acquisition occurs during both the forward and backward movement of the scanning beam.

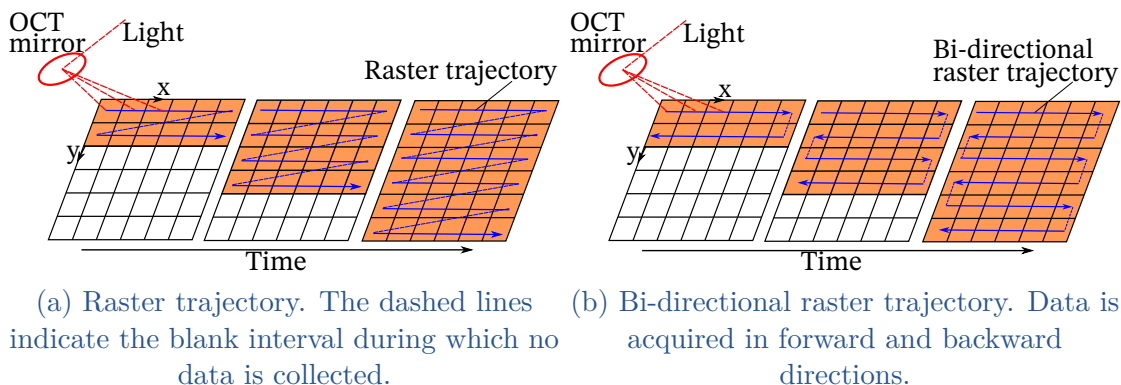


Figure 2.3 – Illustration of the scan trajectory based on the raster (a) and bi-directional raster (b) as they evolve with time.

### 2.2.2 Other scan families: non-raster scan trajectories

Non-raster (also referred to as continuous or non-Cartesian) scanning is an alternative to raster scanning whereby the light continuously scans the object without any acquisition dead times. These scan trajectories include spiral, Lissajous, rosette, splines, etc. The resulting concatenation of A-scans obtained using a parametric non-raster trajectory results in a free-form B-scan as shown in Figure 2.4b and 2.5c.

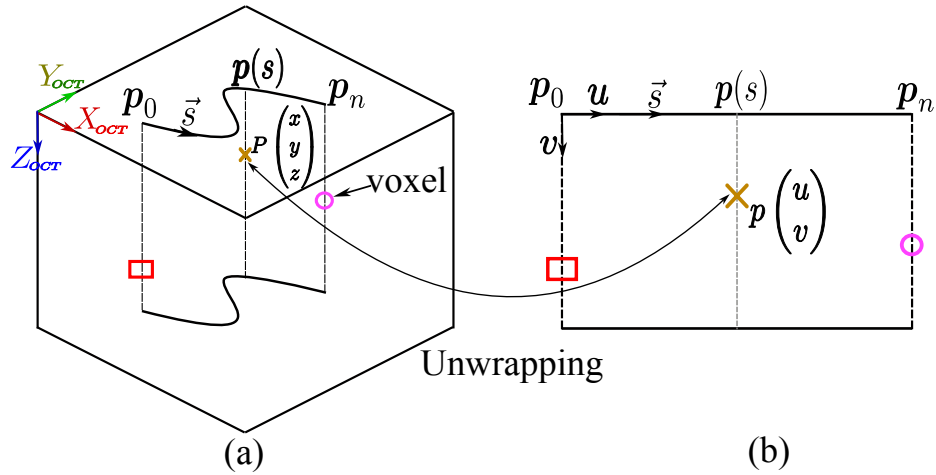


Figure 2.4 – (a) 3D view of a free-form B-scan of a smooth trajectory, (b) Unwrapped B-scan.

The top-view ( $x - y$  plane) of the non-raster trajectory is illustrated in Figure 2.5a and 2.5b.

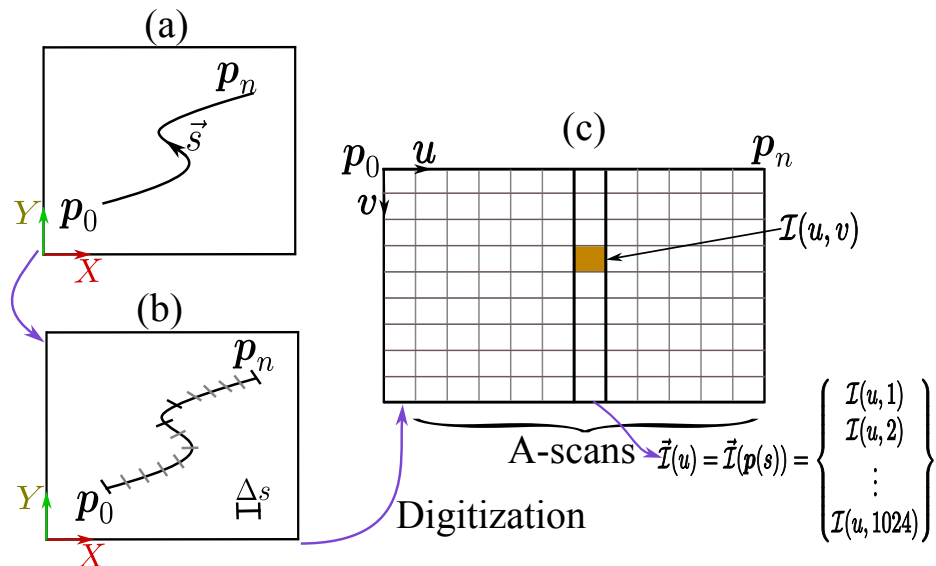


Figure 2.5 – (a) Top view of a free-form smooth trajectory, (b) Segmented free-form smooth trajectory, (c) Unwrapped and digitized B-scan illustrating A-scans and voxels.



OCT data is collected at a scan position  $\mathbf{p}(s)$  along the trajectory (as illustrated in Figure 2.4a), producing an A-scan,  $\vec{\mathbf{I}}(u)$  represented by a set of voxels. A voxel is the basic unit of an A-scan, defined by coordinates  $x, y, z$  and an intensity value. The segmentation in depth is determined by a distance of  $\frac{\text{max OCT penetration depth}}{\text{number of depth locations}}$ . With 1024 depth locations during OCT data acquisition, a single A-scan would comprise 1024 voxels, as illustrated in Figure 2.5c.

### 2.2.2.a Spiral trajectory

A spiral trajectory is a smooth curve that fills a 2D space without any intersections. Spiral scanning has been applied to achieve high-speed scanning in atomic force microscopy (AFM) [Mahmood 11] and magnetic resonance imaging [Delattre 10]. Spiral scanning was also used in OCT [Carrasco-Zevallos 18] where it was experimentally demonstrated to have achieved greater sampling uniformity as compared to the bi-directional raster scanning given equivalent transverse sampling parameters for both scan types. The scan position distribution of spiral scanning is shown in Figure 2.6 at different time intervals. Considering the Archimedean spiral, it can either be a constant angular velocity (CAV) spiral or a constant linear velocity (CLV) spiral depending on how the trajectory is traced.

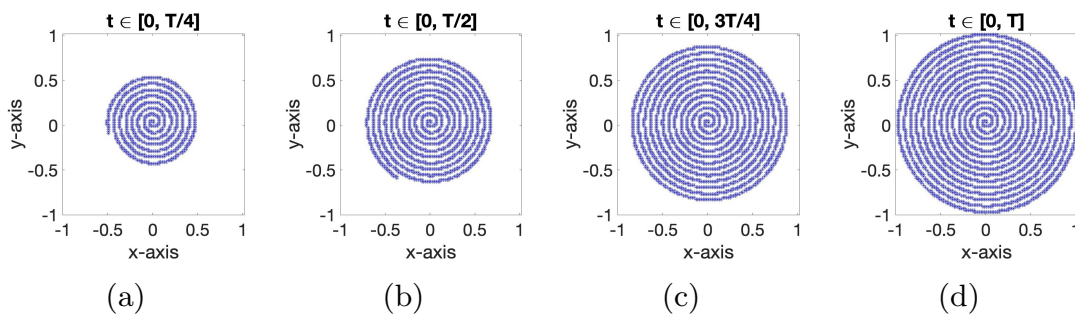


Figure 2.6 – Spiral scan trajectory at different time intervals. (a) At time  $t \in [0, T/4]$ . (b) At time  $t \in [0, T/2]$ . (c) At time  $t \in [0, 3T/4]$ . (d) At time  $t \in [0, T]$ .  $T$  is the period of scanning.

For the CAV spiral, the equation to generate the required waveform is [Sang 16]:

$$\begin{aligned} x_a(t) &= r_a(t)\cos(\theta_a) \\ y_a(t) &= r_a(t)\sin(\theta_a) \end{aligned} \quad (2.2)$$

where  $\theta_a = \omega_a t$ ,  $\omega_a = 2\pi f$  and  $r_a$  is the instantaneous radius at time  $t$ .

Similarly, the equation to generate the CLV spiral is [Mahmood 10]:

$$\begin{aligned} x_l(t) &= r_l(t)\cos(\theta_l) \\ y_l(t) &= r_l(t)\sin(\theta_l) \end{aligned} \quad (2.3)$$

where  $\theta_l$  for time varying  $\omega_l$  is obtained as:  $\theta_l = \sqrt{\frac{4\pi vt}{P}}$  where  $v$  is the linear velocity and  $P$  the pitch of the spiral.

## 2.2.2.b Lissajous trajectory

A Lissajous scan trajectory is obtained when the scanner lateral axes track purely sinusoidal waveforms having fixed amplitudes but different frequencies in an odd ratio. The Lissajous trajectory has been implemented in atomic force microscopy, scanning probe microscopy (SPM) and recently in OCT where it was shown that high-quality images/volumes at much higher frame rates were experimentally achieved at very low voltages by using the resonant modes of the scanner [Bazaei 12, Tuma 12a, Tanguy 20]. The Lissajous scan trajectory scan positions distribution is shown in Figure 2.7 at different time intervals.

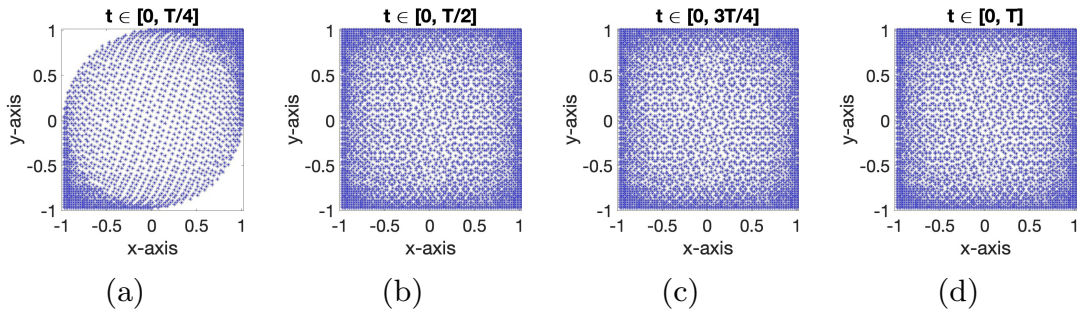


Figure 2.7 – Lissajous scan trajectory at different time intervals. (a) At time  $t \in [0, T/4]$ . (b) At time  $t \in [0, T/2]$ . (c) At time  $t \in [0, 3T/4]$ . (d) At time  $t \in [0, T]$ .  $T$  is the period of scanning.

The Lissajous scan trajectory is generated by making the lateral  $x$  and  $y$  axes of the scanner to track the sinusoidal signals in equation 2.4 [Bazaei 12]:

$$\begin{aligned} x_L(t) &= A_x \cos(\omega_x t) \\ y_L(t) &= A_y \cos(\omega_y t) \end{aligned} \quad (2.4)$$

where  $\omega_x = 2\pi f_x$  and  $\omega_y = 2\pi f_y$  are positive constant frequencies with respect to  $x$  and  $y$  axes respectively. And  $A_x$  and  $A_y$  are positive amplitudes with respect to the  $x$  and  $y$  axes respectively.

## 2.2.2.c Rosette trajectory

The rosette scan trajectory is an epitochoid where the distance between the centre of the rolling circle and the rotating point is equal to the sum of the radii of a fixed and a rolling circle. It intersects itself at specific points creating curvilinear rhombus interstices. In [Nikooienejad 19], a rosette scan pattern was designed and implemented successfully in a commercial atomic force microscopy device with a micro-electromechanical system (MEMS) nano-positioner as the scanning stage. This facilitated continuous sequential atomic force microscopy imaging without the need for a high bandwidth tracking controller. The authors in [Nikooienejad 19] also elaborated that the rosette scan trajectory doesn't require back and forth motions and that the self-intersections of large temporal separation provides information that may be used to detect and remove height drift (image artefacts

where sample features are partially removed or tilted due to the thermal fluctuations of instrument parts, specifically, slow expansion and contraction) in atomic force microscopy images [Meyer 14]. The rosette scan trajectory scan positions distribution is shown in Figure 2.8.

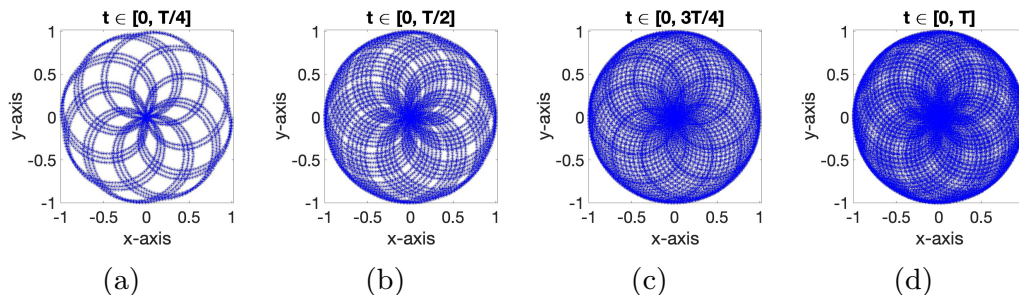


Figure 2.8 – Rosette scan trajectory at different time intervals. (a) At time  $t \in [0, T/4]$ . (b) At time  $t \in [0, T/2]$ . (c) At time  $t \in [0, 3T/4]$ . (d) At time  $t \in [0, T]$ .  $T$  is the period of scanning.

The rosette trajectory is generated when the  $x$  and  $y$  axes of the scanner are made to trace the waveforms as given in [Nikooienejad 19]:

$$\begin{aligned} x_{rs}(t) &= r_{rs} \cos(n\theta_{rs}) \cos(\theta_{rs}) \\ y_{rs}(t) &= r_{rs} \cos(n\theta_{rs}) \sin(\theta_{rs}) \end{aligned} \quad (2.5)$$

where  $r_{rs}$  is the radius,  $\theta_{rs} = 2\pi f_{rs}t$ ,  $f_{rs}$  is the fundamental scan frequency and  $n$  is the irrational number which leads to distinct rosette shapes.

## 2.3 QUALITATIVE ANALYSIS

In this section, subjective judgement is used to assess different criteria of performance of the non-raster scan trajectories against the conventional raster trajectory. Although we haven't explicitly included the bi-directional raster, sinusoidal raster, or other potential OCT scan trajectories (radial, cycloidal, splines, etc) in this assessment, the proposed methodology can be applied to any other OCT scan trajectory.

### 2.3.1 Fast preview

During medical diagnosis, the surgeon relies on B-scans to make informed decisions [Gora 16]. However, if a specific B-scan lacks the necessary information, they must search for another, which can be time-consuming. Alternatively, by quickly previewing the optical biopsy volume (fast preview), the surgeon can have a faster diagnosis. From the conventional raster scan trajectory in Figure 2.3a, the scan progresses sequentially from top to bottom in the  $x - y$  plane. The spiral scan trajectory progresses as well in the  $x - y$  plane either from the centre outwards

with increasing radius or from the maximum radius to the centre as seen in Figure 2.6 (the radial resolution as the spiral radius grows increases proportionally with time). The Lissajous scan trajectory as seen in Figure 2.7 traverses the entire scan area in half a period then navigates in the reverse direction during the second half period [Yong 12a]. The rosette scan pattern intersects itself at specific points as seen in Figure 2.8. The Lissajous and rosette scan trajectories have a faster preview since most of the data in the field of view (FOV) is scanned in half a period (the resolution increases globally in the field of view as time progresses with the rosette being continuously updated in the central region). The raster and spiral scan trajectories have a slower image/volume preview since the field of view scanned increases proportionally with time. Note that, a fast preview can also be achieved by adopting sparse data acquisition strategies. For instance, one can acquire a low-resolution scan using the raster trajectory by scanning every other row and then return to fill in the gaps to obtain a higher resolution scan [McNabb 12, Trout 23]. However, it's worth noting that this approach isn't inherent in the geometric pattern of the raster trajectory (multiple crossings in the field of view would be energetically costly and wear the scanner). Conversely, the Lissajous and rosette trajectories are inherently capable of providing faster previews due to their geometric pattern.

### 2.3.2 Geometric smoothness of the scan trajectory

The smoothness of a scan trajectory has a direct influence on the energy and time spent in OCT data acquisition [Ruiz 20]. The number of sudden turns along the scan trajectory describes the smoothness of a trajectory. Sudden turns are referred to as turning points in the trajectory where the galvanometer scanner needs to stop, change direction and start scanning again. From Figure 2.3a the raster trajectory is characterised by straight lines that run from top to bottom with sharp transitions from right to left. The conventional raster trajectory is a non-smooth trajectory since it is inherently discontinuous. In the literature there have been techniques used to improve the smoothness of the conventional raster trajectory. They include the bi-directional raster scan as seen in Figure 2.3b as well as implementing a sinusoidal return waveform as highlighted in [Tang 21]. In as much as the bi-directional raster trajectory is an improvement (less distortions) over the conventional raster trajectory, discontinuities still persist in velocity and higher-order derivatives and its mechanical regime is still not as smooth as the continuous scan trajectories [Duma 19, Draelos 22]. In an effort to improve the bi-directional raster trajectory, it is proposed in [Draelos 22] to explicitly account for scanner dynamics by making the trajectory optimally accelerate and travel as fast as possible while still respecting the dynamic limits of the system. This consequently minimises the 'off' time when no data is acquired. In this robot motion planning inspired approach, the efficiency of data acquisition is enhanced. In contrast, other non-raster trajectories in Figure 2.6 - 2.8 are inherently continuous and are characterised by curves which indicate smoother transitions as the scan progresses. Furthermore, a greater radius of curvature (the radius of the circular

arc which best approximates the curve at a particular point) of the trajectory indicates a greater degree of smoothness. As an outcome of a smooth trajectory, less time is taken in scanning and less energy is expended in tracking the trajectory. Therefore, the vibrational energy is reduced resulting in less wear and tear of the mechanical scanner which in turn prolongs its life [Ruiz 20, Perez 04].

### 2.3.3 Connection with compressed sensing

For efficient image or volume reconstruction utilising the compressed sensing paradigm, the A-scan positions at which OCT data are obtained, can be sparsely distributed provided they are geometrically incoherent (non-periodic distribution). To visualise the A-scan positions distribution better, the scan resolution of each scan trajectory in Figure 2.9 has been decreased as compared to Figure 2.6 - 2.8.

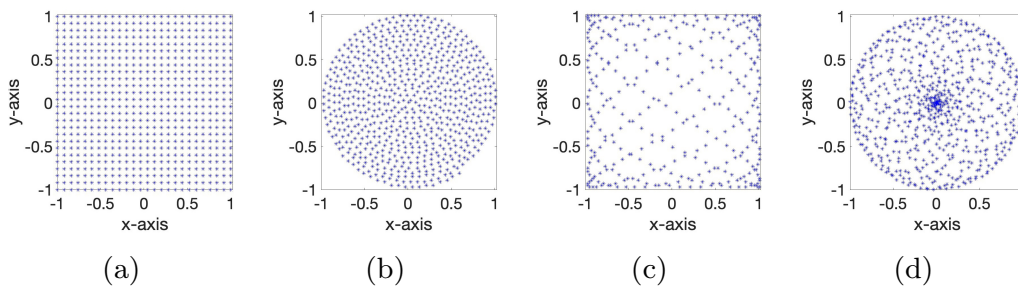


Figure 2.9 – Illustration of data distribution (coherence) for the paradigm of compressed sensing. (a) raster scan trajectory, (b) CLV spiral scan trajectory, (c) Lissajous scan trajectory, (d) rosette scan trajectory.

As seen in Figure 2.9a, the raster trajectory offers high coherence between adjacent scan points, making it well-suited for traditional signal processing techniques. However, in terms of compressed sensing, the regularity and high correlation between adjacent A-scan positions in the raster trajectory may limit the sparsity or compressibility of the OCT data. As a result, compressed sensing reconstruction algorithms may not be able to achieve as significant under-sampling ratios or reconstruction quality as compared to other trajectories. The CLV spiral scan trajectory in Figure 2.9b has a non-uniform sampling pattern, which can be advantageous for compressed sensing. The spiral trajectory introduces diversity and non-locality into the A-scan positions, increasing the potential for sparsity or compressibility of the OCT data. The Lissajous trajectory in Figure 2.9c has a non-linear and non-uniform nature which provides diverse and non-local sampling, promoting sparsity or compressibility in the OCT data. Similarly to the Lissajous trajectory, the rosette trajectory in Figure 2.9d can enhance the sparsity or compressibility of the OCT data, providing advantages for compressed sensing. By exploiting the unique scan pattern of the non-raster trajectories and the resulting diversity, compressed sensing algorithms can achieve improved reconstruction quality and potentially higher under-sampling ratios compared to the raster trajectory with the same resolution.



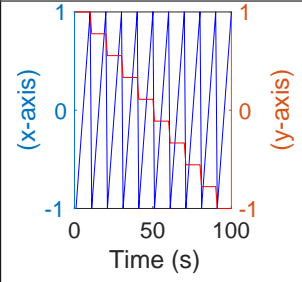
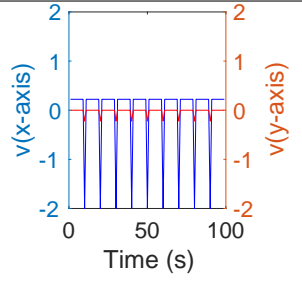
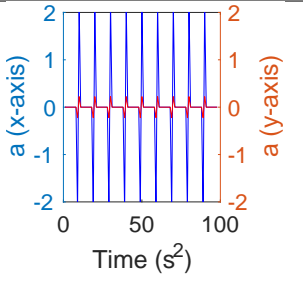
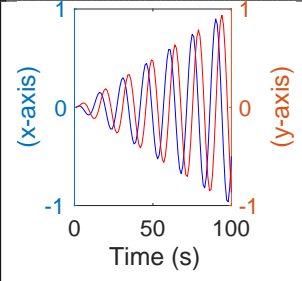
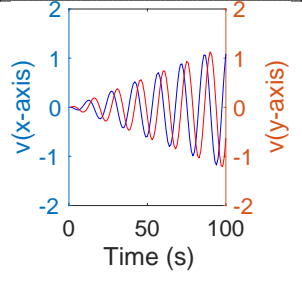
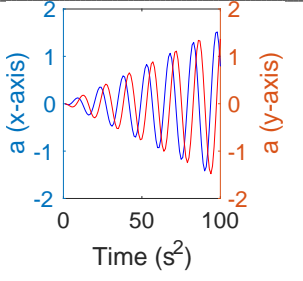
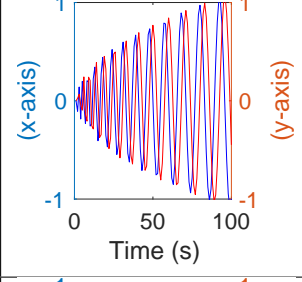
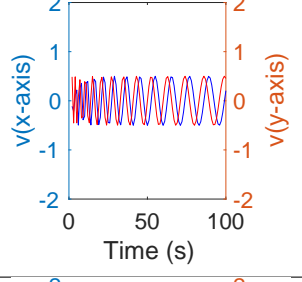
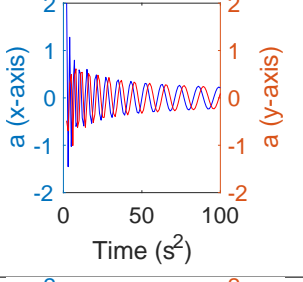
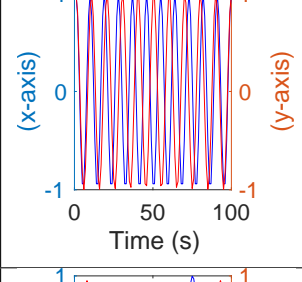
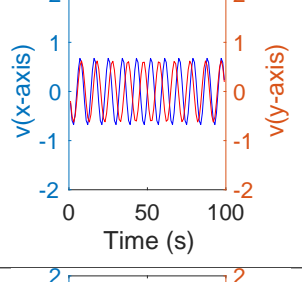
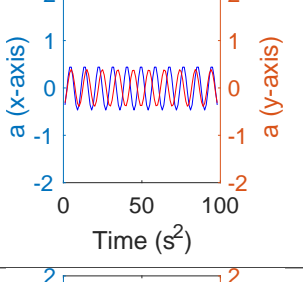
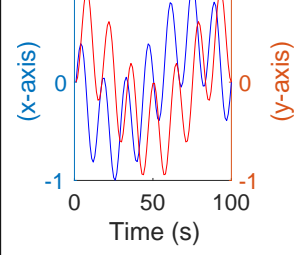
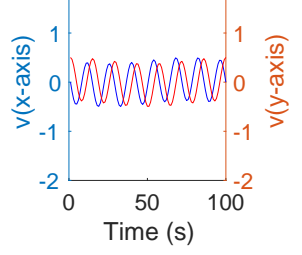
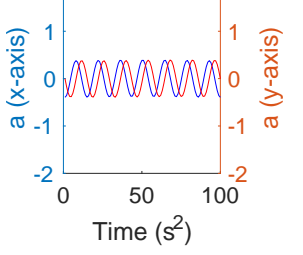
### 2.3.4 Waveforms, velocity, and acceleration profiles of scan trajectories

In Table 2.1 the galvanometer scanner waveforms, the velocity profile and the acceleration profile of both the raster and non-raster scan trajectories are provided in both the  $x$ -axis and  $y$ -axis. The plots were generated using the equations of the scan trajectories (equation 2.2 to 2.5) and have been put side by side for ease of comparison. It is observed that the raster scan trajectory has a fast motion in the  $x$ -axis (left to right) and a slow motion in the  $y$ -axis (top to bottom). The amplitude of the scanner waveforms of the CAV and CLV spiral increases as time progresses. For the Lissajous trajectory, the amplitudes of the scanner waveforms in the  $x$ -axis and  $y$ -axis are fixed but the frequencies are out of phase. For the rosette scan trajectory, the scanner waveforms in the  $x$ -axis and  $y$ -axis are observed to be harmonic. The velocity and acceleration profile of the raster scan trajectory shows increases, then decreases and increases again. This sharp velocity and acceleration peaks particularly in the  $x$ -axis scanner would also correspond to high jerk making the trajectory non-smooth. This non-smooth velocity change results in more energy being expended accelerating the wear and tear of the fast axis scanner as explained in [Duma 11]. For the CAV spiral, the linear velocity and acceleration increases sinusoidally steadily as the scan progresses implying that this trajectory is smoother than the conventional raster. For the CLV spiral, it is observed that the linear velocity stabilises to a constant sinusoidal amplitude while the acceleration decreases rapidly to a slowly varying sinusoidal amplitude as the scan progresses in both the  $x$  and  $y$ -axis. For the Lissajous scan trajectory, the velocity and acceleration of the scanner oscillates around an average velocity and acceleration respectively indicating smoother transitions. For the rosette scan trajectory, the velocity and acceleration of the scanner in both the  $x$  and  $y$ -axis is nearly constant. This is beneficial particularly when considering the smoothness of the trajectory.

### 2.3.5 Conclusion of qualitative analysis

From the qualitative assessment presented, it is deduced that the non-raster scan trajectories have smoother transitions during scanning (as a result less energy is required) as compared to the raster scan trajectory. As similarly seen in [Duma 11], scanning using the sawtooth functions (conventional raster) has mechanical limitations which include vibrations, heating and wear which affect the functioning and life expectancy of the scanner. Conversely, scanning using sinusoidal functions has better advantages from a mechanical point of view (smooth oscillatory regime); there is less vibration and noise as compared to sawtooth or triangular (bi-directional raster) scanning. These non-raster trajectories also provide a fast preview of the scanned object. In addition, non-raster scan trajectories are more suitable for compressed sensing as compared to the raster scan trajectory. Among the non-raster trajectories, the rosette seems to be a qualitative optimum.

Table 2.1 – Waveforms, velocity and acceleration profiles of scan trajectories. The double horizontal line in the second row separates figures of the raster scan trajectory with the non-raster scan trajectories (blue plot -  $x$  - axis, red plot -  $y$  - axis).

Scan trajectory	Scanner waveform in the $x$ - axis and $y$ - axis (mm)	Velocity profile of the scan trajectory ( $mm s^{-1}$ )	Acceleration profile of the scan trajectory ( $mm s^{-2}$ )
Raster			
CAV spiral			
CLV spiral			
Lissajous			
Rosette			

## 2.4 NOVEL CRITERIA FOR QUANTITATIVE ASSESSMENT OF OCT SCAN TRAJECTORIES

In this section, the objective assessment of the scan trajectories used in experimental OCT data acquisition is presented. The novel criteria ‘exploitation vs exploration’ and ‘smoothness of the scan trajectory’ are investigated. A generic methodology in computing the exploitation/exploration ratio and the spatial resolution of scan trajectories is also proposed.

### 2.4.1 Exploitation vs exploration (local vs global quality)

During scanning of OCT volumes, the concept of exploitation/exploration ratio bio-inspired from the human visual system is explored. The human visual system focuses on the details at the centre of the field of view while at the same time gathers information on the remaining area in the field of view i.e., the periphery. When something of interest such as incoming danger presents itself at the periphery of the eye, the eye moves and the region of focus is modified to obtain this new information. This new information thus becomes a priority in our field of view. Similarly, a robot-held OCT probe considering the endoscopic set-up in the context of intracorporeal optical biopsy, the robot shifts the OCT probe to the line of sight in the same way that the eye shifts to the area of focus having new information. Using the analogy of the human visual system, we look into the exploitation/exploration ratio of different OCT scan trajectories by investigating how well a scan trajectory prioritises the central features as compared to the features at the periphery in the field of view. The human eye focuses on approximately 30% of the features centrally in the field of view and the rest is peripheral vision [Hans 11]. Similarly, when assessing scan trajectories, we compute the ratio of the A-scan locations covering the central 30% of the scan area as compared to the rest of the A-scan locations as illustrated in Figure 2.10. A higher exploitation/exploration ratio is indicative of the scan trajectory to prioritise features at the centre of the field of view and a lower ratio prioritizes features at the periphery. The generic exploitation/exploration ratio,  $\lambda$ , is thus:

$$\lambda = \frac{n_c}{n} \in [0\%, 100\%] \quad (2.6)$$

where;  $n_c$  - number of A-scan locations in the central 30% region of the field of view, and  $n$  - number of A-scan locations in the whole region of the field of view.

It is observed that the CLV spiral and raster scan trajectory have a 30% exploitation score. This means that the distribution of the scan points is uniform and is similar to that of the human eye. The CAV spiral has the highest exploitation score of 54% indicating a high data density at the centre, the rosette has a



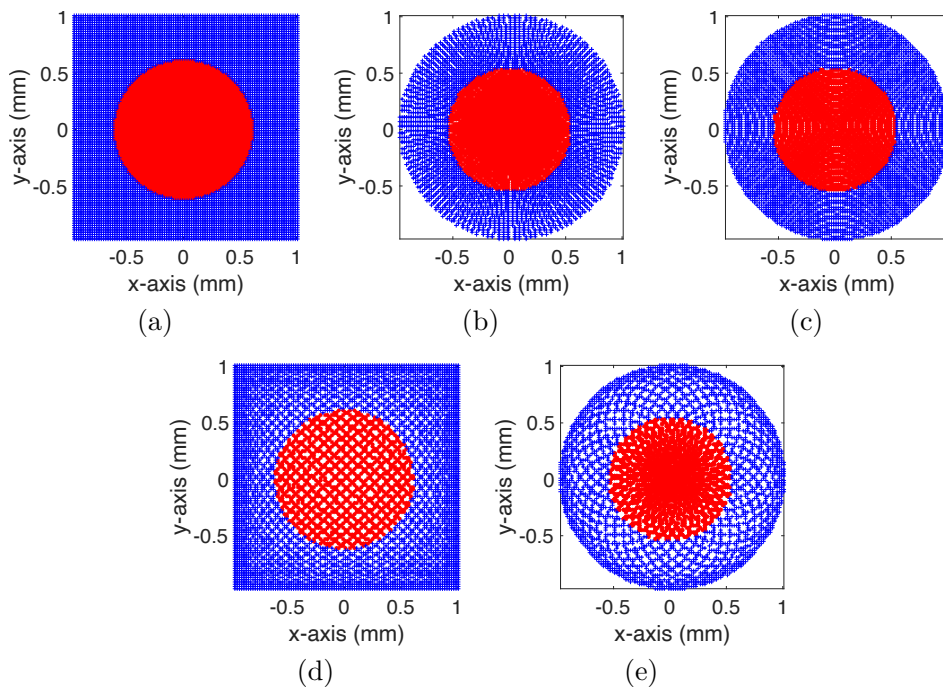


Figure 2.10 – Exploitation/exploration ratio of scan trajectories (blue region - exploration, red region - exploitation). (a) raster,  $\lambda = 0.30$ , (b) CAV spiral,  $\lambda = 0.54$ , (c) CLV spiral,  $\lambda = 0.30$ , (d) Lissajous,  $\lambda = 0.14$ , (e) rosette,  $\lambda = 0.37$ .

balanced score of 37% and the Lissajous has a score of 14% which is the least. The poor ratio of the Lissajous trajectory implies that it is worse at obtaining features at the centre.

## 2.4.2 Smoothness of the scan trajectory

As defined in equation 2.1, the scan trajectory should have  $C^1$  continuity or even  $C^2$ .  $C^1$  refers to continuity of the tangent vector while  $C^2$  is the continuity of the acceleration vector. The non-raster trajectories chosen for the assessment are all  $C^2$ . To quantify the smoothness of a trajectory, we computed its mean and maximum velocity, acceleration and jerk. The velocity, acceleration and jerk were analysed for different configurations. The field of view was fixed, however, the number of scan positions was different. The field of view in the  $x - y$  plane was  $6mm \times 6mm$  and the number of scan positions considered were 1600, 3600, 6400, 10000, 14400 and 22500. In the design of all these configurations the resolution of the scan trajectories was made similar. The data collected from all these configurations had a similar trend in terms of the global ranking of the performance of each trajectory in velocity, acceleration and jerk. Analysis for one configuration (10000 scan points) in the  $x - axis$ ,  $y - axis$  and the resulting motion due to both the  $x - axis$  and  $y - axis$  is given in Figure 2.11, 2.12 and 2.13.

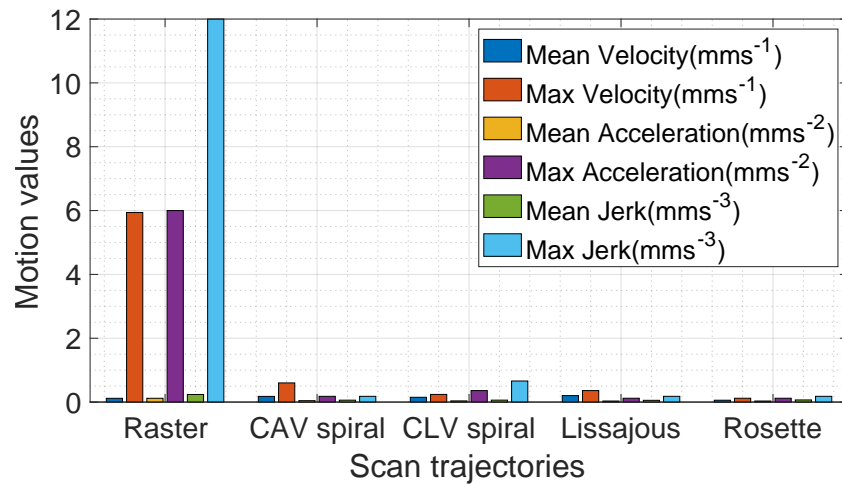


Figure 2.11 – Mean and maximum values of velocity, acceleration and jerk for the scan trajectories in the  $x - axis$ .

For the  $x - axis$  analysis in Figure 2.11, it is observed that the raster scan trajectory has the maximum velocity, acceleration, and jerk as compared to the non-raster trajectories. The  $x - axis$  is the fast axis for the raster trajectory. In the  $y - axis$  analysis, the raster trajectory has lower values in velocity, acceleration and jerk as observed in Figure 2.12. The  $y - axis$  is the slow axis for the raster trajectory. The transition between the fast and the slow axis necessitates the change of scanning velocity characterised by slowing down at sharp turns (for the  $x - axis$ ). From a kinematic point of view, the sharp turns and the abrupt changing of the scan acceleration is not desirable. More energy is expended during these changes and the wear and tear of the scanner also increases. The lower values in acceleration and jerk for the non-raster trajectories imply that these scan trajectories are smoother imposing less wear and tear on the scanner than the raster.

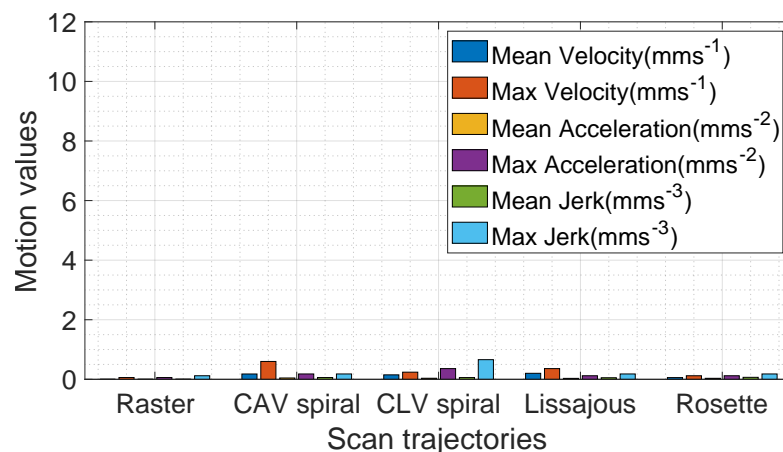


Figure 2.12 – Mean and maximum values of velocity, acceleration and jerk for the scan trajectories in the  $y - axis$ .

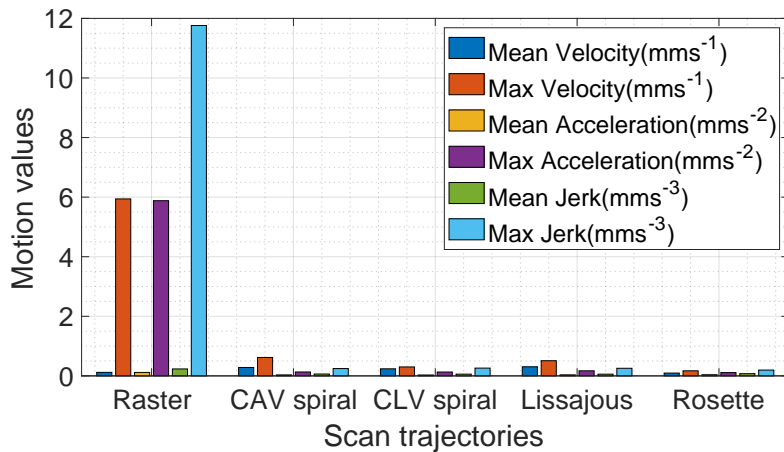


Figure 2.13 – Mean and maximum values of velocity, acceleration and jerk for the scan trajectories in the resulting motion due to both the  $x$  and  $y$  – axis.

### 2.4.3 Spatial resolution of the scan trajectories

The spatial resolution of the raster scan trajectory can be easily defined since the A-scan positions are regularly distributed. In an instance where the A-scan positions are irregularly distributed, it is non-trivial to define the resolution [Tuma 12b]. To obtain the resolution of any scan trajectory, a generic methodology implemented using Delaunay triangulation is defined [Delaunay 34, De Loera 10]. The scan area is subdivided into a triangular mesh with vertices of the triangles obtained from the sampled data. The spatial resolution is given by the largest computed area of the triangles. The resolution of any scan trajectory is defined as:

$$resolution(trajectory): \max\{area(triangle) | \forall triangle \in Delaunay(trajectory)\} \quad (2.7)$$

The Delaunay triangulation of the raster, CAV spiral, CLV spiral, Lissajous and rosette scan trajectories are given in Figure 2.14.

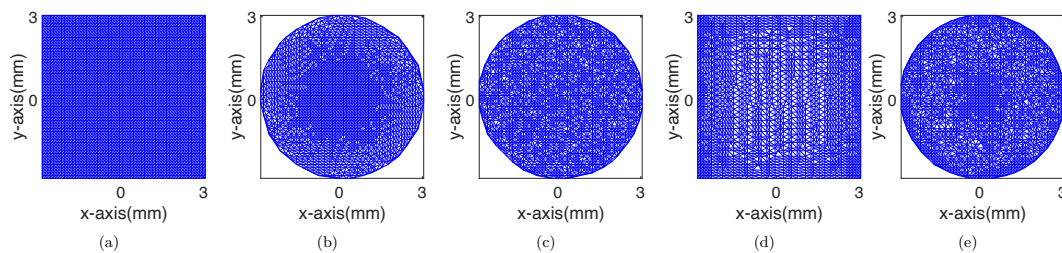


Figure 2.14 – Delaunay triangulation of several scan trajectories. (a) raster scan trajectory, (b) CAV spiral scan trajectory, (c) CLV spiral scan trajectory, (d) Lissajous scan trajectory, (e) rosette scan trajectory.

For the raster it is observed that all the triangles are equal in size indicating that the scan trajectory has a uniform spatial resolution. For the CAV spiral, there are smaller triangles at the centre as compared to the periphery indicating a higher

spatial resolution at the centre. The triangles for the CLV spiral are observed to have almost similar areas which is indicative of uniform spatial resolution similar to the raster. For the Lissajous trajectory there are larger triangles at the central region as compared to the edges indicating that the spatial resolution is higher at the edges as compared to the centre. For the rosette trajectory, the triangles are smaller at the center as well as at the extreme periphery indicating that features at the centre and extreme periphery are prioritized over features lying in the intermediate radius.

In addition, histogram plots were generated to analyse the triangle areas for the scan trajectories, each consisting of 3600 scan positions, as depicted in Figure 2.15. These histograms reveal insights consistent with the earlier discussion. Notably, the histogram for the raster trajectory in Figure 2.15a exhibits uniformly sized triangles across the entire field of view, indicating a consistent resolution. The histograms for the CAV spiral, CLV spiral and the rosette trajectories have almost the same number of triangle counts with similar resolution as seen in Figure 2.15b, c and e. However, their spatial resolution distribution differs within the field of view as illustrated in Figure 2.14b, c and e. In contrast, the histogram for the Lissajous trajectory in Figure 2.15d displays varying triangle areas across the field of view, with larger triangles predominantly in the central region (as shown in Figure 2.14d), indicating lower spatial resolution.

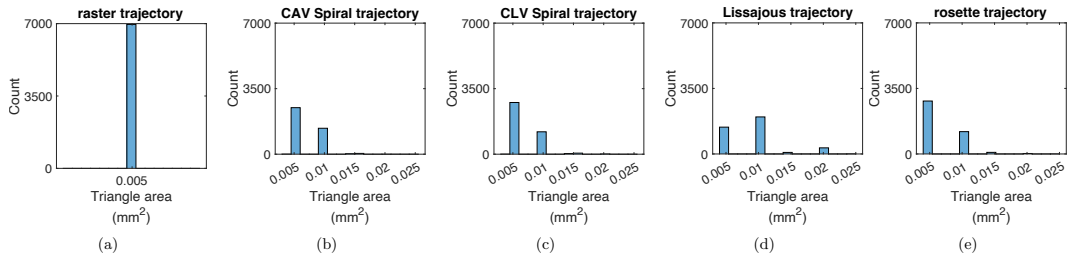


Figure 2.15 – Histogram of the Delaunay triangles area of several scan trajectories. (a) raster scan trajectory, (b) CAV spiral scan trajectory, (c) CLV spiral scan trajectory, (d) Lissajous scan trajectory, (e) rosette scan trajectory.

#### 2.4.4 Conclusion of quantitative analysis

For optimal data acquisition, it is important for the data distribution at the centre to be denser (since that is the region with the most information) and the A-scan positions to be incoherently distributed to fit in the paradigm of compressed sensing. It is also essential for the scan trajectory used in data acquisition to be smooth so that there is less wear and tear on the scanner used in addition to being energy efficient. Given the above considerations, the non-raster trajectories perform better than the raster with the rosette seeming to have a slightly better performance in terms of exploitation/exploration ratio and spatial resolution. This follows the conclusions of the qualitative assessment. To confirm this trend, an experimental assessment is performed.

## 2.5 EXPERIMENTAL ASSESSMENT OF OCT VOLUMES

### 2.5.1 Experimental set-up

The qualitative and quantitative analysis done were validated using the OCT device in Figure 2.16; the Telesto II 1325nm spectral domain device from Thorlabs. It provides 1D depth, 2D cross-section and 3D volumetric images with  $5.5\mu\text{m}$  axial resolution,  $7\mu\text{m}$  lateral resolution and  $3.54\text{mm}$  depth penetration. The OCT device has a maximum field of view of  $10 \times 10 \times 3.54\text{mm}^3$  and a maximum A-scan line rate of 76 kHz.

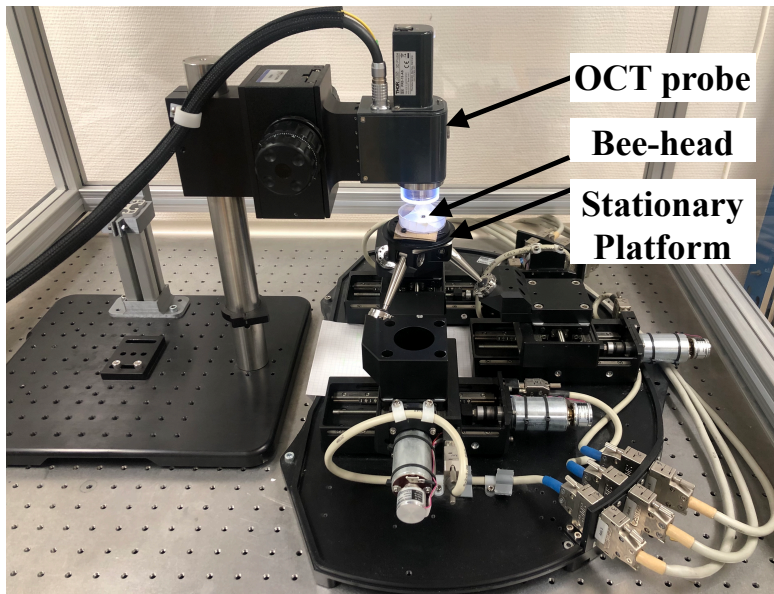


Figure 2.16 – Illustration of the experimental set-up used to validate the qualitative and quantitative analysis (the end effector of the parallel robot serves as the stationary platform).

The OCT volumes used in the experimental assessment were acquired using scan trajectories of different configurations similar to the quantitative analysis presented. The size of the field of view ( $6 \times 6 \times 3.54\text{mm}^3$ ) was similar for all the experiments. However, the number of scan positions used in acquiring the A-scans were different. Six different configurations were used for each scan trajectory; the number of A-scan positions considered were 1600, 3600, 6400, 10000, 14400 and 22500. The scan positions in the  $x$  – axis and  $y$  – axis were then computed for each scan trajectory with respect to each configuration.

### 2.5.2 OCT volume file format

Visualisation and storage of 3D and 2D images from different medical imaging modalities requires the selection of a suitable data format. Image file formats provide a standardised way in which image data is stored in a computer file



[Larobina 14]. File formats currently in use in medical imaging include: Analyze, Neuroimaging Informatics Technology Initiative (NIfTI), Medical Image NetCDF (MINC) and Digital Imaging and Communications in Medicine (DICOM). Multiple file formats limit the access, exchange and usability of medical images and their associated information. In this research we chose to use the point cloud data format. A point cloud is a set of points in space given in the  $x$ ,  $y$  and  $z$  axes of the Cartesian coordinate system that represents a 3D shape or object. It also has attributes such as colour given as an intensity value or in RGB. With the availability of the freely accessible PCL library, manipulation of point cloud data to perform activities such as segmentation and thresholding has been made easier [Rusu 11]. Point cloud data has also facilitated the use of Virtual Reality to display and interact with OCT data [Maloca 18]. This represents the next generation of OCT image display technology and a new tool for patient engagement, medical education and telecommunication.

### 2.5.3 OCT volume similarity assessment to ground truth

Assessment of the quality of OCT data obtained using non-raster trajectories to the ground truth can either be on images or volumes. In [Haydar 20], assessment of reconstructed OCT volumes using compressed sensing was done; however, in that work similarity assessment was primarily done on individual 2D slices (B-scans) as similar as shown in Figure 2.17b that make up the OCT volume. Methods used to assess 2D images include the structural similarity index method (SSIM), peak signal to noise ratio (PSNR) and signal to noise ratio (SNR). In this research, OCT data (stationary bee-head) was acquired experimentally in the lab (micro-manipulation lab of the AS2M department of Femto-ST institute) using the Thorlabs OCT device. Subsequently, a complete 3D point cloud volume was generated from the OCT data by processing each A-scan to its corresponding scan position (and performing thresholding to eliminate noise), as illustrated in Figure 2.17c. Experimental analysis was then conducted on the OCT point cloud volume as a whole (which is seldom done) rather than on individual 2D slices.

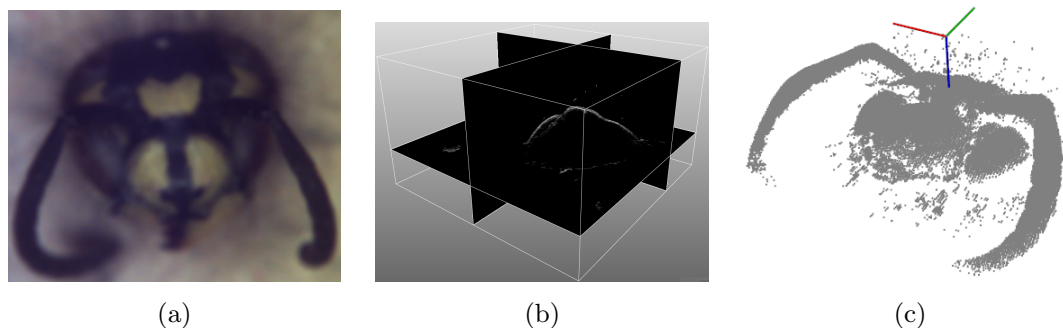


Figure 2.17 – (a) Biological sample (bee-head), (b) Sectional view of the 3D OCT volume, (c) 3D OCT point cloud volume of the biological sample.

To assess the similarity of the OCT point cloud volumes acquired using the scan trajectories to the ground truth, the objective quality metric PointPCA proposed in [Alexiou 21] was used. PointPCA is a full-reference objective quality metric that compares the local shape and appearance between a point cloud under evaluation and its reference. Figure 2.18 illustrates the PointPCA architecture.

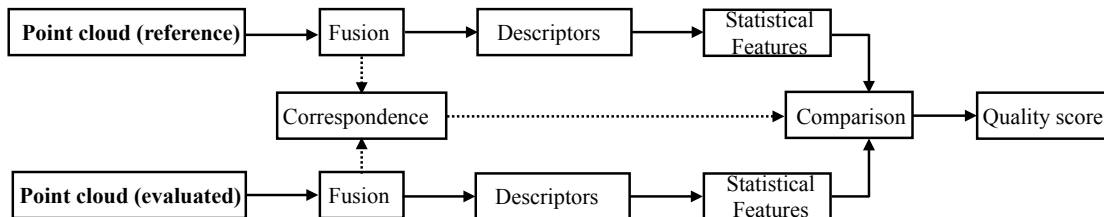


Figure 2.18 – PointPCA architecture [Alexiou 21].

In the PointPCA architecture process, both the reference and the point cloud under evaluation pass through multiple processing stages to compute a quality score. During the fusion step, duplicated points in the cloud are removed, and the corresponding point cloud intensity values averaged. Subsequently, a correspondence between the two point clouds is established using the nearest neighbour algorithm. Specifically, for every point in the reference point cloud, a matching point in the evaluation point cloud is identified as its nearest neighbour in terms of Euclidean distance and registered as its correspondence. Geometric descriptors (eigenvalues, linearity, planarity, sphericity, anisotropy, omnivariance, eigentropy, surface variation, roughness, parallelity) are then defined for each point, based on principal component analysis (PCA), capturing local shape properties with respect to its topology. Textural descriptors (luminance measurement) are also computed based on the intensity values, capturing appearance properties. Statistical functions (mean and standard deviation) are then applied to the geometric and textural descriptor values to capture local relationships among points within the same neighbourhood. These statistical features, are then used to compare the two point clouds. Various comparison methods, such as absolute difference, squared difference, and relative difference, are examined to evaluate the performance of the descriptors. The results of these comparisons are then used to generate a quality score that indicates the overall similarity (geometry and texture) between the two point clouds. Further information and mathematical formulation to the PointPCA metric developed by Alexiou *et al.* are given in Appendix C. An advantage of PointPCA over other objective metrics is that the point cloud volumes to be compared need not be the same size i.e., it is well adapted to sparse data. An alternative approach to perform similarity assessment of point clouds would be to first mesh them and obtain a 3D image then perform similarity assessment. This approach is time consuming and therefore this additional process is commonly lossy [Alexiou 20].

For this research, a similarity score was obtained by evaluating the OCT volumes against a ground-truth reference volume for all the experimental configurations. The ground truth was the raster trajectory having 22500 scan positions.

The similarity score of the scan trajectories for each configuration against the ground truth had a similar ranking i.e., the configuration with less scan positions had lesser scores as compared to those having more scan positions. Therefore, it is only shown here the similarity score results of the configuration having 10000 scan positions. From Figure 2.19, the raster scan trajectory has the highest similarity score. Indeed, the raster trajectory with 10000 scan positions is a subset of the raster trajectory with 22500 scan positions serving as the ground truth. Naturally, this creates a point cloud with a better similarity than a point cloud of the same scene where the scan positions are distributed differently (the non-raster trajectories). Despite this, the score is less than 1 because high frequency information is lost i.e., intermediate samples are lost. Among the non-raster trajectories, the rosette has the highest similarity score while the Lissajous trajectory has the lowest score. These similarity scores are lower since the A-scan positions of the non-raster trajectories are non-colocalised with the A-scan positions of the ground truth volume. Despite using non-raster trajectories to acquire OCT volumetric data, a good enough similarity score to the ground-truth is still obtained.

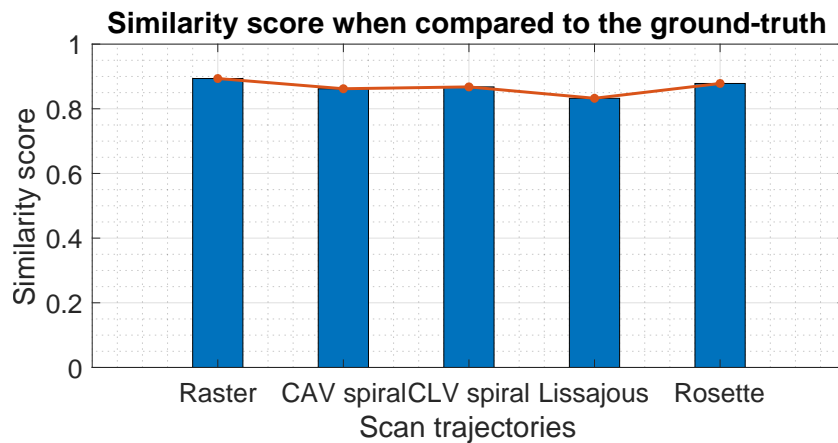


Figure 2.19 – Similarity scores of OCT volumes obtained from scan trajectories when compared to the ground truth.

#### 2.5.4 Exploitation vs exploration

Utilising experimental data, the various non-raster trajectories are investigated to find out which one has a better exploitation than exploration with respect to the criterion definition in sub-section 2.4.1. The OCT volume quality was assessed separately using PointPCA in the central zone (exploitation) of the field of view and in the periphery (exploration). From Figure 2.20, it is observed that the raster scan trajectory has the highest values both in exploration and exploitation. However, for the non-raster scan trajectories, the rosette has the highest scores in both exploration and exploitation. The Lissajous trajectory has the least value in exploitation justifying an earlier analysis in section 2.4 that it performs relatively



poorly than the other scan trajectories at obtaining features at the centre. These results confirm that the rosette trajectory has the best performance with the caveat that it prioritises features at the centre slightly more than at the edges.

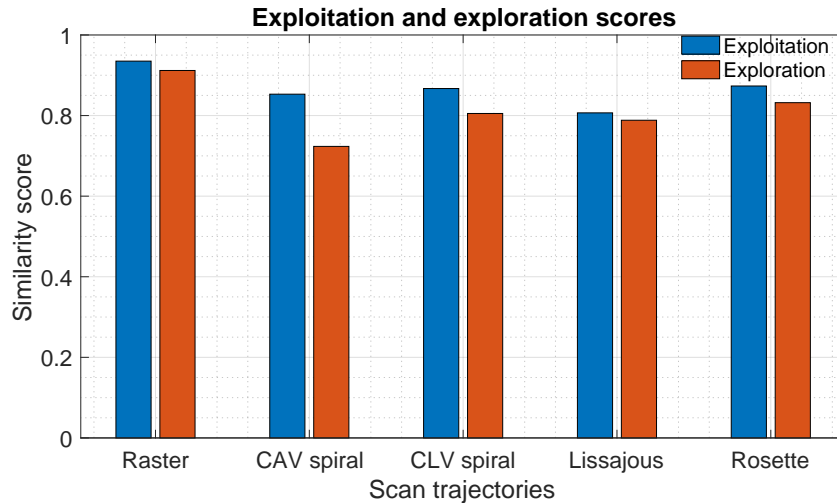
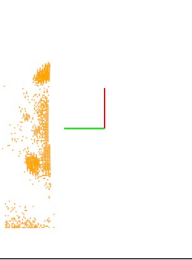
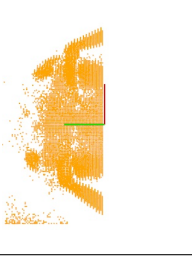
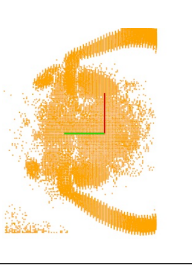


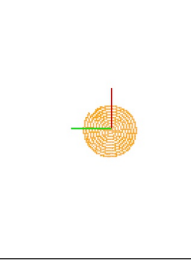
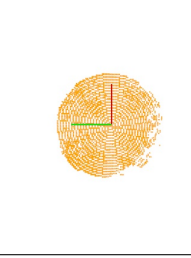
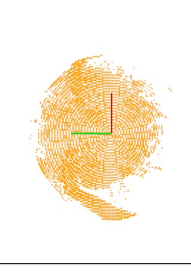
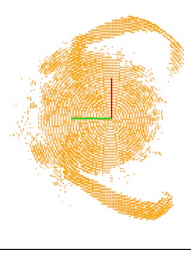

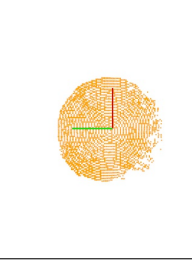
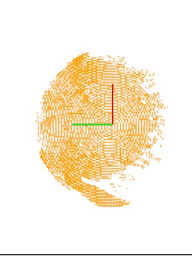
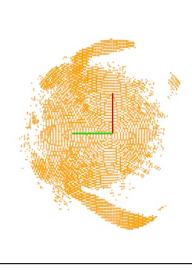
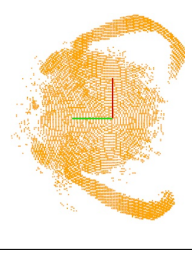








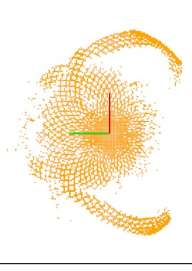




Figure 2.20 – Exploitation/exploration similarity scores of scan trajectories.

### 2.5.5 Progressivity (fast preview) of the scan resolution

The longer the object is scanned, the better the resolution of the volume. Table 2.2 shows the time lapse sequence of the upper volumetric slice ( $x-y$  plane) as data is acquired using different scan trajectories and the final 3D OCT volume. It is observed that for the raster trajectory, the whole image has to be processed before any analysis can be done. This is due to the sequential acquisition of data from top to bottom. It is also observed that for the spiral trajectories, the resolution of the volume increases from the center to the maximum radius. Although the raster and the spiral trajectories have a poor fast preview, they have a dense data distribution at the center by the end of data acquisition. For the rosette, the resolution increases sequentially in a radial manner and has a slightly denser data distribution at the center as compared to the periphery since the data at the center is frequently updated. The Lissajous trajectory traverses through the whole field of view within a short period. It is observed that although a rough preview of the sample is able to be obtained within a short time using the Lissajous trajectory, the resolution does not increase significantly afterwards. Similarity scores using PointPCA were computed on the progressive scans (quarter, half, and three-quarter). From Figure 2.21, it is seen that the rosette has the highest score after acquiring only 25% of the data. Thus, the rosette trajectory has the fastest preview of the non-raster trajectories and the resolution steadily increases afterwards.

Table 2.2 – Time-lapse sequence of scanning a biological sample (bee-head) with different scan trajectories.

	Quarter of the data acquired	Half of the data acquired	Three quarter of the data acquired	Full data acquired	3D OCT volume
Raster					
CAV spiral					
CLV spiral					
Lissajous					
Rosette					

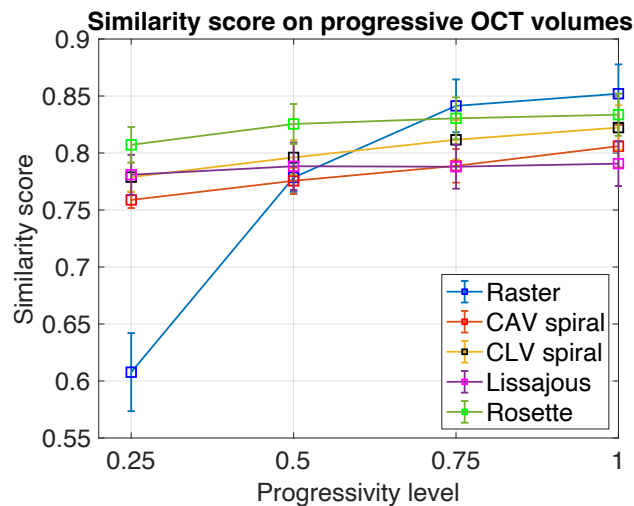


Figure 2.21 – Mean similarity score on progressive scanning for different experimental configurations.

### 2.5.6 Time analysis of the scan trajectories

The time it takes to acquire OCT volumetric data is dependent on; the length of the scan trajectory used, the number of A-scans obtained and the type of scan trajectory. As seen in Figure 2.22, for the same number of A-scans, the raster trajectory is almost twice as slower than the non-raster trajectories. This can be attributed to the smoothness of the continuous trajectories i.e., less time is spent in accelerating and decelerating on the trajectory. The time taken to scan the same number of A-scans using the non-raster trajectories is almost similar.

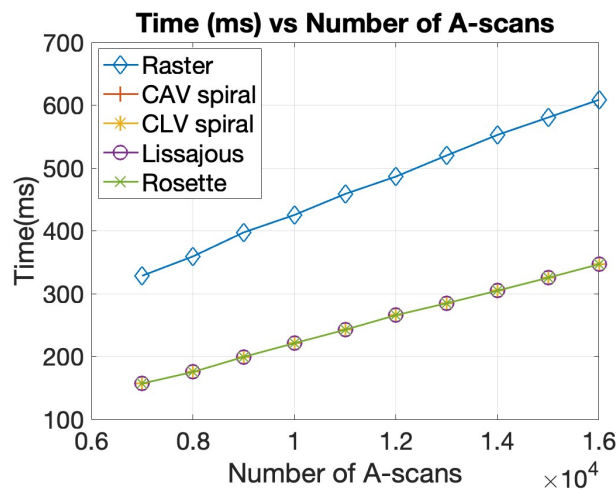


Figure 2.22 – Time taken by different scan trajectories to obtain A-scans. The time taken using non-raster trajectories is almost equal, therefore the curves overlap each other.

### 2.5.7 Summary of scan trajectories assessment

There is a difficulty in providing a unique score in a multi-criteria assessment. A suitable way of scoring the selected criteria is by visualising the performance in a radar diagram as shown in Figure 2.23 because it gives freedom to the system designer or non-expert user to select a scan trajectory depending on their priorities. The radar plot was generated by using data from the quantitative and experimental analysis presented. From the analysis of the time and smoothness criteria of the trajectories, a higher value indicates worse performance. For better visualisation of these two criteria, the negative log of the values were plotted in the radar diagram. When comparing the scan trajectories against different criteria, the scan trajectory with most of its spokes being close to or at the boundary of the plot outline has the best performance. From the radar plot, it is observed that the raster trajectory has most of its spokes close to the centre indicating a poorer performance. The CLV spiral and rosette trajectories have most of their spokes close to the plot outline implying that they have a better performance as compared to the other non-raster trajectories. Nevertheless, on close observation of the area covered by the individual scan trajectory radar plots in Figure 2.23, the rosette scan trajectory has the best performing scores globally.

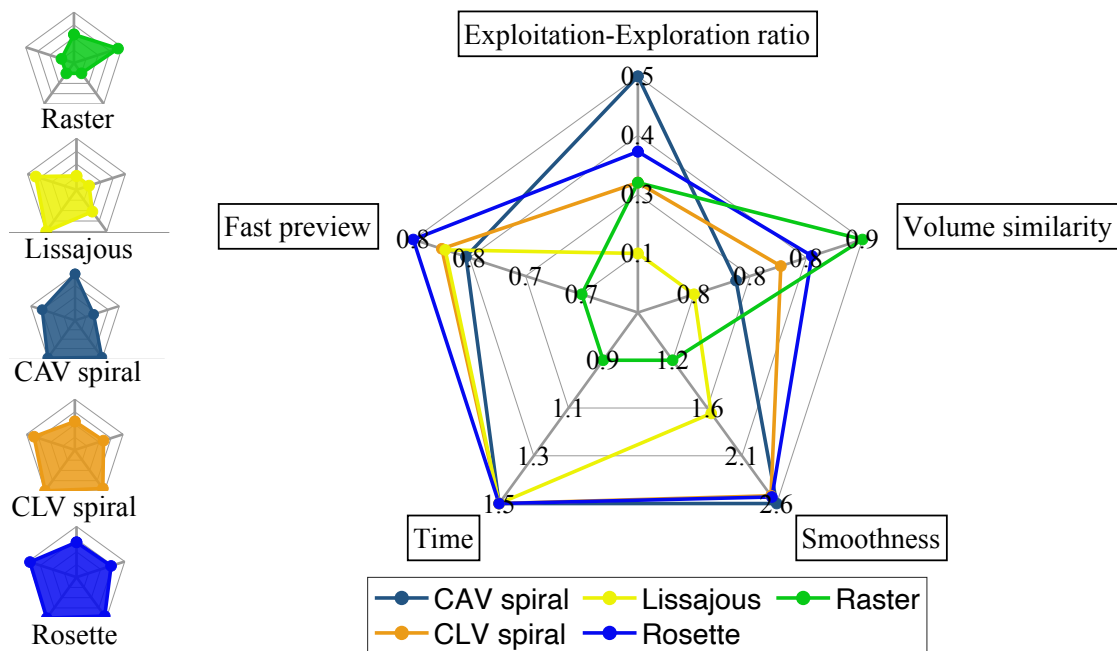


Figure 2.23 – Individual radar plots for each scan trajectory and a combined radar plot comprising all the trajectories for more variability analysis of the multi-criteria assessment.

## 2.6 CONCLUSION

A qualitative, quantitative and experimental multi-criteria analysis with both novel and conventional criteria of non-raster/non-Cartesian trajectories has been presented in this chapter. In particular, it is proposed: a bio-inspired exploitation/exploration criterion, a smoothness criterion (which has an effect on the wear and tear of the scanner as well as the energy expended), and a fast preview criterion of the scan trajectory. A set of non-raster trajectories (constant angular velocity spiral, constant linear velocity spiral, Lissajous and rosette) were selected and assessed. To get the performance information of the scan trajectories at a glance, a radar visualisation plot was used. Quantitative analysis showed that the Lissajous trajectory has the best exploration in the peripheral region, the constant angular velocity spiral trajectory has the best exploitation in the central region and the rosette trajectory has the best trade-off between exploitation and exploration. Experimental analysis indicated that non-raster trajectories were almost twice as fast as raster trajectories without a significant loss in OCT volume quality. Comparing various non-raster trajectories against different criteria revealed that the rosette scan trajectory had the best global performance. The rosette trajectory had a faster volume preview while maintaining a close enough similarity to the ground truth and had a more balanced performance in terms of exploitation and exploration. Furthermore, the exploitation/exploration ratio can be tailored by the system designer to select alternative zones of attention and discovery. This suggested that rosette-like trajectories should be adopted in data acquisition especially in the case of robot-driven intracorporeal OCT probes. To further obtain OCT volume data at a faster rate and higher quality, the design of these scan trajectories would need to be optimised. In addition to optimising these scan trajectories, the use of graphical processing units (GPUs) would accelerate the image acquisition especially in the image processing step. Moreover, the data acquisition using rosette-like trajectories can be accelerated by optimal mechanical designs of the scanner as opposed to the conventional galvanometric scanners. Rather than have two galvanometric scanners for the  $x$  - axis and  $y$  - axis, an optimal design for a scanner with only one actuator that traces the rosette path could be designed. This optimal design would probably use less energy since only one actuator would be needed instead of two. The set of multi-criteria assessment proposed here would be useful in this further optimisation step.

---

---

# Chapter 3

## Optical coherence tomography adaptive scanning

---

<b>3.1</b>	<b>Adaptive scanning</b> .....	62
3.1.1	Existing works on adaptive scanning.....	64
3.1.2	Contributions of this chapter .....	66
<b>3.2</b>	<b>Adaptive scanning protocol</b> .....	67
3.2.1	Conceptual description of adaptive scanning .....	67
3.2.2	Technical description of adaptive scanning .....	71
<b>3.3</b>	<b>Numerical (simulation) validation of adaptive scanning</b> ...	82
3.3.1	Simulation of volumetric OCT data of a tissue sample containing a tumour.....	82
3.3.2	Simulation of adaptive scanning.....	86
<b>3.4</b>	<b>Experimental validation of adaptive scanning</b> .....	89
3.4.1	Experimental set-up procedure .....	90
3.4.2	Experimental adaptive scanning .....	92
3.4.3	Discussion of the simulation and experimental results of adaptive scanning .....	98
<b>3.5</b>	<b>Conclusion</b> .....	99

### 3.1 ADAPTIVE SCANNING

In conventional OCT scanning, volumetric data is acquired using the raster trajectory. The object sample is transversely scanned in both the  $x$  and  $y$  directions to obtain a volume. OCT data acquisition using the raster trajectory is time consuming since data is not acquired during the horizontal retrace when changing direction in each subsequent scan-line from top to bottom [Carrasco-Zevallos 18, Sang 16]. To increase the OCT volumetric acquisition rate without modifying the hardware, several techniques exist:

- i Modification of the scan trajectory to a non-raster one, as discussed in Chapter 2 of this thesis, increases the data acquisition rate without significantly degrading the quality of the obtained data.
- ii Optimisation of the non-raster scan trajectories. This is densely scanning the exploitative region of the sample while sparsely scanning the explorative region of the sample. (In this case any analysis on already acquired OCT data is neglected, the optimisation process is done offline before beginning to scan).
- iii Acquisition of OCT data sparsely and incoherently in the field of view and later reconstruction of the image/volume using compressed sensing algorithms [Haydar 20].

All the mentioned techniques aim at reducing the density of the data acquired, by scanning fewer scan positions optimally throughout the field of view, resulting in less time used to obtain the data. Despite an improvement in the data acquisition rate using these techniques, they are all open-loop processes since during scanning, no use is made of the data that is previously scanned (the scan trajectories are designed offline prior to OCT scanning). In this research objective, it is aimed to propose a closed-loop capable method where a subset of previously acquired data is analysed and used to predict the next scan positions that should be scanned (re-planning the scan trajectory online). By implementing this process, the amount of OCT data acquired can be significantly reduced (and consequently the time) but still glean as much useful information as possible. This method is referred to as adaptive scanning.

#### **Lesion/tumour diagnosis with respect to adaptive scanning**

Diagnosing cancerous lesions/tumours typically involves a physical examination, imaging studies and biopsy. The first step in diagnosing cancerous lesions is a physical examination whereby the doctor looks for any signs or symptoms of a tumour such as a lump or mass [Polat 07, Grutzmann 14]. The next step in the diagnosis is to perform imaging studies. Imaging studies using OCT are used to create detailed images of specific regions of the body to help the doctor identify the size, location and extent of the tumour. OCT volumetric images provide the doctor with information regarding whether a tumour is cancerous or benign. During the treatment and subsequent assessment of the tumour growth, the doctor is mostly concerned with the specific region of the tissue having the tumour/lesion. It is



therefore prudent to obtain a high quality image/volume particularly one having dense data in the tumour/lesion boundary. Therefore, the principle of adaptive scanning with respect to medical diagnosis using an OCT device is to dynamically modify the scanning scheme to ‘deeply’ scan informative locations of the tissue having lesions while limiting the acquisition at other locations in the field of view (reducing exploration and exploitation to only the core details). By performing adaptive scanning, the scan path is replanned iteratively in a supervised manner allowing imaging of the tissue sample at the region of interest with only a fraction of the data.

### Oncology research using OCT and the need for adaptive scanning

In recent years, OCT has gained increased attention in the field of oncology, particularly in gastroenterology, as a tool for the diagnosis and staging of gastrointestinal cancers [Tsai 14]. The development of OCT in oncology has been driven by the ability of the technique to provide detailed information about the microstructure of the tissue, which can aid in the identification and characterisation of neoplastic tissue. Researchers have adopted OCT technology to examine cancer biology and assess treatment response in pre-clinical settings [Vakoc 12]. In one investigation, the volume of tumours implanted in the chambers of the dorsal skin-fold was measured using OCT [Vakoc 09]. In this work, the tumour edges were defined in three dimensions (3D) using a manual segmentation method on two planes ( $x - y$  and  $x - z$ ) as seen in Figure 3.1.

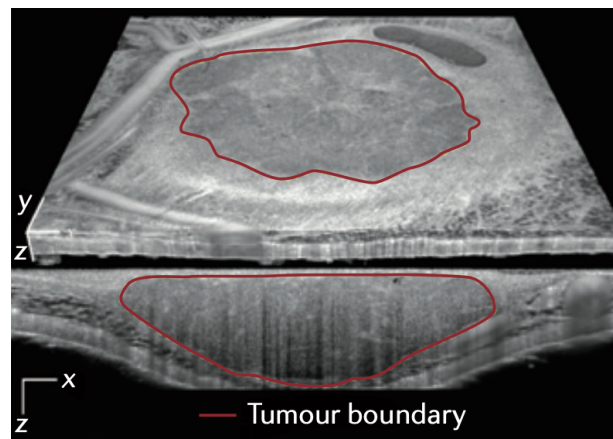


Figure 3.1 – Using microstructural contrast, tumour tissue (an allotransplanted mammary adenocarcinoma) can be differentiated from surrounding host subcutaneous and muscle tissues in a dorsal skin-fold chamber model. By defining the tumour margins, the three-dimensional tumour volume can be calculated.

Transverse extent is  $5mm$  ( $x - axis$ ) and  $4.4mm$  ( $y - axis$ ) [Vakoc 09].

The tumour volume was estimated from these margins and utilised to demonstrate growth inhibition in response to vascular endothelial growth factor receptor 2 (VEGFR2) blockade as well as to designate consistent therapeutic start points across animals in an anti-angiogenic medication research. The authors were able



to use these tumour margins to further segment intra-tumoral and peritumoral veins by simultaneously obtaining architectural and vascular OCT images. This allowed for the differential investigation of vascular response at these sites. Rather than performing manual segmentation which is time consuming, adaptive scanning could provide an OCT volume that is well delineated at the margins. Accurate knowledge of the tumour margin holds significant importance [Wang 17], especially in the early stages of OCT-based controlled surgery for tumour resection. The ability to swiftly obtain this information regarding the border might prompt the surgeon to conduct further in-depth investigation and gather comprehensive data, specifically targeting the critical regions of the tissue, i.e., the tumour border and how deep it has grown. This allows for a more precise and focused approach to the surgical procedure, enhancing the overall efficacy and success of the tumour resection process.

### 3.1.1 Existing works on adaptive scanning

Draelos *et al.* implemented adaptive scanning as a probabilistic approach that balanced re-imaging of known dynamic positions with exploration for undiscovered ones [Draelos 22]. Each scan position in the scene is visited only when necessary rather than in a rigid sequence. After a frame of data is acquired, the scene is analysed using both recently acquired and current data to decide which scan positions to visit in the next frame. Rather than scanning evenly across the scene, the scan positions are concentrated on regions of interest in a bid to minimise the amount of data samples needed to refresh the frame, this is seen in Figure 3.2. Figure 3.2a shows the probabilistic positions that changed greatly between the recently acquired frame and the current frame (the dimension of the scene is  $9mm \times 16mm$  with a resolution of  $250 \times 1000$ ). Figure 3.2b shows the corresponding optimal raster scan trajectory to be used in acquiring the new frame of data.

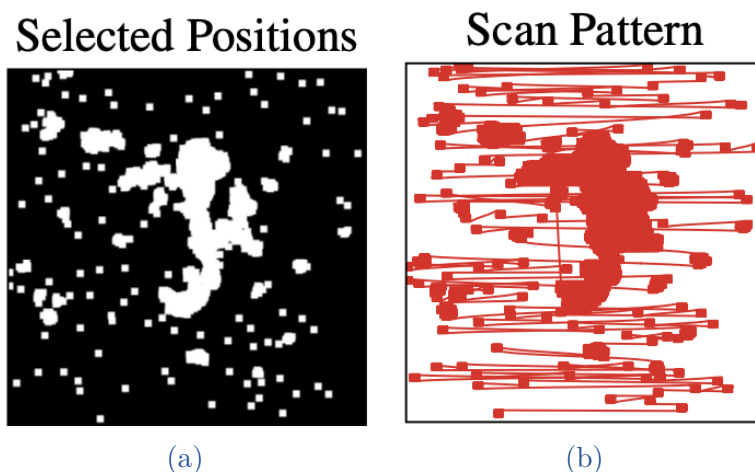


Figure 3.2 – Probabilistic adaptive scanning approach. (a), a subset of the selected scan positions from previous acquisition and (b), an optimised raster scan trajectory designed to acquire data only at those positions [Draelos 22].

In contrast to the approach of Draelos *et al.*, it is proposed in this research, to perform adaptive scanning with the OCT device by replanning a non-raster scan trajectory in real-time based on the analysis of a previously acquired sub-set of data (A-scans) of the object sample being imaged (as opposed to frame after frame scan trajectory optimisation). While Draelos *et al.* used an optimal raster trajectory, we aim at scanning only at the boundary of our target region, in this application case, a lesion/tumour boundary. By implementing adaptive scanning this way, the region that matters most would have been scanned densely and the quality of the OCT volume subsequently improved all while significantly reducing the time it would have taken to scan the whole field of view.

Furthermore, Andersson *et al.* in [Andersson 05, Andersson 07] aimed to reduce the acquisition time in scanning string-like samples such as DNA strands, nanowires, microtubules, and actin strands using the atomic force microscope (AFM) as depicted in Figure 3.3. To achieve this, techniques from mobile robotics and curvature-based control [Zhang 04, Justh 04] were applied to control the AFM tip along the DNA strand. This involved following the path by applying a superimposed oscillatory transverse motion to detect the DNA strand as depicted in Figure 3.3.

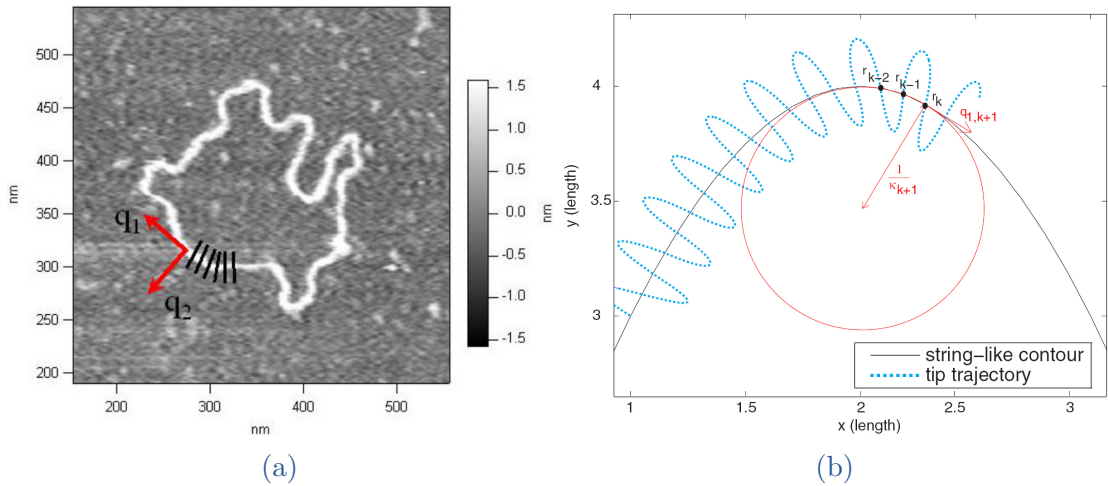


Figure 3.3 – (a) Local raster scanning of a DNA strand using an AFM [Andersson 05], (b) Andersson’s scanning algorithm with smooth trajectory and contour prediction [Zhang 15].

The work by Andersson *et al.* was extended in [Zhang 15], where the scan trajectory was modified to scan precisely at the contour without crossing the sample, as illustrated in Figure 3.4. The primary objective was to control the AFM tip cantilever to follow the topology of biological specimens rather than crossing them during imaging. Crossing the sample with the cantilever could potentially damage the biological specimen or introduce undesirable dynamics, invalidating the data acquisition. While the implementation of adaptive scanning presented in this research objective, in this thesis acknowledges ideas and inspiration from [Andersson 05, Zhang 15], especially in predicting the next scanning position from

previously acquired data, significant technical enhancements have been made. This is particularly evident in the analysis of the data and tumour boundary estimation (working principle of AFM as well as the data is different from OCT) as will be seen in subsequent sub-sections. Moreover, the prediction equations formulated in [Andersson 05] have been reformulated, along with their associated proofs, to anchor them more firmly in differential geometry rather than analytical geometry (see Appendix A.2).

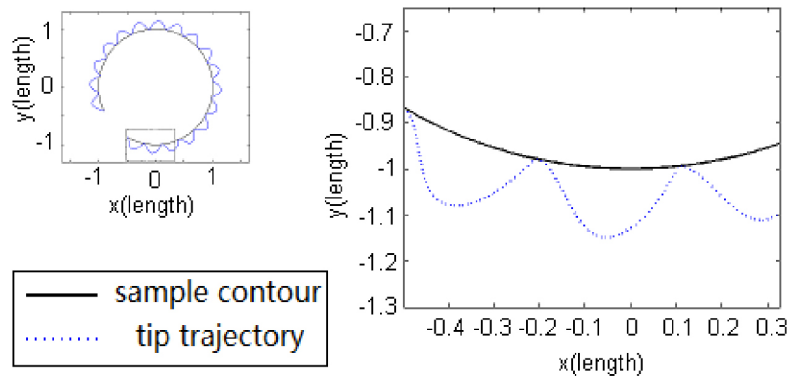


Figure 3.4 – Proposed scan trajectory for atomic force microscope (AFM) data acquisition for biological samples in [Zhang 15].

### 3.1.2 Contributions of this chapter

In this chapter an alternative to acquiring OCT volumetric data as it pertains to optical biopsy of lesions and tumours by performing adaptive scanning is proposed. Adaptive scanning in this context refers to utilising a continuous closed-loop trajectory to acquire data only on informative regions in the field of view of the tissue while neglecting the other non-important regions. It is shown that by acquiring data on a few initial scan positions, it is possible to statistically analyse the progression of the tumour boundary and predict the next scan positions on the tissue to be scanned. Nonetheless, this prediction is heavily dependent on the statistical analysis of the already collected OCT data to differentiate between healthy and cancerous regions and estimate the tumour boundary. In this research objective, an innovative way to do this was to implement k-means clustering based on standard deviation (and not Euclidean distance) of the intensity values of the acquired A-scans; first to determine healthy and tumour regions, and subsequently to estimate a tumour boundary locally. It is revealed that an adaptive scanning strategy significantly increases the information density (ratio of useful acquired A-scans to the total acquired A-scans) of the acquired data thereby potentially increasing the efficiency of the scanning process in applications such as optical biopsy in oncology.

## 3.2 ADAPTIVE SCANNING PROTOCOL

In this research objective, the working hypotheses is that the tumours under consideration have a diameter of  $1 - 6mm$ , making them observable within the OCT field of view while also being large enough to appear suspicious through an external endoscope camera. The aim is to propose a capable method for facilitating early-stage cancer detection. This section outlines the conceptual and technical steps necessary to implement adaptive scanning using OCT.

### 3.2.1 Conceptual description of adaptive scanning

Adaptive scanning is an iterative process that encompasses a concurrent workflow of data acquisition, data analysis and tumour boundary prediction as visually represented in the schematic in Figure 3.5.

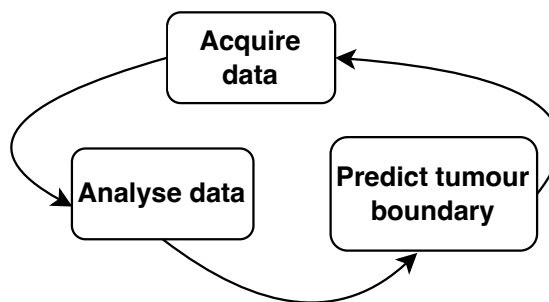


Figure 3.5 – Adaptive scanning process.

After obtaining OCT data from a few scan locations, this data is promptly analysed to identify any potential tumour edges. Upon detecting several tumour edges, the optimal scan position for the next data acquisition is predicted.

#### 3.2.1.a Tumour boundary detection and prediction

To design a scan trajectory that follows a tumour boundary, it is necessary to have some knowledge of the tumour boundary path. One possible way to know this, is to have the surgeon roughly trace a 2D margin on a camera image (a camera is usually attached to the OCT probe) on a hand-held tablet as depicted in Figure 3.6. Another possible approach would be to automatically segment the margin from the image captured by the camera.

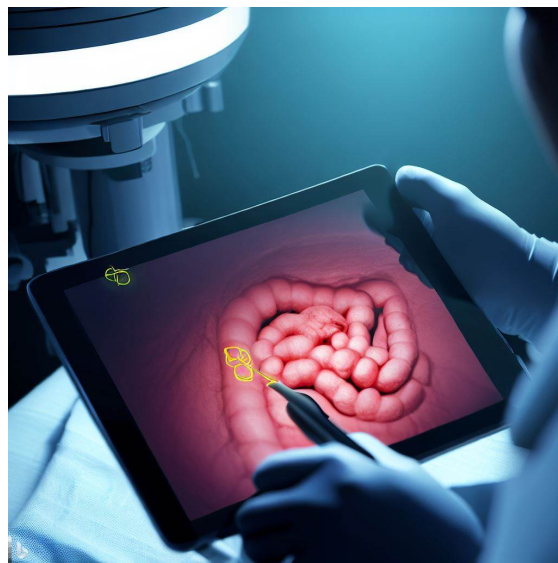


Figure 3.6 – Surgeon tracing a tumour boundary on the large intestine on a tablet [Dalle 23].

The surgeon traces the tumour boundary path based on suspicion of cancer presence, the suspicious region is typically identified by a reddish hue distinguishing it from the surrounding tissue. However, it's important to note that the surgeon's delineation may be incorrect, necessitating the implementation of a closed-loop prediction system for the real-time replanning of the tumour boundary. This involves detecting and predicting the positions of the actual tumour boundary by analysing previously collected OCT data.

To do tumour boundary detection, concepts from the theory of edge detection as used in the field of computer vision are used [Canny 86]. A convenient way to display OCT volumes is using point clouds. In the context of point clouds, edge detection involves identifying areas of significant change or discontinuities often associated with edges or boundaries of objects or structures in the scene [Ahmed 18]. Edge detection algorithms identify edges and represent them, typically as a list of point pairs, a set of lines in images, or a list of vertices or patches/facets in volumes. During OCT data acquisition, tracking 3D boundaries in volumes is more challenging compared to tracking a boundary on a 2D plane. Reason being, the OCT process is a sequential 1D process based on a free-form planar curve that generates a 2D scan which forms a 3D volume. Consequently, tracking an OCT surface is complex, while tracking a 2D curve can be formulated using existing techniques. In this research, we focus on 2D margins only, and tumour boundary detection is now redefined as the process of identifying the 2D tumour region margin in the  $x - y$  plane. By doing this, we project the tumour structure (considering self-contained convex-shapes for the tumours) onto the  $x - y$  surface plane.

To facilitate the generation of a suitable adaptive scan trajectory through tumour boundary prediction, the Frenet-Serret frame formalism is employed. This approach relies on characterising the curve through the presence of a few edge positions, typically a minimum of three. These edge positions provide the neces-

sary information to predict the subsequent evolution of the scan positions along a curve. This prediction is achieved by leveraging two fundamental properties of the curve: its tangent and curvature. The differential geometry nature of the Frenet-Serret frame is crucial in facilitating the smooth process of tumour path following. Nonetheless, tumour margins are usually irregular. OCT data is not acquired directly on the tumour boundary but rather along a smooth band containing the latter. Therefore, we need to design a scan trajectory that can acquire OCT data along the band, with the central path along the band following or being fitted onto the tumour boundary. This way, we can account for some errors in either the detection or prediction of the tumour boundary.

### 3.2.1.b Scan trajectory that follows a tumour boundary

In Figure 3.7, a manually segmented 2D histopathology image that distinguishes healthy and tumour regions during a biopsy within a breast tissue is observed. Similarly, in Figure 3.1, an OCT volume was manually segmented to identify the tumour region.

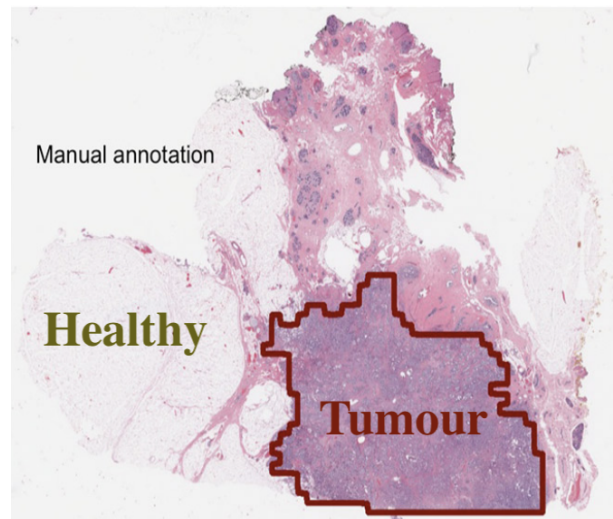


Figure 3.7 – 2D tumour manual delineation [Janowczyk 16, Janowczyk 17].

With an accurate delineation of the tumour in 3D, its volume can be estimated, which would facilitate the monitoring of the progression/treatment of cancer. Similarly, an accurate delineation of the tumour in 2D, provides the surgeon with information in determining the presence or absence of cancer. The tumour boundary is usually irregular as depicted in Figure 3.8; however, the convex hull which is tracked is considered smooth as illustrated in Figure 3.9a. As OCT operates through a sequential scanning process rather than global acquisition like a camera, we can't just acquire the data on the tumour boundary and do software adaptive detection. Instead, it is necessary to integrate data acquisition along a smooth constrained band containing the tumour boundary and implement tumour edge detection. A suitable scan trajectory designed to follow the tumour boundary is the sinusoidal wave as shown in Figure 3.8 and 3.9b

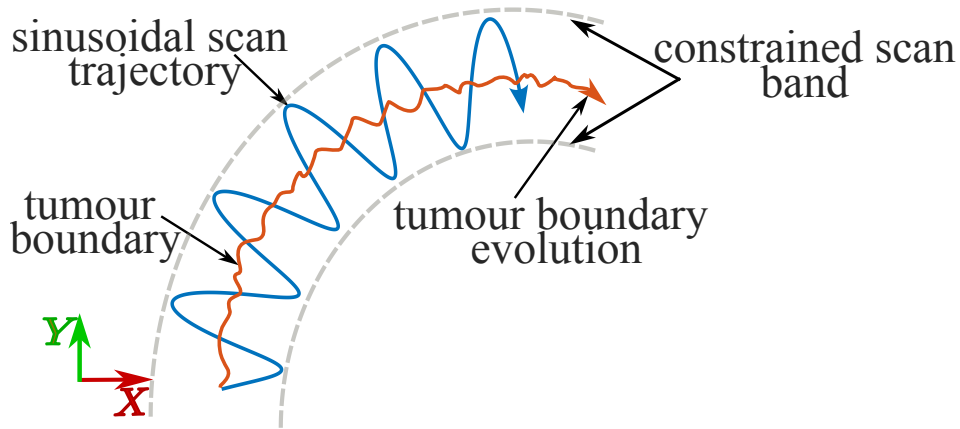


Figure 3.8 – Sinusoidal scan trajectory following the 2D tumour boundary.

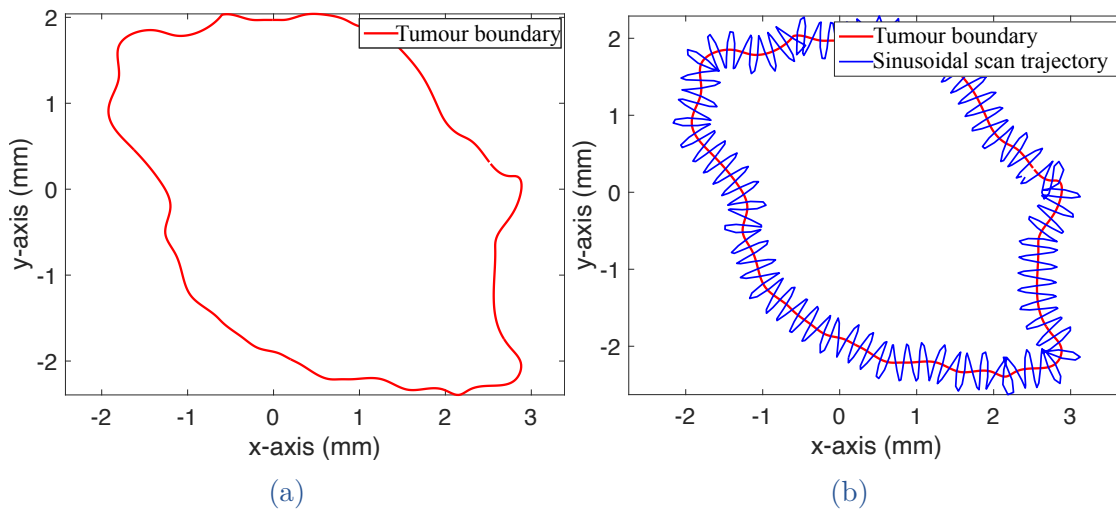


Figure 3.9 – (a) 2D tumour boundary, (b) Sinusoidal scan trajectory following the 2D tumour boundary.



Several factors make the sinusoidal trajectory particularly suitable for this application:

- ✓ Continuity - the sinusoidal trajectory is continuous, characterised by smoothly changing curvatures.
- ✓ Spatial resolution control - by selecting appropriate frequencies and amplitudes, the spatial resolution for capturing tumour related data can be precisely defined. Moreover, these frequency and amplitude parameters can be tailored to align with the resolution capabilities of the OCT device in addition to providing a margin of error in the detection and prediction processes.

### 3.2.2 Technical description of adaptive scanning

In the subsequent sub-sections, the methodology involved in performing adaptive scanning is detailed.

#### 3.2.2.a Spatial evolution of positions along a tumour boundary based on the Frenet-Serret frame

As illustrated in Figure 3.10, the spatial evolution of the positions along the central curve (2D tumour boundary) of a scanning band is modelled using the Frenet-Serret frame [Frenet 52, Serret 51].

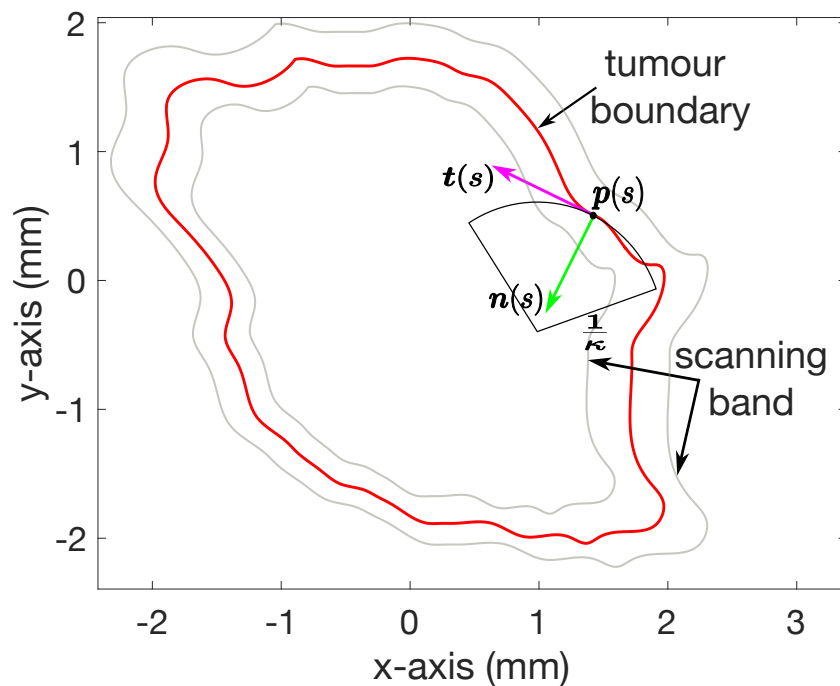


Figure 3.10 – Illustration of the Frenet-Serret frame on a 2D tumour boundary.

The Frenet-Serret frame is a mathematical framework named after the French mathematicians Jean Frenet and Joseph Serret, who developed it in the 19th century. The Frenet-Serret frame can be used to describe the motion of a curve



in three-dimensional space. At each point on a differentiable curve, the Frenet-Serret frame consists of three mutually orthogonal unit vectors: the tangent vector  $\mathbf{t}$ , which points in the direction of the curve, the normal vector  $\mathbf{n}$ , which points in the direction of the curve's curvature, and the binormal vector  $\mathbf{b}$ , which is perpendicular to both  $\mathbf{t}$  and  $\mathbf{n}$  completing the orthogonal frame. Conventionally, the Frenet-Serret frame is used in 3D space. However, in this chapter, we only focus on 2D curves; therefore, the binormal vector  $\mathbf{b}$  is constant and is excluded in our methodology. Therefore, the Frenet-Serret formulae are:

$$\frac{\frac{d\mathbf{p}(s)}{ds}}{\left\|\frac{d\mathbf{p}(s)}{ds}\right\|} = \mathbf{t}(s) \quad (3.1a)$$

$$\frac{d\mathbf{t}(s)}{ds} = \kappa(s)\mathbf{n}(s) \quad (3.1b)$$

$$\frac{d\mathbf{n}(s)}{ds} = -\kappa(s)\mathbf{t}(s) \quad (3.1c)$$

where,

- ❖  $s$  - arc length variable
- ❖  $\mathbf{p}(s)$  - position vector of the tumour boundary in a fixed frame
- ❖  $\mathbf{t}(s)$  - unit tangent vector with respect to a position on the tumour boundary
- ❖  $\mathbf{n}(s)$  - unit normal vector with respect to a position on the tumour boundary
- ❖  $\kappa(s)$  - curvature at a position on the tumour boundary

Knowing the parameters to the Frenet-Serret frame equations and assuming a slowly changing curvature, the next scan positions can be predicted.

### 3.2.2.b Differentiating between cancerous and healthy regions in a tissue

One method to differentiate between cancerous and healthy regions in a tissue, is to compare the optical properties of the different regions. Cancerous tissue typically has different optical scattering and absorption properties compared to a healthy tissue, which can be revealed by OCT imaging. There have been several studies that have demonstrated the ability of OCT to differentiate between cancerous and healthy regions based on their optical properties. For example, a study in [Yao 17] showed that the amplitude and phase of the backscattered light from cancerous regions was significantly different from that of healthy regions in *ex vivo* human breast tissue samples. The OCT B-scans are shown in Figure 3.11.

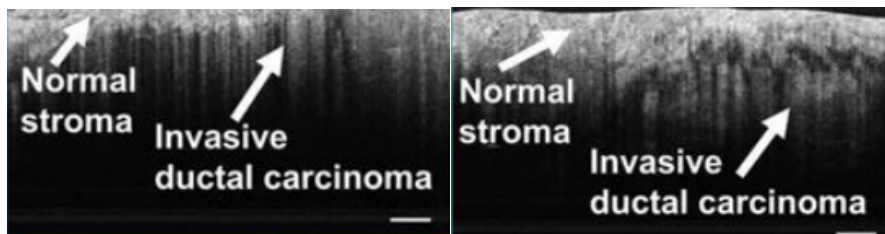
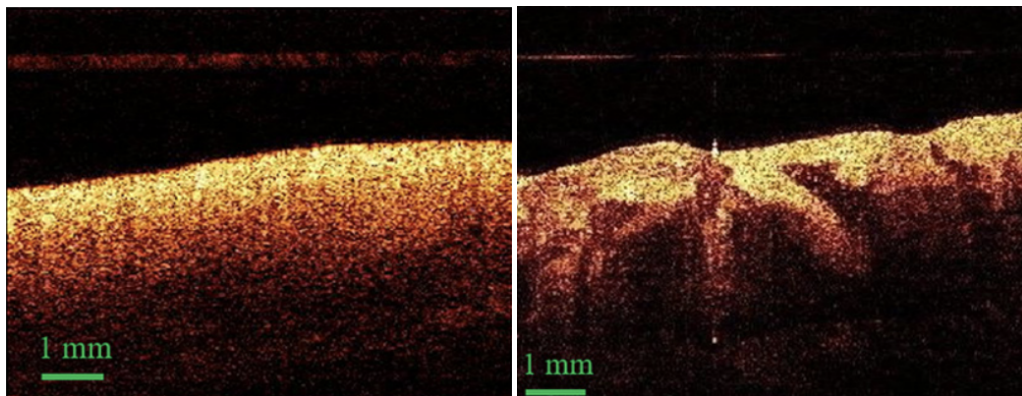


Figure 3.11 – OCT image (B-scan) examples of normal fibrous stroma and invasive ductal carcinoma, scale bar:  $250\mu m$  [Yao 17].

Another study by Badiéyan *et al.* [Badiéyan 19] found that the backscattered light from cancerous regions of *ex vivo* human prostate samples had a different polarization state than that of healthy regions. Furthermore, the use of advanced image analysis techniques such as texture analysis, fractal dimension, and polarimetric parameters have also been used to differentiate between cancerous and healthy regions in OCT images. For instance, Zysk *et al.* [Zysk 06] used texture analysis to differentiate between cancerous and healthy regions of *ex vivo* human breast tissue samples, Pu *et al.* [Pu 12] used fractal dimension to differentiate between cancerous and healthy regions of *ex vivo* human prostate tissue samples and South *et al.* [South 14] used polarimetric parameters to differentiate between cancerous and healthy regions of *ex vivo* human breast tissue samples. These parameters provide detailed information about the tissue microstructure, and reveal changes in the tissue organisation and composition.

In the gut as well, OCT images of healthy and cancerous tissue appear remarkably different as shown in Figures 3.12a and 3.12b. The OCT images of healthy tissue are characterised by visibly smoother and homogenous intensity distribution, while the cancerous tissues have a highly degenerated, fragmented and heterogeneous texture [Luo 19a, Wang 17]. To model the homogenous and heterogeneous texture distribution, Luo *et al.* used the standard deviation statistical parameter. The standard deviation values of the A-scan intensity values in cancerous regions are higher as compared to the healthy regions as detailed in [Luo 19a].



(a) Healthy stomach tissue.

(b) Cancerous stomach tissue.

Figure 3.12 – Healthy and cancerous OCT B-scan images [Luo 19a].

### 3.2.2.c Lesion boundary estimation by statistically analysing OCT data

Let  $\vec{\mathcal{I}}_n(\mathbf{p}(s))$  represent a vector of OCT A-scan intensity values for the position  $\mathbf{p}_n(s)$  as seen in Figure 3.13 as well as in Figure 3.14.

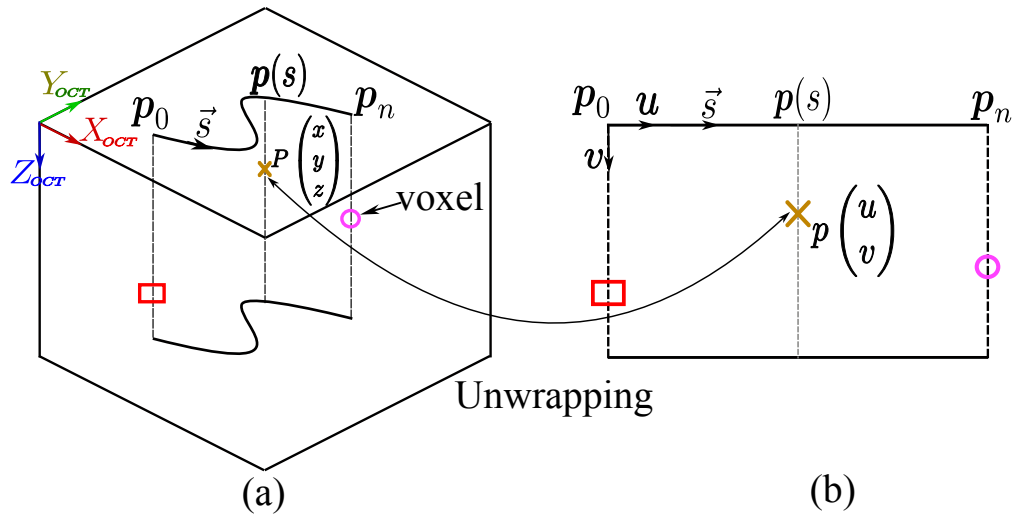


Figure 3.13 – (a) 3D view of a free-form B-scan of a smooth trajectory, (b) Unwrapped B-scan.

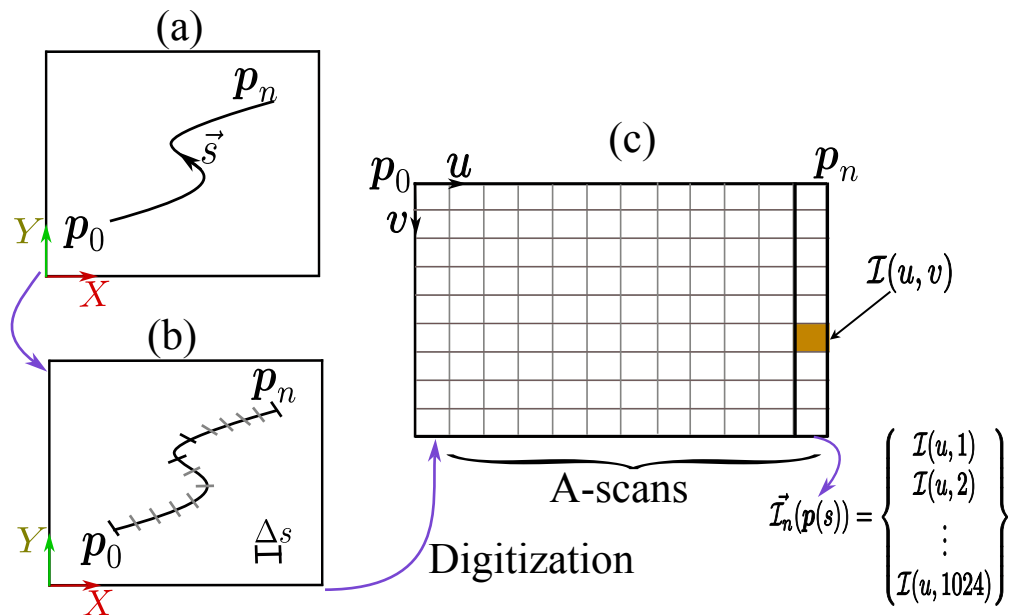


Figure 3.14 – (a) Top view of a free-form smooth trajectory, (b) Segmented free-form smooth trajectory, (c) Unwrapped and digitized B-scan illustrating A-scans and voxels.

It is desired to find  $\mathbf{p}_{n+1}(s)$  which is the next predicted position of the tumour boundary. The first step involves estimating the tumour boundary from a set of previously acquired A-scans. To know whether an A-scan was collected on a healthy or a tumorous region of the tissue, its optical properties are statistically investigated using the standard deviation and is computed using equation 3.2:

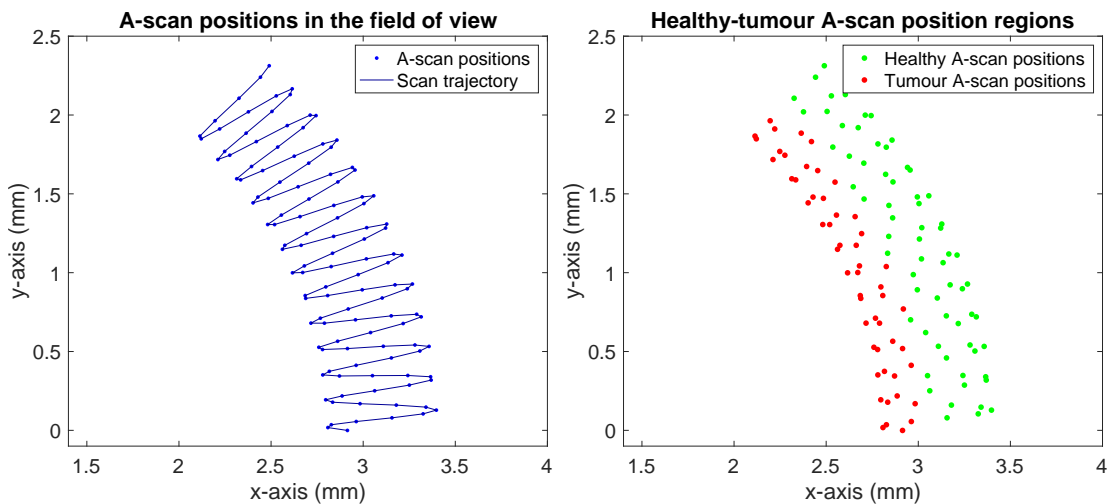
$$\sigma_n(\vec{\mathcal{I}}_n(\mathbf{p}(s))) = \sqrt{\frac{1}{N} \sum_{v=1}^N (\mathcal{I}_{nv} - \frac{1}{N} \sum_{v=1}^N \mathcal{I}_{nv})^2} \quad (3.2)$$

where,

- ❖  $\sigma_n$  - standard deviation of the  $n$ 'th Ascan
- ❖  $N$  - number of voxels in the region of interest
- ❖  $\mathcal{I}_{nv}$  - intensity of the  $v$ 'th voxel in the  $n$ 'th Ascan

The larger the value of the standard deviation, the higher the likelihood that the corresponding A-scan was obtained within the tumour [Luo 19a]. To estimate the edge positions between healthy and tumorous regions within the tissue, edge detection using k-means clustering [Stuart 82, Seber 84, Spath 85, Arthur 07, Jin 10] is used. Contrary to using k-means clustering based on the squared Euclidean distance metric, we use here k-means clustering based on the standard deviation values of the intensity values of each A-scan.

Consider a field of view in the  $x - y$  axis plane of  $6mm \times 6mm$  with several A-scan positions from a sinusoidal scan trajectory. A subset of A-scans is acquired from these positions, as illustrated in Figure 3.15a of a tissue sample having both healthy and tumour regions.



(a) A-scan positions distributed in the field of view.

(b) Healthy and tumour characterisation of A-scan positions.

Figure 3.15 – Detection of individual healthy and tumour A-scan positions using k-means clustering.

In Figure 3.15a, we don't know yet which A-scan positions correspond to healthy or tumour regions. As mentioned in the previous paragraph, a higher standard deviation of the intensity values corresponds to A-scans acquired in the tumour region, while lower values correspond to A-scans in the healthy region. Since we are interested in two clusters representing these two regions, we only need two centroid values to initialise the k-means clustering algorithm. To do this, we obtain the minimum and maximum standard deviation values from the subset of A-scans. These centroid values are then adjusted through several iterations until suitable values are found that best separate the healthy and tumour regions, as seen in Figure 3.15b. In this figure, the clear distinction between the healthy and tumour A-scan regions is evident. Nevertheless, the boundary still needs to be estimated.

To estimate the boundary from point cloud data is a less trivial task than in images, since we have less data which is often noisy. In images, there are several pixels of data that can be used to efficiently compute the edge positions, whereas in our application, we only have a few points. This is because the boundary is determined after the acquisition of OCT data from only a few A-scan positions locally at each iteration of data acquisition. Having the two regions as highlighted in Figure 3.15b, we determine which pairs of A-scan positions from the healthy and tumour regions are closest to each other. From these pairs of positions, we compute the midpoint positions between them, as seen in Figure 3.16a. Smoothing on the midpoint positions is then performed, and a 2<sup>nd</sup> degree spline curve is fitted, as shown in Figure 3.16b.

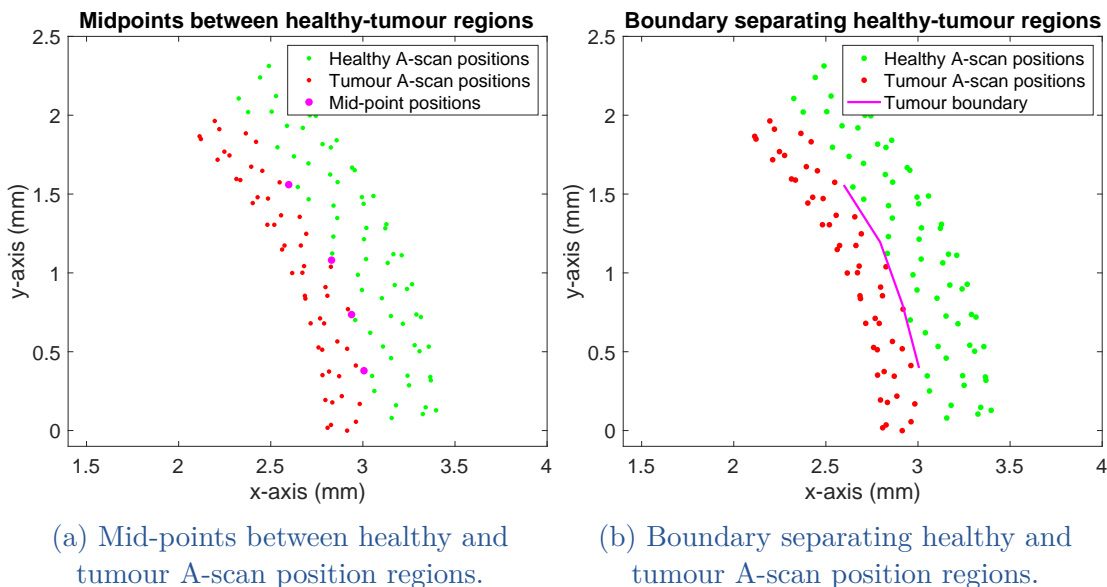


Figure 3.16 – Tumour boundary estimation.

In Figure 3.16b, we can distinctly see the local boundary that separates the healthy and tumour regions in the  $x - y$  plane. The tumour boundary obtained from a subset of A-scan positions then provides information on how the global

tumour boundary evolves. By performing this operation several times while the OCT data is being acquired, we are then able to fully reconstruct the tumour boundary. It is acknowledged that a simple example where we can clearly see the distinction between the two regions has been shown. For more complex data where tumour and healthy regions heavily interconnect with each other, more advanced methods to estimate the correct boundary will need to be developed (however, this is not the purpose of this chapter). The pseudocode for this tumour boundary estimation is provided in Appendix B.1.

Knowing the tumour boundary from the analysis of the subset of the A-scans acquired so far, we can now predict the position of the next A-scan to acquire, based on the Frenet-Serret frame as detailed in [Andersson 05].

#### 3.2.2.d Curvature and heading angle estimation

Considering Figure 3.17, we would like to first compute the curvature and heading angle of the tumour boundary.

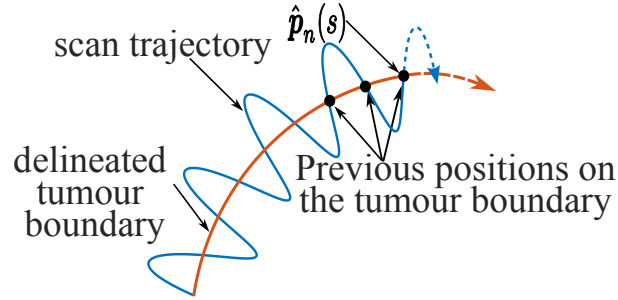


Figure 3.17 – Illustration of the tumour boundary evolution considering previous positions on the tumour boundary.

From the last scan position representing the estimated tumour boundary, obtained after analysing the previously acquired data, we consider the next previous tumour boundary position and compute the tangent using the backward finite difference:

$$\hat{\mathbf{t}}_n = \frac{\hat{\mathbf{p}}_n(s) - \hat{\mathbf{p}}_{n-i}(s)}{\|\hat{\mathbf{p}}_n(s) - \hat{\mathbf{p}}_{n-i}(s)\|} \quad (3.3)$$

where,

- ❖  $\hat{\mathbf{p}}_n(s)$  - the current last position on the tumour boundary.
- ❖  $i$  - the index of the previous position on the tumour boundary.

Having the tangent, the heading angle  $\hat{\theta}$ , which determines where the tumour boundary is headed towards, is estimated using equation 3.4 and is shown in Figure 3.18.

$$\hat{\theta} = \text{atan2}([\hat{\mathbf{t}}_n]_2, [\hat{\mathbf{t}}_n]_1) \quad (3.4)$$

where,

- ❖  $[\hat{\mathbf{t}}_n]_j$  - denotes the  $j^{\text{th}}$  component of  $\hat{\mathbf{t}}_n$
- ❖  $\hat{\theta}$  - the angle  $\hat{\mathbf{t}}_n$  makes with the  $x$  - axis of the global reference frame.

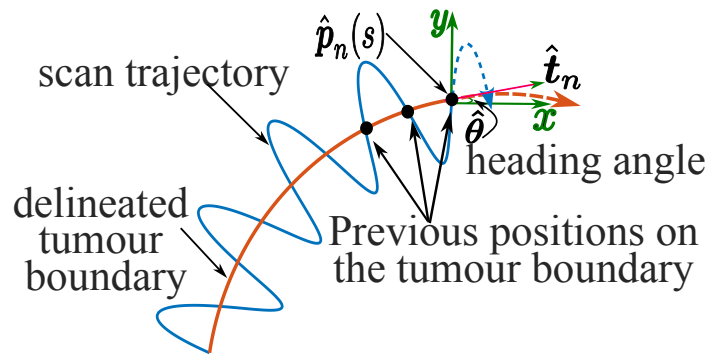


Figure 3.18 – Illustration of the heading angle estimation.

One can then estimate the curvature based on Heron's formula [Calabi 98, Andersson 05]. Using Figure 3.19, let;

$$\begin{aligned} A &= \hat{\mathbf{p}}_{n-2i} \\ B &= \hat{\mathbf{p}}_{n-i} \\ C &= \hat{\mathbf{p}}_n \end{aligned} \quad (3.5)$$

which are the previous locations on the tumour boundary and  $a, b, c$  to denote the Euclidean distances  $d(\cdot, \cdot)$  between these positions.

$$\begin{aligned} a &= d(\hat{\mathbf{p}}_{n-2i}, \hat{\mathbf{p}}_{n-i}) \\ b &= d(\hat{\mathbf{p}}_{n-i}, \hat{\mathbf{p}}_n) \\ c &= d(\hat{\mathbf{p}}_n, \hat{\mathbf{p}}_{n-2i}) \end{aligned} \quad (3.6)$$

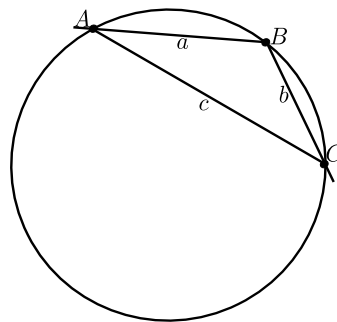


Figure 3.19 – Curvature estimation parameters based on Heron's formula.

The curvature estimation is thus:

$$\kappa(A, B, C) = \pm 4 \frac{\sqrt{l(l-a)(l-b)(l-c)}}{abc} \quad (3.7)$$

where,

$$\diamond l = \frac{1}{2}(a + b + c)$$

The change in the heading angle is computed using:

$$\Delta\hat{\theta} = \kappa\Delta s \quad (3.8)$$

where,

$$\blacklozenge \Delta s = d(B, C)$$

### 3.2.2.e Tumour boundary position prediction

Using the Frenet-Serret equations, we can predict the next position ( $\hat{\mathbf{p}}_{n+1}$  as shown in Figure 3.20) of the tumour boundary to be scanned, having the curvature and the tangent and normal vectors. Assuming local smoothness, the frame undergoes a translation and a rotation that depends on the  $\Delta s$  increment on the boundary. It is easy to show (see Appendix A.2) that the tangent and normal vectors upon the Frenet-Serret model follows a 1<sup>st</sup> order differential equation that can be solved into ( $\boldsymbol{\xi}$  is the axis of rotation):

$$\hat{\mathbf{t}}_{n+1} = \text{Rot}(\boldsymbol{\xi}, \kappa\Delta s)\hat{\mathbf{t}}_n = \cos(\kappa\Delta s)\hat{\mathbf{t}}_n + \sin(\kappa\Delta s)\hat{\mathbf{n}}_n \quad (3.9a)$$

$$\hat{\mathbf{n}}_{n+1} = \text{Rot}(\boldsymbol{\xi}, \kappa\Delta s)\hat{\mathbf{n}}_n = -\sin(\kappa\Delta s)\hat{\mathbf{t}}_n + \cos(\kappa\Delta s)\hat{\mathbf{n}}_n \quad (3.9b)$$

Using this information, we can integrate equation 3.1a so that we extract  $\hat{\mathbf{p}}_{n+1}$ , which is given by equation 3.10 (see extensive demonstration in Appendix A.2).

$$\hat{\mathbf{p}}_{n+1} = \hat{\mathbf{p}}_n + \begin{cases} \frac{1}{\kappa} \left( \sin(\kappa\Delta s)\hat{\mathbf{t}}_n + (1 - \cos(\kappa\Delta s))\hat{\mathbf{n}}_n \right) & , \forall \kappa \neq 0 \\ \Delta s \hat{\mathbf{t}}_n & , \kappa = 0 \end{cases} \quad (3.10)$$

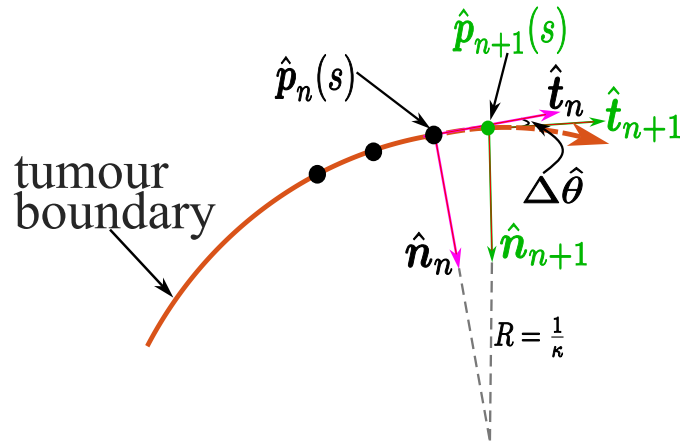


Figure 3.20 – Tumour boundary prediction.



## 3.2.2.f Sinusoidal trajectory that follows a tumour boundary

To generate the sinusoidal trajectory along the tumour boundary as seen in Figure 3.21, equation 3.11 is used:

$$\mathbf{p}_{sin}(s) = \mathbf{p}_n(s) + A_m \sin(\omega) \mathbf{n}_n(s) \quad (3.11)$$

where,

- ❖  $\mathbf{p}_{sin}(s)$  - sinusoidal scan trajectory
- ❖  $A_m$  - amplitude of the scan trajectory
- ❖  $\omega$  - spatial frequency of the scan trajectory
- ❖  $\mathbf{n}_n(s)$  - normal vector with respect to the position,  $\mathbf{p}_n(s)$  on the tumour boundary

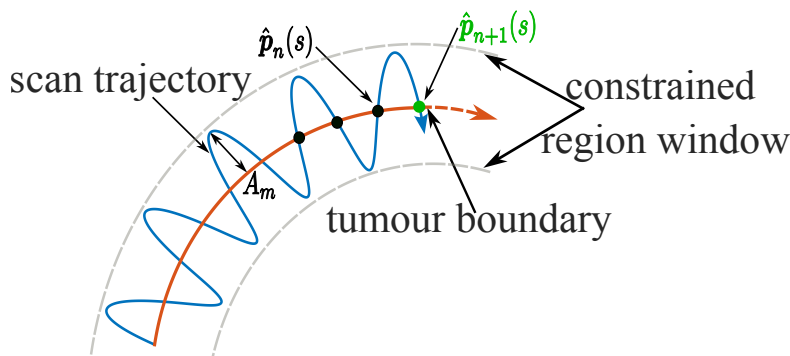


Figure 3.21 – Section of an adaptive scan trajectory.

The constrained region window in the figure is governed by the amplitude and spatial frequency of the sinusoidal scan trajectory in addition to the heading angle estimate of the tumour boundary.

## 3.2.2.g Adaptive scanning flowchart

As has been discussed earlier, we would like to delineate as close as possible the margins of the tumour for medical diagnosis or for the surgeon to resect or ablate it. The flowchart in Figure 3.22 highlights this process of adaptive scanning that has been presented so far, as well as its software development. The flowchart consists of two major phases: initialisation and recurrence. The initialisation phase focuses on identifying the initial three positions along the tumour boundary. Subsequently, the recurrence phase aims to leverage the Frenet-Serret frame for predicting subsequent scan positions. This involves a continual process of data acquisition and analysis, executed recursively until an adequate number of edge positions are accumulated to effectively delineate the whole tumour boundary.

## Initialisation phase

As explained in sub-section 3.2.1.a, the first step in adaptive scanning involves the surgeon roughly outlining the tumour boundary based on visual cues from a camera image. Ideally, the surgeon's drawn boundary would be perfect, and we

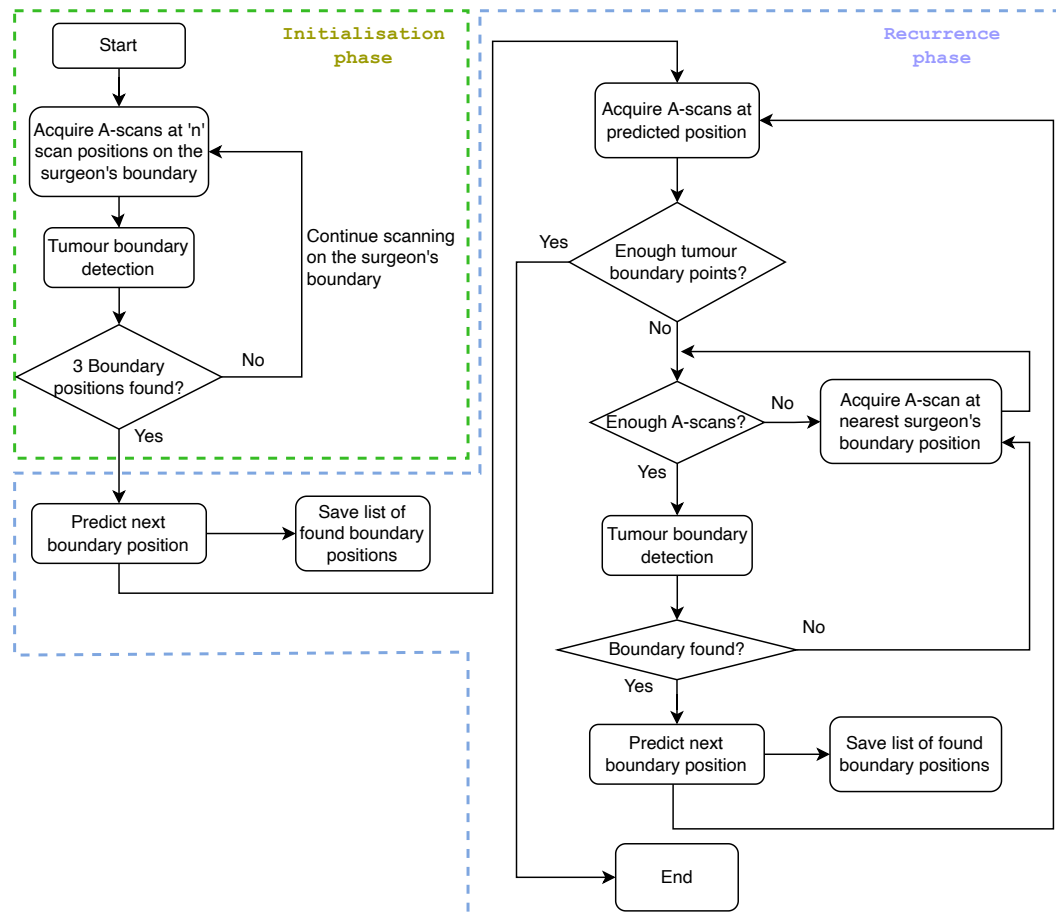


Figure 3.22 – Adaptive scanning flowchart.

would only need to collect OCT data along it. However, in reality, the surgeon's estimation of the tumour boundary may be inaccurate. In the adaptive scanning process, a non-raster sinusoidal trajectory is designed, and data is collected at the first few scan positions along the surgeon's drawn boundary. Once enough tumour edges are detected through the analysis of this initial data, an initial section of the tumour boundary is constructed, marking the completion of the initialisation phase.

### Recurrence phase

With a sufficient number of edge positions obtained during the initialisation phase, the next A-scan location is predicted. However, it's important to note that these predicted scan positions may occasionally be incorrect and not correspond to tumour margins. When the data analysis process does not yield enough tumour edge positions to make accurate predictions, a fallback solution is implemented: data is collected at the nearest scan position along the surgeon's drawn boundary. This iterative process continues until an adequate number of tumour boundary positions have been identified.

### 3.3 NUMERICAL (SIMULATION) VALIDATION OF ADAPTIVE SCANNING

In this section, the adaptive scanning protocol as illustrated in the flowchart in Figure 3.22 is validated through simulation. Firstly, a generic OCT volumetric data is designed and generated. This generic OCT volumetric data is then utilized in the simulation study.

#### 3.3.1 Simulation of volumetric OCT data of a tissue sample containing a tumour.

##### 3.3.1.a A-scan simulation

The simulated OCT data is of a tissue sample containing both healthy and tumour regions. As discussed in sub-section 3.2.2.b, healthy tissue regions exhibit homogenous layers, while tumour regions exhibit heterogenous layers. The designed A-scans will have the following general characteristics:

- Number of voxel depth locations in the  $z$  direction; 1024
- A-scan depth;  $3.54mm$

To accurately reflect the operation of the OCT device, a single A-scan is divided into three sections: an air section, a tissue section, and a ‘too deep’ section. Figure 3.23 illustrates the A-scan design and each section. The intensity values of voxels in the air and ‘too deep’ sections are relatively lower than those in the tissue section. In typical tissue OCT imaging, the OCT is not in direct contact with the tissue, therefore, only noisy data is collected in the air section. Moreover, the light used in OCT imaging does not penetrate too deep into the tissue typically stopping at around  $2mm$ . The depth of the tissue and ‘too deep’ section is indeed dependent on the type of body organ tissue being imaged.

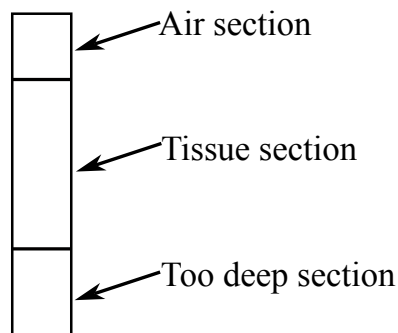


Figure 3.23 – Illustration of sections in a simulated A-scan.

The A-scans designed for healthy regions have the statistical characteristics displayed in Table 3.1. The statistical parameters chosen are the mean and standard deviation of the intensity values.

Table 3.1 – A-scan design in a healthy tissue region.

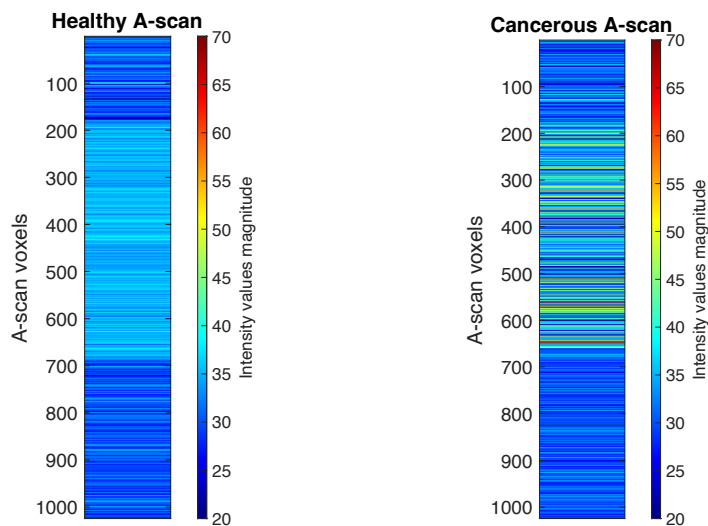
<b>A-scan section</b> <b>Intensity value</b> <b>statistic measure</b>	Air	Tissue	Too deep
Mean	30	35	30
Standard deviation	4	2	3

The A-scans designed for the tumorous (cancerous) regions have the statistical characteristics displayed in Table 3.2. Generally, the standard deviation of the intensity values of the A-scans obtained in a cancerous region are higher than those obtained in a healthy region of the tissue [Luo 19a].

Table 3.2 – A-scan design in a tumorous tissue region.

<b>A-scan section</b> <b>Intensity value</b> <b>statistic measure</b>	Air	Tissue	Too deep
Mean	30	35	30
Standard deviation	4	9	3

An A-scan simulated in the healthy and cancerous tissue region is shown in Figure 3.24a and 3.24b respectively. It is seen that the cancerous A-scan has a greater degree of variation in the intensity values indicating a heterogenous texture while the healthy A-scan displays a homogeneous texture with minimal variation in the magnitude of the intensity values.



(a) Simulated healthy A-scan. (b) Simulated cancerous A-scan.

Figure 3.24 – Healthy and cancerous OCT A-scan data.

## 3.3.1.b C-scan simulation

It is necessary to also design a scan trajectory for simulating the OCT tissue volume. For simplicity, we will use the conventional raster scan pattern with the following characteristics:

- Field of view size;  $6\text{mm} \times 6\text{mm}$
- Number of voxel locations in the  $x - y$  plane;  $100 \times 100$

Next, we design two shapes to represent the tumour boundary in the  $x - y$  plane; a circle and an irregular shape. Figures 3.25a and 3.25b illustrate the distribution of scan positions in both the healthy and cancerous regions within the chosen field of view for the two shapes.

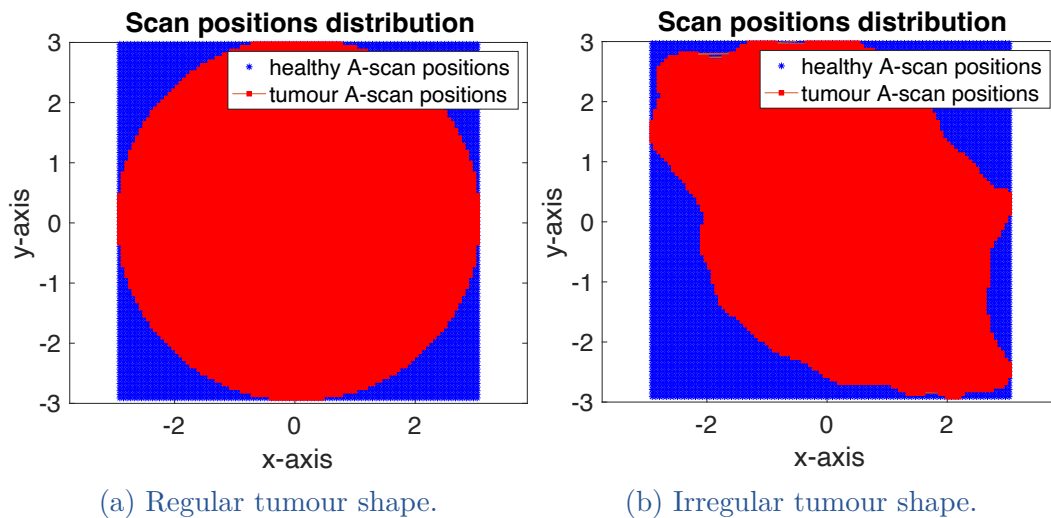


Figure 3.25 – Distribution of healthy and tumour boundary scan positions.

In designing the OCT volume, we make the strong assumption that the tumour boundary is clearly distinguishable using OCT data and that the depth is fairly uniform throughout the entire tumour. The point cloud of the OCT volumes depicting a tissue sample is shown in Figure 3.26. Furthermore, a B-scan is extracted from each of the volumes at  $y = 0$ , and is plotted in Figure 3.27.

The point cloud volumes in Figure 3.26 depict the distribution and spatial arrangement of data points obtained utilising the OCT. The A-scans within the tumour region have distinct features associated with cancerous tissues such as irregularities, increased scattering or abnormal architectural patterns. The simulated point cloud provides valuable insights into how the tumour boundary is delineated and the characterisation of the pathological region within a tissue. Filtering out the simulated noisy data, Figure 3.26 illustrates the point cloud volumes to be used in the subsequent steps. In these point cloud volumes, the hypothesis is that the tumour boundary can clearly be seen. In addition, the standard deviation of the A-scans are also plotted for the OCT volumes. They are shown in Figure 3.28a and 3.28b respectively for the circular and irregular shaped tumour in the  $x - y$  plane.

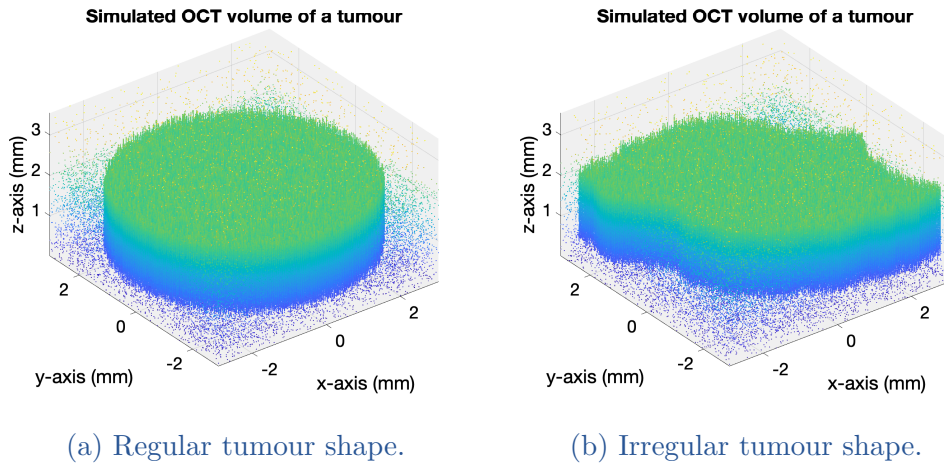


Figure 3.26 – Simulated OCT point cloud volumes of a tissue sample.

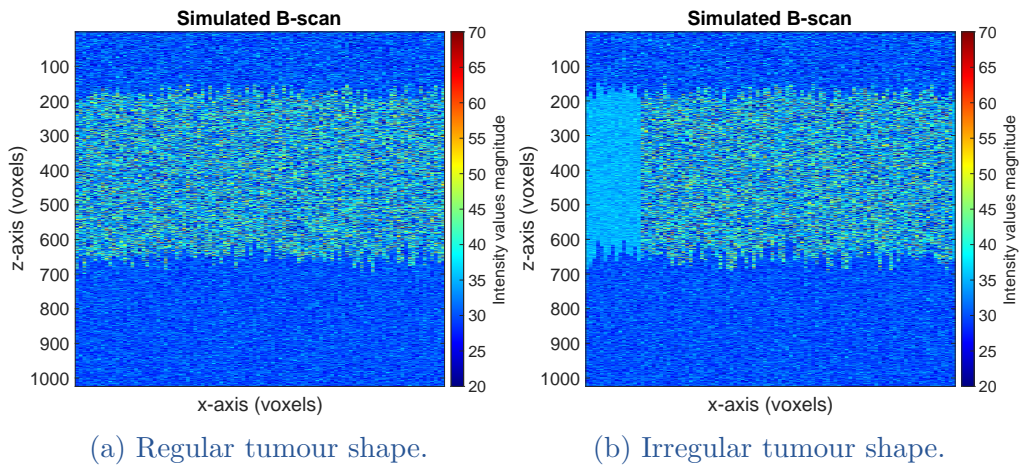


Figure 3.27 – B-scan of the simulated OCT point cloud volumes in Figure 3.26 of a tissue sample at  $y = 0$ .

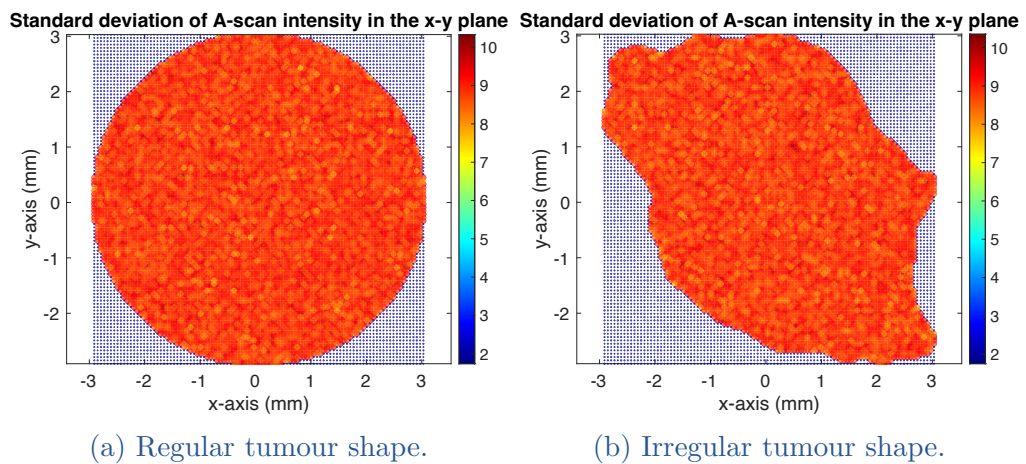


Figure 3.28 – Standard deviation of A-scan intensity values.



### 3.3.2 Simulation of adaptive scanning

To simulate adaptive scanning, two approaches will be presented:

- ✓ For the first approach, OCT data is intentionally obtained directly on the tumour boundary during the scanning process.
- ✓ For the second approach, OCT data is collected under realistic experimental conditions (noisy data), and it may incidentally fall on the tumour boundary.

The second approach aims to replicate the challenges faced during real-world data acquisition, where obtaining precise data of the tumour boundary may not always be guaranteed. By incorporating both approaches, we can assess the effectiveness of the adaptive scanning protocol in accurately capturing data from the tumour boundary, leading to improved imaging outcomes in clinical applications.

#### 3.3.2.a Intentional OCT data acquisition on the tumour boundary (direct targeting of the tumour boundary)

Using the simulated OCT volume and implementing the adaptive scanning protocol as illustrated in the flowchart in Figure 3.22, the adaptive scan trajectory shown in Figure 3.29 is obtained. In the initial phase of adaptive scanning, OCT data is collected at a few initial scan positions and analysed to detect and locate tumour edges. Once at least three edge positions are identified, the scan trajectory is replanned, and the protocol transitions to the recurring phase. In the recurring phase, the process of acquiring and analysing data, as well as predicting the next scan positions to be scanned, is recursively repeated. This iterative process continues until a sufficient number of tumour boundary positions are identified. The effectiveness of the adaptive scanning protocol in accurately capturing tumour boundary data is demonstrated in Figure 3.29a and 3.29b (for a regular and an irregular shaped tumour), showcasing the automatic and online generation of the adaptive scan trajectory in an ideal scenario.

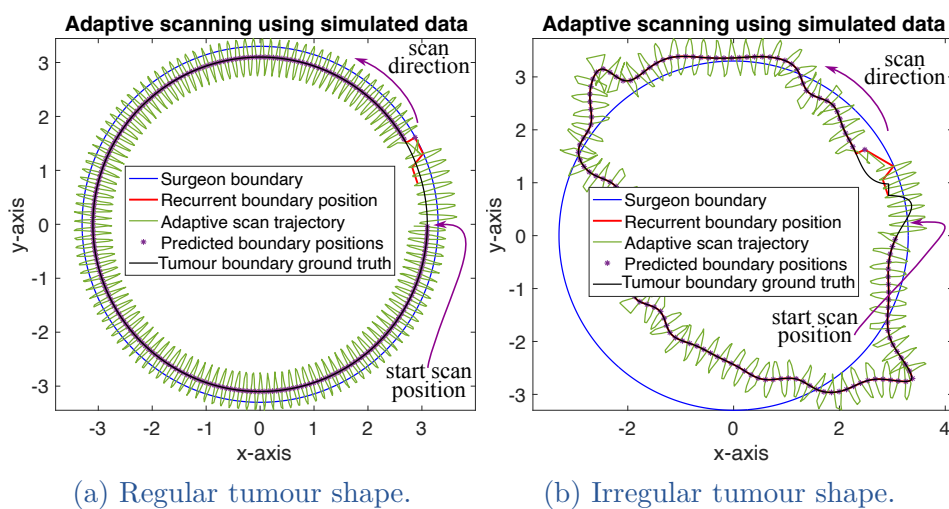


Figure 3.29 – Adaptive scan trajectory using simulated data in an ideal scenario.

Using the generated adaptive scan trajectory, the point cloud OCT volumes for the regular and irregular shaped tumours are shown in Figure 3.30a and 3.30b respectively. From these two point cloud volumes, the tumour boundary is clearly visible. As explained earlier, having information on the tumour boundary during diagnosis and surgical treatment is of utmost importance to the surgeon. In this case, by obtaining less but useful data on the tissue through the adaptive scanning approach, the tumour boundary is clearly delineated. Consequently, the data acquisition time is significantly reduced compared to the time needed to collect data in the whole field of view using a raster trajectory (a raster trajectory covering the whole field of view requires more time compared to acquiring only a fraction of data assuming that the acquisition time for each A-scan is similar).

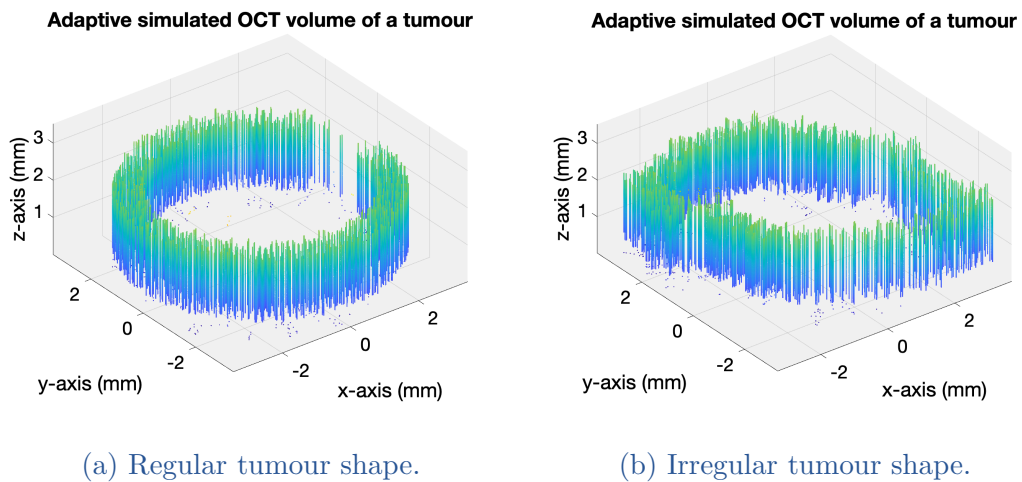


Figure 3.30 – Simulated OCT point cloud volumes obtained using an adaptive scan trajectory in an ideal scenario.

### 3.3.2.b Incidental OCT data acquisition on the tumour boundary (realistic scenario in OCT data acquisition)

In this approach, the simulation aimed to mimic real-world performance in data acquisition by having Gaussian random noise in the simulated A-scans. This means that, not all the tumour boundary positions will be detected accurately. Figure 3.31 shows the adaptive scan trajectory obtained.

Comparing this adaptive scan trajectory to the one in the ideal scenario, it is observed that it appears to be less smooth in different sections during scanning. Of particular interest, once a tumour edge is detected, the protocol attempts to replan the scan trajectory. However, due to less tumour edge detection scan positions accurately detected, the adaptive scan trajectory tends to obtain data while following the surgeon’s tumour boundary more often. Another notable observation is that, in cases where data is not collected on the tumour boundary (thereby, no tumour edge detection), the adaptive scan trajectory precisely tracks the surgeon’s drawn boundary (as mention in subsection 3.2.2.g, when the boundary is



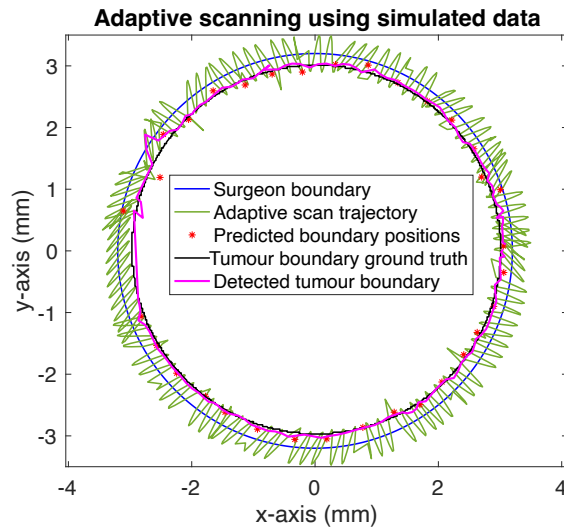


Figure 3.31 – Adaptive scan trajectory using simulated data in a realistic like scenario.

not detected, the fallback solution is to acquire data at the nearest scan position along the surgeon’s drawn boundary). Nonetheless, the tumour boundary positions detected by the k-means clustering algorithm are flagged and shown in Figure 3.31 by the magenta curve (it is non-smooth). This detected tumour boundary is smoothed, and the sinusoidal scan trajectory re-generated as shown in Figure 3.32. For a more accurate tumour boundary delineation, OCT data is adaptively acquired once more on this second adaptive scan trajectory.

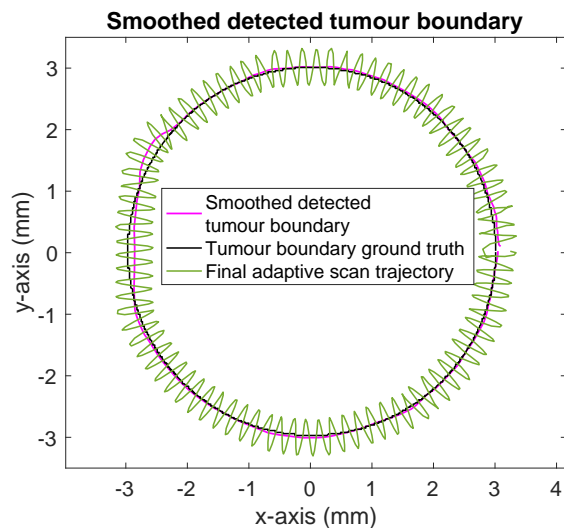


Figure 3.32 – Detected tumour boundary after first loop of adaptive scanning.

Figure 3.33 displays the point cloud volume obtained using the final adaptive scan trajectory. Even with the limited amount of data collected, the circular boundary of the tumour is still discernible.

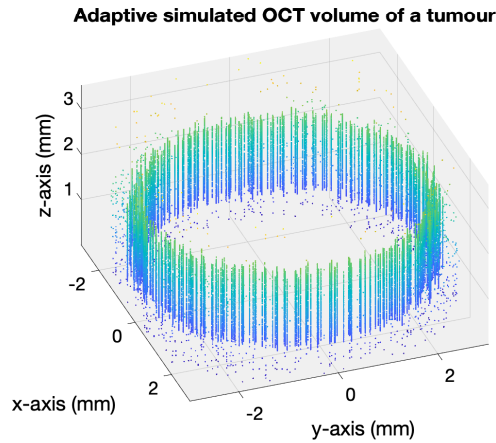


Figure 3.33 – Simulated OCT point cloud volume obtained using an adaptive scan trajectory in a realistic like scenario.

After performing k-means clustering to separate the tumour and healthy regions, we obtain Figure 3.34. From this figure, we can see that the two regions are perfectly separated by the tumour boundary ground truth demonstrating that indeed the tumour boundary can be estimated. In addition, the adaptive tumour boundary fits almost perfectly with the tumour boundary ground truth.

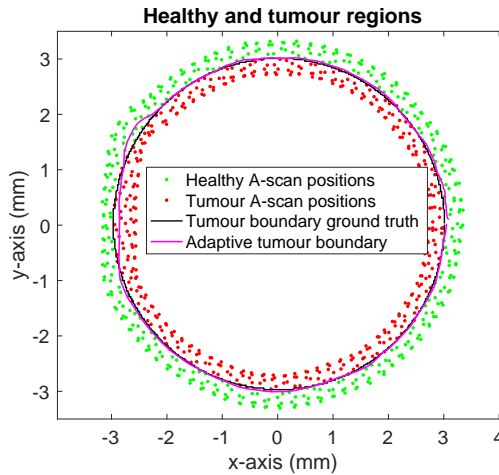


Figure 3.34 – Healthy and tumour regions delineated using k-means clustering.

### 3.4 EXPERIMENTAL VALIDATION OF ADAPTIVE SCANNING

In this section, the adaptive scanning protocol as illustrated in the flowchart in Figure 3.22 is validated by obtaining data on a tissue phantom mimicking a tumour using a Telesto II 1325nm spectral domain OCT device from Thorlabs.

The OCT device provides 1D depth (A-Scan), 2D cross-section (B-Scan) and 3D volumetric (C-Scan) images with  $5.5\mu m$  axial resolution,  $7\mu m$  lateral resolution and  $3.54mm$  depth penetration. The device has a maximum A-Scan (optical core) acquisition rate of  $76kHz$  with a maximum field-of-view of  $10 \times 10 \times 3.54mm^3$ . It is equipped with a conventional CCD camera with a resolution of  $640 \times 480$  pixels at 25 frames per second rigidly fixed to the OCT probe to visualise the object to be scanned. The experimental setup is shown in Figure 3.35. An experimental set-up procedure used to prepare the tissue phantom and collect OCT data is first presented. The results and analysis are then highlighted.

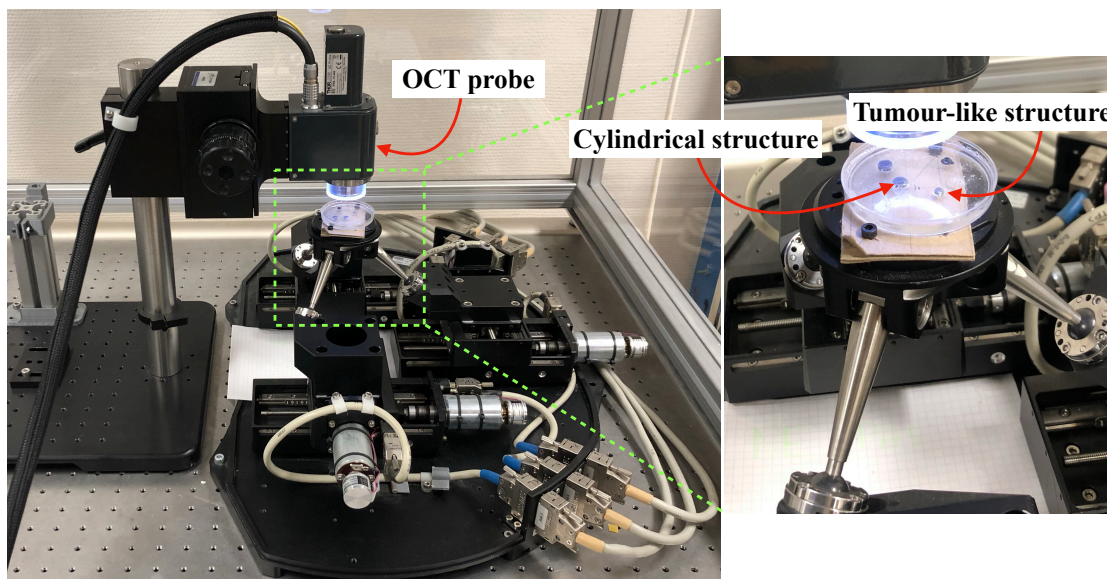


Figure 3.35 – Illustration of the experimental set-up used to validate the adaptive scanning protocol.

### 3.4.1 Experimental set-up procedure

The objective of this experimental setup procedure is to implement adaptive scanning in OCT that could be useful for early cancer detection in the gut. To simulate the gut tissues, a gelatine tissue phantom is used as a substitute (obtaining approval to use human gut tissues is hindered by long bureaucratic processes and strict ethical guidelines as is expected from a regulatory stand point).

#### 3.4.1.a Gelatine tissue phantom preparation

To prepare the tissue phantom to be used in the adaptive scanning protocol validation, the following steps were followed:

- A gelatine mixture was prepared by dissolving gelatine sheets as shown in Figure 3.36 in water. 2 sheets each weighing  $2g$  was dissolved in  $100ml$  of water. To extend the shelf-life (about two months) of the tissue phantom,  $10ml$  of glycerine was added to the mixture.



Figure 3.36 – Gelatine sheets used to prepare the tissue phantom.

- The gelatine mixture was then stirred thoroughly to ensure homogeneity and to remove any bubbles. While the manufacturer’s instructions suggested allowing the gelatine mixture to solidify at room temperature, we find that placing it in the fridge results in faster solidification without any degradation in quality. Alternatively, a suitable mold in the shape of the gut could be used to give the tissue phantom the desired shape.
- Tumour-like structures such as a 3D-printed insert shaped like a tumour and a cylindrical structure as shown in Figures 3.37 and 3.38, were placed inside the gelatine mixture before it completely thickened.

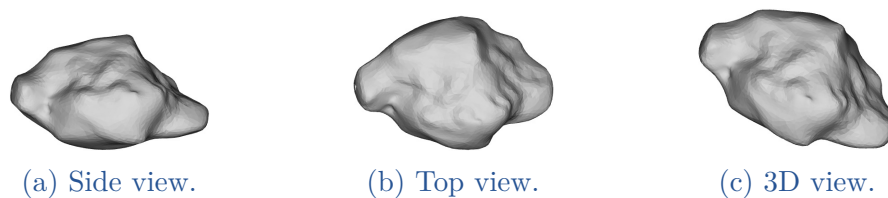


Figure 3.37 – Illustration of the tumour-like structure used.

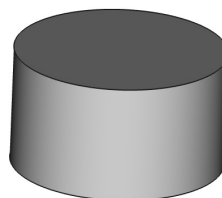


Figure 3.38 – Illustration of the cylindrical structure used.

The resulting tissue phantom with the tumour-like structures is illustrated in Figure 3.39. Alternatively, orange or apple seeds could have been used as tumour-like structures.

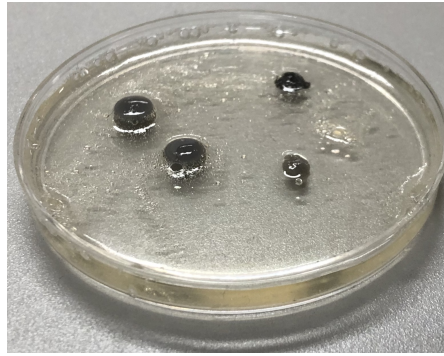


Figure 3.39 – Gelatine tissue phantom with tumour-like structures.

#### 3.4.1.b Experimental design and data acquisition

To prepare the OCT device for data acquisition, the OCT probe was carefully aligned perpendicular to the platform where the tissue phantom would be placed, ensuring its proper stabilisation to minimise motion artefacts and cover the desired field of view. Before commencing OCT data acquisition, the raster and adaptive scanning software was developed using C++. These two types of scanning protocols were implemented as follows:

- A conventional raster scan trajectory was designed offline to cover the desired fixed square field of view of  $6\text{mm} \times 6\text{mm}$  and  $100 \times 100$  A-scan locations.
- The adaptive scanning protocol from the flow chart in Figure 3.22 was implemented to selectively scan the margins of the tumour-like structure within the gelatine phantom.

OCT data was then acquired using the conventional raster scan trajectory as well as the adaptive scan trajectory.

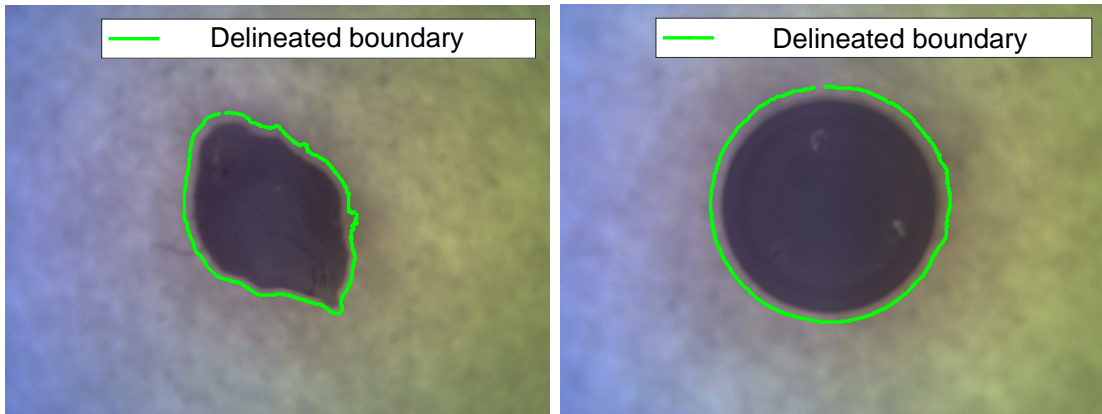
### 3.4.2 Experimental adaptive scanning

To carry out the experimental validation of adaptive scanning, two different samples were used: a gelatine tissue phantom with a tumour-like structure as well as a cylindrical structure. These samples were selected to represent different scenarios for testing the adaptive scanning protocol. The tissue phantom with the tumour-like structure allows to simulate real-world conditions and evaluate how well the protocol could delineate the boundaries of an irregularly shaped tumour. On the other hand, the cylindrical structure provides a controlled and well-defined object to test the accuracy and precision of the adaptive scanning in a simpler environment. By using these two diverse samples, we are able to comprehensively assess the performance and applicability of the adaptive scanning protocol in various practical scenarios.



### Initial boundary delineation

To implement the adaptive scanning protocol, an emulation of the surgeon drawing an outline of the suspicious region on the tissue was first done (first step of the adaptive scanning protocol in the flowchart as shown in Figure 3.22). In Figure 3.40, the surgeon-like delineated boundary on the tumour-like and cylindrical structure is given by the green outline, showing how the adaptive scanning process could be initiated based on a surgeon's input. This process allows the surgeon to target specific areas of interest within the tissue and efficiently guide the OCT data acquisition process for further analysis and diagnosis.



(a) Tumour-like structure.

(b) Cylindrical tumour structure.

Figure 3.40 – Photo of the samples with an initial boundary drawn on it.

To achieve the emulation of the surgeon drawing an outline of a tumour boundary, a photo of the tissue phantom was taken. The OpenCV library in C++ was then used for contour detection, providing an outline of the boundary. Since the contour detection process provides pixel locations of the tumour boundary, the pixel locations were converted from the pixel coordinate frame to the Cartesian frame. This allowed an initialisation for the adaptive scan protocol to focus on a particular region of interest.

### Planned scan trajectory generation

With the surgeon's boundary delineation, a sinusoidal scan trajectory is generated to follow the tumour border, as depicted in Figure 3.41. The amplitude and frequency of the sinusoidal trajectory plays a crucial role in determining the resolution of the OCT data obtained (It should be noted that suitable values for the amplitude and frequency are selected in accordance with the inherent resolution constraint limit of the OCT device). By adjusting these parameters, the scanning process can be optimised to capture the required level of detail enhancing accurate analysis and diagnosis. A higher amplitude and frequency value increases the region window through which the tumour boundary should be detected as well as the amount of data to be collected (selection of these values is subjective).

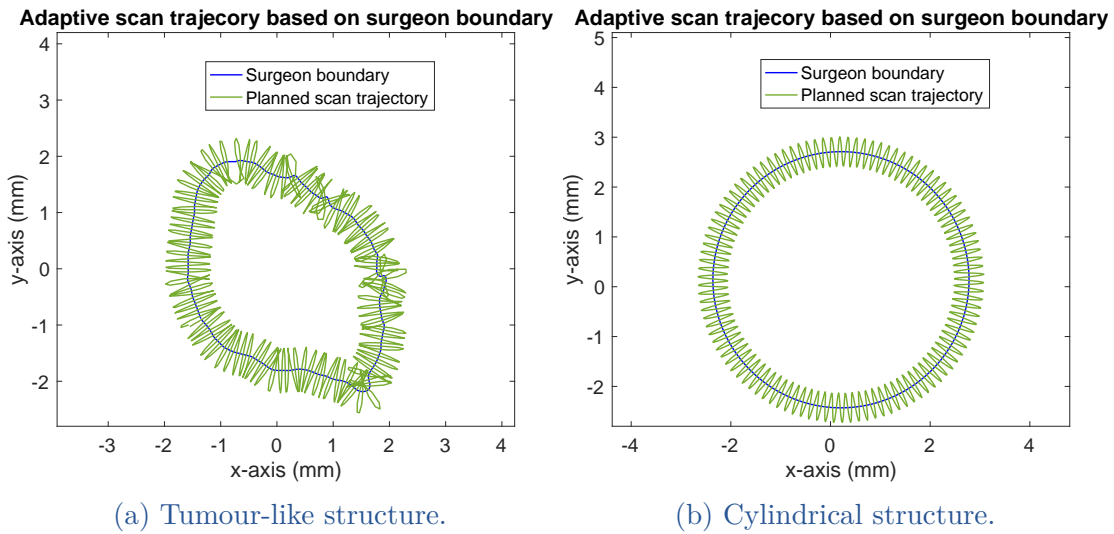


Figure 3.41 – Plot of the surgeon’s boundary and the corresponding planned scan trajectory.

### Adaptive scanning

Using the planned scan trajectory, OCT data is collected at a few initial scan positions. This initial data is analysed, and once tumour edges are detected, the trajectory is adapted according to the proposed algorithm in Figure 3.22. If no tumour edges are detected, OCT data is continuously acquired on the planned scan trajectory. From experimental OCT data, only a few tumour edges are detected, unlike in simulation; therefore, the scan trajectory is not completely modified. Nonetheless, the tumour edge positions are flagged, and the detected tumour boundary is traced, as illustrated in Figure 3.42 by the magenta curve.

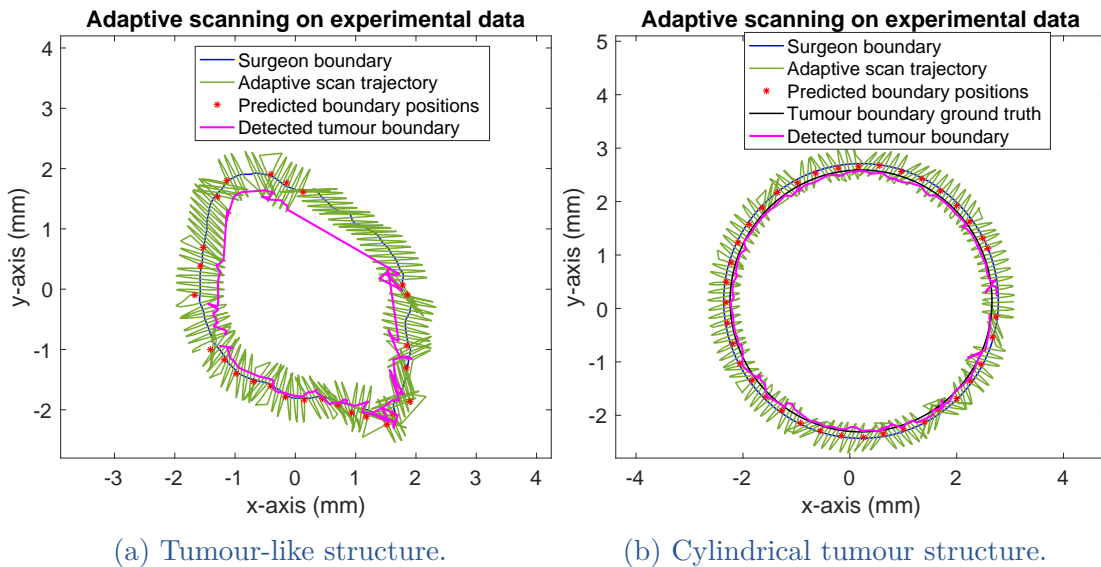


Figure 3.42 – Adaptive scanning on experimental OCT data.

Adaptive scanning once again

To delineate the tumour boundary more accurately, it is proposed to collect OCT data once more. The detected tumour boundary from the first adaptive scanning process is smoothed (using a moving average filter), and a new sinusoidal scan trajectory is developed for OCT data acquisition, as shown in Figure 3.43

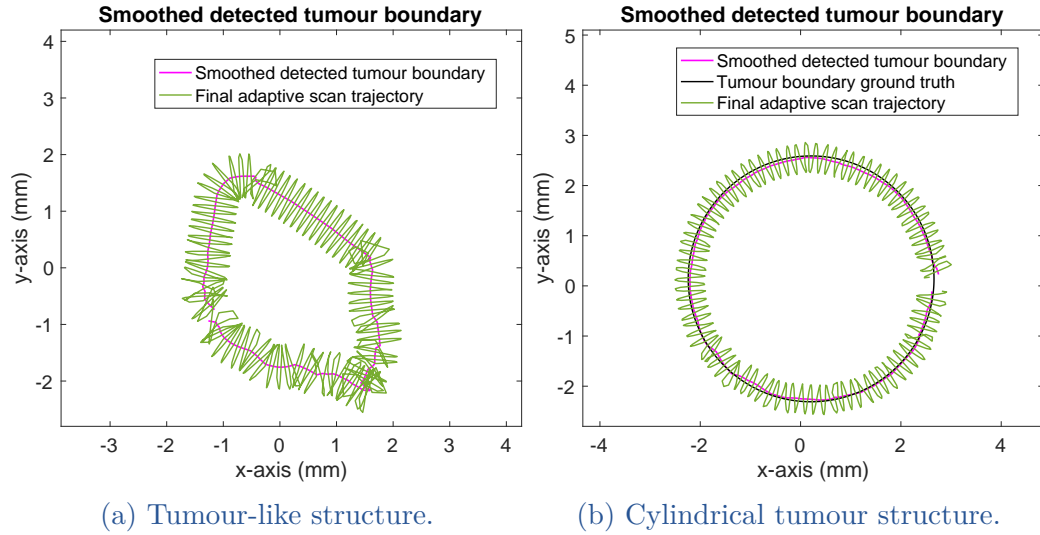


Figure 3.43 – Detected tumour boundary after first loop of adaptive scanning.

3.4.2.a Adaptive scanning and conventional raster scanning analysis

Utilising OCT data obtained from the scan trajectory based on the smoothed detected tumour boundary, the point cloud is processed and is shown in Figure 3.44. The boundaries of the tumour-like structure and the cylindrical tumour structure can be discerned in Figures 3.44a and 3.44b.

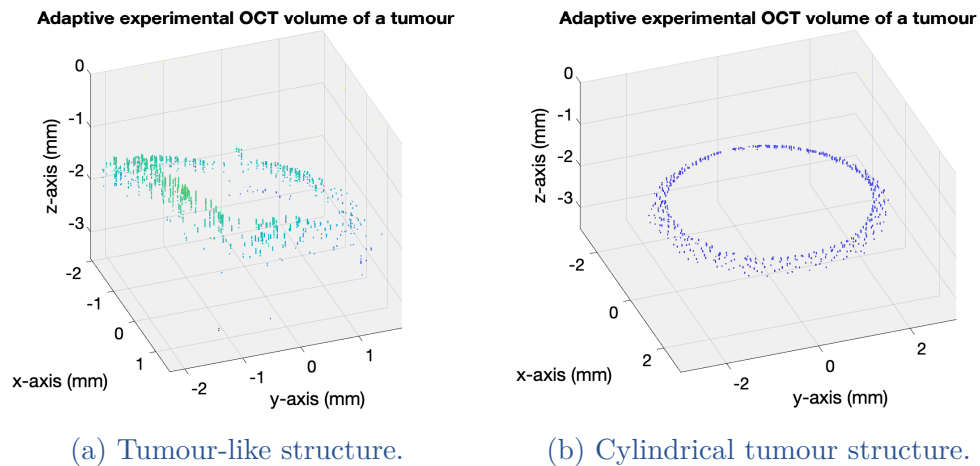


Figure 3.44 – Experimental point cloud volume of the tumour boundary.



OCT volumetric data was also acquired using the conventional raster scan trajectory ( $100 \times 100$  A-scan locations) as shown in Figure 3.45. On performing a qualitative (subjective) comparison analysis to Figure 3.44, we see that the adaptive scan trajectory successfully captures information on the boundary of the tumour. This boundary information can then serve as prior knowledge for conducting a deeper and more detailed scan.

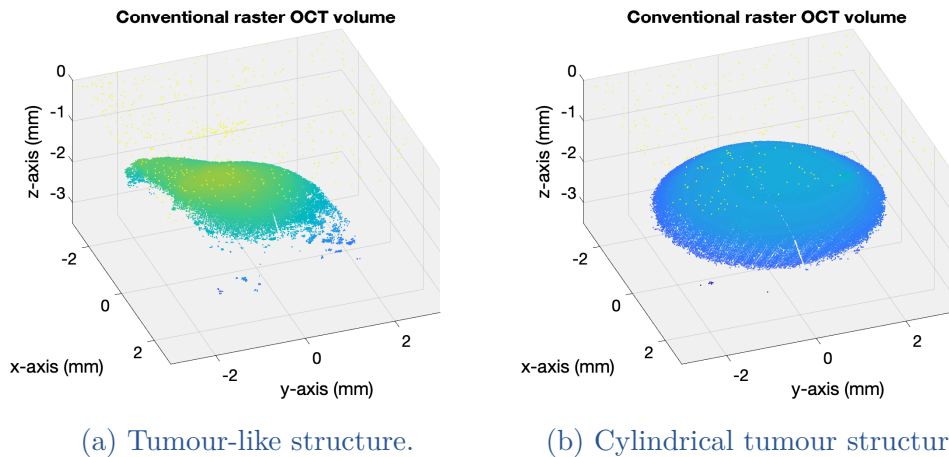


Figure 3.45 – Experimental full point cloud OCT volumes.

Additionally, the OCT data collected is analysed to determine which A-scans were obtained in the healthy or tumour regions using k-means clustering, as illustrated in Figure 3.46. The purpose of this, is to check whether the tumour A-scan positions are within the detected tumour boundary. It is observed that the A-scans in the tumour region are all within the detected tumour boundary except for a few A-scan positions for the tumour-like structure.

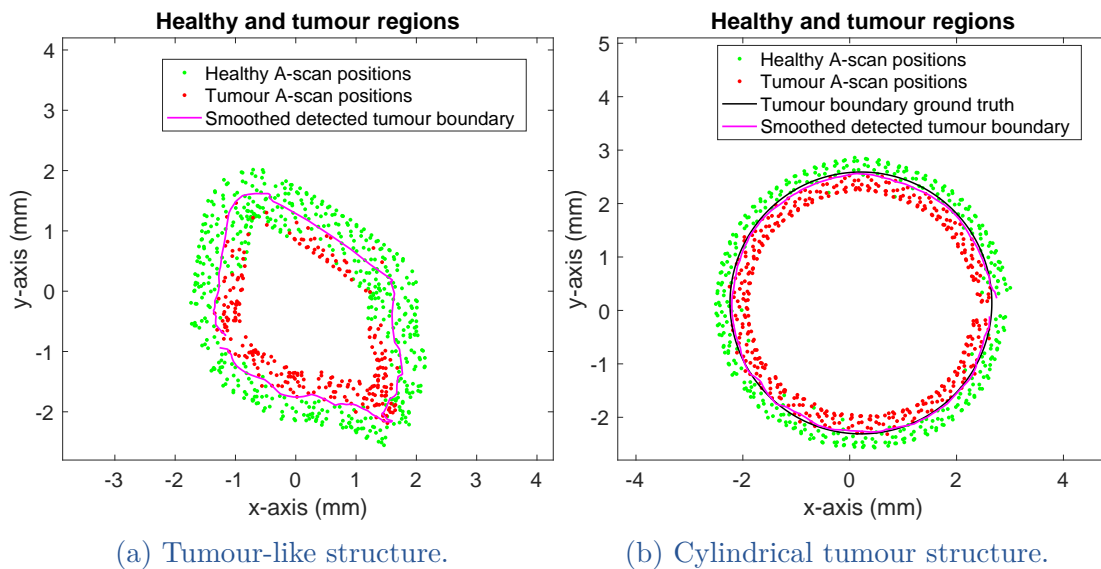


Figure 3.46 – Healthy and tumour regions delineated using k-means clustering.

Similarly, the healthy and tumour regions were determined for the OCT data collected using the conventional raster scan trajectory using the k-means clustering as shown in Figure 3.47. We also observe that the detected tumour boundary from adaptive scanning fits well in distinguishing the healthy and the tumour regions.

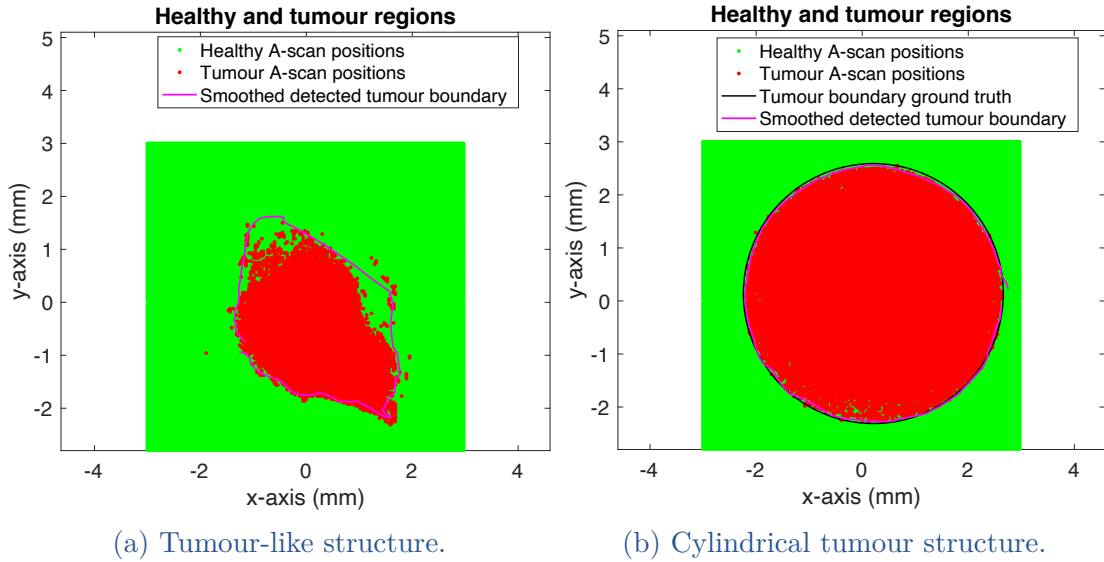


Figure 3.47 – Healthy and tumour regions delineated using k-means clustering.

Thereafter, the ratio between the number of A-scans acquired during adaptive scanning to the conventional raster trajectory (illustrated in Figure 3.44 and 3.45) was computed. For the tumour-like structure, the ratio was 0.094, and for the cylindrical tumour structure, the ratio was 0.08. These ratios indicate a significant reduction in the amount of data acquired, demonstrating the efficiency of adaptive scanning in providing useful information with only a fraction of the data.

Before delving into the time analysis, it is essential to remark that, for the conventional raster trajectory, the scan trajectory is pre-designed before data acquisition, whereas for adaptive scanning, the trajectory is continuously modified during OCT data acquisition. This continuous modification could potentially incur computational time costs. Additionally, the experimental setup that was used has some hardware and software limitations. The API (application programming interface) provided by Thorlabs allows scan trajectory design offline, enabling OCT data acquisition from the supplied positions. It also has a pre-processing step just before data acquisition, which includes apodisation, memory allocation, etc. Nevertheless, the pre-processing section of the software, which is not accessible to the user, limits the direct implementation of the adaptive scanning process. As an alternative implementation strategy, the data acquisition process is modified to a position-by-position acquisition. In this approach, the next scan position to acquire data is sent to the galvanometer, the galvanometer moves to this position, the data is acquired, saved, and the subsequent position sent. This iterative process continues until all the required data is acquired. This approach is inefficient since processes that could have been parallelised have not been, for example, data

acquisition and saving of data. This makes this approach slower. Nonetheless, with the modified approach for both adaptive scanning and using the conventional raster, the ratio (time to acquire data during adaptive scanning to the time to acquire data using the conventional raster) for the tumour-like structure is 0.19, and for the cylindrical like structure is 0.17. This is still a considerable reduction in the time taken, taking into account that for adaptive scanning, the computation time is considered. Therefore, the adaptive scanning protocol results in higher information density compared to the conventional raster scan. A higher information density indicates that fewer but more relevant data are acquired [Dahmouche 12]. It is important to distinguish information density from data density. Data can be dense (more data is collected) but poorly informative. On the other hand, data can be less dense (fewer data collected) but highly informative, resulting in higher information density. The information density can thus be computed using the formula:

$$\text{information density} = \frac{\text{useful acquired Ascans}}{\text{total acquired Ascans}} \quad (3.12)$$

### 3.4.3 Discussion of the simulation and experimental results of adaptive scanning

From the simulation and experimental study presented, it is observed that adaptive scanning is a promising and interesting approach for acquiring OCT data. It can be particularly useful during the initial preview of the tissue by the surgeon, providing enough data to determine the extent of the tumour. In some scenarios, the tumour boundary may be large enough for the surgeon to reliably conclude that resection is needed after the initial adaptive scan. However, in cases where the tumour is not clearly defined, more information on the tissue micro-structure is required. In such situations, the surgeon can switch to a deeper scanning mode, utilising prior knowledge of the already defined boundary to perform a higher resolution scan only in informative regions. This second phase may involve a higher resolution scan using techniques such as rosette (as seen in chapter 2 of this thesis) or optimised scanning, focusing only on exploiting the region within the tumour boundaries. This second mode will take more time, but will provide crucial additional information. This approach draws an analogy to the Pareto distribution [Pareto 97], where we use 20% of the time to obtain 80% of the relevant information for an initial diagnosis. Then, we invest the remaining 80% of the time to gather the remaining 20% of information. In applications such as OCT-controlled robot-assisted tumour resection, having precise knowledge of the tumour border is a crucial initial step that can significantly impact the success of the surgical procedure. Adaptive scanning offers a valuable tool to achieve this goal efficiently and effectively.

While a gelatine tissue phantom was utilised in this study instead of actual gut tissues, alternative phantom materials with optical properties more closely resembling those of the gut could be considered. Options include fibrin, silicon,

or polyvinyl alcohol cryogels (PVA-C) [Lamouche 12]. Fibrin is particularly advantageous when optical scattering characteristics need to incorporate tissue constituents. Nevertheless, for real-world applications involving actual human tissues, the adaptive scanning protocol developed in this research is a feasible approach to consider.

## 3.5 CONCLUSION

Adaptive scanning significantly reduces overall data acquisition time by efficiently utilising available scan time, focusing only on informative regions, and excluding tissue-irrelevant areas (reducing exploration and exploitation to only the core details). Due to this approach, the area to be scanned is reduced and dead times eliminated allowing for an increase in both axial and lateral resolution. Consequently, the number of A-scans and voxels per A-scan can be increased within the same time frame as a conventional raster scan, leading to higher-quality OCT data with a given system. An essential advantage is that, this improved data quality is achieved through software modifications without requiring any changes to the OCT hardware. The novelty in the adaptive scanning approach, lies in its effectiveness in potentially enabling the surgeon to gather essential data on the tumour boundaries. This allows for a more targeted, and efficient exploitation of the tumour interior. By combining the initial adaptive scan with subsequent deeper scans, the surgeon can obtain a comprehensive understanding of the tumour structure and characteristics, facilitating improved diagnosis and surgical planning. Implementation of the adaptive scanning approach holds the potential to efficiently collect data and enhance capabilities in early cancer detection and robot-assisted surgical guidance. To further refine the adaptive scanning approach, more complex strategies, such as machine learning, could be employed to discriminate between tumour and healthy regions in tissue during OCT scanning. This improvement would enhance the delineation of tumour boundaries, especially when tumour and healthy regions heavily interconnect in tissue. Moreover, the adaptive scanning approach could be extended to determine boundaries not only in the  $x - y$  plane but also in the  $x - z$  plane. This would involve delineating tumour boundaries at different depths by detecting tumour and healthy transitions in an A-scan.



---

---

# Chapter 4

## Exploitation of motion artefacts in optical coherence tomography

---

<b>4.1</b>	<b>Motion artefacts</b> . . . . .	102
4.1.1	Motion artefacts/rolling shutter in cameras . . . . .	104
4.1.2	Motion artefacts in optical coherence tomography. . . . .	105
4.1.3	Contributions of this chapter . . . . .	106
<b>4.2</b>	<b>State of the art in motion artefacts compensation of optical coherence tomography data</b> . . . . .	107
4.2.1	Intra-processing methods . . . . .	107
4.2.2	Post-processing methods. . . . .	110
<b>4.3</b>	<b>Modelling of motion artefacts in optical coherence tomography</b> . . . . .	111
4.3.1	Mathematical formalisation of motion artefacts in OCT. . . . .	112
4.3.2	Simulation of OCT volumes with motion artefacts . . . . .	114
4.3.3	Experimental validation . . . . .	117
<b>4.4</b>	<b>Proposed method for estimating 3D motion from an OCT volume with motion artefacts</b> . . . . .	120
4.4.1	Numerical (simulation) validation . . . . .	123
4.4.2	Experimental validation . . . . .	130
<b>4.5</b>	<b>3D Shape and motion estimation from a single unknown OCT volume obtained using a non-raster scan trajectory</b> . . . . .	134
4.5.1	Motion artefacts in optical coherence tomography during raster and non-raster scanning. . . . .	134
4.5.2	The rosette scan trajectory and its peculiarities . . . . .	138
4.5.3	Proposed shape and motion estimation method from a single OCT volume . . . . .	139
4.5.4	Numerical (simulation) validation . . . . .	143
4.5.5	Experimental validation . . . . .	148
<b>4.6</b>	<b>Motion artefacts during adaptive scanning in OCT</b> . . . . .	152
<b>4.7</b>	<b>Conclusion</b> . . . . .	152

## 4.1 MOTION ARTEFACTS

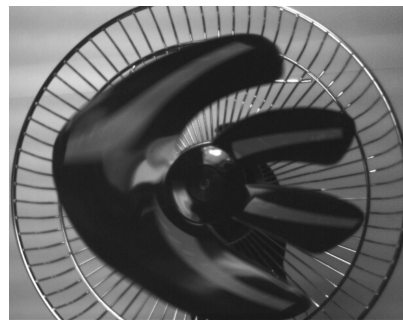
Motion artefacts refer to distortions or inconsistencies that arise in images due to either movement of the imaged object or movement of the imaging device itself [Ait-Aider 06]. These artefacts can significantly degrade image quality and impede accurate interpretation [Liang 08]. The extent of motion artefacts varies across different imaging modalities, owing to the diverse technologies employed for image acquisition as well as the specific circumstances under which the images are captured. In everyday scenarios, utilising cameras without image stabilisation capabilities can lead to blurry images when capturing fast-moving objects or taking photos while in motion as shown in Figure 4.1 and 4.2.



Figure 4.1 – A photo from an iPhone 3GS camera acquired during fast motion [Forssén 10]. The pole holding the signs is slanted instead of being straight.



(a) Distortion of the image due to non-uniform camera motion [Magerand 14].

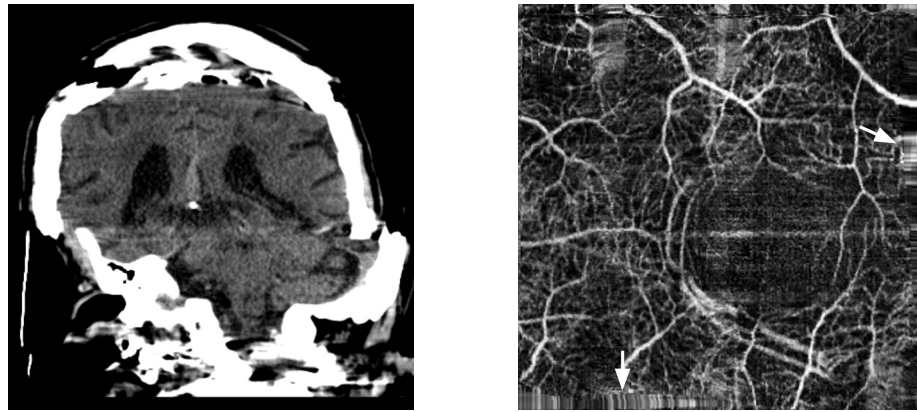


(b) Distortion of the image due to the rotating fan motion [Tanner 01].

Figure 4.2 – Motion artefacts due to relative motion during image acquisition.

In the realm of medical imaging, motion artefacts can arise from both voluntary and involuntary patient movements during the image acquisition process. Involuntary movements, like respiration, and voluntary actions due to patient discomfort (such as being instructed to remain perfectly still or hold one's breath, as seen in magnetic resonance imaging), can manifest as blurring, streaking, or shading within the captured images [Forssén 10]. Examples of medical images affected by motion artefacts are shown in Figure 4.3a and 4.3b.





(a) Computed tomography (CT) brain scan image with severe motion artefacts [Murphy 23]. (b) Stretch artefacts highlighted by two white arrows observed in an OCT angiography image [Spaide 15].

Figure 4.3 – Motion artefacts from medical images.

Ignoring patient movement (and consequently tissue motion) during image acquisition and later on processing, degrades the image quality which can result in inaccurate diagnoses by medical professionals [Walther 08]. In the context of 2D and particularly 3D data acquisition using OCT, motion becomes a critical issue as depicted in Figure 4.4.

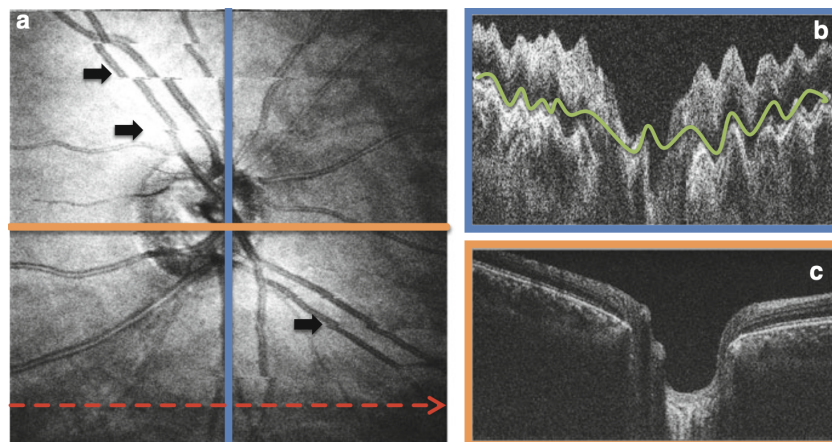


Figure 4.4 – Example of motion artefacts in a raster-scanned 3D OCT volume. The volume consists of 400 by 400 A-Scans sampled over 6mm by 6mm centred on the optic nerve head. (a) *En face* fundus projection of the volume. The dotted red line marks the fast scan direction of the volume. The black arrows indicate motion artefacts caused by transverse eye motion that create discontinuities in the vessel pattern. (b) Central slice of the volume along the slow scan direction (blue line in a). Axial motion leads to a wavy deformation of the retina in axial direction (green curve). (c) Central slice of the volume along the fast scan direction (orange line in a). The spatial structure of the retina remains intact along the fast scan direction [Kraus Martin 15].

To further explore the issue of motion artefacts, we will briefly delve into their occurrence in cameras and the concept of ‘rolling shutter’. This will first provide a foundational understanding of their causes and effects. Subsequently, we will transition into the examination of motion artefacts in OCT, offering a deeper insight into the unique challenges and solutions within this context.

### 4.1.1 Motion artefacts/rolling shutter in cameras

Cameras and camcorders are equipped with either complementary-metal-oxide-semiconductor (CMOS) sensors or charge coupled device (CCD) sensors [Liang 08, Forssén 10]. Presently, CMOS sensors are more commonly used in imaging devices worldwide. CMOS sensors offer cost advantages, on-chip processing capabilities, and various acquisition modes compared to CCD sensors [Magerand 10]. Most CMOS sensors operate in a mode known as rolling shutter (RS), hence the term ‘rolling shutter camera’. Rolling shutter cameras excel at capturing fast frame rates while consuming less power and generating minimal heat [Kavanaughy 23]. In a rolling shutter camera, detector rows are sequentially read and reset, as depicted in Figure 4.5b. Each row is exposed during a slightly different time window, with the top line of the frame captured at a slightly different time than the bottom line [Cho 07]. On the other hand, cameras equipped with CCD sensors operate in a global shutter mode [Ait-Aider 07]. In this mode, all pixels collect light during the same time interval and are reset simultaneously, as shown in Figure 4.5a. Moreover, CCD-based cameras are more expensive and challenging to manufacture [Kavanaughy 23].

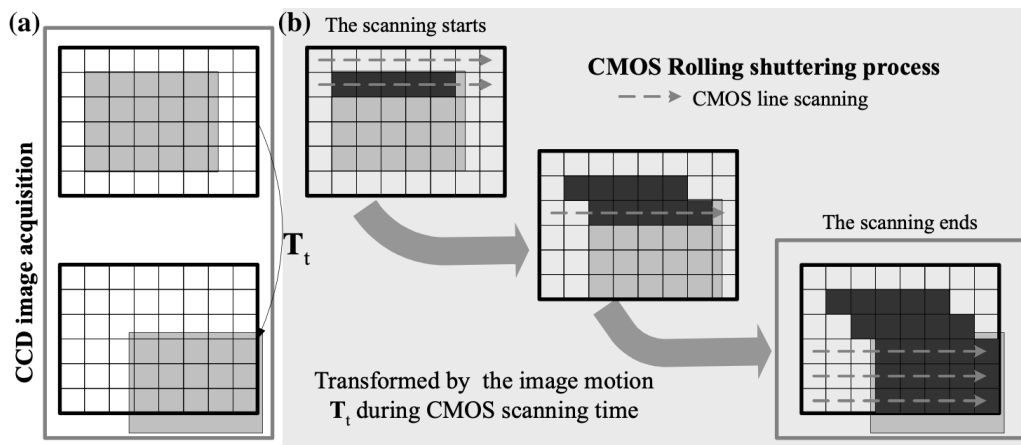


Figure 4.5 – Image acquisition process in (a), CCD and (b), CMOS sensor [Cho 07].

One major drawback of rolling shutter cameras is the introduction of geometric distortions in acquired images when either the camera or the target is in motion. These distortions occur because pixels are acquired at different points in time. The slight time lag during acquisition leads to undesirable distortions, especially when imaging fast-moving objects [Lao 20]. Figure 4.6 illustrates examples of

geometric distortions caused by this phenomenon. The target in the image may appear slanted, shrunk, or elongated. When there is relative motion between the camera and the target in the Cartesian plane  $z$  –  $axis$  direction, depth perception information is lost. In the case of motion along the  $x$  –  $axis$ , the image appears slanted, as depicted in Figure 4.6 a and b. Similarly, when the relative motion is along the  $y$  –  $axis$ , the target in the image appears stretched or shrunk, as shown in Figure 4.6 c and d.

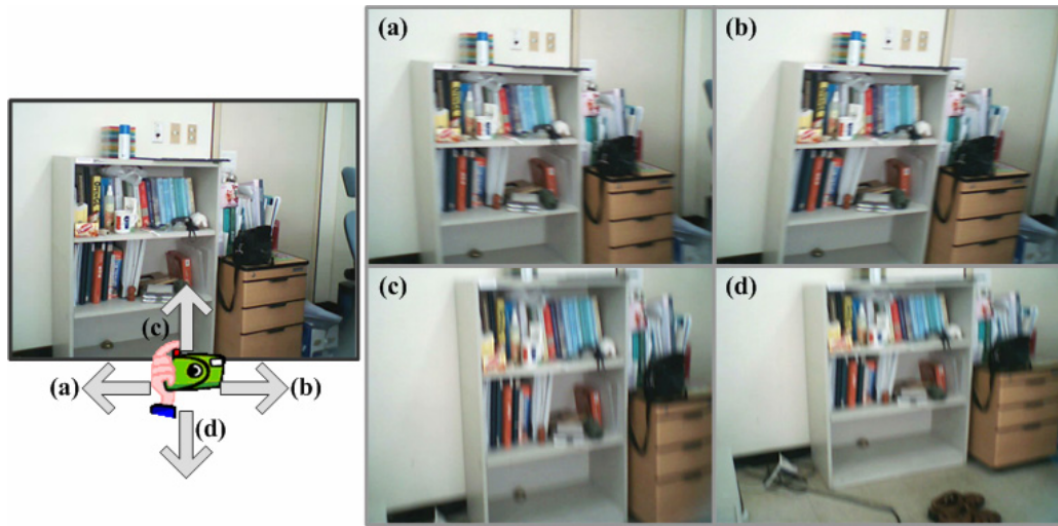


Figure 4.6 – Rolling shutter effect in cameras [Cho 07].

#### 4.1.2 Motion artefacts in optical coherence tomography

Throughout OCT data acquisition, scanning is performed within a scan coordinate system that encompasses the  $x$  and  $y$  positions of the scanning mechanism and the axial depth along the light beam ( $z$ ) [Rao 15]. An OCT image or volume does not represent a single moment in time, but rather it is a concatenation of one-dimensional data captured over a period of time. The OCT device sequentially records the intensity and delay of reflections along the path of the light beam through an object [Izatt 08]. Motion artefacts are inherent to OCT imaging due to the principle of data acquisition, in addition to the object motion that can occur in various imaging scenarios. When scanning a stationary object relative to the OCT device, each set of scanning mechanism positions correspond to a specific path of light through the object. Alongside the axial coordinate system, there exists a fixed relationship between the scan coordinate system and the object positions. However, when object motion (linear,  $V$  and angular,  $\Omega$  velocity) occurs during data acquisition, the relative position between the OCT device and the object can change over time. This introduces another coordinate system known as the object coordinate system that has a time-dependent relationship with the scan coordinate system. Any relative motion between the OCT device, and the object being imaged, alters this relationship and introduces distortions in the data

acquired [Kraus Martin 15]. This is illustrated in Figure 4.7b when the object is in motion in the  $x$  – axis while OCT data is being acquired using the raster scan trajectory.

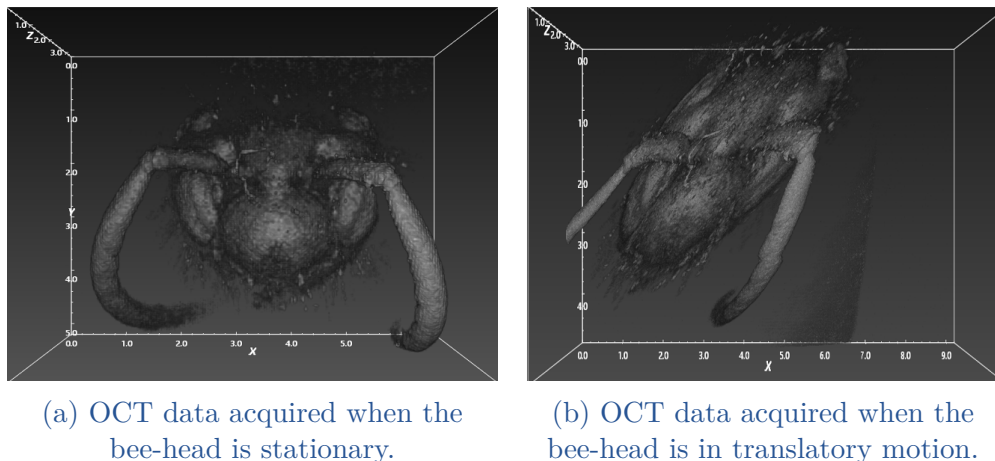


Figure 4.7 – Motion artefacts of a bee-head due to motion in the  $x$  – axis during OCT volume data acquisition.

Therefore, it is essential to develop techniques that measure or correct for object motion in OCT data [Kraus Martin 15]. Motion estimation from OCT data can be used in applications such as visual servoing, tracking etc. Furthermore, motion correction techniques aim to ensure that the individual A-scans in corrected OCT data accurately represent their expected locations, irrespective of any motion that may have occurred during the acquisition process.

### 4.1.3 Contributions of this chapter

In this chapter, the first contribution is the proposal of a novel numerical method that leverages OCT motion artefacts to estimate the motion (linear and angular velocity) that caused the artefacts, drawing inspiration from robotics and computer vision concepts. The method employs a kinematic model to simulate motion artefacts in an OCT point cloud volume, which is subsequently used to estimate the corresponding instantaneous linear and angular velocities responsible for the motion artefacts. These estimated velocities are then utilised to compensate for the artefacts, resulting in a motion-free corrected volume. Importantly, the proposed method is efficient, robust, and does not necessitate any additional hardware or instrumentation. The proposed motion estimation method extends its applicability beyond 2D images with discontinuities to 3D volumes, addressing distortions in 3D OCT volumes. Correcting for motion artefacts in 3D OCT volumes is particularly challenging due to their high dimensionality and the likelihood of distortions occurring within the volume. The proposed approach tackles distortions in 3D OCT volumes by estimating the motion of the sample in all six dimensions of the Cartesian space  $SE(3)$ , and utilising this estimate to compensate

for motion artefacts in the volume. This represents a significant advancement over existing methods, which are typically limited to 2D OCT images and predominantly applied in ophthalmology applications. Furthermore, this chapter presents a second contribution: a novel approach for shape and motion estimation based on a single OCT volume obtained using the rosette non-raster trajectory. This is an approach that marks a paradigm shift from conventional OCT volume motion artefacts compensation which typically relies on two sequential OCT volumes. By eliminating the need for two consecutive volumes, this approach reduces the amount of data required and, consequently, the computation costs needed. These developments open up new avenues for research in motion artefact compensation in OCT imaging and provides a valuable tool for clinical diagnosis and monitoring. Additionally, for the last contribution, experimental datasets of OCT volumes containing motion artefacts were collected, annotated, and archived, making them available for research purposes within the community.

## 4.2 STATE OF THE ART IN MOTION ARTEFACTS COMPENSATION OF OPTICAL COHERENCE TOMOGRAPHY DATA

There are two main ways to correct for motion artefacts in OCT data; intra-processing methods and post-processing methods. Intra-processing methods attempt to mitigate the occurrence of motion artefacts during the data acquisition process through the implementation of specialised/improved system hardware designs. And post-processing methods aim to correct for OCT motion artefacts during the image processing stage i.e., after acquisition of data. These different methods offer valuable solutions for mitigating motion artefacts in OCT data, allowing for improved image quality and more accurate interpretation of the underlying structures. The choice of the specific method depends on the nature of the motion artefacts and the available imaging resources. These two approaches are detailed further.

### 4.2.1 Intra-processing methods

Intra-processing methods focus on improving the hardware components to minimise motion-related issues. One approach involves incorporating advanced optics into the system to enable rapid scanning, thereby reducing the acquisition time. By enhancing the spatial dimension encoding in time, this technique effectively decreases the likelihood of motion-induced artefacts. The improved system design ensures that data is acquired more swiftly, allowing for better temporal synchronisation and minimising the impact of motion. Another intra-processing method involves real-time tracking of OCT measurement deviations caused by changes in the relative position of the imaging system and the object being examined. By



actively monitoring these deviations, corrections can be applied to the positions of the galvanometer mirrors during the data acquisition process. This dynamic adjustment compensates for any motion-related inconsistencies, resulting in more accurate and reliable OCT measurements [Rao 15, Yaqoob 05].

#### 4.2.1.a Faster scanning in OCT

One primary strategy to minimise motion artefacts in OCT imaging is to enhance the imaging speed of the OCT system [Kraus Martin 15]. By increasing the speed, a larger number of A-scans can be acquired within a shorter period, enabling rapid sampling of a specific scan pattern. As motion requires time to occur, acquiring data within sufficiently brief acquisition times effectively ‘freezes out’ motion in specific regions or throughout the entire OCT acquisition process. This approach helps to minimise spatial distortions caused by motion and preserves the integrity of the captured images. However, it is important to consider that high-speed data acquisition may result in a loss of sensitivity [Klein 12]. If there is a limit to the number of photons that can be collected per unit of time, doubling the data acquisition speed would lead to a halved number of photons collected per A-scan. Therefore, an increase in speed comes at the expense of sensitivity. Nevertheless, utilising high-speed OCT systems can not only reduce acquisition time and mitigate motion artefacts but also increase the total number of A-scans collected. This can be achieved through dense sampling or by covering a larger area. The choice between these options depends on the specific data requirements of the imaging application [Kraus Martin 15].

However, it is important to acknowledge that relying solely on speed improvements without significant enhancements in sensitivity is unlikely to provide a comprehensive solution to motion artefacts in OCT, particularly when dense sampling of a clinically significant area with high sensitivity and resolution is necessary [Bonin 10]. Thus, a balanced approach considering both speed and sensitivity improvements is necessary to effectively address motion artefacts in OCT imaging.

#### 4.2.1.b Tracking OCT

This method involves measuring the deviations that originate from changes in relative position, and actively applying corrections to the scanning mechanism positions and/or the reference arm mirror during data acquisition [Kraus Martin 15]. By compensating for these deviations, motion artefacts in OCT imaging as a result of object motion can be effectively mitigated. Several key factors play a vital role in tracking in OCT. Firstly, the accuracy of measuring the deviation and applying the correction is crucial. Precise and reliable measurements are essential to ensure accurate compensation for motion-induced deviations. Secondly, the update rate of the system is significant, as it determines how quickly the system can respond to changes in relative position caused by motion. A high update rate enables swift adjustments, allowing for effective real-time compensation [Kraus Martin 15].

While axial tracking in OCT has received some attention [Pircher 07], tracking is more commonly employed for correcting transverse motion. For example, Ferguson *et al.* [Ferguson 04] utilised a secondary sensing beam to perform rapid scanning in a circular region on the fundus, such as around the optic nerve head. This secondary channel facilitated the extraction of correction information in a closed-loop system operating at a frequency of  $1kHz$ . The acquired correction data was then used to precisely adjust the galvanometer mirrors. Notably, the reported accuracy of this technique was found to be less than one spot diameter, highlighting its effectiveness in motion correction.

Commercial OCT devices, such as the Heidelberg Engineering Spectralis, also employs transverse tracking techniques [Heidelberg 13]. In this approach, a scanning laser ophthalmoscope (SLO) is utilised to rapidly capture 2D images of the fundus. These acquired images are then registered with a reference SLO view. By measuring the shift between the registered images, the corresponding deviation in scan angle is determined. To compensate for this deviation, a correction signal is applied to the galvanometer mirrors. By implementing this tracking technique, the system becomes capable of acquiring multiple 2D B-scans at approximately the same location. These scans can then be averaged to reduce speckle noise and enhance the overall signal-to-noise ratio, leading to improved image quality and more accurate visualisation of structural details in the OCT scans [Kraus Martin 15].

An example of a tracking scanning laser ophthalmoscope (TSLO) system is as illustrated in Figure 4.8. The TSLO captures retina images at a rate of 30 frames per second. Leveraging the capabilities of the GPU and FPGA, it extracts motion data from the SLO frames, ensuring a tracking signal of exceptional quality while minimising latency. This tracking signal, which represents the inverse of eye movement, is carefully scaled to align with the voltage range of the OCT galvanometer scanner. The electronic summing junction (+) integrates the tracking signals with the OCT beam steering signals to compensate for the eye motion. Meanwhile, the tracking validity signal plays a crucial role in identifying B-scans requiring rescanning due to tracking disruptions caused by substantial eye movements or instances of blinking [Vienola 12].

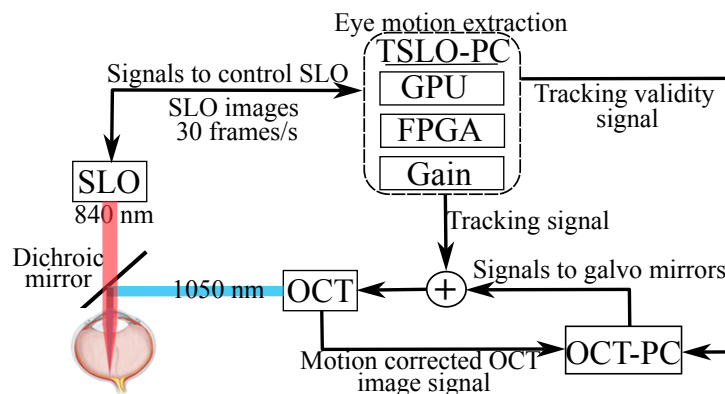


Figure 4.8 – Eye motion compensation for OCT imaging with tracking SLO [Vienola 12].



## 4.2.2 Post-processing methods

Post-processing methods aim to correct for motion artefacts during the OCT data image processing (post-processing) stage [Zawadzki 07, Pappuru 12]. These include; correcting OCT data using images from another modality that is not affected by motion artefacts like OCT and using correlation techniques on successively acquired OCT data to filter out motion effects [Liao 22].

### 4.2.2.a Use of an additional imaging modality

This particular method of motion correction utilises reference image data obtained from a different modality that is unaffected by motion artefacts like OCT [Kraus Martin 15]. By performing registration between the OCT data and data from the reference modality, corresponding locations can be identified between the two images. This enables the mapping of the OCT data into the reference image space. Given that the reference image exhibits minimal motion, accurate mapping between the two images allows for effective motion correction of the OCT data.

Two modalities commonly employed in retinal imaging; fundus camera photography and scanning laser ophthalmoscope (SLO), are not susceptible to motion artefacts encountered in OCT [Kraus Martin 15]. Fundus photography may exhibit blurring effects due to motion; however, short exposure times are typically utilised to mitigate this issue effectively. On the other hand, SLO is a scanning imaging modality similar to OCT. Nonetheless, SLO often operates at a higher scanning speed compared to OCT, allowing for more efficient suppression of motion artefacts. Capps *et al.* [Capps 11] employed an adaptive optics SLO (AO-SLO) that runs simultaneously with OCT acquisition to estimate and correct for lateral motion. Following imaging, the OCT data is registered to the AO-SLO data to calculate the displacement caused by motion per A-scan. Subsequently, the OCT data is resampled onto a regular grid. In another approach, Ricco *et al.* [Ricco 09] registered the OCT fundus view with an SLO reference image to correct for motion. The algorithm utilised vessel patterns visible in both modalities as features for registration. Drift and tremor were corrected in a two-step process: firstly, an elastic registration technique based on patch-wise constant affine transformations between the two images was employed. Secondly, the objective was to address discontinuities resulting from micro-saccades occurring along the fast scan direction. To achieve this, the OCT *en face* pixels are treated as a signal in the time domain. Dynamic time warping was then employed to determine the optimal alignment between the OCT *en face* signal and the reference image. This alignment process helped rectify any disruptions caused by micro-saccades, ensuring a more seamless and coherent representation of the data.

This technique leverages the complementary information provided by other imaging modalities, such as SLO and fundus photography, to address motion artefacts in OCT, enabling accurate registration and correction for motion-induced distortions.

#### 4.2.2.b Consecutive data correlation

Data correlation algorithms assume that the OCT data is densely sampled and inherently smooth, and that jumps between consecutively acquired A-scans and B-scans are induced by motion alone. In [Swanson 93], a method was proposed to correct the axial motion artefacts within an A-scan by computing the 1D cross-correlation between consecutive time domain OCT A-scans within a 2D intensity B-scan, denoted as  $I(x, z)$ . The authors calculated the axial shift, represented as  $\delta z$ , between consecutive A-scans that maximises the cross-correlation coefficient  $\rho(x, \delta z(x))$  for each A-scan:

$$\rho(x, \delta z(x)) = \sum_z I(x, z)I(x + 1, z + \delta z(x)) \quad (4.1)$$

To obtain an absolute motion profile, all the  $\delta z$  values between the A-scans were summed. This 1D motion profile was then filtered and applied to each A-scan of the distorted image to remove axial motion and correct for the motion artefacts. To correct for motion artefacts in 2D, a cross-correlation coefficient between two consecutive B-scans, denoted as  $I_1(x, z)$  and  $I_2(x, z)$ , can be calculated. This approach is suitable for cases involving 2D movement with a global shift  $(\delta x, \delta z)$  in position between the two B-scan images. The objective function was computed as follows:

$$\rho(\delta x, \delta z) = \sum_x \sum_z I_1(x, z)I_2(x + \delta x, z + \delta z) \quad (4.2)$$

To account for tilt motion in the axial direction, which can occur due to transverse eye motion, an objective function utilising the sum of squared differences (SSD) measure was used instead of cross-correlation. The objective function was expressed as follows:

$$\rho(\delta x, \delta z, m_z) = \sum_x \sum_z (I_1(x, z) - I_2(x + \delta x, z + \delta z, m_z x))^2 \quad (4.3)$$

By calculating the correlation coefficient  $\rho(\delta x, \delta z, m_z)$ , both 2D global motion and tilt can be corrected. The objective function can be minimised using numerical optimisation techniques [Nocedal 06].

## 4.3 MODELLING OF MOTION ARTEFACTS IN OPTICAL COHERENCE TOMOGRAPHY

In this section, a comprehensive mathematical model that accurately describes the occurrence and characteristics of motion artefacts in OCT imaging is proposed. Motion in the proposed model can occur through pure translations, pure rotations, or a combination of both. The proposed model is subsequently validated to ensure its effectiveness and reliability in capturing the underlying mechanisms of motion artefacts.

### 4.3.1 Mathematical formalisation of motion artefacts in OCT

Due to the sequential nature of OCT data acquisition, all the voxels of the object are not acquired simultaneously, as in the case of a global shutter camera. Instead, each voxel is acquired one after the other in a sequential manner. Therefore, when there is instantaneous motion during data acquisition, distortions are introduced in the resulting OCT volume just as distortions are introduced in a rolling shutter camera image. To develop a generic model of rolling shutter in OCT, one voxel is considered in the A-scan of an OCT volume of an object given by  $P_i(t_0)$  in the object frame  $\mathcal{F}_{B(t_0)}$ , as shown in Figure 4.9 ( $t_0$  is the initial time before any motion). At time  $t$ , the object would have undergone a displacement due to the instantaneous motion,  $\vec{V}$  and  $\vec{\Omega}$ . The motion and the time delay between the acquisition of voxels introduces a transformation ( ${}^{B(t_0)}T_{B(t)}$ ) that shifts the location of the object frame, and thus of each voxel, to a different location (taking into account motion during time  $t_0$  to  $t$ ), as illustrated in Figure 4.9.

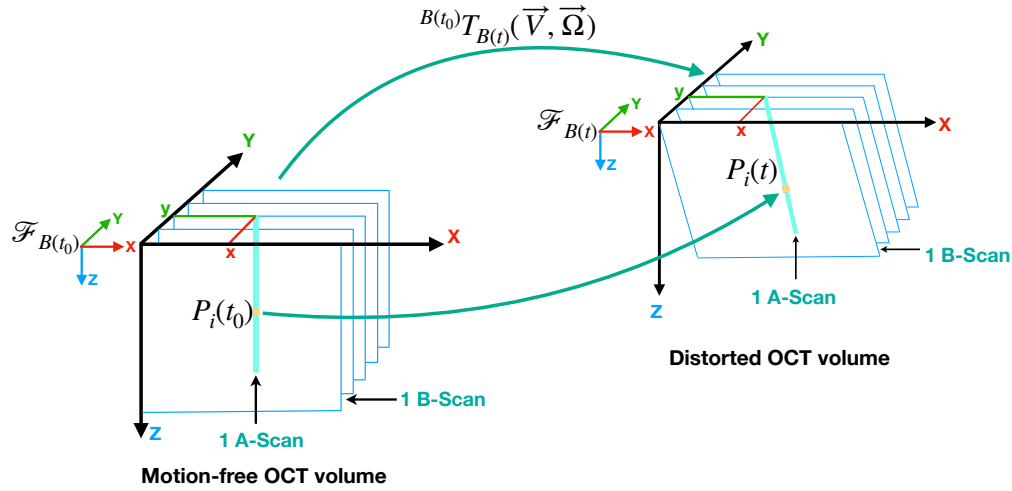


Figure 4.9 – Schematic of a distorted OCT volume due to motion during data acquisition.

The homogeneous coordinates of one voxel at time  $t_0$  in the object frame,  $\mathcal{F}_{B(t_0)}$  is:

$${}^{B(t_0)}\tilde{P}_i(t_0) = \begin{bmatrix} x_i \\ y_i \\ z_i \\ 1 \end{bmatrix} = \begin{bmatrix} {}^{B(t_0)}P_i(t_0) \\ 1 \end{bmatrix} \quad (4.4)$$

At time  $t$ , the voxel has undergone a transformation due to the instantaneous motion during time  $t - t_0$ :

$${}^{B(t)}\tilde{P}_i = {}^{B(t_0)}T_{B(t)}^{-1} * {}^{B(t_0)}\tilde{P}_i \quad (4.5)$$

It is necessary to estimate the motion model;  ${}^{B(t_0)}T_{B(t)}$ . Solving for all voxels,  $P_i \dots n$ , individually could get complex, we therefore make two assumptions;

- Rigid body motion (the volume is non-deforming) i.e.,  ${}^{B(t)}\tilde{P}_i(t) = {}^{B(t_0)}\tilde{P}_i(t_0)$
- Constant velocity of the object in its local frame i.e.,  ${}^{B(t)}\vec{V} = \vec{V}$ ,  ${}^{B(t)}\vec{\Omega} = \vec{\Omega}$

From now on  $P_i$  will be represented as  $P$  for clarity and readability. Due to the object motion, the total velocity of the single voxel is given by:

$${}^{B(t)}\dot{P}(t) = {}^{B(t)}\vec{V}_{B(t)} + {}^{B(t)}\vec{\Omega} \wedge {}^{B(t)}P(t) \quad (4.6)$$

where  $\vec{V}$  is the linear velocity and  $\vec{\Omega}$  is the angular velocity of the rigid object at time  $t$ , and  $\wedge$  is the cross product symbol. Re-writing equation 4.6 in homogeneous coordinates results in:

$${}^{B(t)}\dot{\tilde{P}}(t) = \begin{bmatrix} {}^{B(t)}\dot{P}(t) \\ 0 \end{bmatrix} = \begin{bmatrix} {}^{B(t)}\vec{V}_{B(t)} + {}^{B(t)}\vec{\Omega} \wedge {}^{B(t)}P(t) \\ 0 \end{bmatrix} \quad (4.7)$$

Re-arranging equation 4.7 using the skew-symmetric matrix  $[\vec{\Omega}]_{\wedge}$  yields,

$${}^{B(t)}\dot{\tilde{P}}(t) = \begin{bmatrix} [{}^{B(t)}\vec{\Omega}]_{\wedge} & {}^{B(t)}\vec{V}_{B(t)} \\ 0 & 0 \end{bmatrix} * {}^{B(t)}\tilde{P}(t) \quad (4.8)$$

Equation 4.8 is a 1<sup>st</sup> order ODE in  $\mathbb{R}^4$ . Leveraging on the concept of the exponential map (Lie theory) as detailed in [Solà 18, Deray 20], it solves, such that:

$${}^{B(t)}\tilde{P}(t) = \expm \left( \begin{bmatrix} [{}^{B(t)}\vec{\Omega}]_{\wedge} & {}^{B(t)}\vec{V}_{B(t)} \\ 0 & 0 \end{bmatrix} (t - t_o) \right) * {}^{B(t_0)}\tilde{P}(t_o) \quad (4.9)$$

Therefore, the motion model (transformation of the object at time  $t_0$  to object at time  $t$ ) i.e., during movement and OCT scanning is:

$${}^{B(t_0)}T_{B(t)} = \expm \left( \begin{bmatrix} [{}^{B(t)}\vec{\Omega}]_{\wedge} & {}^{B(t)}\vec{V}_{B(t)} \\ 0 & 0 \end{bmatrix} (t - t_o) \right) \quad (4.10)$$

So far, we haven't considered the observation of the object from the OCT frame (the OCT volumes are processed in the OCT frame) as shown in Figure 4.10. Taking the analogy of rolling shutter in OCT, the equation of motion of the voxel at time  $t$  in the OCT frame,  $\mathcal{F}_{oct}$  is thus given by:

$${}^{oct}\tilde{P}(t) = {}^{oct}T_{B(t)} * {}^{B(t)}\tilde{P}(t) \quad (4.11)$$

The transformation of the object from the object frame to the OCT frame is as given in equation 4.12:

$${}^{oct}\tilde{P}(t) = {}^{oct}T_{B(t_0)} * {}^{B(t_0)}T_{B(t)} * {}^{B(t)}\tilde{P}(t) \quad (4.12)$$

Knowing the instantaneous linear and angular velocities, simulated distorted OCT volumes can be obtained using equation 4.12.

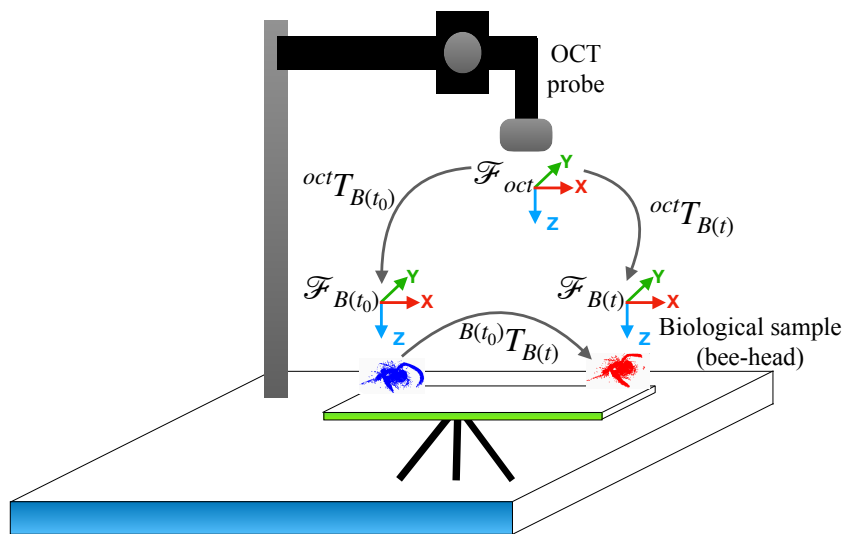


Figure 4.10 – Schematic of the OCT and object frames.

### 4.3.2 Simulation of OCT volumes with motion artefacts

To simulate the rolling shutter effect, a point cloud volume of a static object, specifically the head of a bee, was initially acquired using the OCT device, as shown in Figure 4.11.

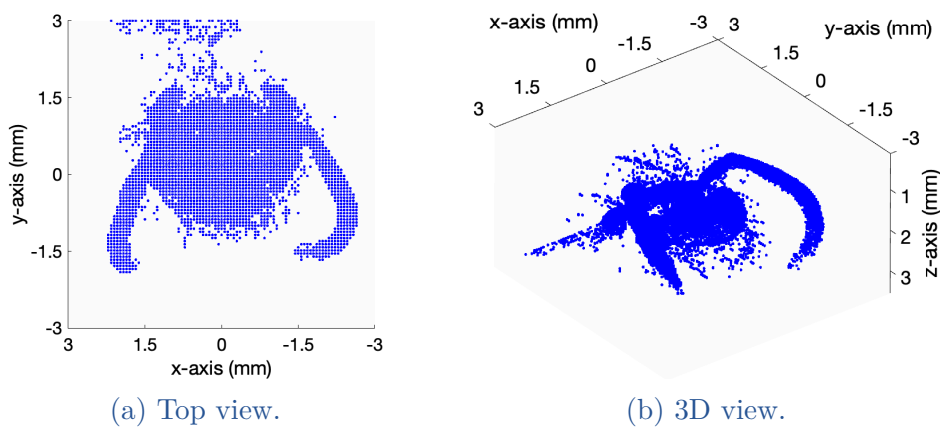


Figure 4.11 – OCT point cloud volume of a stationary bee-head.

Subsequently, motion artefacts were numerically introduced into the volume along the  $x$ ,  $y$ , and  $z$  axes, utilising the formulated model presented in Equation 4.12 (the transformation  ${}^{oct}T_{B(t_0)}$  was taken to be the identity matrix for simulation purposes). The resulting distorted point cloud volumes are given in Table 4.1 and 4.2. By introducing motion artefacts in a controlled manner, the simulation provides a means to study and analyse the impact of the rolling shutter effect on OCT imaging. The numerically distorted point cloud volumes allow for the evaluation and development of motion correction techniques, ultimately improving the accuracy and quality of OCT images in the presence of motion.

Table 4.1 – Motion artefacts due to translatory motions (blue points - motion-free volume, red points - motion-distorted volume).

Applied motion	Distorted volume (top view)	Distorted volume (3D view)	Motion-free and distorted volume (3D view)
$V_x = 2\text{mm/s}$ $V_y = 0\text{mm/s}$ $V_z = 0\text{mm/s}$ $\Omega_x = 0\text{rad/s}$ $\Omega_y = 0\text{rad/s}$ $\Omega_z = 0\text{rad/s}$			
$V_x = 0\text{mm/s}$ $V_y = 2\text{mm/s}$ $V_z = 0\text{mm/s}$ $\Omega_x = 0\text{rad/s}$ $\Omega_y = 0\text{rad/s}$ $\Omega_z = 0\text{rad/s}$			
$V_x = 0\text{mm/s}$ $V_y = 0\text{mm/s}$ $V_z = 2\text{mm/s}$ $\Omega_x = 0\text{rad/s}$ $\Omega_y = 0\text{rad/s}$ $\Omega_z = 0\text{rad/s}$			
$V_x = 2\text{mm/s}$ $V_y = 2\text{mm/s}$ $V_z = 2\text{mm/s}$ $\Omega_x = 0\text{rad/s}$ $\Omega_y = 0\text{rad/s}$ $\Omega_z = 0\text{rad/s}$			

Table 4.2 – Motion artefacts due to rotary and compound motions (blue points - motion-free volume, red points - motion-distorted volume).

Applied motion	Distorted volume (top view)	Distorted volume (3D view)	Motion-free and distorted volume (3D view)
$V_x = 0\text{mm/s}$ $V_y = 0\text{mm/s}$ $V_z = 0\text{mm/s}$ $\Omega_x = 0.01\text{rad/s}$ $\Omega_y = 0\text{rad/s}$ $\Omega_z = 0\text{rad/s}$			
$V_x = 0\text{mm/s}$ $V_y = 0\text{mm/s}$ $V_z = 0\text{mm/s}$ $\Omega_x = 0\text{rad/s}$ $\Omega_y = 0.01\text{rad/s}$ $\Omega_z = 0\text{rad/s}$			
$V_x = 0\text{mm/s}$ $V_y = 0\text{mm/s}$ $V_z = 0\text{mm/s}$ $\Omega_x = 0\text{rad/s}$ $\Omega_y = 0\text{rad/s}$ $\Omega_z = 0.01\text{rad/s}$			
$V_x = 0\text{mm/s}$ $V_y = 0\text{mm/s}$ $V_z = 0\text{mm/s}$ $\Omega_x = 0.01\text{rad/s}$ $\Omega_y = 0.01\text{rad/s}$ $\Omega_z = 0.01\text{rad/s}$			
$V_x = 1\text{mm/s}$ $V_y = 1\text{mm/s}$ $V_z = 1\text{mm/s}$ $\Omega_x = 0.01\text{rad/s}$ $\Omega_y = 0.01\text{rad/s}$ $\Omega_z = 0.01\text{rad/s}$			



Table 4.1 and 4.2 shows simulated volumes having distortions due to pure translations, pure rotations as well as compound motions in all the axes. The distorted point cloud appears slanted due to motion in the  $x$  – axis; appears stretched due to motion in the  $y$  – axis; and loses some depth information due to motion in the  $z$  – axis. From the figures in Table 4.1 and 4.2, it can be inferred that motion artefacts alter the appearance of acquired OCT volumes. It is also evident that significant distortion occurs, especially when there is compound motion (a combination of translatory and rotary motion in all axes) during data acquisition. To recover the lost information and generate accurate point clouds depicting the object being scanned, compensation for these motion artefacts is absolutely necessary.

### 4.3.3 Experimental validation

For the experimental validation, an OCT device was mounted in an eye-to-hand configuration onto a parallel robotic platform as seen in Figure 4.12. The biological sample was placed on the platform during the experiments. The parallel robotic platform was then used to introduce motion to the object during data acquisition. This setup allowed for realistic motion scenarios to be executed and accurate assessment of the effectiveness of a motion estimation method.

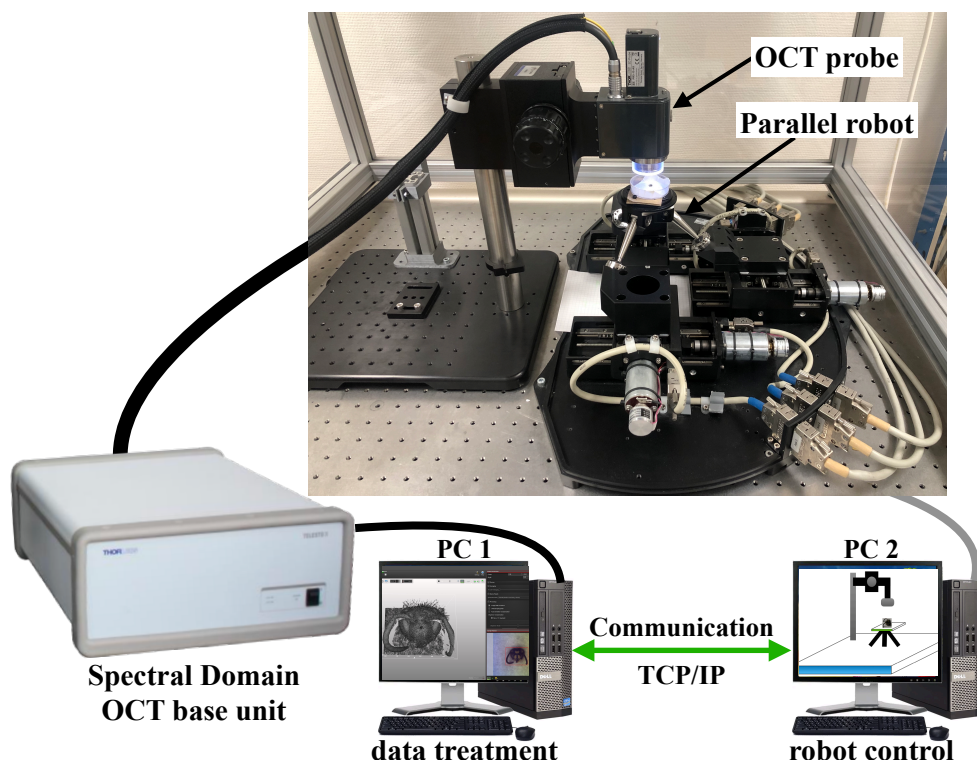


Figure 4.12 – Illustration of the experimental setup used to execute motions during OCT volume data acquisition.

#### 4.3.3.a Experimental setup description

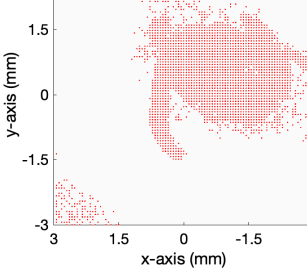
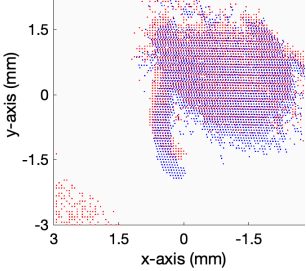
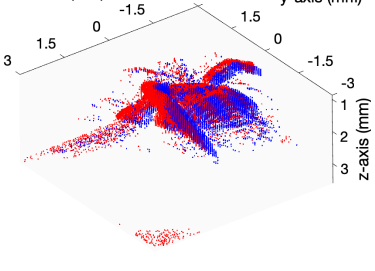
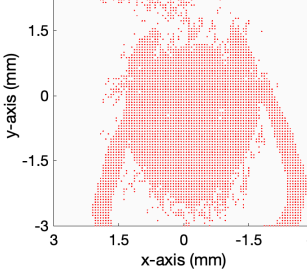
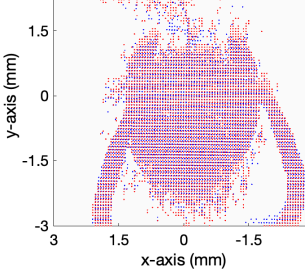
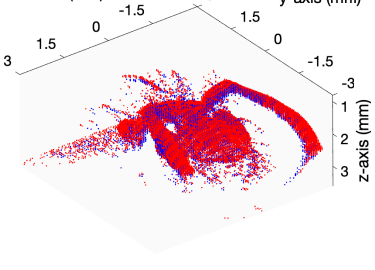
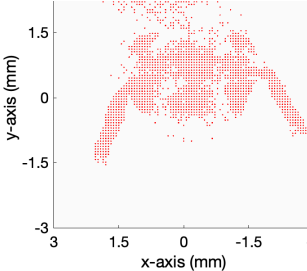
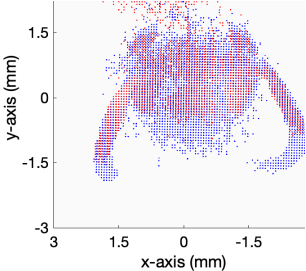
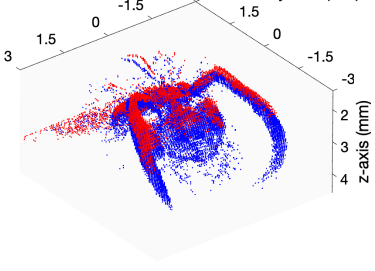
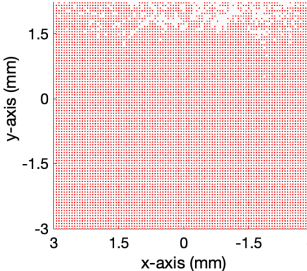
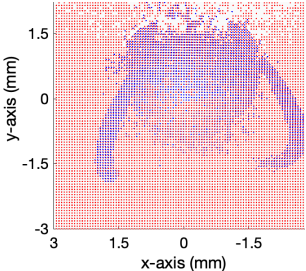
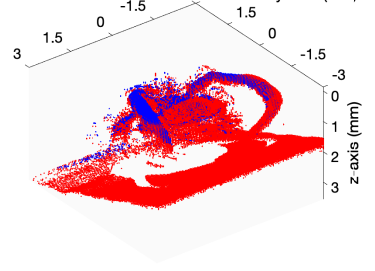
To obtain OCT distorted volumes due to motion, the OCT device used is the Telesto II 1325nm spectral domain from Thorlabs as shown in Figure 4.12. It provides 1D depth (A-Scan), 2D cross-section (B-Scan) and 3D volumetric (C-Scan) images with  $5.5\mu m$  axial resolution,  $7\mu m$  lateral resolution and  $3.54mm$  depth penetration. The device has a maximum A-Scan (optical core) acquisition rate of  $76k Hz$  with a maximum field-of-view of  $10 \times 10 \times 3.54mm^3$ .

The object to be scanned is placed on a fixed robotic platform; a 6-DoF 3PPSR parallel robot from Physical Instruments (SpaceFAB SF-3000 BS). It has the following characteristics: a maximum space reachable in translation of  $(t_x, t_y, t_z) = (50mm, 100mm, 12.7mm)$  and a maximum space reachable in rotation of  $(r_x, r_y, r_z) = (10^\circ, 10^\circ, 10^\circ)$ . Its linear resolution is  $0.2\mu m$  with a repeatability of  $\pm 0.5\mu m$  and its angular resolution is  $0.0005^\circ$  with a repeatability of  $\pm 0.0011^\circ$ . Two computers are used to carry out the experiments; the first (a 3.70 GHz Intel Xeon W-2145 CPU with 32Gb RAM and Windows 10 OS) is used for OCT data acquisition as well as data processing, and the second (a 3.20 GHz Intel Core CPU with 4Gb RAM and Windows 7 OS) is dedicated for the control of the parallel robot. These two computers communicate with each other asynchronously via the TCP/IP protocol.

#### 4.3.3.b Validation of motion artefact modelling

To validate our OCT motion artefact model, a comparative analysis is conducted between the simulated data and the experimental data that exhibit motion artefacts. This study aims to assess the similarity and correspondence between the two datasets. The experimental data used in the validation process consists of real-world OCT volumes captured under conditions where motion artefacts were present. The biological object being scanned (head of a bee) was placed on the mobile end-effector platform of the parallel robot. Translation and rotary motions were then produced by the parallel robot during data acquisition. Table 4.3 shows a comparison between the numerically simulated OCT volumes having motion artefacts as well as experimentally acquired volumes having motion artefacts. From qualitative analysis of the images in Table 4.3, we see that the simulated and experimental images are almost similar except for some slight discrepancies. Indeed, during experimental data acquisition, the object might be displaced to an area outside the field of view of the OCT resulting in missing data; in the second row, second column of Table 4.3, part of the antennae of the bee-head has been truncated due to a positive motion in the  $x - axis$ . Similarly, in the fourth row, second column of Table 4.3, part of the bee-head body has been truncated as well due to a negative motion in the  $z - axis$ . In addition, undesired motion might result in the OCT device acquiring data in an unwanted region; in the fifth row of Table 4.3, the OCT acquired data of the platform on which the bee-head was placed due to a positive motion in the  $z - axis$ . This significantly introduces noise to the acquired data.

Table 4.3 – Comparison study between some simulated data and experimental data (blue points - simulated motion-distorted volume, red points - experimentally motion-distorted volume). The units for the linear velocities,  $V$ , are in  $mm/s$  and angular velocities,  $\Omega$ , are in  $1e - 2rad/s$ .

Applied motion	Experimental volume (top view)	Experimental and simulated volume (top view)	Experimental and simulated volume (3D view)
$V_x = 5.00$ $V_y = 0.00$ $V_z = 0.00$ $\Omega_x = 0.50$ $\Omega_y = 0.00$ $\Omega_z = 0.00$			
$V_x = 0.00$ $V_y = 5.00$ $V_z = 0.00$ $\Omega_x = 0.50$ $\Omega_y = 0.00$ $\Omega_z = 0.00$			
$V_x = 0.00$ $V_y = 0.00$ $V_z = -5.00$ $\Omega_x = 0.50$ $\Omega_y = 0.00$ $\Omega_z = 0.00$			
$V_x = 0.00$ $V_y = 0.00$ $V_z = 5.00$ $\Omega_x = 0.00$ $\Omega_y = 0.00$ $\Omega_z = 0.50$			

## 4.4 PROPOSED METHOD FOR ESTIMATING 3D MOTION FROM AN OCT VOLUME WITH MOTION ARTEFACTS

In this thesis, it is proposed to use a software based approach for motion artefact correction. Software based approaches have the benefit that they can be used on any OCT device without making any major modifications on the hardware. Approaches to the proposed motion estimation are;

1. Top down approach: In this method:

- The shape of the object being scanned is known.

Knowing the shape of the object and having OCT data of the distorted shape, the instantaneous motion (linear and angular velocity) that introduces distortions to the OCT volume can be estimated (3D pose and velocity estimation). Using the estimated motion, motion artefacts on the distorted OCT data can be compensated for.

2. Bottom up approach: In this method:

- The shape of the object being scanned is unknown.
- After taking the C-scan (3D OCT volume), one view does not give enough information to differentiate between a static deformed object and a moving non deformed object.

To obtain more information on the OCT data acquired, multiple sequential C-scans are taken [Kraus 12]. Voxels in these C-scans are matched against each other using point cloud descriptors to determine the motion that resulted in their movement. Using the estimated motion, correction on the OCT data is then done.

Motion compensation in volumes differs from motion compensation in 2D images due to differences in dimensionality (voxels instead of pixels), and most notably, the complexity involved in performing matching. Matching between two volumes necessitates estimating the distance between them rather than calculating the sum of square distances between matched points. As a result, the process would involve computing the full corrected volume and subsequently comparing it to the reference volume. This comparison can be conducted B-scan by B-scan or slice (*en face* image in the  $x - y$  plane) by slice but is rather complex for volume by volume.

Therefore, in this section, it is proposed to use the top down approach in addition to a volume-wise criterion of similarity. Assuming that the imaged object is inherently smooth, jumps between consecutively acquired OCT volumes are induced by motion only. To perform motion correction of OCT data as illustrated in Figure 4.13, it is necessary to estimate the instantaneous linear ( $\vec{V}$ ) and angular velocity ( $\vec{\Omega}$ ) in addition to the pose  ${}^{oct}T_{B(t_0)}$ . This is achieved by minimising an objective function that reduces the similarity error between a corrected volume

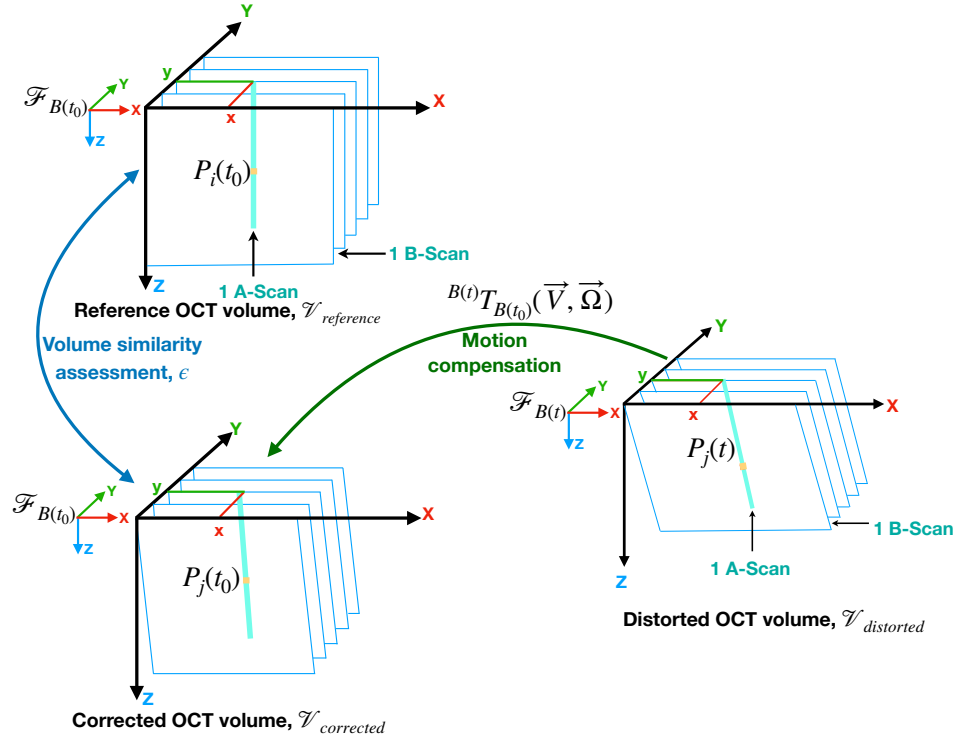


Figure 4.13 – Illustration of the proposed motion estimation process knowing the OCT volume reference shape.

and a corresponding reference volume. Implementing a volume-wise criterion of similarity, is the novelty of this proposed method. To compute this similarity error  $\epsilon$ , equation 4.13 is used:

$$\epsilon(\vec{V}, \vec{\Omega}, {}^{oct}T_{B(t_0)}) = \text{similarity error}(\mathcal{V}_{reference}, \mathcal{V}_{corrected}) \quad (4.13)$$

where the reference volume,  $\mathcal{V}_{reference}$ , is defined by:

$$\mathcal{V}_{reference} = \underbrace{\left\{ {}^{B(t_0)}P_i(t_0) \quad \forall i \in [1, n] \right\}}_{\text{reference volume}}, \quad (4.14a)$$

the corrected volume,  $\mathcal{V}_{corrected}$ , is calculated by:

$$\mathcal{V}_{corrected} = \underbrace{\left\{ {}^{B(t_0)}T_{B(t)}^{-1} * {}^{oct}T_{B(t_0)}^{-1} * \underbrace{{}^{oct}P_j(t)}_{\text{distorted volume due to } V, \Omega} \quad \forall j \in [1, m] \right\}}_{\text{corrected volume due to } V, \Omega}, \quad (4.14b)$$

and  $n$  and  $m$  is the number of voxels in the respective volumes.

${}^{B(t_0)}T_{B(t)}$  depends on  $(\vec{V}, \vec{\Omega})$  by equation 4.10. And equation 4.14b (which performs motion compensation) derives by the inversion of equation 4.12 such that:

$${}^{B(t_0)}\tilde{P}(t_0) = {}^{B(t)}\tilde{P}(t) = {}^{B(t_0)}T_{B(t)}^{-1} * {}^{oct}T_{B(t_0)}^{-1} * {}^{oct}\tilde{P}(t) \quad (4.15)$$

In practice, to compute  $\epsilon$ , we chose here the objective quality metric, PointPCA [Alexiou 21] as used in Chapter 2, subsection 2.5.3 on assessment of OCT volumes. PointPCA is a full-reference quality metric that compares the local shape and appearance between a point cloud under evaluation and its reference (comprehensive description is given in Appendix C).

Formally, the determination of the optimal motion correction values is expressed as a nonlinear minimisation problem:

$$(\vec{V}^*, \vec{\Omega}^*, {}^{oct}T_{B(t_0)}^*) = \underset{\{\vec{V}, \vec{\Omega}, {}^{oct}T_{B(t_0)}\}}{\operatorname{argmin}} \epsilon(\vec{V}, \vec{\Omega}, {}^{oct}T_{B(t_0)}) \quad (4.16)$$

This problem involves a total of 12 unknowns, which consist of the linear and angular velocities of the observed motion, as well as the transformation pose that encompasses translation and rotation. Therefore, starting with an initial guess for  $\vec{V}$ ,  $\vec{\Omega}$  and  ${}^{oct}T_{B(t_0)}$ , an iterative process, as illustrated in Figure 4.14, will execute motion correction to address the induced distortion.

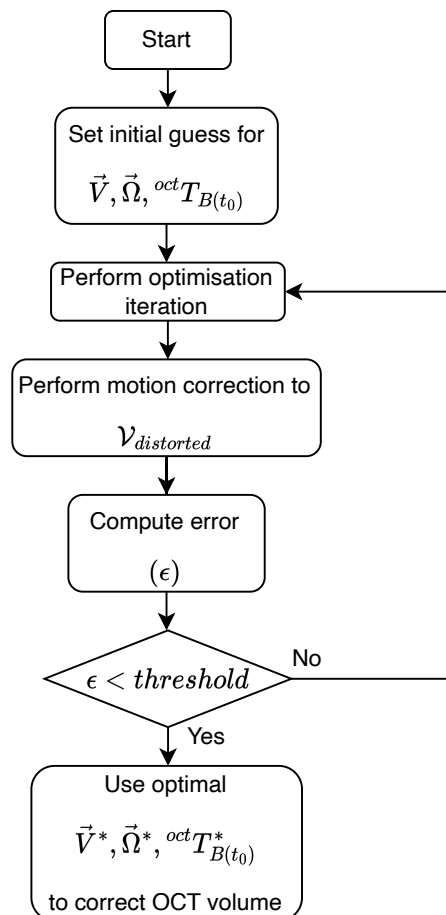


Figure 4.14 – Algorithm to estimate the linear ( $V$ ) and angular velocity ( $\Omega$ ) in addition to the pose  ${}^{oct}T_{B(t_0)}$ .



To obtain a corrected OCT volume, we compute the inverse transformation for each voxel in the distorted OCT volume using equation 4.14b. This equation takes into account the previously estimated instantaneous linear and angular velocity values as well as the transformation pose. By applying this inverse transformation to every voxel in the distorted OCT volume, we can effectively correct the motion artefacts and generate a desired corrected volume. This process ensures that each voxel is appropriately adjusted based on the corresponding motion information, resulting in an artefact-free representation of the volume. The quality of this correction is then assessed using equation 4.13 to further update the estimation of  $\vec{V}$ ,  $\vec{\Omega}$  and  ${}^{oct}T_{B(t_0)}$ . Upon successful iterations, the process determines the optimal  $\vec{V}^*$ ,  $\vec{\Omega}^*$ ,  ${}^{oct}T_{B(t_0)}^*$ , and does the compensation using them, making the corrected volume similar to the known reference one.

To estimate  $\vec{V}$ ,  $\vec{\Omega}$  and  ${}^{oct}T_{B(t_0)}$ , optimisation is done using the genetic algorithm function *ga* in MATLAB. A genetic algorithm is a method inspired by the process of natural selection to solve for both constrained and unconstrained optimisation problems. The algorithm repeatedly modifies a population of individual solutions. At each step, the genetic algorithm randomly selects individuals from the current population and uses them as parents to produce children for the next generation. Over successive generations, the population ‘evolves’ towards an optimal solution. The genetic algorithm can be applied to solve problems that are not well suited for standard optimisation algorithms, particularly problems in which the objective function is discontinuous, non-differentiable, stochastic or highly non-linear [Goldberg 89].

The proposed method of motion estimation and consequently motion correction is validated through simulation and experimental studies. The simulation study will be presented first, followed by the experimental validation.

#### 4.4.1 Numerical (simulation) validation

The pose  ${}^{oct}T_{B(t_0)}$ , was considered as the identity matrix. This was done to test the feasibility and core functionality of the method which is motion estimation. Indeed, for the experimental study, the pose needs to be taken into account. The objective function is thus simplified to:

$$(\vec{V}^*, \vec{\Omega}^*) = \underset{\{\vec{V}, \vec{\Omega}\}}{\operatorname{argmin}} \epsilon(\vec{V}, \vec{\Omega}) \quad (4.17)$$

The objective function in equation 4.17 was implemented in MATLAB and the *ga* function selected for the optimisation process. To test the stability as well as the consistency of the optimisation process, and consequently the motion estimation, a random design of experiment was done [Caliński 00].

##### 4.4.1.a Random design of experiment

The following steps were followed to implement the random design of experiment:



- The minimum and maximum boundaries for the instantaneous linear velocities in the  $x, y$  and  $z$  axes were selected. The lower bound was  $-3\text{mm/s}$  and upper bound  $3\text{mm/s}$ . Uniform random instantaneous linear velocities to introduce distortions in an OCT volume were then generated with respect to the mentioned bounds for 50 runs.
- The minimum and maximum boundaries for the instantaneous angular velocities in the  $x, y$  and  $z$  axes were selected. The lower bound was  $-0.03\text{rad/s}$  and upper bound  $0.03\text{rad/s}$ . Uniform random instantaneous angular velocities to introduce distortions in an OCT volume were then generated with respect to the mentioned bounds for 50 runs.
- Initial values to the optimal motion estimation process were also randomly generated for the linear and angular velocities with respect to the mentioned bounds in the previous two steps.
- The motion estimation process was then run for 100 iterations and optimal values to the linear and angular velocities obtained.

Furthermore, Gaussian noise with a mean of 0 and a standard deviation of 10 was introduced to 50% of the data. This noise was applied to the intensity value of each voxel in the distorted OCT volume.

#### 4.4.1.b Motion estimation results

A qualitative analysis will be first presented to validate the motion estimation method and later on statistical analysis will be presented on the motion estimation errors.

#### Qualitative analysis

Figure 4.15 shows the motion-free OCT volume ( $x - y$  plane view and 3D view) of a bee-head. This will be the reference volume from which the motion will be estimated on, from the motion-distorted volumes.

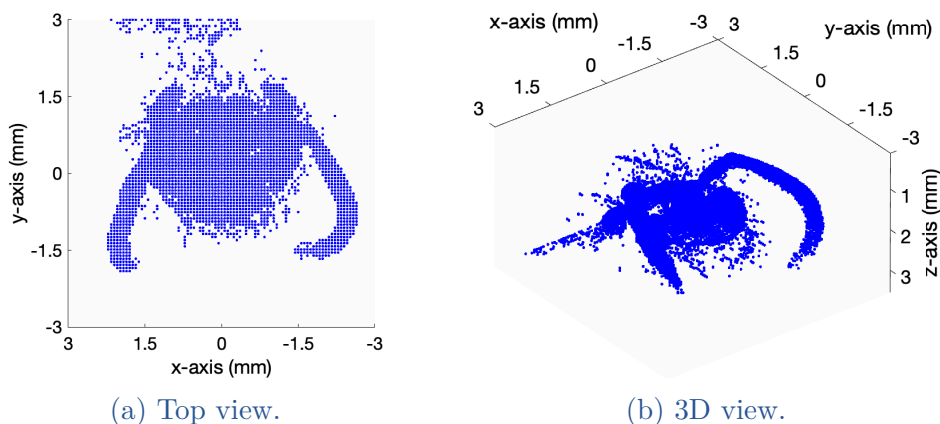


Figure 4.15 – OCT point cloud volume of a stationary bee-head.

Table 4.4 and 4.5 shows the distorted OCT volume with motion artefacts and the corrected OCT volume for some of the optimisation runs. The linear and angular velocities that were used to simulate the distorted volumes are provided as well as the estimated velocities after the motion estimation process. From the columns of distorted volumes (top view and 3D view) in Table 4.4 and 4.5, we see the significant effects of motion artefacts. In most of the images, the distorted OCT volume is barely recognisable from the motion-free OCT volume (see for instance the third row in Table 4.4 and the second row in Table 4.5 ). However after motion estimation and later on correction, the volumes are closely similar to the motion-free OCT volume (as illustrated in the sixth column of the Tables). These results show that the proposed 3D motion estimation method in SE(3) works.

Table 4.4 – Results from a few motion estimation runs (blue points - reference volume, red points - motion-distorted volume, green points - corrected volume). The units for the linear velocities,  $V$ , are in  $mm/s$  and angular velocities,  $\Omega$ , are in  $1e-2rad/s$ .

Applied motion	Reference and distorted volume (top view)	Reference and distorted volume (3D view)	Estimated applied motion	Reference and corrected volume (top view)	Reference and corrected volume (3D view)
$V_x = -1.77$ $V_y = 2.05$ $V_z = -2.97$ $\Omega_x = -1.39$ $\Omega_y = -1.46$ $\Omega_z = -1.26$			$V_x = -1.79$ $V_y = 2.03$ $V_z = -2.97$ $\Omega_x = -1.40$ $\Omega_y = -1.45$ $\Omega_z = -1.26$		
$V_x = 2.58$ $V_y = 1.18$ $V_z = 2.69$ $\Omega_x = 2.22$ $\Omega_y = 0.89$ $\Omega_z = -2.19$			$V_x = 2.58$ $V_y = 1.19$ $V_z = 2.69$ $\Omega_x = 2.23$ $\Omega_y = 0.89$ $\Omega_z = -2.19$		
$V_x = -1.72$ $V_y = -1.26$ $V_z = -2.53$ $\Omega_x = -0.36$ $\Omega_y = 1.18$ $\Omega_z = 0.01$			$V_x = -1.71$ $V_y = -1.22$ $V_z = -2.53$ $\Omega_x = -0.34$ $\Omega_y = 1.17$ $\Omega_z = 0.01$		

Table 4.5 – Results from a few motion estimation runs (blue points - reference volume, red points - motion-distorted volume, green points - corrected volume). The units for the linear velocities,  $V$ , are in  $mm/s$  and angular velocities,  $\Omega$ , are in  $1e - 2rad/s$ .

Applied motion	Reference and distorted volume (top view)	Reference and distorted volume (3D view)	Estimated applied motion	Reference and corrected volume (top view)	Reference and corrected volume (3D view)
$V_x = -1.88$ $V_y = -2.91$ $V_z = 0.95$ $\Omega_x = 1.81$ $\Omega_y = -1.13$ $\Omega_z = 1.37$			$V_x = -1.86$ $V_y = -2.88$ $V_z = 0.92$ $\Omega_x = 1.83$ $\Omega_y = -1.15$ $\Omega_z = 1.37$		
$V_x = -1.83$ $V_y = -2.31$ $V_z = 1.14$ $\Omega_x = -1.33$ $\Omega_y = 2.82$ $\Omega_z = 1.60$			$V_x = -1.80$ $V_y = -2.24$ $V_z = 1.17$ $\Omega_x = -1.28$ $\Omega_y = 2.80$ $\Omega_z = 1.62$		
$V_x = -2.29$ $V_y = -2.60$ $V_z = 2.92$ $\Omega_x = -2.36$ $\Omega_y = 2.07$ $\Omega_z = -1.17$			$V_x = -2.29$ $V_y = -2.60$ $V_z = 2.92$ $\Omega_x = -2.36$ $\Omega_y = 2.07$ $\Omega_z = -1.17$		

### Statistical analysis

The absolute difference between the expected and the initial linear and angular velocities was computed for each axis; in addition, the difference between the expected and the final optimised values was also computed. These errors are plotted in Figure 4.16, in the order of increasing initialisation error.

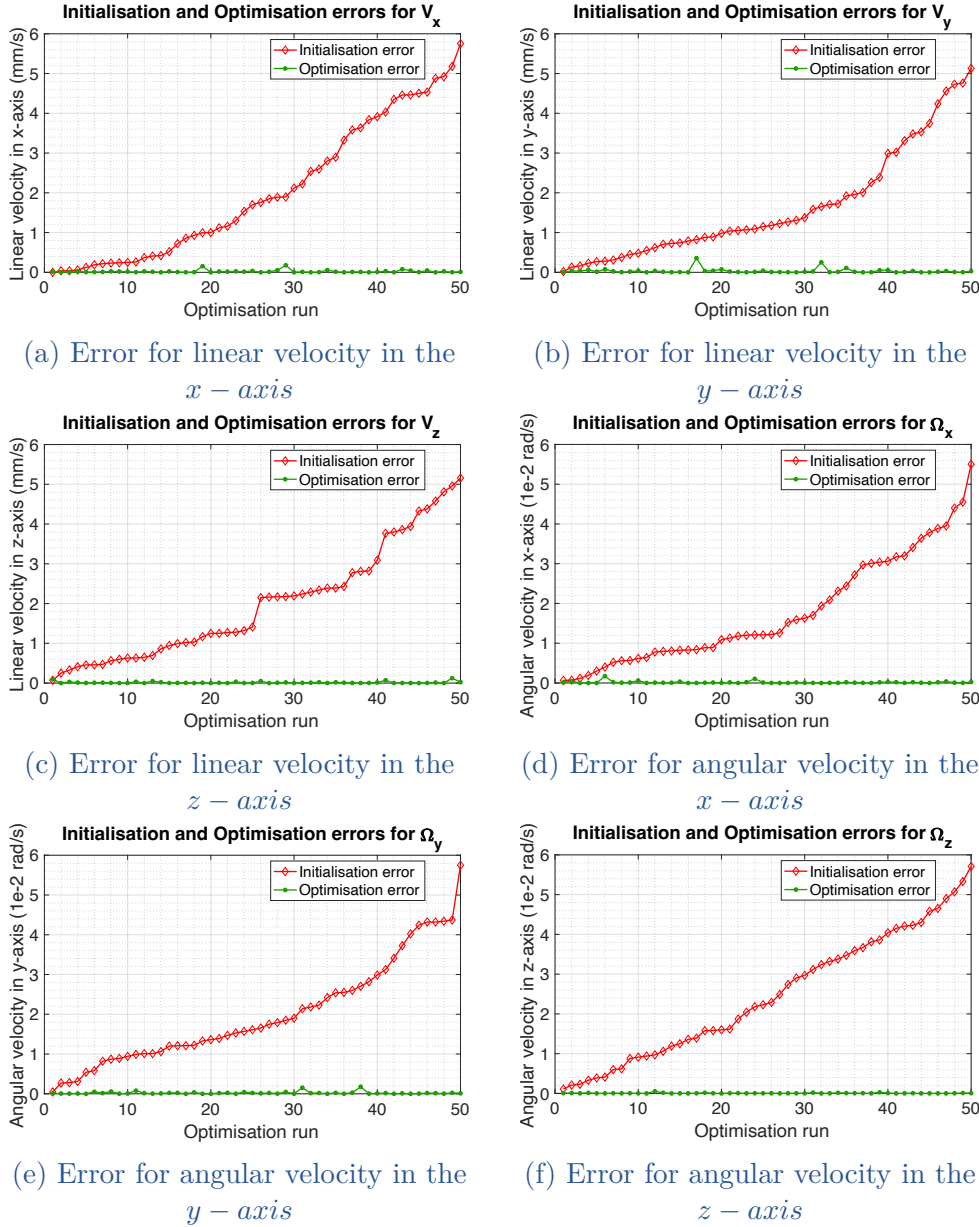


Figure 4.16 – Optimisation errors

From Figure 4.16, we observe a steady optimisation error of almost zero in all the axes for all of the optimisation runs even though the initialisation error increases. This validates that the proposed 3D motion estimation method in SE(3) is robust to the initialisation guesses.

Furthermore, Table 4.6 showcases the computation of maximum, mean, and root mean square (RMSE) errors of the initialisation and final optimised values of the linear and angular velocities in each axis. Particularly, values marked in bold within the table signify the axis with the highest error, while those in italics indicate the axis with the lowest error within the corresponding columns for both linear and angular velocities. It is observed that there is no clear correlation indicating which axis is more likely to have the highest or lowest error, demonstrating a non-linear behaviour.

Table 4.6 – Numerical simulation errors.

Variable	Max initial error	Max final error	Mean initial error	Mean final error	RMSE initial error	RMSE final error
$V_x(mm/s)$	<b>5.7514</b>	0.1775	<b>2.0525</b>	0.0218	<b>2.6764</b>	0.0400
$V_y(mm/s)$	<i>5.1300</i>	<b>0.3550</b>	<i>1.6575</i>	<b>0.0330</b>	<i>2.1550</i>	<b>0.0690</b>
$V_z(mm/s)$	5.1557	<i>0.1231</i>	2.0004	<i>0.0153</i>	2.4557	<i>0.0285</i>
$\Omega_x(1e - 2 rad/s)$	<i>5.5000</i>	<b>0.1709</b>	<i>1.7942</i>	<b>0.0162</b>	<i>2.2496</i>	<b>0.0329</b>
$\Omega_y(1e - 2 rad/s)$	<b>5.7479</b>	0.0656	2.0092	0.0093	2.3955	0.0155
$\Omega_z(1e - 2 rad/s)$	5.7100	<i>0.0535</i>	<b>2.4716</b>	<i>0.0058</i>	<b>2.9253</b>	<i>0.0106</i>

Both the initial and final PointPCA similarity error value,  $\epsilon$  that is minimised during the optimisation process is plotted as illustrated in Figure 4.17. We observe that the similarity error after optimisation is nearly zero in all the runs. This is indicative of the accurate 3D motion estimation in SE(3) from an OCT volume having geometric motion artefacts.

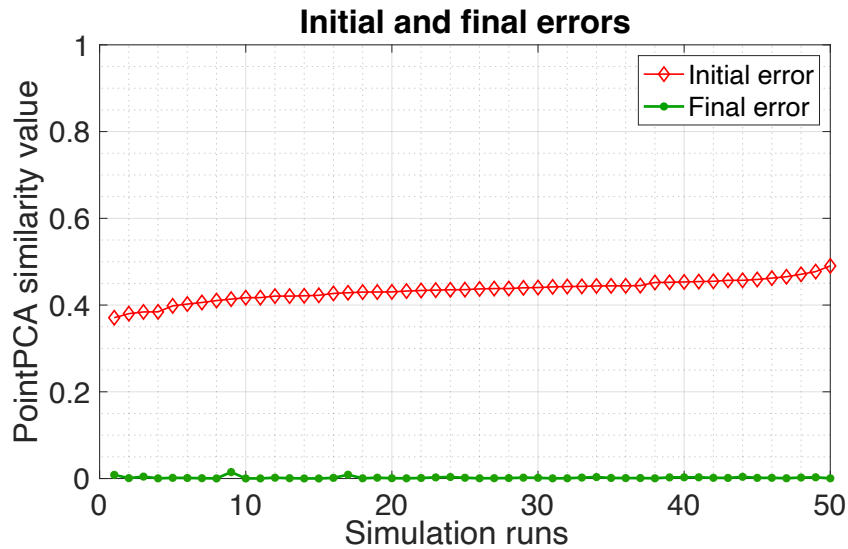


Figure 4.17 – Initial vs final (after optimisation) PointPCA error.

## 4.4.2 Experimental validation

For the experimental validation, the setup described in subsection 4.3.3.a and as shown in Figure 4.12 was used. Additionally, in our experiments, the scanning of the bee-head always starts from the same position. Therefore, we consider the pose  ${}^{oct}T_{B(t_0)}$  to be the identity matrix.

### 4.4.2.a Motion estimation results

As in simulation, we split here the analysis into a qualitative, and then a quantitative one.

#### Qualitative analysis

Figure 4.18 shows the motion-free OCT volume (top view and 3D view). This volume will be the reference volume against which the motion will be estimated when dealing with experimentally obtained OCT volumes having motion artefacts.

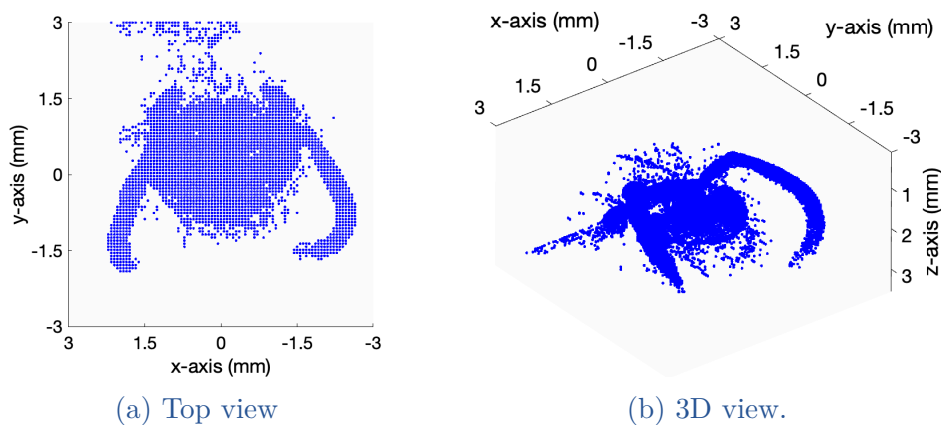


Figure 4.18 – OCT point cloud volume of a stationary bee-head.

Table 4.7 and 4.8 shows the experimental OCT volumes with motion artefacts and the corrected OCT volumes.

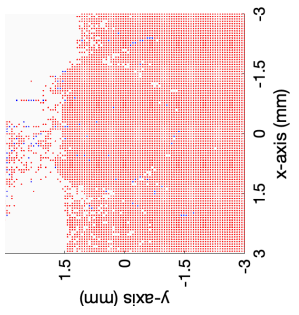
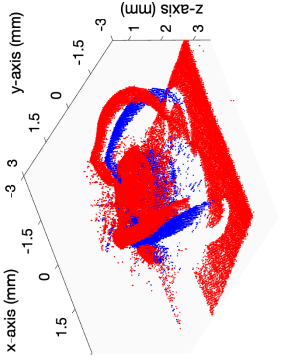
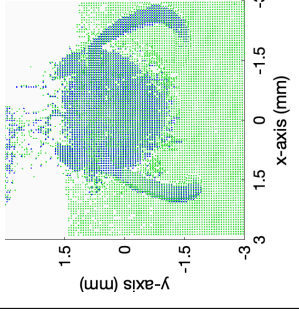
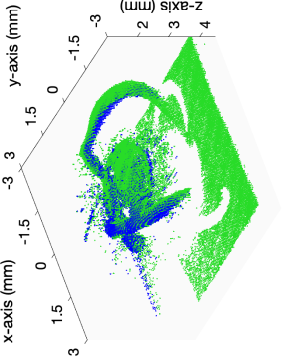
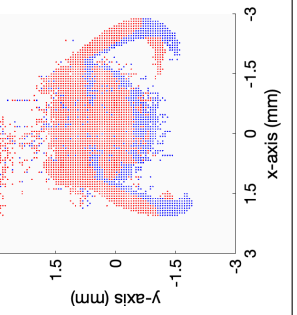
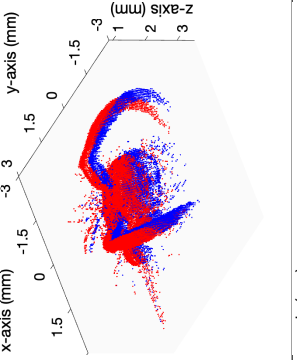
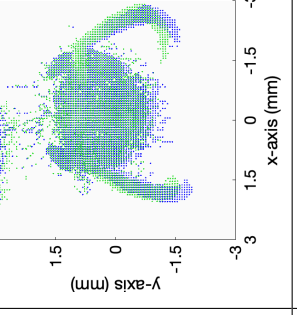
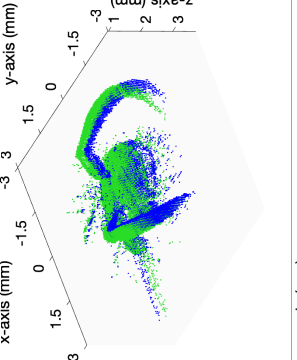
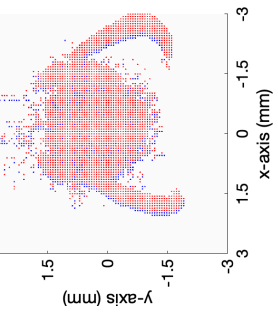
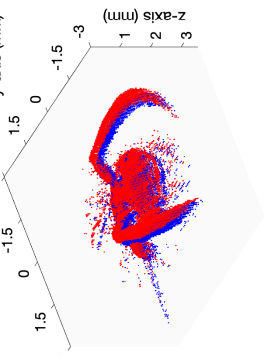
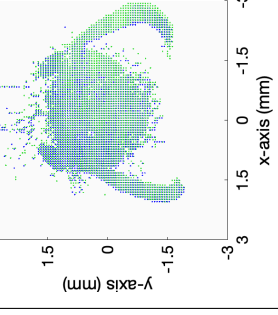
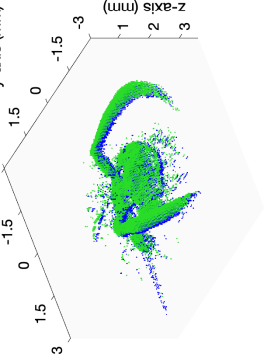


4.4. Proposed method for estimating 3D motion from an OCT volume with motion artefacts

Table 4.7 – Results from the motion estimation process using experimental data (blue points - reference volume, red points - motion-distorted volume, green points - corrected volume). The units for the linear velocities,  $V$ , are in  $mm/s$  and angular velocities,  $\Omega$ , are in  $1e - 2rad/s$ .

Applied motion	Reference and distorted volume (top view)	Reference and distorted volume (3D view)	Estimated applied motion	Reference and corrected volume (top view)	Reference and corrected volume (3D view)
$V_x = 6.00$ $V_y = 0.00$ $V_z = 0.00$ $\Omega_x = 0.05$ $\Omega_y = 0.00$ $\Omega_z = 0.00$			$V_x = 5.25$ $V_y = 0.00$ $V_z = 0.00$ $\Omega_x = 0.10$ $\Omega_y = 0.00$ $\Omega_z = 0.00$		
$V_x = 3.00$ $V_y = 0.00$ $V_z = 0.00$ $\Omega_x = 0.00$ $\Omega_y = 0.00$ $\Omega_z = 0.00$			$V_x = 2.79$ $V_y = 0.00$ $V_z = 0.00$ $\Omega_x = 0.00$ $\Omega_y = 0.00$ $\Omega_z = 0.00$		
$V_x = 0.00$ $V_y = 3.00$ $V_z = 0.00$ $\Omega_x = 0.00$ $\Omega_y = 0.00$ $\Omega_z = 0.00$			$V_x = 0.00$ $V_y = 2.82$ $V_z = 0.00$ $\Omega_x = 0.00$ $\Omega_y = 0.00$ $\Omega_z = 0.00$		

Table 4.8 – Results from the motion estimation process using experimental data (blue points - reference volume, red points - motion-distorted volume, green points - corrected volume). The units for the linear velocities,  $V$ , are in  $mm/s$  and angular velocities,  $\Omega$ , are in  $1e-2rad/s$ .

Applied motion	Reference and distorted volume (top view)	Reference and distorted volume (3D view)	Estimated applied motion	Reference and corrected volume (top view)	Reference and corrected volume (3D view)
$V_x = 0.00$ $V_y = 0.00$ $V_z = 3.00$ $\Omega_x = 0.00$ $\Omega_y = 0.00$ $\Omega_z = 0.00$			$V_x = 0.00$ $V_y = 0.00$ $V_z = 2.52$ $\Omega_x = 0.00$ $\Omega_y = 0.00$ $\Omega_z = 0.00$		
$V_x = 0.00$ $V_y = 0.00$ $V_z = 0.00$ $\Omega_x = 0.06$ $\Omega_y = 0.00$ $\Omega_z = 0.00$			$V_x = 0.00$ $V_y = 0.00$ $V_z = 0.00$ $\Omega_x = 0.07$ $\Omega_y = 0.00$ $\Omega_z = 0.00$		
$V_x = 0.00$ $V_y = 0.00$ $V_z = 0.00$ $\Omega_x = 0.00$ $\Omega_y = 0.00$ $\Omega_z = 0.06$			$V_x = 0.00$ $V_y = 0.00$ $V_z = 0.00$ $\Omega_x = 0.00$ $\Omega_y = 0.00$ $\Omega_z = 0.06$		

From the qualitative analysis results, it is observed that the corrected OCT volumes closely resemble the motion-free volumes. Notably, in the experimentally distorted volume (second column) and subsequently in the second and third rows of Table 4.7, some details, such as part of the antennae of the bee-head, are missing and truncated. Nonetheless, after motion estimation and correction, the corrected volume aligns and recovers the shape of the motion-free OCT volume, as observed in the sixth column of Table 4.7. Also, despite the experimentally distorted volume containing unwanted data (robot platform) as observed in the second row, second and third column of Table 4.8, the motion causing the distortion is able to be estimated, and the shape recovered, as seen in the sixth column.

### Quantitative analysis

Both the initial and final PointPCA similarity error value,  $\epsilon$  that is minimised during the motion estimation process for the experimentally distorted volumes is plotted as illustrated in Figure 4.19.

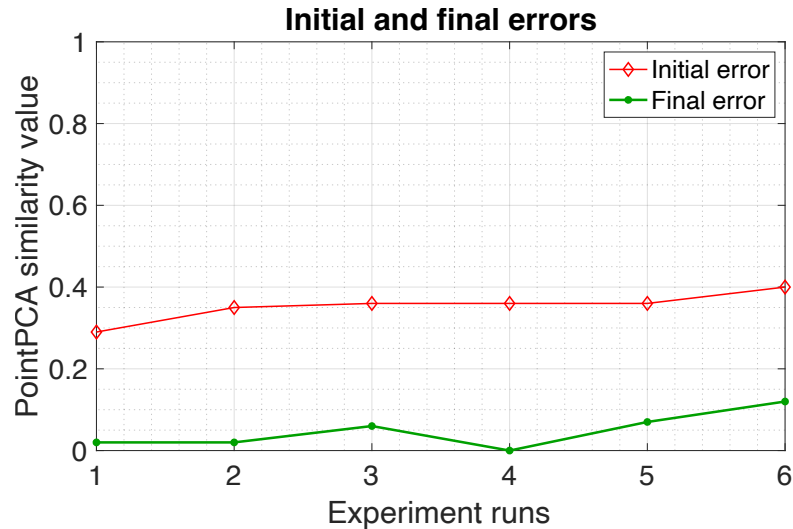


Figure 4.19 – Initial vs final (after optimisation) PointPCA error.

We observe that the similarity error after optimisation is minimised for all the experimental runs. However, there are instances when the final similarity error is not zero. Reasons for this discrepancy in accurate motion estimation may be due to;

- ✘ Occurrences of missing data. This may occur when the object moves out of the field of view, resulting in missing data within the obtained volume.
- ✘ Introduction of unnecessary data. the OCT device may capture data from undesired regions, particularly when there is a translatory motion in the  $z$  - *axis* (as seen in the second row of Table 4.8).
- ✘ The numerical optimisation process getting stuck at a local minimum.
- ✘ Modelling errors.

Nevertheless, despite these challenges, the analysis demonstrates that the shape and motion estimation works fairly well.

## 4.5 3D SHAPE AND MOTION ESTIMATION FROM A SINGLE UNKNOWN OCT VOLUME OBTAINED USING A NON-RASTER SCAN TRAJECTORY

In contrast to section 4.4 where shape and motion estimation was performed using a known reference OCT volume, in this section, a method is proposed to estimate the 3D shape and motion from a single distorted OCT volume without prior knowledge of the shape. The distorted OCT volume is acquired during motion and using the rosette scan trajectory. The efficacy of the proposed method is validated using numerical simulations as well as using experimental data.

### 4.5.1 Motion artefacts in optical coherence tomography during raster and non-raster scanning

So far, we have only observed motion artefacts in OCT when the raster trajectory is used. However, what occurs when non-raster trajectories are used during data acquisition when the object being imaged is in motion? As discussed in Chapter 2 of this thesis, the spiral, Lissajous and rosette scan trajectories are suitable non-raster trajectories to be used in OCT data acquisition. A study by Bush *et al.* [Bush 20] demonstrated that by acquiring magnetic resonance images (MRI) using the rosette trajectory, motion artefacts were reduced, and thus there was no need for motion compensation. Therefore, in their image reconstruction model, motion was not taken into account. In contrast, for OCT, we observe different phenomena. Figures in Tables 4.9 to 4.11 display the OCT point cloud volumes of the same object acquired during motion, employing both the raster, and the non-raster trajectories. Indeed, motion artefacts are more pronounced in the case of the non-raster trajectories. For the same compound motion during data acquisition, the OCT volumes obtained using the rosette (row 4 and 5 in column 4 of Table 4.9) and the Lissajous trajectory (row 2 and 3 in column 4 of Table 4.10) are significantly distorted as compared to the volume obtained by the spiral trajectory (row 4 and 5 in column 4 of Table 4.10). Upon close observation, it is evident that the distorted OCT volume obtained using the Lissajous trajectory exhibits a shape that appears to overlap itself twice. On the other hand, the distorted volume obtained using the rosette trajectory shows a shape that appears to overlap itself several times (it is important to note that the shape is significantly distorted when a larger magnitude of motion is applied, as illustrated in Table 4.11). The Lissajous trajectory repeats itself in reverse during the second half of its period [Bazaei 12] while the rosette has several self-intersections (this is the nature of the rosette pattern as will be explored further in a subsequent subsection). While the resulting distorted volumes obtained using the non-raster trajectories (specifically the Lissajous and rosette) might appear somewhat blurrier compared to those obtained using the raster trajectory, they could offer the advantage of providing additional information about the motion-induced artefacts. To estimate the 3D

4.5. 3D Shape and motion estimation from a single unknown OCT volume obtained using a non-raster scan trajectory

shape and motion using a single volume, only the rosette and Lissajous trajectories can be considered since they have intersections and repeated scan positions. The spiral scan trajectory has no repeated scan positions to take advantage of.

Table 4.9 – Motion artefact effects on volumes obtained using the raster and non-raster scan trajectories. The units for the linear velocities,  $V$ , are in  $mm/s$  and angular velocities,  $\Omega$ , are in  $1e - 2rad/s$ .

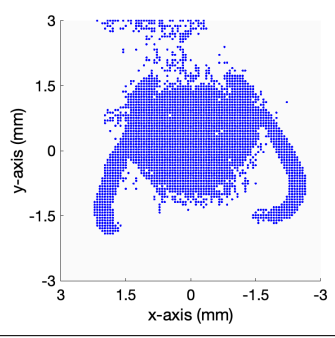
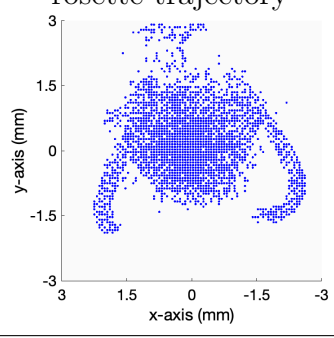
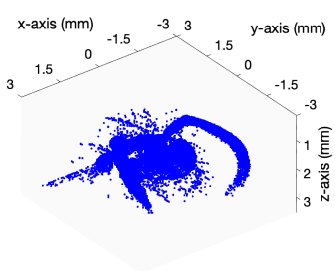
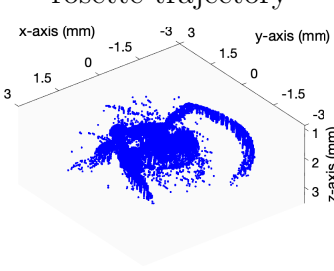
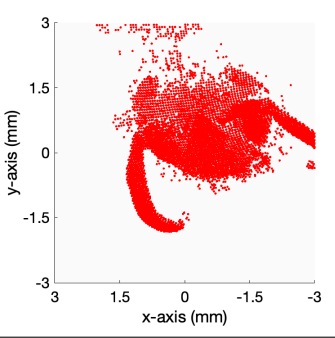
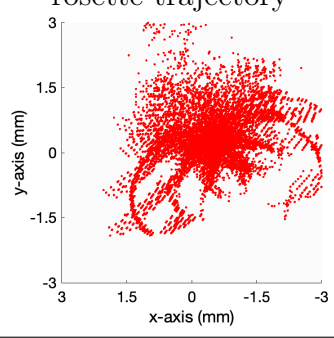
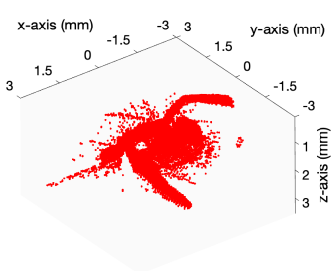
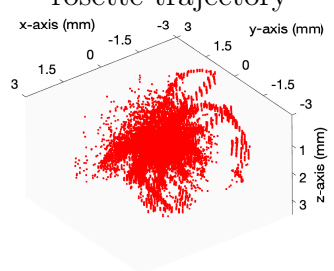
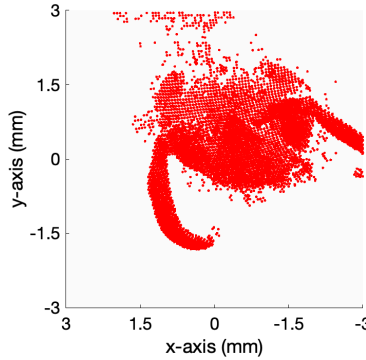
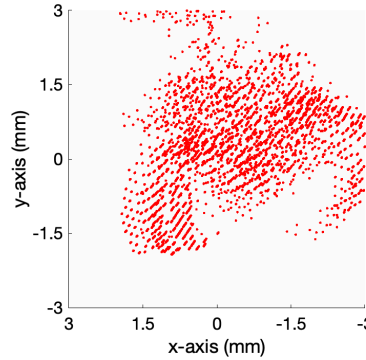
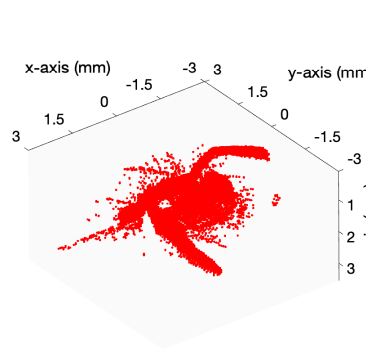
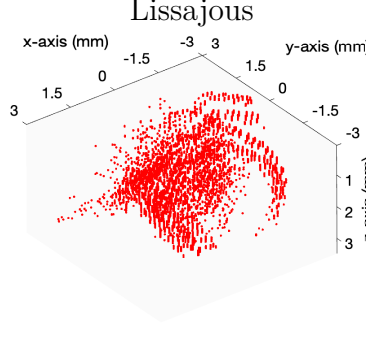
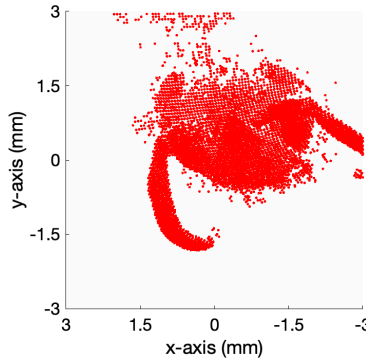
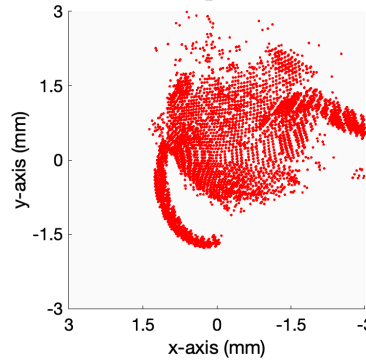
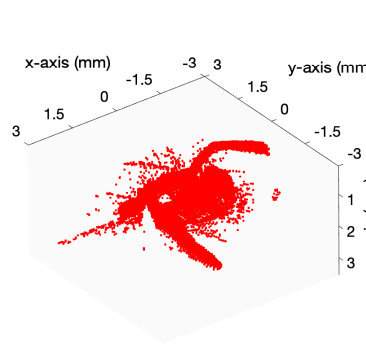
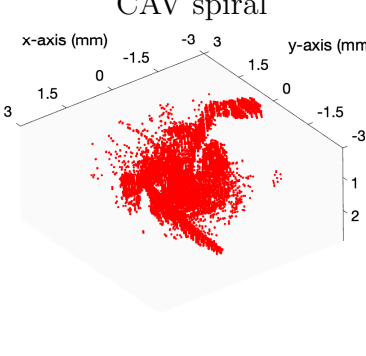
		Raster scan trajectory	Non-raster scan trajectory
motion-free	top view		rosette trajectory 
	3D view		rosette trajectory 
$V_x = 1.00$ $V_y = 1.00$ $V_z = 1.00$ $\Omega_x = 1.00$ $\Omega_y = 1.00$ $\Omega_z = 1.00$	top view		rosette trajectory 
	3D view		rosette trajectory 

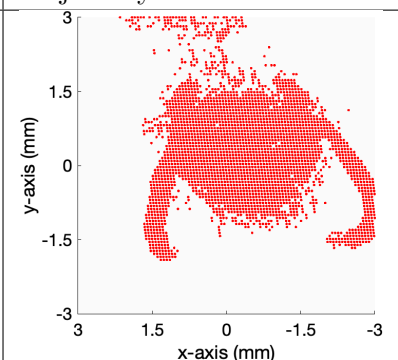
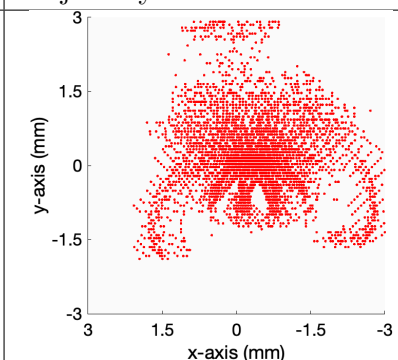
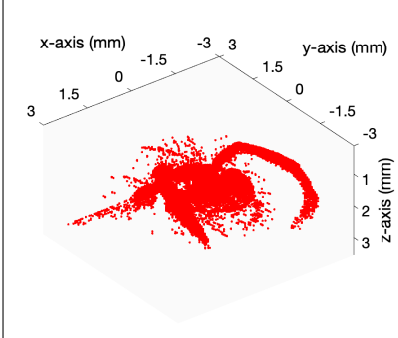
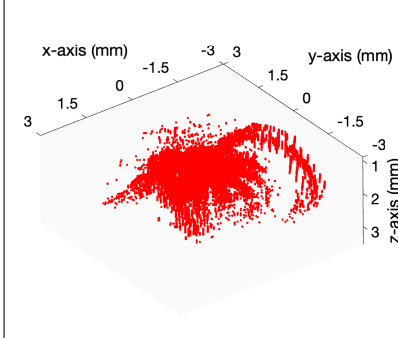
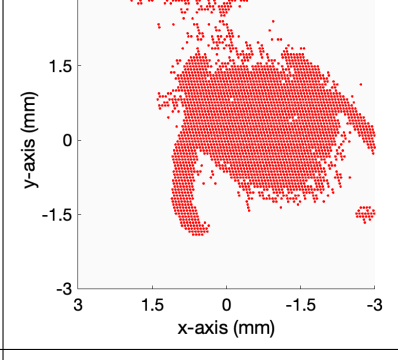
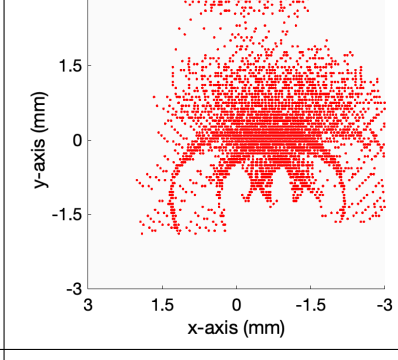
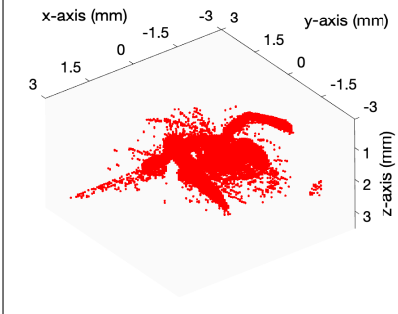
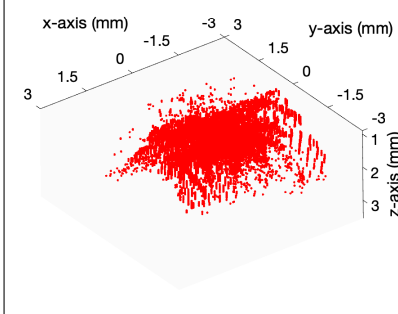
Table 4.10 – Motion artefact effects on volumes obtained using the raster, Lissajous and continuous angular velocity (CAV) spiral scan trajectories. The units for the linear velocities,  $V$ , are in  $mm/s$  and angular velocities,  $\Omega$ , are in  $1e - 2rad/s$ .

		Raster scan trajectory	Non-raster scan trajectory
$V_x = 1.00$ $V_y = 1.00$ $V_z = 1.00$ $\Omega_x = 1.00$ $\Omega_y = 1.00$ $\Omega_z = 1.00$	top view		<b>Lissajous</b> 
	3D view		<b>Lissajous</b> 
$V_x = 1.00$ $V_y = 1.00$ $V_z = 1.00$ $\Omega_x = 1.00$ $\Omega_y = 1.00$ $\Omega_z = 1.00$	top view		<b>CAV spiral</b> 
	3D view		<b>CAV spiral</b> 



4.5. 3D Shape and motion estimation from a single unknown OCT volume obtained using a non-raster scan trajectory

Table 4.11 – Motion artefact effects on volumes obtained using the raster and rosette scan trajectories. The units for the linear velocities,  $V$ , are in  $mm/s$  and angular velocities,  $\Omega$ , are in  $1e - 2rad/s$ .

		Raster scan trajectory	Rosette scan trajectory
$V_x = 2.00$ $V_y = 0.00$ $V_z = 0.00$ $\Omega_x = 0.00$ $\Omega_y = 0.00$ $\Omega_z = 0.00$	top view		
	3D view		
$V_x = 4.00$ $V_y = 0.00$ $V_z = 0.00$ $\Omega_x = 0.00$ $\Omega_y = 0.00$ $\Omega_z = 0.00$	top view		
	3D view		



### 4.5.2 The rosette scan trajectory and its peculiarities

As detailed in Chapter 2 of this thesis, the rosette trajectory is the recommended non-raster scanning approach for OCT volumetric acquisitions. Moreover, employing the rosette trajectory allows for significant time savings without a substantial sacrifice in OCT volume quality. The rosette scan trajectory is an epitochroid where the distance between the centre of the rolling circle and the rotating point is equal to the sum of the radii of a fixed and a rolling circle. It is a periodic pattern that repeats itself over a certain time interval intersecting itself at specific points [Nikooienejad 19]. The authors in [Meyer 14] elaborate that self-intersections of large temporal separation provides information that may be used to detect and remove height drift in atomic force microscopy images. As shown in Figure 4.20a, we see the intersections of three successive petals of the rosette pattern highlighted by different colours along with their midlines and bisectors. The pattern symmetry of the rosette trajectory indicates that the petals intersect not only at the origin but also at their midlines as well as at the bisector of two consecutive midlines. The tangential distance (TD) and radial distance (RD) generate curvilinear rhombuses as shown by the shaded region in grey in Figure 4.20a. In Figure 4.20b, the intersections are shown by  $\times$  and the edge points by  $*$ . We see that the intersections lie on the concentric circles. The intersections that are close to the periphery are located on the first circle and the ones close to the origin remain on the innermost (fourth) concentric circle [Nikooienejad 19].

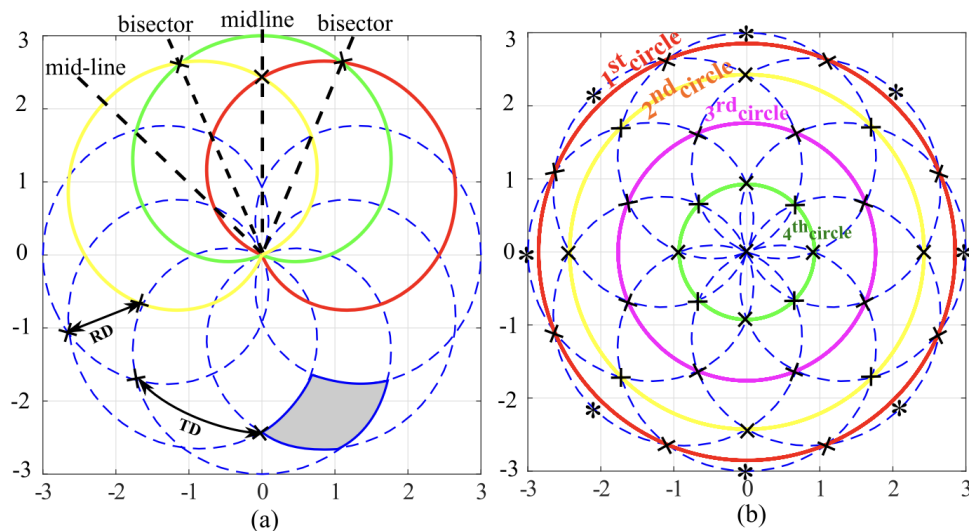


Figure 4.20 – Illustration of the rosette scan pattern; (a) Three successive petals of the pattern depicted by different colours, (b) Concentric circles crossing the intersections - the intersections are shown by  $\times$  and the edge points by  $*$  [Nikooienejad 19].

Taking advantage of the periodicity and the intersecting nature of the rosette pattern, it is proposed to estimate the shape and motion from a single OCT volume acquired using the rosette scan trajectory. This is detailed in the next subsection.

### 4.5.3 Proposed shape and motion estimation method from a single OCT volume

As can be seen in Figure 4.20, the rosette scan trajectory has several intersections within itself. Therefore, during data acquisition, data will be acquired repeatedly on some scan positions. During the point cloud image processing step, we can extract two volumes from the OCT data collected using the rosette trajectory. If the data was acquired while the object is stationary, the two extracted volumes (they will be referred to as sub-volumes from now on) should be completely identical. However, if the data was acquired while the object is in motion, the two sub-volumes will be different to some degree (depending on the magnitude of the motion and due to the sequential nature of OCT data acquisition). As was stated earlier, assuming rigid body motion, we can correct for the motion distortion if we know the linear and angular velocities. What is remarkable is that, when we perform motion correction on the two distorted sub-volumes separately, they revert back to being identical once more. Therefore, if we can extract two sub-volumes from a single OCT volume, motion estimation can be performed. Since it was already established that the rosette trajectory is an optimal OCT scan trajectory, we can further exploit its nature to perform motion estimation by obtaining data only once.

#### 4.5.3.a Extracting two sub-volumes from one OCT volume

An OCT volume obtained using a rosette trajectory is as shown in Figure 4.21.

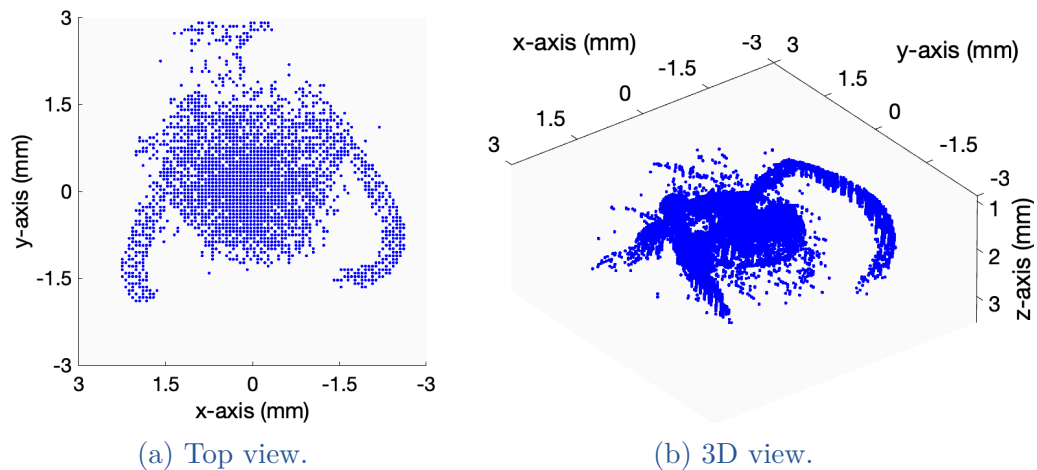


Figure 4.21 – OCT point cloud volume obtained using the rosette scan trajectory.

Leveraging on the repeated scan positions due to the intersections of the rosette trajectory a pair of OCT sub-volumes are extracted from one static OCT volume. Figures in Table 4.12 shows two identical motion-free sub-volumes.

Figures in Table 4.13 shows two distorted sub-volumes extracted from one distorted OCT volume. The distorted volumes are slightly different from each other.

Table 4.12 – Two sub-volumes extracted from one motion-free OCT volume.

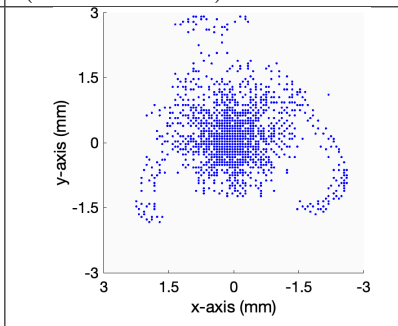
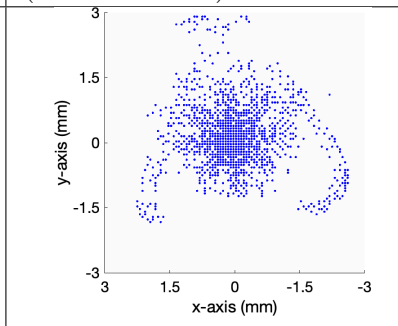
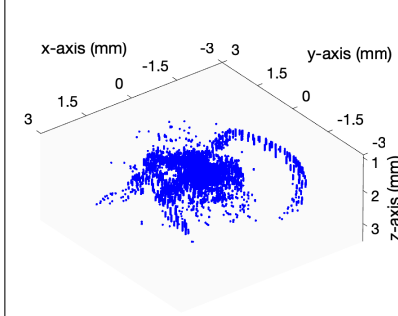
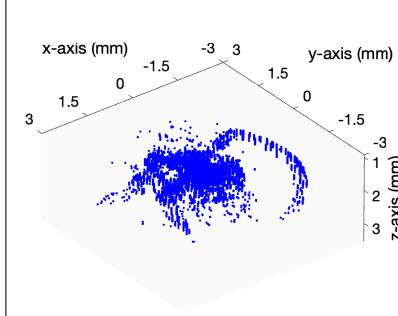
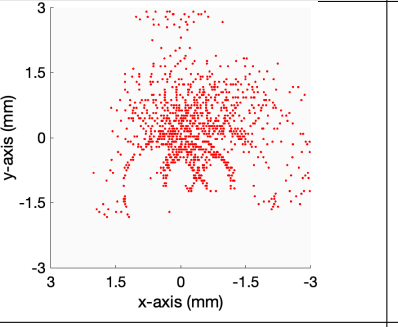
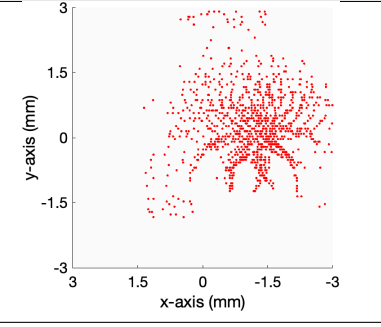
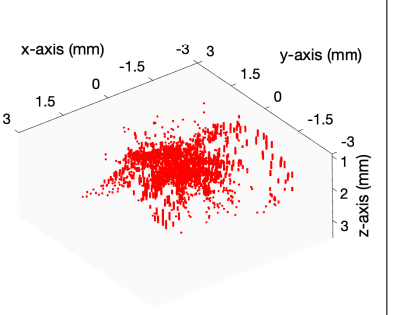
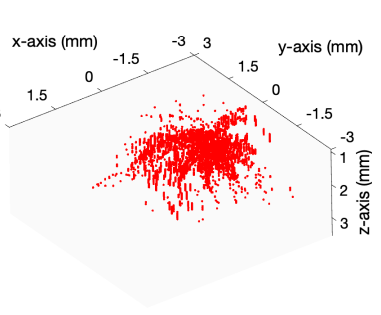
		Rosette scan trajectory (sub-volume 1)	Rosette scan trajectory (sub-volume 2)
motion-free	top view		
	3D view		

Table 4.13 – Two sub-volumes extracted from one motion-distorted OCT volume. The units for the linear velocities,  $V$ , are in  $mm/s$  and angular velocities,  $\Omega$ , are in  $1e - 2rad/s$ .

		Rosette scan trajectory (sub-volume 1)	Rosette scan trajectory (sub-volume 2)
$V_x = 4.00$ $V_y = 0.00$ $V_z = 0.00$ $\Omega_x = 0.00$ $\Omega_y = 0.00$ $\Omega_z = 0.00$	top view		
	3D view		

For a closer observation, Figure 4.22 shows the two sub-volumes extracted from a distorted OCT volume overlaid on each other using different colours. We clearly see that there exists a difference between the two sub-volumes.

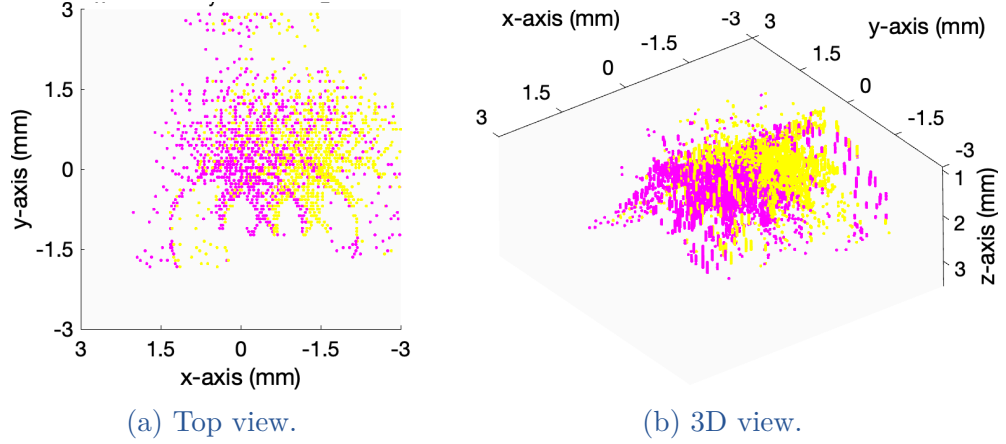


Figure 4.22 – Rosette distorted OCT sub-volumes. (Magenta points - first repeated sub-volume, yellow points - second repeated sub-volume).

#### 4.5.3.b Motion estimation from a single OCT volume

Similarly to how the distortion motion was estimated using two consecutive OCT volumes in subsection 4.4, we can employ a slightly modified version of the method. To begin, Figure 4.23 illustrates an OCT volume  $R_s$  (obtained using the rosette trajectory), from which two sub-volumes,  $S_1$  and  $S_2$ , have been extracted from as explained in subsection 4.5.3.a. The sub-volumes  $S_{1,motion-free}$  and  $S_{2,motion-free}$  each contain a subset of points from  $R_s$ , such that;  $S_{1,motion-free} = \{P_k(t_k), \forall t_k \in [t_0, t']\}$ ,  $S_{2,motion-free} = \{P_l(t_l), \forall t_l \in [t_0, t'']\}$ , where  $P_k$  and  $P_l$  are voxels of the sub-volumes  $S_1$  and  $S_2$  respectively,  $t_0$  is the time at the beginning of OCT data acquisition,  $t'$  and  $t''$  is the time at which the last voxel of  $S_1$  and  $S_2$  respectively has been acquired.

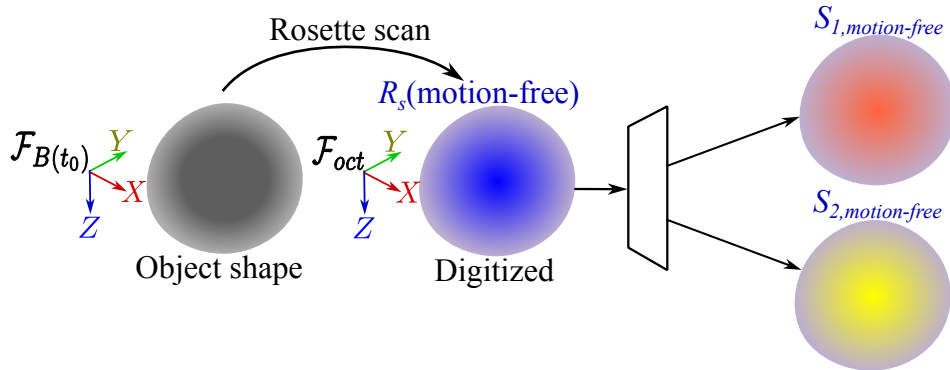


Figure 4.23 – Extraction of two sub-volumes from one static OCT volume.

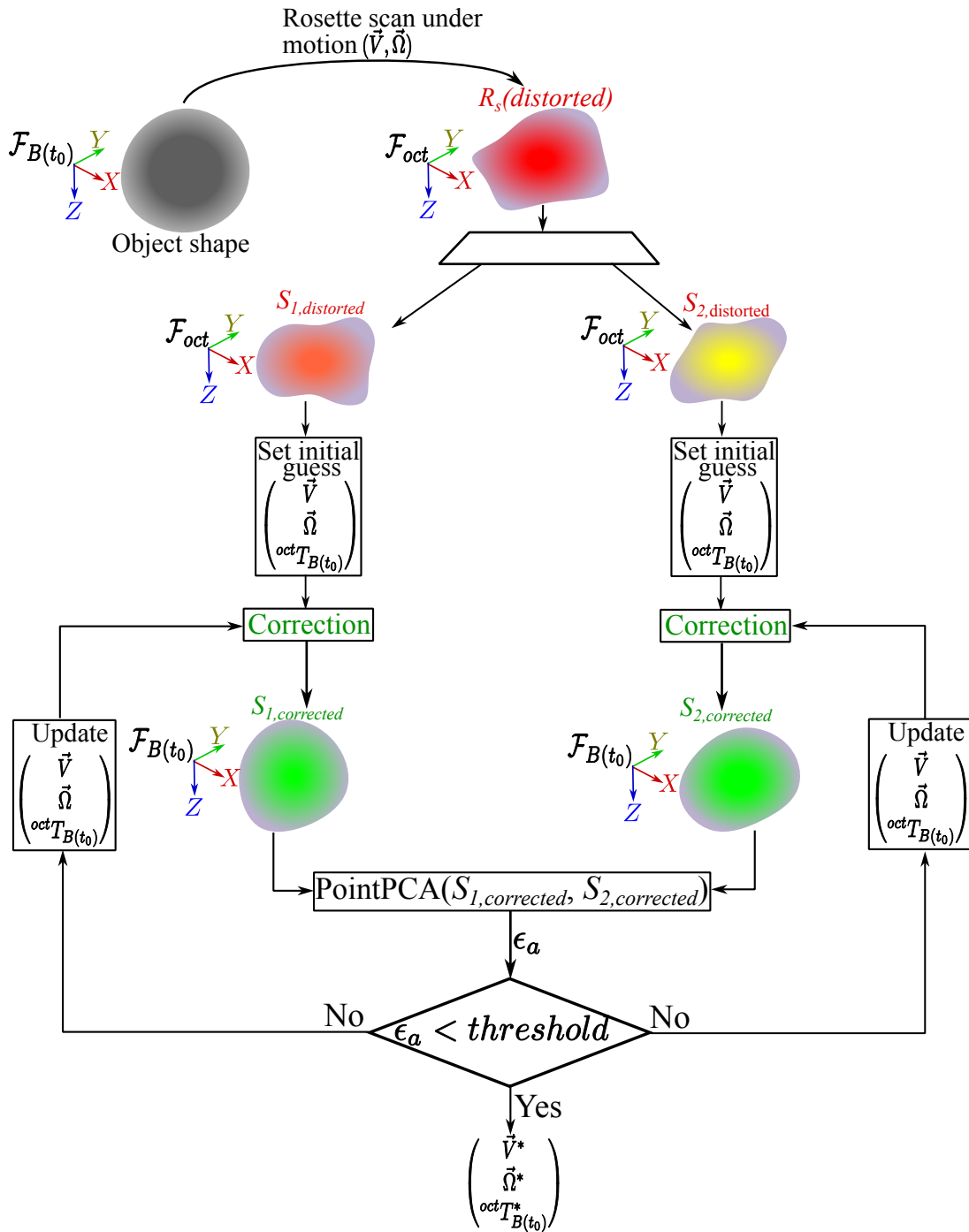


Figure 4.24 – Illustration of the proposed method to estimate the distortion motion from one OCT volume.

Figure 4.24 illustrates the proposed method to estimate the distortion motion from one OCT volume. From Figure 4.24, the objective is to estimate the same linear ( $\vec{V}$ ) and angular ( $\vec{\Omega}$ ) velocity that can be used to correct the two distorted sub-volumes and make them identical i.e., two subsets of one unique set, in the object shape, in the same frame  $\mathcal{F}_{B(t_0)}$  which isn't known beforehand. This is

achieved by minimising an objective function that reduces the similarity error between the corrected sub-volumes. The error  $\epsilon_a$  is computed using equation 4.18. Even though the acquired distorted sub-volumes appear different, when accurately corrected they should be similar.

$$\epsilon_a(\vec{V}, \vec{\Omega}, {}^{oct}T_{B(t_0)}) = \text{similarity error}(S_{1,corrected}, S_{2,corrected}) \quad (4.18)$$

where the two corrected subsets are obtained as in equation 4.14b:

$$S_{1,corrected} = \underbrace{\left\{ {}^{B(t_0)}T_{B(t_k)}^{-1} * {}^{oct}T_{B(t_0)}^{-1} * {}^{oct}P_k(t_k) \quad \forall t_k \in [t_0, t'] \right\}}_{\text{corrected sub-volume 1 due to } V, \Omega} \quad (4.19a)$$

$$S_{2,corrected} = \underbrace{\left\{ {}^{B(t_0)}T_{B(t_l)}^{-1} * {}^{oct}T_{B(t_0)}^{-1} * {}^{oct}P_l(t_l) \quad \forall t_l \in [t_0, t''] \right\}}_{\text{corrected sub-volume 2 due to } V, \Omega} \quad (4.19b)$$

Again, to compute  $\epsilon_a$ , the objective quality metric PointPCA [Alexiou 21] is used. The resulting optimisation problem that needs to be solved using a numerical algorithm to obtain motion correction values is:

$$(\vec{V}^*, \vec{\Omega}^*, {}^{oct}T_{B(t_0)}^*) = \underset{\{\vec{V}, \vec{\Omega}, {}^{oct}T_{B(t_0)}\}}{\text{argmin}} \epsilon_a(\vec{V}, \vec{\Omega}, {}^{oct}T_{B(t_0)}) \quad (4.20)$$

Note that, we assume here that the velocity is constant and equal for each of the two sub-volumes. The optimisation problem to estimate the linear and angular velocities is done using a genetic algorithm as previously described in subsection 4.4.

#### 4.5.4 Numerical (simulation) validation

To validate the proposed method, a simulation study is performed. Similarly to subsection 4.4.1, the pose  ${}^{oct}T_{B(t_0)}$  is considered as the identity matrix. The main aim is to test the feasibility and core functionality of the motion estimation method. Therefore the objective function is simplified to:

$$(\vec{V}^*, \vec{\Omega}^*) = \underset{\{\vec{V}, \vec{\Omega}\}}{\text{argmin}} \epsilon_a(\vec{V}, \vec{\Omega}) \quad (4.21)$$

To test the stability as well as the consistency of the optimisation process, and consequently the motion estimation, a random design of experiment is done [Caliński 00].

##### 4.5.4.a Random design of experiment

The following steps were followed to implement the random design of experiment:

- The minimum and maximum boundaries for the instantaneous linear velocities in the  $x, y$  and  $z$  axes were selected. The lower bound was  $-2mm/s$  and upper bound  $2mm/s$ . Uniform random instantaneous linear velocities to introduce distortions in an OCT volume were then generated with respect to the mentioned bounds for 50 runs.
- The minimum and maximum boundaries for the instantaneous angular velocities in the  $x, y$  and  $z$  axes were selected. The lower bound was  $-0.02rad/s$  and upper bound  $0.02rad/s$ . Uniform random instantaneous angular velocities to introduce distortions in an OCT volume were then generated with respect to the mentioned bounds for 50 runs.
- Initial values to the optimal motion estimation process were also randomly generated for the linear and angular velocities with respect to the mentioned bounds in the previous two steps.
- The motion estimation process was then run for 100 iterations and optimal values to the linear and angular velocities obtained.

#### 4.5.4.b Motion estimation results

A qualitative analysis will be first presented to validate the shape and motion estimation method and later on a quantitative analysis will be presented.

#### Qualitative analysis

Table 4.14 and 4.15 highlights a comparison between the distorted OCT volumes containing motion artefacts and the corresponding corrected OCT volumes for a selection of the optimisation runs. The tables include information about the linear and angular velocities used to simulate the distorted volumes and the estimated velocities obtained through the motion estimation process. Upon examining the columns displaying the distorted volumes from both top and 3D views, the pronounced impact of motion artefacts is evident. In most cases, the distorted OCT volume bears little resemblance to the motion-free OCT volume. However, following the motion estimation and subsequent correction, the volumes closely resemble the motion-free OCT volume. For instance, in row 3 of Table 4.14 and in row 4 of Table 4.15, the motion-distorted OCT volume exhibits a significant deterioration compared to the motion-free volume. Despite this considerable geometric distortion, the 3D motion in  $SE(3)$  that caused the distortion can be estimated, and a correction applied. Upon comparing the corrected volume with the motion-free volume, they closely resemble each other as seen in the fifth and sixth columns of the Tables. These results convincingly demonstrate the effectiveness of the proposed shape and motion estimation method from just one distorted OCT volume obtained using the rosette scan trajectory.



4.5. 3D Shape and motion estimation from a single unknown OCT volume obtained using a non-raster scan trajectory

Table 4.14 – Results from a few motion estimation runs from a single distorted OCT volume (blue points - motion-free volume, red points - motion-distorted volume, green points - corrected volume). The units for the linear velocities,  $V$ , are in  $mm/s$  and angular velocities,  $\Omega$ , are in  $1e-2rad/s$ .

Applied motion	Motion-free and distorted volume (top view)	Motion-free and distorted volume (3D view)	Estimated applied motion	Motion-free and corrected volume (top view)	Motion-free and corrected volume (3D view)
$V_x = 0.70$ $V_y = 1.36$ $V_z = -0.68$ $\Omega_x = -1.90$ $\Omega_y = -1.05$ $\Omega_z = -1.40$			$V_x = 0.69$ $V_y = 1.42$ $V_z = -0.66$ $\Omega_x = -1.87$ $\Omega_y = -1.04$ $\Omega_z = -1.40$		
$V_x = 0.07$ $V_y = 0.03$ $V_z = 1.88$ $\Omega_x = -1.02$ $\Omega_y = 1.17$ $\Omega_z = 0.22$			$V_x = 0.08$ $V_y = 0.05$ $V_z = 1.89$ $\Omega_x = -1.01$ $\Omega_y = 1.16$ $\Omega_z = 0.22$		
$V_x = -1.90$ $V_y = -0.27$ $V_z = -1.59$ $\Omega_x = -0.09$ $\Omega_y = 0.17$ $\Omega_z = 0.57$			$V_x = -1.88$ $V_y = -0.15$ $V_z = -1.61$ $\Omega_x = -0.03$ $\Omega_y = 0.16$ $\Omega_z = 0.57$		

Table 4.15 – Results from a few motion estimation runs from a single distorted OCT volume (blue points - motion-free volume, red points - motion-distorted volume, green points - corrected volume). The units for the linear velocities,  $V$ , are in  $mm/s$  and angular velocities,  $\Omega$ , are in  $1e-2rad/s$ .

Applied motion	Motion-free and distorted volume (top view)	Motion-free and distorted volume (3D view)	Estimated applied motion	Motion-free and corrected volume (top view)	Motion-free and corrected volume (3D view)
$V_x = 1.65$ $V_y = -1.52$ $V_z = 1.88$ $\Omega_x = -0.91$ $\Omega_y = -0.94$ $\Omega_z = 1.34$			$V_x = 1.65$ $V_y = -1.51$ $V_z = 1.88$ $\Omega_x = -0.90$ $\Omega_y = -0.94$ $\Omega_z = 1.34$		
$V_x = 1.63$ $V_y = -1.84$ $V_z = -0.32$ $\Omega_x = -1.53$ $\Omega_y = -0.21$ $\Omega_z = -0.18$			$V_x = 1.59$ $V_y = -1.74$ $V_z = -0.32$ $\Omega_x = -1.48$ $\Omega_y = -0.19$ $\Omega_z = -0.18$		
$V_x = 1.84$ $V_y = -0.36$ $V_z = -1.79$ $\Omega_x = -0.73$ $\Omega_y = 1.70$ $\Omega_z = -0.07$			$V_x = 1.83$ $V_y = -0.41$ $V_z = -1.79$ $\Omega_x = -0.75$ $\Omega_y = 1.69$ $\Omega_z = -0.08$		

### Statistical analysis

The absolute difference between the expected and initial linear and angular velocities were calculated individually for each axis, and likewise, the discrepancies between the expected and the final optimised values were computed. These deviations were then graphically illustrated in Figure 4.25, sorted in ascending order based on the initial error magnitude.

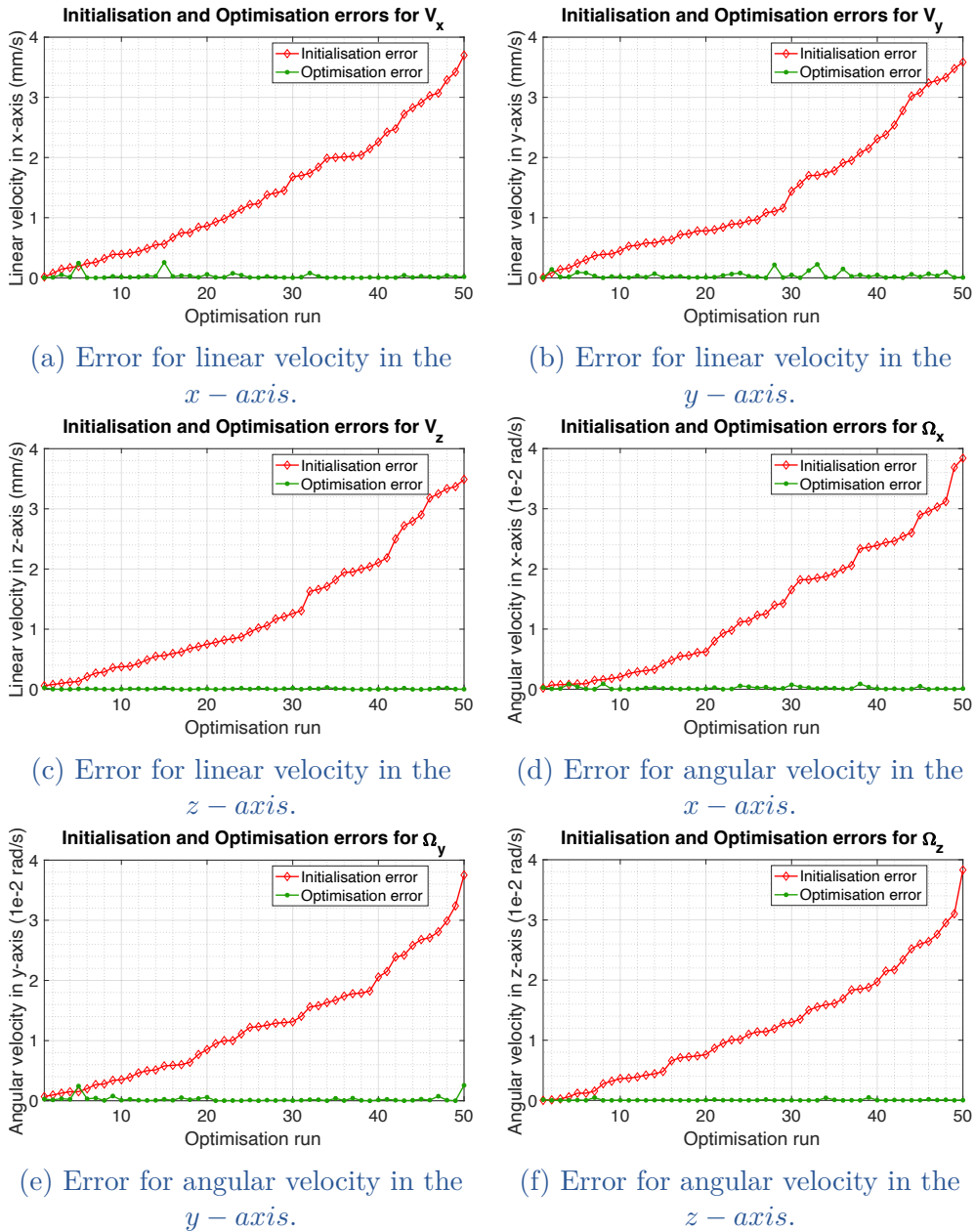


Figure 4.25 – Optimisation errors.

Figure 4.25 demonstrates a consistent final error that approaches nearly zero in all axes across all the optimisation runs, despite the initial error increasing. This observation affirms the robustness of the proposed 3D motion estimation method in SE(3) to variations in the initial guess values.

On plotting both the initial and final PointPCA similarity error value,  $\epsilon_a$  that is minimised during the optimisation process as illustrated in Figure 4.26, we observe that the similarity error after optimisation is nearly zero in all the runs. This is indicative of the accurate shape and motion estimation from one OCT volume obtained using the rosette scan trajectory and having motion artefacts.

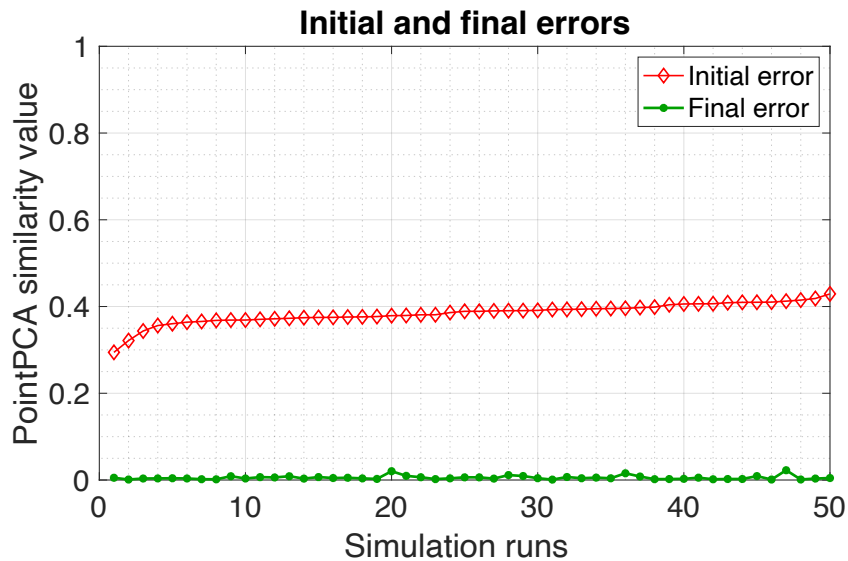


Figure 4.26 – Initial vs final (after optimisation) PointPCA error.

### 4.5.5 Experimental validation

To perform experimental validation, the experimental setup as detailed in subsection 4.3.3.a was used. Table 4.16 and 4.17 shows experimentally distorted OCT volumes obtained using the rosette scan trajectory and the corrected OCT volumes after motion estimation.

4.5. 3D Shape and motion estimation from a single unknown OCT volume obtained using a non-raster scan trajectory

Table 4.16 – Results from a few motion estimation runs from a single distorted OCT volume using experimental data (blue points - motion-free volume, red points - motion-distorted volume, green points - corrected volume). The units for the linear velocities,  $V$ , are in  $mm/s$  and angular velocities,  $\Omega$ , are in  $1e - 2rad/s$ .

Applied motion	Motion-free and distorted volume (top view)	Motion-free and distorted volume (3D view)	Estimated applied motion	Motion-free and corrected volume (top view)	Motion-free and corrected volume (3D view)
$V_x = 0.07$ $V_y = 0.03$ $V_z = 1.88$ $\Omega_x = -1.02$ $\Omega_y = 1.17$ $\Omega_z = 0.22$			$V_x = 0.14$ $V_y = -0.42$ $V_z = 1.98$ $\Omega_x = -1.12$ $\Omega_y = 1.02$ $\Omega_z = 0.11$		
$V_x = -1.90$ $V_y = -0.27$ $V_z = -1.59$ $\Omega_x = -0.09$ $\Omega_y = 0.17$ $\Omega_z = 0.57$			$V_x = -1.81$ $V_y = -0.21$ $V_z = -1.81$ $\Omega_x = -0.27$ $\Omega_y = 0.19$ $\Omega_z = -0.04$		
$V_x = 1.65$ $V_y = -1.52$ $V_z = 1.88$ $\Omega_x = -0.91$ $\Omega_y = 0.94$ $\Omega_z = 1.34$			$V_x = 1.38$ $V_y = -1.50$ $V_z = 1.49$ $\Omega_x = -0.52$ $\Omega_y = 0.90$ $\Omega_z = 1.04$		

Table 4.17 – Results from a few motion estimation runs from a single distorted OCT volume using experimental data (blue points - motion-free volume, red points - motion-distorted volume, green points - corrected volume). The units for the linear velocities,  $V$ , are in  $mm/s$  and angular velocities,  $\Omega$ , are in  $1e - 2rad/s$ .

Applied motion	Motion-free and distorted volume (top view)	Motion-free and distorted volume (3D view)	Estimated applied motion	Motion-free and corrected volume (top view)	Motion-free and corrected volume (3D view)
$V_x = 1.00$ $V_y = 1.00$ $V_z = 1.00$ $\Omega_x = 1.00$ $\Omega_y = 1.00$ $\Omega_z = 1.00$			$V_x = 0.87$ $V_y = 0.80$ $V_z = 1.13$ $\Omega_x = 0.69$ $\Omega_y = 0.88$ $\Omega_z = 0.81$		
$V_x = 2.00$ $V_y = 2.00$ $V_z = 2.00$ $\Omega_x = 2.00$ $\Omega_y = 2.00$ $\Omega_z = 2.00$			$V_x = 2.17$ $V_y = 2.05$ $V_z = 2.28$ $\Omega_x = 2.37$ $\Omega_y = 2.14$ $\Omega_z = 1.51$		
$V_x = -0.03$ $V_y = -1.23$ $V_z = 1.55$ $\Omega_x = 0.77$ $\Omega_y = 0.66$ $\Omega_z = 0.01$			$V_x = -0.27$ $V_y = -1.03$ $V_z = 1.70$ $\Omega_x = 0.57$ $\Omega_y = 0.14$ $\Omega_z = 0.14$		



### Qualitative analysis

Qualitatively analysing the results in Table 4.16 and 4.17, we observe that the corrected OCT volume closely resemble the motion-free volumes. Notably, in the experimentally motion-distorted volume (third column) and subsequently in the third and fourth rows of Table 4.16, the antennae of the bee-head is skewed from the motion-free volume. However, after motion estimation and correction, the corrected volume recovers the shape and the antennae is aligned to the motion-free OCT volume as observed in the sixth column of Table 4.16. Similarly, in Table 4.17, in the third row, third column, the bee-head appears to be significantly distorted. However, in the third row, in the sixth column of Table 4.17, the corrected volume recovers the shape.

### Quantitative analysis

The initial and final PointPCA similarity error value,  $\epsilon_a$  that is minimised during the motion estimation process for the experimentally motion-distorted volumes is plotted as illustrated in Figure 4.27. It is observed that the similarity error after optimisation is minimised for all the runs, however, the final similarity error is not zero in all instances. This discrepancy in accurate motion estimation likely arises due to;

- ✗ Noisy experimental OCT data.
- ✗ The numerical optimisation process getting stuck at a local minimum.

Nonetheless, despite these challenges, the analysis demonstrates that the 3D shape and motion estimation works fairly well.

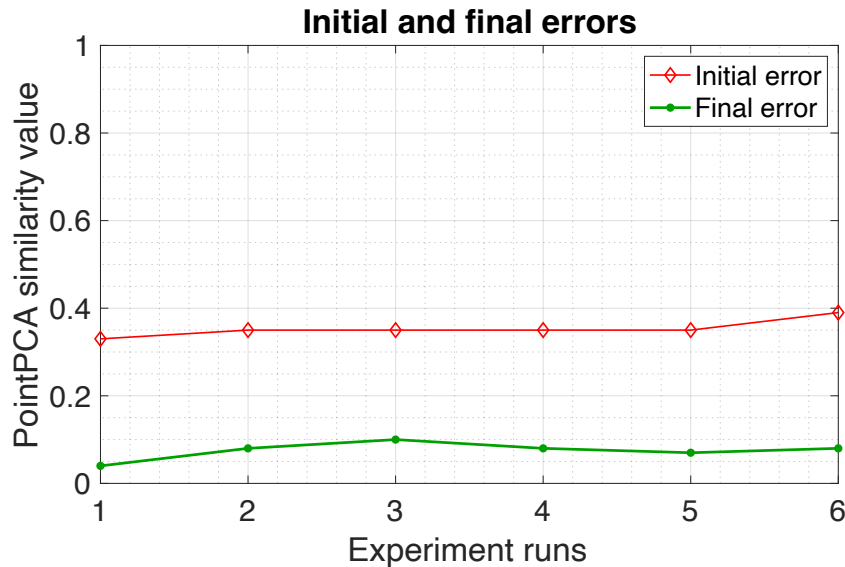


Figure 4.27 – Initial vs final (after optimisation) PointPCA error.



## 4.6 MOTION ARTEFACTS DURING ADAPTIVE SCANNING IN OCT

So far, a method to compensate for motion artefacts using a single OCT volume has been proposed and validated. However, a lingering question might remain: could the adaptive scanning method proposed in Chapter 3 reduce motion artefacts during OCT data acquisition? As detailed in subsection 4.2.1.a, one strategy to mitigate motion artefacts in OCT is through faster scanning, achievable through hardware enhancements in the OCT device. Despite the potential advantages of high-speed scanning in mitigating motion artefacts, there exists a limit to how fast the scanning frequency can be improved due to a potential loss in sensitivity [Klein 12]. This limitation arises from the finite number of photons that can be collected per unit of time; doubling the data acquisition speed, for instance, would result in halving the number of photons collected per A-scan. An interesting alternative for achieving faster scans without modifying the hardware, especially in medical applications such as tumour delineation, is through adaptive scanning, as expounded in Chapter 3. The investigation revealed a significant time gain, (a factor of 81%), by selectively scanning pertinent data within the field of view. This implies that, through adaptive scanning, the data acquisition rate could be increased, albeit through a software approach. Such an increase in acquisition rate would potentially result in fewer artefacts when the object being scanned is in motion. Although investigating the impact of adaptive scanning on motion artefacts could be highly valuable, technical constraints, as discussed in Chapter 3, subsection 3.4.2.a, hindered a comprehensive exploration in this study.

## 4.7 CONCLUSION

In this chapter, a novel method to exploit motion artefacts in OCT volumes so as to estimate the 3D motion (linear and angular velocity) in  $SE(3)$  that caused the motion artefacts has been presented. The proposed method addresses distortions within 3D OCT volumes by estimating the object motion across all three dimensions and employing this estimation to compensate for motion artefacts throughout the volume. This marks a significant advancement over existing techniques, which are primarily limited to 2D OCT images and primarily applied in ophthalmology. In addition, this chapter introduces an innovative shape and motion estimation approach based on a single OCT volume and without prior knowledge of the shape. The OCT volume is acquired using the rosette non-raster scan trajectory. This represents a novel strategy that departs from the conventional method of compensating for OCT volume motion artefacts, which would typically rely on two sequential OCT volumes. By eliminating the need for consecutive volumes, this approach reduces data requirements and consequently, computation costs. The method feasibility has been demonstrated and validated. These advancements

open up new research avenues in motion artefact compensation within OCT imaging and offers a valuable tool for clinical diagnosis and monitoring. In this research objective, for the case of 3D shape and motion estimation from one OCT volume, only two sub-volumes were used. However, depending on the design of the rosette scan trajectory, more than two sub-volumes could be extracted. Incorporating these extra sub-volumes into the existing methodology could improve the accuracy in estimating the motion (consequently motion compensation), especially in scenarios involving non-constant velocity in real-world situations. Finally, it would be worthwhile to investigate the mitigation of motion artefacts during adaptive scanning in OCT.



# General conclusions and perspectives

## GENERAL CONCLUSION

This research has focused on enhancing 3-dimensional Optical Coherence Tomography (OCT) data acquisition by incorporating strategies inspired by mechatronics, computer vision and robotics. Over the past three decades, OCT has played a critical role in the medical field, providing high-resolution images and volumes that reveal micro-structural information. In oncology applications, OCT has been particularly valuable for the early detection of malignant tumours and optical biopsy. Early cancer detection significantly improves patient survival rates, and optical biopsy mitigates some of the risks associated with physical biopsy procedures. Nevertheless, the sequential and mechanical nature of OCT scanning poses challenges, particularly in the time taken to acquire volumetric data for large fields of view. To enhance the data acquisition rate, the mechanical scan frequency can be increased through hardware approaches or the data processing can be improved through numerical techniques such as compressed sensing. However, there's a delicate balance, as faster scanning may compromise data quality in terms of sensitivity and resolution. Conversely, slower scanning ensures high sensitivity and resolution but extends the time required. Additionally, the mechanical scan introduces a sequential acquisition mode similar to rolling shutter in conventional cameras, leading to geometric artefacts due to the relative motion between the imaged object and the OCT probe.

To address these challenges, the primary objectives of this thesis were: i) propose acquisition of OCT data using non-raster trajectories, along with a set of criteria to assess the scan trajectories and the resulting volumetric data, ii) propose an adaptive strategy in OCT data acquisition, wherein data is selectively acquired in informative regions of the field of view, optimising the scanning process and potentially reducing overall acquisition time, and iii) propose a methodology for estimating motion from geometrically motion-distorted OCT volumes, particularly addressing the challenge of motion compensation from only one OCT volume without prior knowledge of its shape. The following paragraphs provide a brief description of the main results along with a summary of their conclusions.

In Chapter 2 of this thesis, it was proposed to acquire OCT data using non-raster trajectories (constant angular velocity spiral, constant linear velocity spiral, Lissajous, and rosette) instead of the conventional raster trajectory. A set of criteria were then proposed to assess both the scan trajectories and the OCT volumes acquired. The set of novel criteria includes, a bio-inspired exploitation/exploration criterion, a smoothness criterion, and a fast preview criterion, in addition to conventional criteria such as time and quality (expressed as volume similarity rather

than slice-by-slice image quality). Experimental results demonstrated that the non-raster trajectories were almost twice as fast as the raster trajectory without a significant loss in quality. To visualise the performance of the scan trajectories at a glance, a radar visualisation diagram was employed. This radar diagram provides flexibility for a system designer or non-expert OCT user to select a scan trajectory based on their priorities. Comparing the selected non-raster trajectories against the proposed criteria revealed that the rosette trajectory exhibited the best overall performance.

In Chapter 3 of this thesis, it was proposed to acquire OCT data selectively in informative regions of the imaged field of view, especially during tumour diagnosis or resection. To implement this adaptive strategy, OCT data is initially acquired at a few scan positions. This acquired data (set of A-scans) is then analysed using the standard deviation statistical measure to determine whether a particular A-scan was acquired in a tumorous or healthy region. The k-means clustering algorithm, based on the standard deviation, is then employed to discriminate between healthy and tumour regions. Following this analysis, a section of the tumour boundary is delineated. From these tumour boundary positions, the next scan position is then predicted using the Frenet-Serret frame formalism. This iterative process continues until the entire tumour boundary is well delineated, which would potentially facilitate a diagnosis by medical professionals. By implementing an adaptive strategy, less but useful data is acquired, consequently leading to a reduction in the overall acquisition time.

In Chapter 4 of this thesis, the focus was on exploitation of motion artefacts in OCT. Due to the sequential one-dimensional nature of OCT data acquisition, relative motion between the imaged object and the probe introduces geometric distortions to the OCT volume. A methodology inspired by computer vision and robotics is developed to analyse two consecutively acquired volumes to estimate the 3D motion in  $SE(3)$  that caused the artefacts. After validating this methodology, it is further enhanced and improved to estimate the motion that caused geometric artefacts from only one OCT volume acquired using the rosette scan trajectory (no prior knowledge of the shape). The estimated motion from the distorted volumes is then used in a correction process to obtain motion-free volumes.

In summary, this research work proposes strategies that offer potential solutions to enhance the quality, speed and efficiency of OCT scanning, ultimately improving its applicability in medical settings. The thesis contributes to the ongoing efforts to advance imaging technologies and addresses the challenges associated with obtaining high-quality OCT volumetric data in a timely manner.

## PERSPECTIVES

Certainly, the proposed strategies in this thesis open up several promising lines of research for further exploration. Here are some potential avenues:

### Visual servoing based on non-raster trajectories

The integration of OCT with visual servoing in carrying out robot-assisted optical biopsies during medical diagnosis is a valuable application. Visual servoing using OCT becomes particularly useful when the doctor wants to monitor the progression (shape, texture, size) of treatment of a tumour or abnormality in the body at the same tissue location, but at different time periods. While Ourak *et al.* [Ourak 16] used B-scan images from the OCT device to perform visual servoing, Dahroug *et al.* [Dahroug 20] improved further the technique by using C-scans (volumetric OCT data) as an input signal to the visual servoing controller. Dahroug *et al.* utilised principal component analysis (PCA) for extracting descriptive features from OCT volumes. However, the time-consuming nature of acquiring full OCT volumes at each iteration step poses a challenge. The non-raster trajectories introduced in this research offer a viable solution to expedite the process. By employing these trajectories, the amount of data acquired is reduced, as well as the acquisition time, without a significant loss in OCT volume quality. This reduction in acquisition time is crucial, since it would reduce the time it takes to perform visual servoing. Furthermore, as discussed in Chapter 2, employing non-raster trajectories that are self-repeating like the Lissajous and rosette trajectories provides a preliminary preview of the scanned object after acquiring a fraction of the data, in contrast to the conventional raster trajectory. Hence, a rolling buffer strategy could be implemented when these non-raster trajectories are used, to parallelise the acquisition, processing, display of data and control.

### Optimal design for the scanning mechanism in OCT

It has been demonstrated in this thesis that data acquisition using non-raster trajectories is faster than the raster trajectory for a given amount of A-scans without a significant loss in quality. The rosette trajectory has been identified as globally optimal among the assessed non-raster trajectories. Further acceleration of data acquisition using rosette-like trajectories could be accomplished through optimal mechanical designs of the scanner, diverging from conventional galvanometric scanners. Rather than employing separate galvanometric scanners for the  $x$ -axis and  $y$ -axis, an optimal design for a scanner with a single actuator that traces the rosette path could be developed. Such an optimised design would likely consume less energy, as only one actuator would be needed instead of two.

### Template based adaptive scanning

In the proposed adaptive scanning approach so far, the focus has been on delineating a single tumour. However, what if there are several tumours in the field of view? As an enhancement to the adaptive scanning approach already presented, a template based adaptive scanning could be implemented. Here, the surgeon delineates the lesion boundary, and a modulated Lissajous trajectory is designed with the  $x, y$  positions of the surgeon's delineated boundary as the weights. These weights are used to modify the Lissajous trajectory such that most of the scan

positions are in the regions of interest in the field of view, as illustrated in Figure 5.1 (the numbers in bold in the figure detail the number of scan positions in the redish desired region). From the collected OCT data, probable regions where the lesion boundary passes are then detected. These regions are then used to update the weights for the modulated Lissajous trajectory for the next frame. Nonetheless, the feasibility of implementing this proposed method would rely on the permissible field of view of the OCT device and the dimensions of the lesions/tumours. If only a single lesion/tumour is discernible in the field of view due to its size, this method may not be advantageous, and the approach proposed in Chapter 3 would be more applicable.

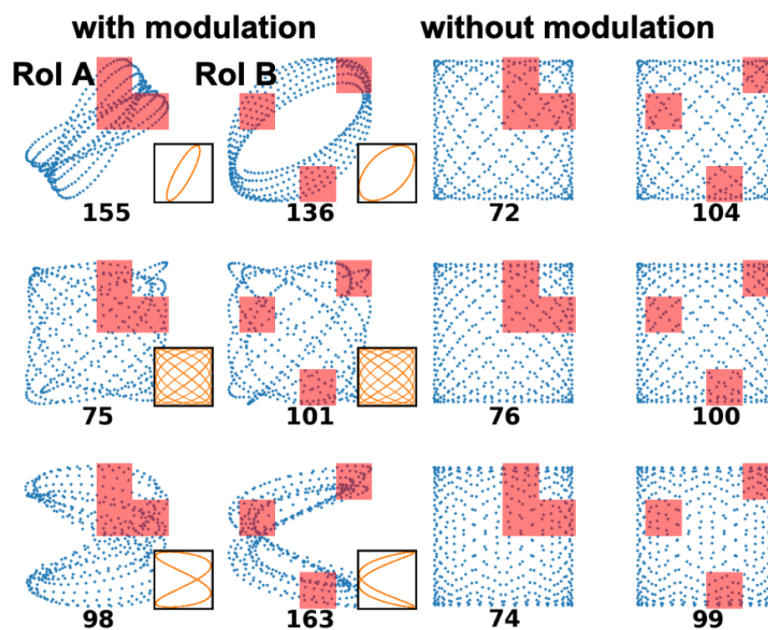


Figure 5.1 – Examples of modulated Lissajous scan trajectories [Sun 21].

### 3D adaptive scanning

In this thesis, for adaptive scanning in optical coherence tomography, the consideration was limited to 2D tumour boundaries in the  $x - y$  plane. However, there is potential for further improvement by extending the methodology to 3D. This enhancement would involve implementing the adaptive scanning strategy to detect and predict the next scan positions simultaneously in two planes; the  $x - y$  plane and the  $x - z$  plane. This would necessitate a sliding computation of the standard deviation in an acquired A-scan to detect healthy/tumorous transitions depth-wise. Additionally, the introduction of machine learning approaches could enhance the lesion boundary detection step in adaptive scanning, especially in tissues where tumour and healthy regions are intricately interconnected.



### **Further exploitation of the rosette trajectory in 3D shape and motion estimation from a single OCT volume**

To further refine the 3D shape and motion estimation from a single OCT volume, it could be valuable to delve deeper into the peculiarities of the rosette scan trajectory. The number of distinct intersections in a particular rosette pattern could potentially yield more than two volumes. By extracting these additional sub-volumes, and integrating the use of more than two sub-volumes to the existing proposed methodology, the implementation has the potential to relax certain assumptions, such as constant velocity.

To enhance the accuracy in real-world implementations, the complexity of the proposed 3D shape and motion estimation model could be increased. This would involve incorporating intrinsic parameters of both the parallel robot and the OCT into the model. For example, factors like the apodisation time of the OCT and software memory allocation time before scanning, could be introduced to the model.

### **Modification of the proposed strategies to enable scanning in the lumen**

The experimental configuration for this thesis featured the OCT in a table-top position. Nevertheless, the strategies proposed in this research could potentially find implementation in a miniaturised OCT probe tailored for endoscopic scanning within luminal structures. Achieving this transition necessitates a modification of the proposed strategies to align with the specific requirements and challenges associated with scanning tubular hollow structures.



---

---

# Appendix A

## The Frenet-Serret frame

---

<b>A.1</b>	<b>Description of the Frenet-Serret frame.....</b>	<b>162</b>
<b>A.2</b>	<b>Predicting an <math>(n + 1)</math> curve position using the Frenet-Serret frame .....</b>	<b>163</b>

## A.1 DESCRIPTION OF THE FRENET-SERRET FRAME

The Frenet-Serret frame (also referred to as TNB frame) is a mathematical framework named after the French mathematicians Jean Frenet and Joseph Serret, who developed it independently in the 19th century. At each point on a differentiable curve, the Frenet-Serret frame consists of three mutually orthogonal unit vectors: the tangent vector  $\mathbf{t}$ , the normal vector  $\mathbf{n}$ , and the binormal vector  $\mathbf{b}$  as shown in Figure A.1<sup>1</sup>. The tangent vector  $\mathbf{t}$  points in the direction of the curve, the normal vector  $\mathbf{n}$  points in the direction of the curve's curvature, and the binormal vector  $\mathbf{b}$  is perpendicular to both  $\mathbf{t}$  and  $\mathbf{n}$ , completing the orthogonal frame.

The Frenet-Serret frame can be used to describe the motion of a rigid body along a curve in three-dimensional space (model the shape of a curve i.e., locus of all points). The tangent vector  $\mathbf{t}$  represents the direction and speed of motion along the curve. The normal vector  $\mathbf{n}$  represents the curvature of the curve, or the rate at which the direction of motion is changing. The binormal vector  $\mathbf{b}$  introduces a second curvature; torsion of the curve. To model how a point moves along the curve, the set of differential equations that describe how the  $\mathbf{t}$ ,  $\mathbf{n}$ , and  $\mathbf{b}$  vectors change as the curve moves along are used. These equations are known as the Frenet-Serret equations and can be derived using calculus. Knowing the Frenet-Serret equations, the motion of the curve can be predicted in three-dimensional space. For example, given the initial position and orientation of a curve, one can use the Frenet-Serret equations to predict the curve position and orientation at a future time. This can be useful in a variety of applications, such as computer graphics, robotics, and physics simulations.

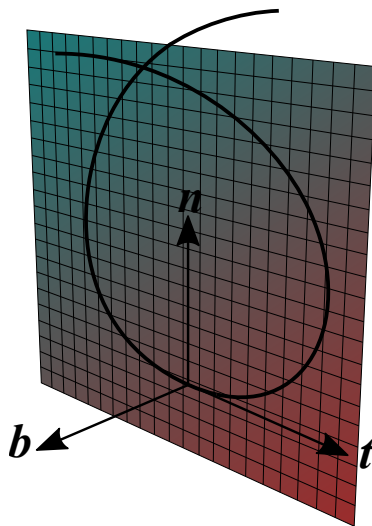


Figure A.1 – A space curve; the vectors  $\mathbf{t}$ ,  $\mathbf{n}$ , and  $\mathbf{b}$ ; and the osculating plane spanned by  $\mathbf{t}$  and  $\mathbf{n}$ .

1. ©Popletibus / <https://commons.wikimedia.org/wiki/File:Frenet.svg> / CC BY-SA 4.0

## A.2 PREDICTING AN $(n+1)$ CURVE POSITION USING THE FRENET-SERRET FRAME

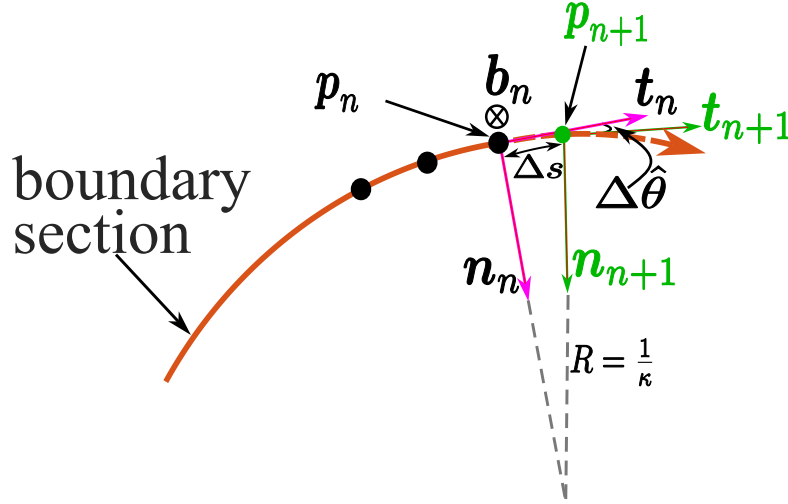


Figure A.2 – Section of a scan trajectory.

We would like to estimate  $\mathbf{p}_{n+1}, \mathbf{t}_{n+1}, \mathbf{n}_{n+1}$ . Knowing the parameters to the Frenet-Serret frame equations and assuming a slowly changing curvature, the next scan position can be predicted.

Let  $\alpha : I \rightarrow \mathbb{R}^3$  be a curve parametrised by a variable arclength  $s \in I \subset \mathbb{R}$  such that  $\alpha \in C^3(I)$ . A point  $\mathbf{p}$  on  $\alpha$  crossed at time  $t$  thus lies at arclength  $s$ . It is of the form  $\mathbf{p} = \alpha(s)$ <sup>2</sup>. Sampling at a period  $\Delta s = \text{constant}$ , one obtains a sequence  $\{\mathbf{p}_n = \alpha(s_n), s_n = n\Delta s, n \in 1 : N\}$ . In any point,  $\mathbf{p}_n$  of that sequence, one can compute the tangent  $\mathbf{t}_n = \mathbf{t}(s)$  to the continuous curve  $\alpha$  by:

$$\mathbf{t}_n = \frac{\frac{d\mathbf{p}_n}{ds}}{\left\| \frac{d\mathbf{p}_n}{ds} \right\|} \quad (\text{A.1})$$

Note that  $\mathbf{t}_n$  is a unique unit vector unless  $\left\| \frac{d\mathbf{p}_n}{ds} \right\| = 0$ , which would mean that the curve  $\alpha$  is restricted to a point. In that case,  $\mathbf{t}_n$  is not uniquely defined and  $s \in \{0\}$ . By taking the derivative of the tangent, one defines the normal to the curve  $\mathbf{n}_n = \mathbf{n}(s)$  as:

$$\mathbf{n}_n = \frac{\frac{d\mathbf{t}_n}{ds}}{\left\| \frac{d\mathbf{t}_n}{ds} \right\|} \quad (\text{A.2})$$

which is orthogonal to  $\mathbf{t}_n$ , because  $\mathbf{t}_n$  is a unit vector. Also note that, when  $\left\| \frac{d\mathbf{t}_n}{ds} \right\| = 0$ , it means that  $\mathbf{p}_n$  is an inflexion point or that  $\alpha$  is locally straight in  $\mathbf{p}_n$ . In that case,  $\mathbf{n}_n$  isn't uniquely defined but still exists. Moreover, there is a

---

2. The relation between time  $t$  and arclength  $s$  depends on the velocity  $v$ . However, the following analysis is independent from  $v$ , provided that  $v \neq 0$ .

unique unit vector  $\mathbf{b}_n = \mathbf{b}(s)$  orthogonal to  $\mathbf{t}_n$  and  $\mathbf{n}_n$  ( $\mathbf{b}_n = \mathbf{t}_n \wedge \mathbf{n}_n$ ). Away from the singularities  $\|\frac{d\mathbf{p}_n}{ds}\| = 0$  and  $\|\frac{d\mathbf{t}_n}{ds}\| = 0$ , the Frenet-Serret differential equations in 3D are;

$$\frac{d\mathbf{p}_n}{ds} = \mathbf{t}_n \quad (\text{A.3a})$$

$$\frac{d\mathbf{t}_n}{ds} = \kappa\mathbf{n}_n \quad (\text{A.3b})$$

$$\frac{d\mathbf{n}_n}{ds} = -\kappa\mathbf{t}_n + \tau\mathbf{b}_n \quad (\text{A.3c})$$

$$\frac{d\mathbf{b}_n}{ds} = -\tau\mathbf{n}_n \quad (\text{A.3d})$$

where,

- ❖  $s$  - arc length variable
- ❖  $\mathbf{p}_n$  - position vector of the boundary in a fixed frame
- ❖  $\mathbf{t}_n$  - unit tangent vector with respect to  $\mathbf{p}_n$  on the boundary
- ❖  $\mathbf{n}_n$  - unit normal vector with respect to  $\mathbf{p}_n$  on the boundary
- ❖  $\mathbf{b}_n$  - unit binormal vector with respect to  $\mathbf{p}_n$  on the boundary
- ❖  $\kappa(s)$  - in-plane curvature of the curve at a position on the boundary
- ❖  $\tau(s)$  - out-of-plane torsion of the curve at a position on the boundary

In 2D, the binormal vector  $\mathbf{b}_n$  is constant. Therefore:

$$\frac{d\mathbf{b}_n}{ds} = 0 \quad (\text{A.4})$$

which implies that,

$$\tau = 0 \quad (\text{A.5})$$

Therefore, in 2D, the Frenet-Serret differential equations become:

$$\frac{d\mathbf{p}_n}{ds} = \mathbf{t}_n \quad (\text{A.6a})$$

$$\frac{d\mathbf{t}_n}{ds} = \kappa\mathbf{n}_n \quad (\text{A.6b})$$

$$\frac{d\mathbf{n}_n}{ds} = -\kappa\mathbf{t}_n \quad (\text{A.6c})$$

This system of differential equations can be solved to find  $\mathbf{p}_{n+1}$ ,  $\mathbf{t}_{n+1}$ ,  $\mathbf{n}_{n+1}$  from  $\mathbf{p}_n$ ,  $\mathbf{t}_n$ ,  $\mathbf{n}_n$ ,  $\kappa$  and  $\Delta s$  (the sampling period of  $s$ ). First, one solves for  $\mathbf{t}_{n+1}$ . The constraint on the norm of the unit tangent vector:

$$\|\mathbf{t}_n\| = 1 \quad (\text{A.7})$$

implies that,

$$\frac{d\mathbf{t}_n}{ds} \perp \mathbf{t}_n \quad (\text{A.8})$$

Therefore, there exists some instantaneous rotation vector,  $\Upsilon$  such that:

$$\frac{d\mathbf{t}_n}{ds} = \Upsilon \wedge \mathbf{t}_n \quad (\text{A.9})$$

where  $\Upsilon$  decomposes into its axis,  $\boldsymbol{\xi}$  and rotation velocity,  $\omega$ . Since  $\mathbf{t}_n$  is restricted to move in the boundary plane, the axis  $\boldsymbol{\xi}$  is constant and perpendicular to the plane. Thus  $\boldsymbol{\xi} = \mathbf{b}_n$ , and:

$$\Upsilon = \omega \boldsymbol{\xi} \quad (\text{A.10})$$

which implies that:

$$\frac{d\mathbf{t}_n}{ds} = \omega \boldsymbol{\xi} \wedge \mathbf{t}_n = \omega \mathbf{n}_n \quad (\text{A.11})$$

Using equation A.3b, we can identify that:

$$\kappa = \omega \quad (\text{A.12})$$

which implies that,

$$\frac{d\mathbf{t}_n}{ds} = \kappa [\boldsymbol{\xi}] \wedge \mathbf{t}_n \quad (\text{A.13})$$

whereby, equation A.13 is a 1<sup>st</sup> order differential equation for  $\mathbf{t}_n \in \mathbb{R}^3$ . Integrating between  $s_n$  and  $s_n + \Delta s$  on the unit sphere  $\|\mathbf{t}_n\| = 1$ , [Solà 18, Deray 20] yields for  $\Delta s$ , the finite step from  $\mathbf{p}_n$  to  $\mathbf{p}_{n+1}$  along the curve, yet sufficiently small for  $\kappa$  to be assumed constant:

$$\mathbf{t}_{n+1} = \text{expm}([\boldsymbol{\xi}] \wedge \kappa \Delta s) \mathbf{t}_n \quad (\text{A.14a})$$

$$\boxed{\mathbf{t}_{n+1} = \text{Rot}(\boldsymbol{\xi}, \kappa \Delta s) \mathbf{t}_n} \quad (\text{A.14b})$$

Similarly, one can solve for  $\mathbf{n}_{n+1}$ :

$$\boxed{\mathbf{n}_{n+1} = \text{Rot}(\boldsymbol{\xi}, \kappa \Delta s) \mathbf{n}_n} \quad (\text{A.15})$$

To compute  $\mathbf{p}_{n+1}$ , one must integrate equation A.3a between  $s_n$  and  $s_n + \Delta s$ :

$$\mathbf{p}_{n+1} = \mathbf{p}_n + \int_{s_n}^{s_n + \Delta s} \frac{d\mathbf{p}(s)}{ds} ds \quad (\text{A.16a})$$

since  $\frac{d\mathbf{p}(s)}{ds} = \mathbf{t}$  one gets:

$$\mathbf{p}_{n+1} = \mathbf{p}_n + \int_{s_n}^{s_n + \Delta s} \mathbf{t} ds \quad (\text{A.16b})$$

When  $\kappa \neq 0$ , solving the integral with the change of variable  $u = s_n + s$  and  $du = ds$ :

$$\int_{s_n}^{s_n + \Delta s} \mathbf{t}(u) du = \int_0^{\Delta s} \mathbf{t}(s_n + s) ds \quad (\text{A.17a})$$



From equation A.14a,

$$\int_0^{\Delta s} \mathbf{t}(s_n + s) ds = \left( \int_0^{\Delta s} \expm([\boldsymbol{\xi}]_{\wedge} \kappa s) ds \right) \mathbf{t}_n \quad (\text{A.17b})$$

Developing equation A.17b using the exponential matrix series yields,

$$\int_0^{\Delta s} \mathbf{t}(s_n + s) ds = \left( \int_0^{\Delta s} \sum_{n=0}^{+\infty} \frac{\kappa^n s^n [\boldsymbol{\xi}]_{\wedge}^n}{n!} ds \right) \mathbf{t}_n \quad (\text{A.17c})$$

Swapping the integral and sum in equation A.17c results in:

$$\int_0^{\Delta s} \mathbf{t}(s_n + s) ds = \left( \sum_{n=0}^{+\infty} \frac{\kappa^n}{n!} [\boldsymbol{\xi}]_{\wedge}^n \int_0^{\Delta s} s^n ds \right) \mathbf{t}_n \quad (\text{A.17d})$$

Now, the integral in equation A.17d is easy to solve which yields:

$$\int_0^{\Delta s} \mathbf{t}(s_n + s) ds = \left( \sum_{n=0}^{+\infty} \frac{\kappa^n}{n!} [\boldsymbol{\xi}]_{\wedge}^n \frac{(\Delta s)^{n+1}}{n+1} \right) \mathbf{t}_n \quad (\text{A.17e})$$

Re-ordering equation A.17e results in:

$$\int_0^{\Delta s} \mathbf{t}(s_n + s) ds = \left( \frac{1}{\kappa} \sum_{n=0}^{+\infty} \frac{\kappa^{n+1}}{(n+1)!} (\Delta s)^{n+1} [\boldsymbol{\xi}]_{\wedge}^n \right) \mathbf{t}_n \quad (\text{A.17f})$$

Moreover,  $[\boldsymbol{\xi}]_{\wedge}^0 = I$ , and for all  $n > 0$ :

$$[\boldsymbol{\xi}]_{\wedge}^{2n} = (-1)^{n+1} [\boldsymbol{\xi}]_{\wedge}^2 \quad \text{and,} \quad (\text{A.18a})$$

$$[\boldsymbol{\xi}]_{\wedge}^{2n+1} = (-1)^n [\boldsymbol{\xi}]_{\wedge} \quad (\text{A.18b})$$

Thereby, for all  $n > 0$ :

$$[\boldsymbol{\xi}]_{\wedge}^{2n+1} \mathbf{t}_n = [\boldsymbol{\xi}]_{\wedge} \mathbf{t}_n = (-1)^n \mathbf{n}_n \quad \text{and,} \quad (\text{A.19a})$$

$$[\boldsymbol{\xi}]_{\wedge}^{2n} \mathbf{t}_n = [\boldsymbol{\xi}]_{\wedge}^2 \mathbf{t}_n = (-1)^{n+1} \mathbf{t}_n \quad (\text{A.19b})$$

Hence, expand equation A.17f and factorise along  $\mathbf{t}_n$  and  $\mathbf{n}_n$  to get:

$$\int_{s_n}^{s_n + \Delta s} \mathbf{t} ds = \frac{1}{\kappa} \left( \kappa \Delta s - \frac{\kappa^3 \Delta s^3}{3!} + \frac{\kappa^5 \Delta s^5}{5!} + \dots \right) \mathbf{t}_n + \frac{1}{\kappa} \left( \frac{\kappa^2 \Delta s^2}{2!} - \frac{\kappa^4 \Delta s^4}{4!} + \frac{\kappa^6 \Delta s^6}{6!} + \dots \right) \mathbf{n}_n \quad (\text{A.20})$$

where we recognise the Taylor series expansion of  $\sin(\kappa \Delta s)$  and  $(1 - \cos(\kappa \Delta s))$ . Equation A.16b and A.20 can thus be simplified into:

$$\mathbf{p}_{n+1} = \mathbf{p}_n + \frac{\sin(\kappa\Delta s)}{\kappa}\mathbf{t}_n + \frac{(1 - \cos(\kappa\Delta s))}{\kappa}\mathbf{n}_n \quad (\text{A.21})$$

When  $\kappa = 0$ , the computation of  $\mathbf{p}_{n+1}$  is straightforward:

$$\int_0^{\Delta s} \text{Rot}(\boldsymbol{\xi}, \kappa\Delta s)\mathbf{t}_n ds = \int_0^{\Delta s} \mathbf{t}_n ds = \Delta s \mathbf{t}_n \quad (\text{A.22})$$

Thus  $\mathbf{p}_{n+1} = \mathbf{p}_n + \Delta s \mathbf{t}_n$  when  $\kappa = 0$ . This is consistent with the limit of equation A.21 when  $\kappa \rightarrow 0$ .

Finally, the solution of the Frenet-Serret equations for  $\mathbf{p}_{n+1}$  is:

$$\mathbf{p}_{n+1} = \mathbf{p}_n + \begin{cases} \frac{1}{\kappa} (\sin(\kappa\Delta s)\mathbf{t}_n + (1 - \cos(\kappa\Delta s))\mathbf{n}_n) & , \forall \kappa \neq 0 \\ \Delta s \mathbf{t}_n & , \kappa = 0 \end{cases} \quad (\text{A.23})$$



---

---

# Appendix B

## Some pseudocodes to mentioned algorithms in the thesis

---

<b>B.1</b>	<b>Tumour boundary estimation .....</b>	<b>170</b>
<b>B.2</b>	<b>Shape and motion estimation from a single OCT volume obtained using the rosette scan trajectory .....</b>	<b>171</b>

## B.1 TUMOUR BOUNDARY ESTIMATION

```
1 function [tumour_boundary] = ...
   TumourBoundaryEstimation(OCT_scan_positions, OCT_scan_data)
2 %TumourBoundaryEstimation Pseudocode for Tumour Boundary ...
   Estimation from OCT scan positions styled using MATLAB.
3 %   Input:
4 %   OCT_scan_positions: Matrix containing the x-y ...
   coordinates of scan positions.
5 %   OCT_scan_data: Matrix containing OCT A-scan intensity data.
6 %   Output:
7 %   tumour_boundary: spline curve representing the estimated ...
   boundary that separates healthy and tumour regions
8
9   % Load the OCT scan positions data
10  load ('OCT_scan_positions.mat', 'OCT_scan_positions');
11  load ('OCT_scan_data.mat', 'OCT_scan_data');
12  % Standard Deviation Calculation:
13  % Calculate the standard deviation values for each A-scan ...
   in OCT_scan_data.
14  standard_deviations = ...
   calculate_standard_deviations(OCT_scan_data);
15  % k-means Clustering:
16  % Perform k-means clustering on OCT_scan_positions using ...
   the standard deviation values to separate healthy and ...
   tumour regions.
17  % Assign each scan position to one of two clusters: ...
   healthy_positions or tumour_positions.
18  [healthy_positions, tumour_positions] = ...
   kmeans_clustering(OCT_scan_positions, standard_deviations);
19  % Pair Selection:
20  % For each pair of positions (P1, P2) where P1 is in ...
   healthy_positions and P2 is in tumour_positions, ...
   calculate the distance between P1 and P2.
21  % Identify and store pairs where the distance is below a ...
   certain threshold indicating proximity(close to each ...
   other from both regions).
22  position_pairs = ...
   find_close_position_pairs(healthy_positions, ...
   tumour_positions);
23  % Midpoint Calculation:
24  % Compute the midpoints of the selected pairs and store ...
   them in the array midpoints.
25  midpoints = calculate_midpoints(position_pairs);
26  % Smoothing:
27  % Apply a smoothing technique to midpoints to reduce noise ...
   and obtain smoothed_midpoints(a moving average or other ...
   technique).
28  smoothed_midpoints = smooth_midpoints(midpoints);
29  % Curve Fitting:
```

```
30 % Fit a spline curve to the smoothed midpoints, resulting ...
    in the tumour_boundary curve.
31 tumour_boundary = fit_spline(smoothed_midpoints);
32 % Output:
33 % Return tumour_boundary as the estimated boundary between ...
    healthy and tumour regions.
34 plot(tumour_boundary);
35 end
```

## B.2 SHAPE AND MOTION ESTIMATION FROM A SINGLE OCT VOLUME OBTAINED USING THE ROSETTE SCAN TRAJECTORY

```
1 function [V, Omega, Pose] = ...
    ShapeMotionEstimation(OCT_distorted_volume)
2 %ShapeMotionEstimation Pseudocode for Motion estimation from ...
    one OCT volume styled using MATLAB.
3 % Input:
4 %   OCT_distorted_volume: Matrix containing OCT point cloud ...
    data.
5 % Output:
6 %   V: Estimated linear velocity
7 %   Omega: Estimated angular velocity
8 %   Pose: Estimated pose
9
10 Extract two sub-volumes from one OCT volume
11
12 Set initial guess: V, Omega and Pose
13
14 while (1)
15
16     Perform correction on the sub-volumes using V, Omega ...
        and Pose
17
18     Compute similarity error between the two corrected ...
        sub-volumes using PCA
19
20     if similarity_error < threshold || max_iterations_exceeded
21         break
22     end
23
24     Update V, Omega and Pose using genetic algorithm
25 end
26 % Output: Return V, Omega and Pose
27 end
```





---

---

Appendix C  
PointPCA similarity error computation

---

## POINTPCA ARCHITECTURE

To assess the similarity of the OCT point cloud volumes acquired using the scan trajectories to the ground truth, the objective quality metric PointPCA proposed by Alexiou *et al.* was used. This appendix section provides detailed information about the method from [Alexiou 21]. PointPCA is a full-reference objective quality metric that compares the local shape and appearance between a point cloud under evaluation and its reference. Figure C.1 illustrates the PointPCA architecture.

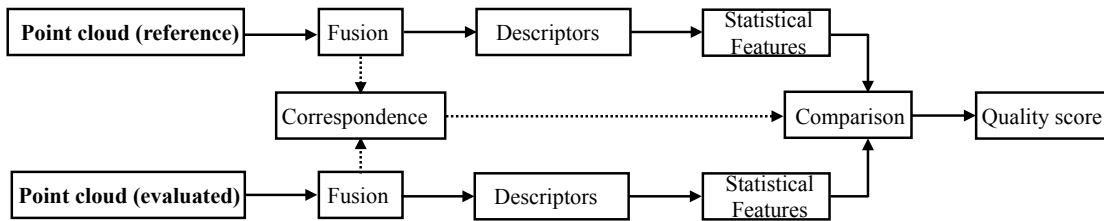


Figure C.1 – PointPCA architecture [Alexiou 21].

The total quality score between two point clouds is computed as a linear combination of individual quality predictions. A set of geometric and textural descriptors are defined per point in order to reflect local properties of a point cloud with respect to its topology and appearance respectively. The PointPCA architecture is composed into 5 stages:

- ✓ Fusion
- ✓ Correspondence
- ✓ Descriptors
- ✓ Statistical features
- ✓ Comparison

In the PointPCA architecture process, both the reference and the point cloud under evaluation pass through multiple processing stages to compute a quality score. During the fusion step, duplicated points in the cloud are removed, and the corresponding point cloud intensity values averaged. Subsequently, a correspondence between the two point clouds is established using the nearest neighbour algorithm. Specifically, for every point in the reference point cloud, a matching point in the evaluation point cloud is identified as its nearest neighbour in terms of Euclidean distance and registered as its correspondence.

### Descriptors

Geometric descriptors are then defined for each point, based on principal component analysis (PCA), capturing local shape properties with respect to its topology. Textural descriptors (luminance measurement) are also computed based on the intensity values, capturing appearance properties. The geometric  $\mathbf{d}^g \in \mathbb{R}^{1 \times 15}$  and textural  $\mathbf{d}^t \in \mathbb{R}^{1 \times 1}$  descriptors are as defined and described in Table C.1.

Table C.1 – Definition of geometric and textural descriptors.

Descriptor	Definition	Description
Eigenvalues	$d_v^g = \lambda_v$ , with $v \in \{1, 2, 3\}$	Denotes the individual eigen values, i.e., dispersion magnitudes for the points distribution across the principal axis.
Sum of eigenvalues	$d_4^g = \sum_v \lambda_v$	Aggregated sum of the eigen values.
Linearity	$d_5^g = (\lambda_1 - \lambda_2)/\lambda_1$	Reveals behaviours of a neighbourhood's point arrangement capturing the dimensionality of the local surface.
Planarity	$d_6^g = (\lambda_2 - \lambda_3)/\lambda_1$	
Sphericity	$d_7^g = \lambda_3/\lambda_1$	
Anisotropy	$d_8^g = (\lambda_1 - \lambda_3)/\lambda_1$	Indicates the shape of the local point distribution and focuses on the data variation across the 1 <sup>st</sup> and 3 <sup>rd</sup> principal directions.
Omnivariance	$d_9^g = \sqrt[3]{\lambda_1 \cdot \lambda_2 \cdot \lambda_3}$	Provides an estimate of the spread considering all principal axes.
Eigentropy	$d_{10}^g = -\sum_v \lambda_v \cdot \ln(\lambda_v)$	Provides an estimate of the uncertainty considering all principal axes.
Surface variation	$d_{11}^g = \lambda_3 / \sum_v \lambda_v$	Provides an estimate of the variation of the underlying surface considering all principal axes.
Roughness	$d_{12}^g =  (\mathbf{p}_i - \bar{\mathbf{p}}) \cdot \mathbf{e}_3 $	Depends on the third eigenvector, $\mathbf{e}_3$ , and quantifies the projected error of the queries point from the centroid of the set, across the linearly approximated local surface.
Parallelity <sub>x</sub>	$d_{13}^g = 1 -  \mathbf{u}_x \cdot \mathbf{e}_3 $	Measures the projected error of the estimated normal vector (i.e., $\mathbf{e}_3$ ) across unit vectors parallel to the coordinate system axes where a point cloud is laying.
Parallelity <sub>y</sub>	$d_{14}^g = 1 -  \mathbf{u}_y \cdot \mathbf{e}_3 $	
Parallelity <sub>z</sub>	$d_{15}^g = 1 -  \mathbf{u}_z \cdot \mathbf{e}_3 $	
Luminance	$\mathbf{d}^t \in \mathbb{R}^{1 \times 1}$	luminance of every point serves as the descriptor.

where,

- ✓  $\mathbf{p}_i = (x_i, y_i, z_i)^T$ , is a given query point.
- ✓  $\mathbf{e}_1, \mathbf{e}_2, \mathbf{e}_3$ , denotes the eigenvectors corresponding to the eigenvalues  $\lambda_1, \lambda_2, \lambda_3$  with  $\lambda_1 > \lambda_2 > \lambda_3$ . Eigenvalues and eigenvectors are employed in measurements that estimate interpretable local 3D shape properties.

- ✓  $\mathbf{u}_x = (1, 0, 0)^T$ ,  $\mathbf{u}_y = (0, 1, 0)^T$ ,  $\mathbf{u}_z = (0, 0, 1)^T$  are unit vectors across the  $x, y, z$  axes respectively.

### Statistical features

Statistical functions are then applied on geometric and textural descriptor values, which are computed per point, in order to capture inter-point relations that lie in the same neighbourhood. They include:

- ✓ Mean - computed in order to reflect a smoother estimate of the surface property, accounting for a broader region. Considering a query point  $\mathbf{p}_i$  and a set of neighbours  $\mathbf{p}_{\hat{n}} \in \hat{\mathbf{P}}_i$ , the mean is:

$$\boldsymbol{\mu}_i = \frac{1}{|\hat{\mathbf{P}}_i|} \sum_{\hat{n}=1}^{|\hat{\mathbf{P}}_i|} \mathbf{d}_{\hat{n}} \quad (\text{C.1})$$

where,  $\mathbf{d}_{\hat{n}} = [\mathbf{d}_{\hat{n}}^g, \mathbf{d}_{\hat{n}}^t] \in \mathbb{R}^{1 \times 16}$  is a row vector of concatenated geometric and textural descriptors that correspond to  $\mathbf{p}_{\hat{n}}$ .

- ✓ Standard deviation - quantifies the level of variation of a surface property in the surrounding area. It is computed by:

$$\boldsymbol{\sigma}_i = \sqrt{\frac{1}{|\hat{\mathbf{P}}_i|} \sum_{\hat{n}=1}^{|\hat{\mathbf{P}}_i|} (\mathbf{d}_{\hat{n}} - \boldsymbol{\mu}_i)^2} \quad (\text{C.2})$$

A complete statistical features vector is then composed of both terms and is annotated by:

$$\boldsymbol{\phi}_i = [\boldsymbol{\mu}_i, \boldsymbol{\sigma}_i] \in \mathbb{R}^{1 \times 32} \quad (\text{C.3})$$

### Comparison

Given a correspondence function  $c^{\mathcal{B}, \mathcal{A}}(\mathbf{b}_i) = \mathbf{a}_i$ , the  $j$ 'th statistical feature of point  $\mathbf{b}_i \in \mathcal{B}$ , namely  $\phi_{i,j}^{\mathcal{B}}$  is compared to the  $j$ 'th statistical feature of point  $\mathbf{a}_i \in \mathcal{A}$ , namely  $\phi_{i,j}^{\mathcal{A}}$ , as shown in equation C.4:

$$r_{i,j}^{\mathcal{B}, \mathcal{A}} = \frac{|\phi_{i,j}^{\mathcal{A}} - \phi_{i,j}^{\mathcal{B}}|}{\max(|\phi_{i,j}^{\mathcal{A}}|, |\phi_{i,j}^{\mathcal{B}}|) + \varepsilon} \quad (\text{C.4})$$

where,  $r_{i,j}^{\mathcal{B}, \mathcal{A}}$  indicates the relative difference that corresponds to  $\mathbf{b}_i$ ,  $1 \leq i \leq |\mathcal{B}|$ ,  $1 \leq j \leq 32$  while,  $\varepsilon$  represents a small constant to avoid undefined operations; in this case we use the machine rounding errors for floating point numbers. For every statistical feature  $j$ , a corresponding predictor is exported after pooling across all points of  $\mathcal{B}$  as shown in equation C.5:

$$s_j^{\mathcal{B}, \mathcal{A}} = \frac{1}{|\mathcal{B}|} \sum_{i=1}^{|\mathcal{B}|} r_{i,j}^{\mathcal{B}, \mathcal{A}} \quad (\text{C.5})$$

---

The same computations are repeated after setting the point cloud  $\mathcal{B}$  as the reference and computing a correspondence function  $c^{\mathcal{A},\mathcal{B}}(\mathbf{a}_k) = \mathbf{b}_k$ . In an analogous way, for every statistical feature  $j$ , a corresponding predictor  $s_j^{\mathcal{A},\mathcal{B}}$  is derived, and a symmetric quantity is obtained after a max operation:

$$s_j = \max \left( s_j^{\mathcal{B},\mathcal{A}}, s_j^{\mathcal{A},\mathcal{B}} \right) \quad (\text{C.6})$$

### Quality score

Each predictor  $s_j$  essentially provides a quality rating based on the  $j$ 'th statistical feature. A total quality score can be obtained as a linear combination of domain-specific, or across domain predictors:

$$q^\alpha = \frac{\sum_{m=1}^{|\mathcal{S}^\alpha|} w_m \cdot s_m^\alpha}{\sum_{m=1}^{|\mathcal{S}^\alpha|} w_m} \quad (\text{C.7})$$

in which  $\alpha = \{g, t, g \cup t\}$  denotes geometry, texture and geometry plus texture attribute domains respectively,  $s_m^\alpha \in \mathcal{S}^\alpha$  indicates a subset of predictors with  $\mathcal{S}^\alpha \subseteq \mathcal{S}, \mathcal{S} = \{s_j\}$ , and  $1 \leq j \leq 32$ , while  $m \in \{1, \dots, N^\alpha\}$ , with  $N^\alpha$  the number of selected predictors, and  $w_m$  the corresponding weight. Such weights can be either manually set to specific values, e.g., giving equal weight to each predictor, or can be learned. In our case, the latter is performed through an optimization problem minimizing the distance between the predicted and the ground truth Mean Opinion Score (MOS):

$$\begin{aligned} & \underset{\mathbf{w}}{\operatorname{argmin}} \left| \operatorname{MOS} - f \left( \sum_{m=1}^{|\mathcal{S}^\alpha|} w_m \cdot s_m^\alpha \right) \right|_2^2 \\ & \text{s.t. } w_m \in [0, 1], \\ & \sum_{m=1}^{|\mathcal{S}^\alpha|} w_m = 1 \end{aligned} \quad (\text{C.8})$$

with  $f(\cdot)$  representing the selected fitting function to map the objective score to the MOS.

In case of domain-specific quality scores, a final quality score encompassing both domains can be computed using the following linear combination:

$$\tilde{q} = \omega \cdot q^g + (1 - \omega) \cdot q^t \quad (\text{C.9})$$

with  $\omega$  a regularization term to drive the contributions of geometry and texture.



# Bibliography

- [Abhishek 15] K. Abhishek & N. Khunger. *Complications of skin biopsy*. Journal of cutaneous and aesthetic surgery, vol. 8, no. 4, pages 239–241, 2015.
- [Ahmed 18] S. M. Ahmed, Y. Z. Tan, C. M. Chew, A. A. Mamun & F. S. Wong. *Edge and Corner Detection for Unorganized 3D Point Clouds with Application to Robotic Welding*. IEEE International Conference on Intelligent Robots and Systems (IROS), pages 7350–7355, 2018.
- [Ahronovich 23] E. Z. Ahronovich, N. Shihora, J.-h. Shen, K. Joos & N. Simaan. *Exploring An External Approach to Subretinal Drug Delivery via Robot Assistance and B-Mode OCT*. In 2023 IEEE International Conference on Robotics and Automation (ICRA), pages 6795–6801, London, 2023.
- [Ait-Aider 06] O. Ait-Aider, N. Andreff, J. M. Lavest & P. Martinet. *Simultaneous object pose and velocity computation using a single view from a rolling shutter camera*. In European Conference on Computer Vision (ECCV), volume 3952, pages 56–68, 2006.
- [Ait-Aider 07] O. Ait-Aider, A. Bartoli & N. Andreff. *Kinematics from lines in a single rolling shutter image*. In Proceedings of the IEEE Computer Society Conference on Computer Vision and Pattern Recognition (CVPR), 2007.
- [Akyol 21] E. Akyol, A. M. Hagag, S. Sivaprasad & A. J. Lotery. *Adaptive optics: principles and applications in ophthalmology*. Eye, vol. 35, no. 1, pages 244–264, 2021.
- [Alexiou 20] E. Alexiou & T. Ebrahimi. *Towards a point cloud structural similarity metric*. In 2020 IEEE International Conference on Multimedia and Expo Workshops (ICMEW), pages 1–6. IEEE, 2020.
- [Alexiou 21] E. Alexiou, I. Viola & P. Cesar. *PointPCA: Point Cloud Objective Quality Assessment Using PCA-Based Descriptors*. 2021.
- [Alfano 13] R. Alfano & Y. Pu. *Optical biopsy for cancer detection*. In H. Jelínková, editor, Lasers for Medical Applications, Woodhead Publishing Series in Electronic and Optical Materials, pages 325–367. Woodhead Publishing, 2013.



- [Andersson 05] S. B. Andersson & J. Park. *Tip steering for fast imaging in AFM*. Proceedings of the American Control Conference, vol. 4, pages 2469–2474, 2005.
- [Andersson 07] S. B. Andersson. *Curve tracking for rapid imaging in AFM*. IEEE Transactions on Nanobioscience, vol. 6, no. 4, pages 354–361, 2007.
- [Arthur 07] D. Arthur & S. Vassilvitskii. *K-means++: The Advantages of Careful Seeding*. SODA '07: Proceedings of the Eighteenth Annual ACM-SIAM Symposium on Discrete Algorithms, pages 1027–1035, 2007.
- [ASCO 21] ASCO. *Can a Biopsy Make My Cancer Spread?*, 2021.
- [Aumman 19] S. Aumman, D. Sabine, J. Fischer & M. Frank. *Optical Coherence Tomography (OCT): Principle and Technical Realization*. In J. F. Bille, editor, High Resolution Imaging in Microscopy and Ophthalmology, pages 59 – 85. Springer Nature Switzerland AG, 2019.
- [Badiéyan 19] S. Badiéyan, A. Ameri, M. R. Razzaghi, H. Rafii-Tabar & P. Sasanpour. *Mueller matrix imaging of prostate bulk tissues; Polarization parameters as a discriminating benchmark*. Photodiagnosis and Photodynamic Therapy, vol. 26, pages 90–96, 2019.
- [Balicki 09] M. Balicki, J.-H. Han, I. Iordachita, P. Gehlbach, J. Handa, R. Taylor & J. Kang. *Single fiber optical coherence tomography microsurgical instruments for computer and robot-assisted retinal surgery*. International Conference on Medical Image Computing and Computer-Assisted Intervention (MICCAI), vol. 12, pages 108–115, 2009.
- [Baran 17] Y. Baran, K. Rabenorosa, G. J. Laurent, P. Rougeot, N. Andreff & B. Tamadazte. *Preliminary results on OCT-based position control of a concentric tube robot*. In IEEE International Conference on Intelligent Robots and Systems (IROS), pages 3000–3005, Vancouver, 2017.
- [Baumann 17] B. Baumann. *Polarization sensitive optical coherence tomography: A review of technology and applications*. Applied Sciences, vol. 7, no. 5, 2017.
- [Bazaei 12] A. Bazaei, Y. K. Yong & S. O. Moheimani. *High-speed Lissajous-scan atomic force microscopy: Scan pattern planning and control design issues*. Review of Scientific Instruments, vol. 83, no. 6, pages 1–10, 2012.
- [Bernardes 12] R. Bernardes & J. Cunha-Vaz. *Optical Coherence Tomography A Clinical and Technical Update*. Springer Heidelberg New York Dordrecht London, Heidelberg New York Dordrecht London, 1st edition, 2012.

- 
- [Bhende 17] M. Bhende, S. Shetty, M. K. Parthasarathy & S. Ramya. *Optical coherence tomography: A guide to interpretation of common macular diseases*. Indian Journal of Ophthalmology, no. 66, pages 20–35, 2017.
- [Bille 19] J. F. Bille, S. W. Hell & R. N. Weinreb. *High Resolution Imaging in Microscopy and Ophthalmology*. Springer Nature Switzerland AG, 2019.
- [Bonin 10] T. Bonin, G. Franke, M. Hagen-Eggert, P. Koch & G. Huttmann. *In vivo Fourier-domain full-field OCT of the human retina with 1.5 million A-lines/s*. Optics letters, vol. 35, pages 3432 – 3434, 2010.
- [Boppart 97] S. A. Boppart, B. E. Bouma, C. Pitris, G. J. Tearney, J. G. Fujimoto & M. E. Brezinski. *Forward-imaging instruments for optical coherence tomography*. Optics letters, vol. 22, no. 21, pages 1618–1620, nov 1997.
- [Boppart 98] S. A. Boppart, B. E. Bouma, C. Pitris, G. J. Tearney, J. F. Southern, M. E. Brezinski & J. C. Fujimoto. *Intraoperative assessment of microsurgery with three-dimensional optical coherence tomography*. Radiology, vol. 208, no. 1, pages 81–86, 1998.
- [Boppart 99] S. A. Boppart, J. Herrmann, C. Pitris, D. L. Stamper, M. E. Brezinski & J. G. Fujimoto. *High-resolution optical coherence tomography-guided laser ablation of surgical tissue*. Journal of Surgical Research, vol. 82, no. 2, pages 275–284, 1999.
- [Boppart 01] S. A. Boppart, J. M. Herrmann, C. Pitris, D. L. Stamper, M. E. Brezinski & J. G. Fujimoto. *Real-time optical coherence tomography for minimally invasive imaging of prostate ablation*. Computer Assisted Surgery, vol. 6, no. 2, pages 94–103, 2001.
- [Brezinski 97] M. E. Brezinski, G. J. Tearney, S. A. Boppart, E. A. Swanson, J. F. Southern & J. G. Fujimoto. *Optical biopsy with optical coherence tomography: feasibility for surgical diagnostics*. The Journal of surgical research, vol. 71, no. 1, pages 32–40, 1997.
- [Bush 20] A. M. Bush, C. M. Sandino, S. Ramachandran, F. Ong, N. Dwork, E. J. Zucker, A. B. Syed, J. M. Pauly, M. T. Alley & S. S. Vasanaawala. *Rosette Trajectories Enable Ungated, Motion-Robust, Simultaneous Cardiac and Liver T2\* Iron Assessment*. Journal of Magnetic Resonance Imaging, vol. 52, no. 6, pages 1688–1698, 2020.
- [Byakodi 23] R. Byakodi. *Overview of Stomach Cancer: Causes, symptoms, and treatment*, 2023.
-

- [Calabi 98] E. Calabi, P. J. Olver, C. Shakiban, A. Tannenbaum & S. Haker. *Differential and Numerically Invariant Signature Curves Applied to Object Recognition*. International Journal of Computer Vision (IJCV), vol. 26, no. 2, pages 107–135, 1998.
- [Caliński 00] T. Caliński & S. Kageyama. Block designs: A Randomization approach, Volume I: Analysis. Springer, New York, 2000.
- [Canny 86] J. Canny. *A Computational Approach to Edge Detection*. IEEE Transactions on Pattern Analysis and Machine Intelligence, vol. PAMI-8, no. 6, pages 679–698, 1986.
- [Capps 11] A. G. Capps, R. J. Zawadzki, Q. Yang, D. W. Arathorn, C. R. Vogel, B. Hamann & J. S. Werner. *Correction of eye-motion artifacts in AO-OCT data sets*. In Proc. SPIE 7885, Ophthalmic Technologies XXI, page 78850, 2011.
- [Caroll 05] J. Carroll, D. C. Gray, A. Roorda & D. R. Williams. *Recent Advances in Retinal Imaging With Adaptive Optics*. Optics and Photonics News, vol. 16, no. 1, pages 36–42, 2005.
- [Carrasco-Zevallos 17] O. M. Carrasco-Zevallos, C. Viehland, B. Keller, M. Draelos, A. N. Kuo, C. A. Toth & J. A. Izatt. *Review of intraoperative optical coherence tomography: technology and applications [Invited]*. Biomedical Optics Express, vol. 8, no. 3, page 1607, 2017.
- [Carrasco-Zevallos 18] O. M. Carrasco-Zevallos, C. Viehland, B. Keller, R. P. McNabb, A. N. Kuo & J. A. Izatt. *Constant linear velocity spiral scanning for near video rate 4D OCT ophthalmic and surgical imaging with isotropic transverse sampling*. Biomedical Optics Express, vol. 9, no. 10, page 5052, 2018.
- [Cheon 15] G. W. Cheon, Y. Huang, J. Cha, P. L. Gehlbach & J. U. Kang. *Accurate real-time depth control for CP-SSOCT distal sensor based handheld microsurgery tools*. Biomedical optics express, vol. 6, no. 5, pages 1942–1953, may 2015.
- [Cheung 18] A. H. K. Cheung, C. Chow & K. F. To. *Latest development of liquid biopsy*. Journal of Thoracic Disease, vol. 10, no. Suppl 14, pages S1645–S1651, 2018.
- [Chinn 97] S. R. Chinn, E. A. Swanson & J. G. Fujimoto. *Optical coherence tomography using a frequency-tunable optical source*. Opt. Lett., vol. 22, no. 5, pages 340–342, mar 1997.
- [Cho 07] W.-h. Cho, D.-W. Kim & K.-S. Hong. *CMOS Digital Image Stabilization*. IEEE Transactions on Consumer Electronics, vol. 53, no. 3, pages 979–986, aug 2007.

- [Choma 03] M. Choma, M. Sarunic, C. Yang & J. Izatt. *Sensitivity advantage of swept source and Fourier domain optical coherence tomography*. Optics Express, vol. 11, no. 18, pages 2183–2189, 2003.
- [Dahmouche 12] R. Dahmouche, N. Andreff, Y. Mezouar, O. Ait-Aider & P. Martinet. *Dynamic visual servoing from sequential regions of interest acquisition*. International Journal of Robotics Research, vol. 31, no. 4, pages 520–537, 2012.
- [Dahroug 20] B. Dahroug, B. Tamadazte & N. Andreff. *PCA-Based visual servoing using optical coherence tomography*. IEEE Robotics and Automation Letters, vol. 5, no. 2, pages 3430–3437, 2020.
- [Dalle 23] Dalle. <https://www.bing.com/images>, 2023.
- [de Boer 03] J. F. de Boer, B. Cense, B. H. Park, M. C. Pierce, G. J. Tearney & B. E. Bouma. *Improved signal-to-noise ratio in spectral-domain compared with time-domain optical coherence tomography*. Opt. Lett., vol. 28, no. 21, pages 2067–2069, nov 2003.
- [De Boer 17] J. F. De Boer, C. K. Hitzenberger & Y. Yasuno. *Polarization sensitive optical coherence tomography*. Biomedical Optics Express, vol. 8, no. 3, pages 1838–1873, 2017.
- [De Loera 10] J. De Loera, J. Rambau & F. Santos. *Configurations, Triangulations, Subdivisions, and Flips*. In M. Bronstein, A. M. Cohen, H. Cohen, D. Eisenbud & B. Sturmfels, editors, Triangulations: Structures for Algorithms and Applications, pages 43–92. Springer, Berlin, Heidelberg, 1 edition, 2010.
- [Delattre 10] B. M. Delattre, R. M. Heidemann, L. A. Crowe, J. P. Vallée & J. N. Hyacinthe. *Spiral demystified*. Magnetic Resonance Imaging, vol. 26, no. 6, pages 862–881, 2010.
- [Delaunay 34] B. Delaunay. *Sur la sphère vide. A la mémoire de Georges Voronoï*. Bulletin de l’Académie des Sciences de l’URSS, Classe des Sciences Mathématiques et Naturelles, vol. 1, no. 6, pages 793–800, 1934.
- [Deray 20] J. Deray & J. Solà. *Manif: A micro Lie theory library for state estimation in robotics applications*. Journal of Open Source Software, vol. 5, no. 46, page 1371, 2020.
- [Donoho 06] D. Donoho. *Compressed Sensing*. IEEE Transactions on Information Theory, vol. 52, no. 4, 2006.
- [Draelos 22] M. Draelos, C. Viehland, R. McNabb, A. Kuo & J. Izatt. *Adaptive point-scan imaging beyond the frame rate-resolution limit with scene-reactive scan trajectories*. Optica, vol. 9, no. 11, pages 1276–1288, 2022.

- [Drexler 10] W. Drexler. *Optical coherence tomography*. Elsevier, 2010.
- [Duguay 71a] M. Duguay. *Light photographed in flight*. American Scientist, no. 59, pages 551–556, 1971.
- [Duguay 71b] M. Duguay & A. Mattick. *Ultra-high Speed Photography of Picosecond Light Pulses and Echoes*. Applied Optics, no. 10, pages 2162–2170, 1971.
- [Duma 11] V. F. Duma, K. S. Lee, P. Meemon & J. P. Rolland. *Experimental investigations of the scanning functions of galvanometer-based scanners with applications in OCT*. Applied Optics, vol. 50, no. 29, pages 5735–5749, 2011.
- [Duma 15] V. F. Duma, P. Tankam, J. Huang, J. Won & J. P. Rolland. *Optimization of galvanometer scanning for optical coherence tomography*. Applied Optics, vol. 54, no. 17, pages 5495–5507, 2015.
- [Duma 19] V. F. Duma. *Laser scanners with oscillatory elements: Design and optimization of 1D and 2D scanning functions*. Applied Mathematical Modelling, vol. 67, pages 456–476, 2019.
- [ECIS 23] ECIS. *European Cancer Information System*, 2023.
- [Fercher 95] A. F. Fercher, C. K. Hitzenberger, G. Kamp & S. Y. El-Zaiat. *Measurement of intraocular distances by backscattering spectral interferometry*. Optics Communications, vol. 117, no. 1, pages 43–48, 1995.
- [Ferguson 04] D. Ferguson, D. Hamer, L. Paunescu, B. Siobahn & S. Joel. *Tracking optical coherence tomography*. Optics letters, vol. 29, no. 18, pages 2139–2141, 2004.
- [Forssén 10] P. E. Forssén & E. Ringaby. *Rectifying rolling shutter video from hand-held devices*. Proceedings of the IEEE Computer Society Conference on Computer Vision and Pattern Recognition (CVPR), pages 507–514, 2010.
- [Frenet 52] J. F. Frenet. *Sur les courbes à double courbure*. Journal de Mathématiques Pures et Appliquées, vol. 1, no. 17, pages 437–447, 1852.
- [Fujimoto 03] J. G. Fujimoto. *Optical coherence tomography for ultrahigh resolution in vivo imaging*. Nature biotechnology., vol. 21, no. 11, pages 1361–1367, 2003.
- [Fujimoto 15] J. Fujimoto & W. Drexler. *Introduction to OCT*. In W. Drexler & J. G. Fujimoto, editors, Optical Coherence Tomography, Technology and Applications, pages 3 – 64. Springer International Publishing, Vienna, 2nd edition, 2015.

- 
- [Fujimoto 16] J. Fujimoto & E. Swanson. *The development, commercialization, and impact of optical coherence tomography*. Investigative Ophthalmology and Visual Science, vol. 57, no. 9, 2016.
- [Godara 10] P. Godara, A. M. Dubis, A. Roorda, J. L. Duncan & J. Carroll. *Adaptive optics retinal imaging: Emerging clinical applications*. Optometry and Vision Science, vol. 87, no. 12, pages 930–941, 2010.
- [Goldberg 89] D. E. Goldberg. Genetic Algorithms in Search, Optimization and Machine Learning. Addison-Wesley Longman Publishing Co., Inc., Boston, MA, United States, 1989.
- [Golubovic 97] B. Golubovic, B. E. Bouma, G. J. Tearney & J. G. Fujimoto. *Optical frequency-domain reflectometry using rapid wavelength tuning of a Cr<sup>4+</sup>:forsterite laser*. Opt. Lett., vol. 22, no. 22, pages 1704–1706, nov 1997.
- [Gora 13a] M. J. Gora, J. S. Sauk, R. W. Carruth, K. A. Gallagher, M. J. Suter, N. S. Nishioka, L. E. Kava, M. Rosenberg, B. E. Bouma & G. J. Tearney. *Tethered capsule endomicroscopy enables less invasive imaging of gastrointestinal tract microstructure*. Nature Medicine, vol. 19, no. 2, pages 238–240, 2013.
- [Gora 13b] M. J. Gora, J. S. Sauk, R. W. Carruth, W. Lu, D. T. Carlton, A. Soomro, M. Rosenberg, N. S. Nishioka & G. J. Tearney. *Imaging the upper gastrointestinal tract in unselected patients using tethered capsule endomicroscopy*. Gastroenterology, vol. 145, no. 4, pages 723–725, 2013.
- [Gora 16] M. J. Gora & G. J. Tearney. Enhanced Imaging of the Esophagus: Optical Coherence Tomography. Elsevier Inc., 2016.
- [Gorecki 21] C. Gorecki & S. Bargiel. *MEMS scanning mirrors for optical coherence tomography*. Photonics, vol. 8, no. 1, pages 1–25, 2021.
- [Grutzmann 14] R. Grutzmann. Molecular diagnostics and treatment of pancreatic cancer systems and network biology approaches. Academic Press, London, 2014.
- [Hans 11] S. Hans, R. Ingo & M. Juttner. *Peripheral vision and pattern recognition: A review*. Journal of vision, vol. 11, no. 13, 2011.
- [Hariri 13] L. P. Hariri, M. Villiger, M. B. Applegate, M. Mino-Kenudson, E. J. Mark, B. E. Bouma & M. J. Suter. *Seeing beyond the bronchoscope to increase the diagnostic yield of*
-



- bronchoscopic biopsy*. American journal of respiratory and critical care medicine, vol. 187, no. 2, pages 125–129, jan 2013.
- [Haydar 20] B. Haydar, S. Chrétien, A. Bartoli & B. Tamadazte. *Three-dimensional OCT Compressed Sensing using the shearlet transform under continuous trajectories sampling*. Informatics in Medicine Unlocked, vol. 19, 2020.
- [Heidelberg 13] E. Heidelberg. *SPECTRALIS Product Page – Heidelberg Engineering*, 2013.
- [Huang 14] Y. Huang, G. J. Furtmüller, D. Tong, S. Zhu, W. P. Lee, G. Brandacher & J. U. Kang. *MEMS-based handheld fourier domain doppler optical coherence tomography for intraoperative microvascular anastomosis imaging*. PLoS ONE, vol. 9, no. 12, pages 1–14, 2014.
- [Hwang 17] K. Hwang, Y. H. Seo & K. H. Jeong. *Microscanners for optical endomicroscopic applications*. Micro and Nano Systems Letters, vol. 5, no. 1, pages 1–11, 2017.
- [Izatt 08] J. A. Izatt & M. A. Choma. *Theory of Optical Coherence Tomography*, pages 47–72. Springer Berlin Heidelberg, Berlin, Heidelberg, 2008.
- [Janowczyk 16] A. Janowczyk & A. Madabhushi. *Deep learning for digital pathology image analysis: A comprehensive tutorial with selected use cases*. Journal of Pathology Informatics, vol. 7, no. 1, 2016.
- [Janowczyk 17] A. Janowczyk & A. Madabhushi. *Deep-learning network possible step toward automating biopsy slide analysis*, 2017.
- [Jayabalan 19] G. S. Jayabalan & J. F. Bille. *The Development of Adaptive Optics and Its Application in Ophthalmology*. In J. F. Bille, editor, High Resolution Imaging in Microscopy and Ophthalmology. Springer Nature Switzerland AG, 2019.
- [Jin 10] X. Jin & J. Han. *K-Means Clustering*, pages 563–564. Springer US, Boston, MA, 2010.
- [Justh 04] E. W. Justh & P. S. Krishnaprasad. *Equilibria and steering laws for planar formations*. Systems and Control Letters, vol. 52, no. 1, pages 25–38, 2004.
- [Kang 15] W. Kang, X. Qi, H. Wang & A. M. Rollins. *Optical Coherence Tomography for Gastrointestinal Endoscopy*. In J. Fujimoto & W. Drexler, editors, Optical Coherence Tomography, Technology and Applications, pages 2051–2075. Springer International Publishing, Switzerland, 2015.
- [Kaur 20] M. Kaur, P. M. Lane & C. Menon. *Endoscopic optical imaging technologies and devices for medical purposes: State of the art*. Applied Sciences, vol. 10, no. 19, 2020.



- 
- [Kavanaugh 23] T. Kavanaugh & K. Waltz. *What is the rolling shutter effect?*, 2023.
- [Kenton 11] B. Kenton, A. J. Fleming & K. K. Leang. *Compact ultra-fast vertical nanopositioner for improving scanning probe microscope scan speed*. Review of Scientific Instruments, vol. 82, no. 12, 2011.
- [Kiseleva 15] E. Kiseleva, M. Kirillin, F. Feldchtein, A. Vitkin, E. Sergeeva, E. Zagaynova, O. Streltsova, B. Shakhov, E. Gubarkova & N. Gladkova. *Differential diagnosis of human bladder mucosa pathologies in vivo with cross-polarization optical coherence tomography*. Biomedical optics express, vol. 6, no. 4, pages 1464–1476, apr 2015.
- [Klein 12] T. Klein, W. Wieser, R. Andre, T. Pfeiffer, E. C. M & R. Huber. *Multi-MHz FDML OCT: snapshot retinal imaging at 6.7 million axial-scans per second*. In Optical Coherence Tomography and Coherence Domain Optical Methods in Biomedicine XVI, volume Xvi, page 8213, California, 2012. SPIE.
- [Kraus Martin 15] H. J. Kraus Martin. *OCT Motion Correction*. In W. Drexler & F. James, editors, Optical Coherence Tomography, Technology and Applications, pages 459–476. Springer International Publishing, 2015.
- [Kraus 12] M. F. Kraus, B. Potsaid, M. A. Mayer, R. Bock, B. Baumann, J. J. Liu, J. Hornegger & J. G. Fujimoto. *Motion correction in optical coherence tomography volumes on a per A-scan basis using orthogonal scan patterns*. Biomedical Optics Express, vol. 3, no. 6, pages 1182–1199, 2012.
- [Krawitz 16] B. Krawitz, S. Mo & R. Rosen. *Adaptive Optics Retinal Imaging: Applications and Clinical Implications*. Retinal Physician, 2016.
- [Krepelkova 19] I. Krepelkova. *Colorectal Cancer – More People Screened, More Lives Saved*, 2019.
- [Lamouche 12] G. Lamouche, B. F. Kennedy, K. M. Kennedy, C.-E. Bisailon, A. Curatolo, G. Campbell, V. Pazos & D. D. Sampson. *Review of tissue simulating phantoms with controllable optical, mechanical and structural properties for use in optical coherence tomography*. Biomedical Optics Express, vol. 3, no. 6, pages 1381 – 1398, 2012.
- [Lankenau 07] E. Lankenau, D. Klinger, C. Winter, A. Malik, H. H. Müller, S. Oelckers, H.-W. Pau, T. Just & G. Hüttmann. *Combining Optical Coherence Tomography (OCT) with an Operating Microscope*. Advances in Medical Engineering, vol. 114, pages 343–348, 2007.
-

- [Lao 20] Y. Lao, O. Ait-Aider & A. Bartoli. *Solving Rolling Shutter 3D Vision Problems using Analogies with Non-rigidity*. International Journal of Computer Vision, vol. 129, pages 100–122, 2020.
- [Larobina 14] M. Larobina & L. Murino. *Medical image file formats*. Journal of Digital Imaging, vol. 27, no. 2, pages 200–206, 2014.
- [LaRocca 16] F. LaRocca, D. Nankivil, T. DuBose, C. A. Toth, S. Farsiu & J. A. Izatt. *In vivo cellular-resolution retinal imaging in infants and children using an ultracompact handheld probe*. Nature Photonics, vol. 10, no. 9, pages 580–584, 2016.
- [Leitgeb 03] R. Leitgeb, C. Hitzenberger & A. Fercher. *Performance of fourier domain vs time domain optical coherence tomography*. Optics Express, vol. 11, no. 8, page 889, 2003.
- [Leitgeb 14] R. A. Leitgeb, R. M. Werkmeister, C. Blatter & L. Schmetterer. *Doppler Optical Coherence Tomography*. Progress in Retinal and Eye Research, vol. 41, pages 26–43, 2014.
- [Li 14] Z. Li, J. H. Shen, J. A. Kozub, R. Prasad, P. Lu & K. M. Joos. *Miniature forward-imaging B-scan optical coherence tomography probe to guide real-time laser ablation*. Lasers in surgery and medicine, vol. 46, no. 3, pages 193–202, mar 2014.
- [Liang 08] C. K. Liang, L. W. Chang & H. H. Chen. *Analysis and compensation of rolling shutter effect*. IEEE Transactions on Image Processing, vol. 17, no. 8, pages 1323–1330, 2008.
- [Liang 11] C.-P. Liang, J. Wierwille, T. Moreira, G. Schwartzbauer, M. S. Jafri, C.-M. Tang & Y. Chen. *A forward-imaging needle-type OCT probe for image guided stereotactic procedures*. Optics express, vol. 19, no. 27, pages 26283–26294, dec 2011.
- [Liang 15] K. Liang, G. Traverso, H.-C. Lee, O. O. Ahsen, Z. Wang, B. Potsaid, M. Giacomelli, V. Jayaraman, R. Barman, A. Cable, H. Mashimo, R. Langer & J. G. Fujimoto. *Ultra-high speed en face OCT capsule for endoscopic imaging*. Biomedical Optics Express, vol. 6, no. 4, page 1146, 2015.
- [Liao 22] G. Liao, O. Caravaca-Mora, B. Rosa, P. Zanne, D. Dall’Alba, P. Fiorini, M. de Mathelin, F. Nageotte & M. J. Gora. *Distortion and instability compensation with deep learning for rotational scanning endoscopic optical coherence tomography*. Medical Image Analysis, vol. 77, page 102355, 2022.

- 
- [Lopater 16] J. Lopater, P. Colin, F. Beuvon, M. Sibony, E. Dalimier, F. Cornud & N. B. Delongchamps. *Real-time cancer diagnosis during prostate biopsy: ex vivo evaluation of full-field optical coherence tomography (FFOCT) imaging on biopsy cores*. World Journal of Urology, vol. 34, no. 2, pages 237–243, 2016.
- [Lu 14] C. D. Lu, M. F. Kraus, B. Potsaid, J. J. Liu, W. Choi, V. Jayaraman, A. E. Cable, J. Hornegger, J. S. Duker & J. G. Fujimoto. *Handheld ultrahigh speed swept source optical coherence tomography instrument using a MEMS scanning mirror*. Biomed. Opt. Express, vol. 5, no. 1, pages 293–311, jan 2014.
- [Luo 19a] S. Luo, Y. Fan, W. Chang, H. Liao, H. Kang & L. Huo. *Classification of human stomach cancer using morphological feature analysis from optical coherence tomography images*. Laser Physics Letters, vol. 16, no. 9, page ab3638, 2019.
- [Luo 19b] Y. Luo & S. B. Andersson. *A continuous sampling pattern design algorithm for atomic force microscopy images*. Ultramicroscopy, vol. 196, no. September 2018, pages 167–179, 2019.
- [Maass Marco 17] Maass Marco, A. Mandy, B. Anna, K. Fabrice, P. Huy, B. Thorsten & A. Mertins. *A Trajectory Study for Obtaining MPI System Matrices in a Compressed-Sensing Framework*. International journal on Magnetic Particle Imaging, vol. 3, no. 2, page 14, 2017.
- [Magerand 10] L. Magerand & A. Bartoli. *A generic rolling shutter camera model and its application to dynamic pose estimation*, 2010.
- [Magerand 14] L. Magerand. *Dynamic pose calculation with CMOS cameras using sequential acquisition*, 2014.
- [Mahmood 10] I. A. Mahmood & S. O. Reza Moheimani. *Spiral-scan atomic force microscopy: A constant linear velocity approach*. In 10th IEEE Conference on Nanotechnology, pages 115–120. IEEE, 2010.
- [Mahmood 11] I. A. Mahmood, S. O. R. Moheimani & B. Bhikkaji. *A New Scanning Method for Fast Atomic Force Microscopy*. IEEE Transactions on Nanotechnology, vol. 10, no. 2, pages 1–14, 2011.
- [Maloca 18] P. M. Maloca, J. E. R. de Carvalho, T. Heeren, P. W. Hasler, F. Mushtaq, M. Mon-Williams, H. P. Scholl, K. Balaskas, C. Egan, A. Tufail, L. Witthauer & P. C. Cattin. *High-performance virtual reality volume rendering of origi-*
-

- nal optical coherence tomography point-cloud data enhanced with real-time ray casting*. Translational Vision Science and Technology, vol. 7, no. 4, 2018.
- [Manen 18] L. V. Manen, J. Dijkstra, C. Boccara, E. Benoit, A. L. Vahrmeijer, M. J. Gora & J. S. D. Mieog. *The clinical usefulness of optical coherence tomography during cancer interventions*. Journal of Cancer Research and Clinical Oncology, vol. 144, no. 10, pages 1967–1990, 2018.
- [Maroufi 15] M. Maroufi, A. Bazaei & S. O. Reza Moheimani. *A high-bandwidth MEMS nanopositioner for on-chip AFM: Design, characterization, and control*. IEEE Transactions on Control Systems Technology, vol. 23, no. 2, pages 504–512, 2015.
- [Martin 22] S. Martin, C. Rashidifard, D. Norris, A. Goncalves, C. Vercollone & M. E. Brezinski. *Minimally Invasive Polarization Sensitive Optical Coherence Tomography (PS-OCT) for assessing Pre-OA, a pilot study on technical feasibility*. Osteoarthritis and Cartilage Open, vol. 4, no. 4, page 100313, 2022.
- [McCormick 06] D. T. McCormick, W. Jung, Y.-C. Ahn, V. Milanovic, Z. Chen & N. C. Tien. *A MEMS based Optical Coherence Tomography Imaging System and Optical Biopsy Probes for Real-Time, High Resolution In-Vivo and In-Vitro 2-D or 3-D Imaging*. In IEEE/LEOS International Conference on Optical MEMS and Their Applications Conference, pages 162–163, 2006.
- [Mcnabb 12] R. P. McNabb, F. Larocca, S. Farsiu, A. N. Kuo & J. A. Izatt. *Distributed scanning volumetric SDOCT for motion corrected corneal biometry*. Biomedical Optics Express, vol. 3, no. 9, pages 2050–2065, 2012.
- [MedlinePlus 21] MedlinePlus. *Culture of gastric tissue biopsy*, 2021.
- [Meek 20] R. D. Meek, M. K. Mills, C. J. Hanrahan, B. R. Beckett, R. L. Leake, H. Allen, D. D. Williams, M. Tommack, S. Schmahmann & B. G. Hansford. *Pearls and Pitfalls for Soft-Tissue and Bone Biopsies: A Cross-Institutional Review*. RadioGraphics, vol. 40, no. 1, pages 266–290, 2020.
- [Meyer 14] T. R. Meyer, D. Ziegler, C. Brune, A. Chen, R. Farnham, N. Huynh, J. M. Chang, A. L. Bertozzi & P. D. Ashby. *Height drift correction in non-raster atomic force microscopy*. Ultramicroscopy, vol. 137, pages 48–54, 2014.
- [Microsystems 15] L. Microsystems. *Intraoperative OCT imaging system EnFocus*, 2015.

- 
- [Mora 20] O. C. Mora, P. Zanne, L. Zorn, F. Nageotte, N. Zulina, S. Gravelyn, P. Montgomery, M. de Mathelin, B. Dallemagne & M. J. Gora. *Steerable OCT catheter for real-time assistance during teleoperated endoscopic treatment of colorectal cancer*. Biomedical Optics Express, vol. 11, no. 3, page 1231, 2020.
- [Morgner 00] U. Morgner, W. Drexler, F. X. Kärtner, X. D. Li, C. Pitris, E. P. Ippen & J. G. Fujimoto. *Spectroscopic optical coherence tomography*. Opt. Lett., vol. 25, no. 2, pages 111–113, jan 2000.
- [Murphy 23] A. Murphy, P. Iftaq & J. Keshavamurthy. *Motion artifact*, 2023.
- [Nam 18] H. S. Nam & H. Yoo. *Spectroscopic optical coherence tomography: A review of concepts and biomedical applications*. Applied Spectroscopy Reviews, vol. 53, pages 91 – 111, 2018.
- [Nikooienejad 19] N. Nikooienejad, M. Maroufi & S. O. Moheimani. *Rosette-scan video-rate atomic force microscopy: Trajectory patterning and control design*. Review of Scientific Instruments, vol. 90, no. 7, pages 1–10, 2019.
- [Nocedal 06] J. Nocedal & S. J. Wright. Numerical Optimization. Springer, New York, 2nd edn edition, 2006.
- [OECD 23] OECD. EU Country Cancer Profile: France 2023. 2023.
- [Ourak 16] M. Ourak, B. Tamadazte & N. Andreff. *Partitioned camera-OCT based 6 DOF visual servoing for automatic repetitive optical biopsies*. IEEE International Conference on Intelligent Robots and Systems (IROS), pages 2337–2342, 2016.
- [Palanker 10] D. V. Palanker, M. S. Blumenkranz, D. Andersen, M. Wiltberger, G. Marcellino, P. Gooding, D. Angeley, G. Schuele, B. Woodley, M. Simoneau, N. J. Friedman, B. Seibel, J. Batlle, R. Feliz, J. Talamo & W. Culbertson. *Femtosecond laser-assisted cataract surgery with integrated optical coherence tomography*. Science Translational Medicine, vol. 2, no. 58, pages 1–11, 2010.
- [Pan 20] L. Pan, F. Shi, D. Xiang, K. Yu, L. Duan, J. Zheng & X. Chen. *Octrexpert: A feature-based 3D registration method for retinal OCT images*. IEEE Transactions on Image Processing, vol. 29, no. c, pages 3885–3897, 2020.
- [Pappuru 12] R. R. Pappuru, C. Briceno, Y. Ouyang, A. C. Walsh & S. R. Sadda. *Clinical significance of B-scan averaging with SD-OCT*. Ophthalmic Surgery Lasers and Imaging, vol. 43, no. 1, pages 63–68, 2012.
-

- [Pareto 97] V. Pareto. *Cours d'Économie Politique*. Lausanne, Paris, 1897.
- [Park 14] H.-C. Park, Y.-H. Seo & K.-H. Jeong. *Lissajous fiber scanning for forward viewing optical endomicroscopy using asymmetric stiffness modulation*. *Optics Express*, vol. 22, no. 5, page 5818, 2014.
- [Perez 04] H. Perez, Q. Zou & S. Devasia. *Design and control of optimal scan trajectories: Scanning tunneling microscope example*. *Journal of Dynamic Systems, Measurement and Control, Transactions of the ASME*, vol. 126, no. 1, pages 187–197, 2004.
- [Pircher 07] M. Pircher, B. Baumann, E. Gotzinger, H. Sattmann & H. C. K. *Simultaneous SLO/OCT imaging of the human retina with axial eye motion correction*. *Optics Express*, vol. 15, pages 16922 – 16932, 2007.
- [Pircher 11] M. Pircher, C. K. Hitzenberger & U. Schmidt-Erfurth. *Polarization sensitive optical coherence tomography in the human eye*. *Progress in Retinal and Eye Research*, vol. 30, no. 6, pages 431–451, 2011.
- [Pircher 17] M. Pircher & R. J. Zawadzki. *Review of adaptive optics OCT (AO-OCT): principles and applications for retinal imaging [Invited]*. *Biomedical optics express*, vol. 8, no. 5, pages 2536–2562, may 2017.
- [Polat 07] K. Polat & S. Güneş. *Breast cancer diagnosis using least square support vector machine*. *Digital Signal Processing*, vol. 17, no. 4, pages 694–701, 2007.
- [Pu 12] Y. Pu, W. Wang, M. Al-Rubaiee, S. K. Gayen & M. Xu. *Determination of optical coefficients and fractal dimensional parameters of cancerous and normal prostate tissues*. *Applied Spectroscopy*, vol. 66, no. 7, pages 828–834, 2012.
- [Radhakrishnan 01] S. Radhakrishnan, A. M. Rollins, J. E. Roth, S. Yazdanfar, V. Westphal, D. S. Bardenstein & J. A. Izatt. *Real-time optical coherence tomography of the anterior segment at 1310 nm*. *Archives of Ophthalmology*, vol. 119, no. 8, pages 1179–1185, 2001.
- [RadiologyInfo 22] RadiologyInfo. *General Biopsy*, 2022.
- [Rana 12] M. S. Rana, H. R. Pota & I. R. Petersen. *Model Predictive Control of Atomic Force Microscope for Fast Image Scanning*. In 2012 IEEE 51st IEEE Conference on Decision and Control (CDC), pages 2477–2482. IEEE, 2012.



- 
- [Rao 15] Y. Rao, N. P. Sarwade & R. Makkar. *Modeling and simulation of Optical Coherence Tomography on Virtual OCT*. In *Procedia Computer Science*, volume 45, pages 644–650. Elsevier B.V., 2015.
- [Ren 09] H. Ren, W. C. Waltzer, R. Bhalla, J. Liu, Z. Yuan, C. S. Lee, F. Darras, D. Schulsinger, H. L. Adler, J. Kim, A. Mishail & Y. Pan. *Diagnosis of Bladder Cancer With Microelectromechanical Systems-based Cystoscopic Optical Coherence Tomography*. *Urology*, vol. 74, no. 6, pages 1351–1357, 2009.
- [Ricco 09] S. Ricco, M. Chen, H. Ishikawa, G. Wollstein & J. Schuman. *Correcting motion artifacts in Retinal Spectral Domain Optical Coherence Tomography via Image Registration*. *National institute of health*, vol. 12, no. 1, pages 100–107, 2009.
- [Ruiz 20] S. G. Ruiz, L. V. Calderita, A. Hidalgo-Paniagua & J. P. Bandera Rubio. *Measuring smoothness as a factor for efficient and socially accepted robot motion*. *Sensors (Switzerland)*, vol. 20, no. 23, pages 1–20, 2020.
- [Rusu 11] R. B. Rusu & S. Cousins. *3D is here: Point Cloud Library (PCL)*. In *2011 IEEE International Conference on Robotics and Automation*, pages 1–4, Shanghai, 2011. IEEE.
- [Samel 19] N. S. Samel & H. Mashimo. *Application of OCT in the gastrointestinal tract*. *Applied Sciences (Switzerland)*, vol. 9, no. 15, 2019.
- [Sang 16] X. Sang, A. R. Lupini, R. R. Unocic, M. Chi, A. Y. Borisevich, S. V. Kalinin, E. Endeve, R. K. Archibald & S. Jesse. *Dynamic scan control in STEM: spiral scans*. *Advanced Structural and Chemical Imaging*, vol. 2, no. 1, 2016.
- [Seber 84] G. A. F. Seber. *Multivariate Observations*. John Wiley and Sons, Inc., Hoboken, NJ, 1984.
- [Serret 51] J. A. Serret. *Sur quelques formules relatives à la théorie des courbes à double courbure*. *Journal de Mathématiques Pures et Appliquées*, vol. 1, no. 16, pages 193–207, 1851.
- [Shakhov 01] A. V. Shakhov, A. B. Terentjeva, V. A. Kamensky, L. B. Snopova, V. M. Gelikonov, F. I. Feldchtein & A. M. Sergeev. *Optical coherence tomography monitoring for laser surgery of laryngeal carcinoma*. *Journal of surgical oncology*, vol. 77, no. 4, pages 253–258, 2001.
- [Solà 18] J. Solà, J. Deray & D. Atchuthan. *A micro Lie theory for state estimation in robotics*. vol. IRI-TR-18-, pages 1–17, 2018.
-



- [Song 13] C. Song, D. Y. Park, P. L. Gehlbach, S. J. Park & J. U. Kang. *Fiber-optic OCT sensor guided "SMART" micro-forceps for microsurgery*. Biomedical optics express, vol. 4, no. 7, pages 1045–1050, 2013.
- [Soundararajan 19] R. Soundararajan, T.-W. Hsu, M. Calderon-Delgado, S. Donati, Y. Qin & S.-L. Huang. *Spectroscopic Full-field Optical Coherence Tomography in Dermatology*. In 2019 IEEE International Conference on BioPhotonics (BioPhotonics), pages 1–2, Taipei, Taiwan, 2019. IEEE.
- [South 14] F. A. South, E. J. Chaney, M. Marjanovic, S. G. Adie & S. A. Boppart. *Differentiation of ex vivo human breast tissue using polarization-sensitive optical coherence tomography*. Biomedical Optics Express, vol. 5, no. 10, page 3417, 2014.
- [Spaide 15] R. F. Spaide, J. G. Fujimoto & N. K. Waheed. *Image Artifacts in Optical Coherence Angiography*. Retina, vol. 35, no. 11, pages 2163 – 2180, 2015.
- [Spath 85] H. Spath. The Cluster Dissection and Analysis Theory FORTRAN Programs Examples. Halsted Press, New York United States, translated edition, 1985.
- [Strathman 15] M. Strathman, Y. Liu, E. G. Keeler, M. Song, U. Baran, J. Xi, M.-T. Sun, R. Wang, X. Li & L. Y. Lin. *MEMS scanning micromirror for optical coherence tomography*. Biomedical Optics Express, vol. 6, no. 1, pages 211–224, 2015.
- [Stuart 82] L. Stuart. *Least Squares Quantization in PCM*. IEEE Transactions on Information Theory, vol. 28, no. 2, pages 129 – 137, 1982.
- [Sun 11] J. Sun & H. Xie. *MEMS-based endoscopic optical coherence tomography*. International Journal of Optics, vol. 2011, 2011.
- [Sun 21] Z. Sun, R. Quan & O. Solgaard. *Resonant Scanning Design and Control for Fast Spatial Sampling*. Scientific Reports, vol. 11, no. 20011, pages 1–16, 2021.
- [Surgical 15] H.-S. Surgical. *Haag-Streit Surgical iOCT Product Description*, 2015.
- [Swanson 93] E. A. Swanson, J. A. Izatt, M. R. Hee, D. Huang, C. P. Lin, J. S. Schuman, C. A. Puliafito & J. G. Fujimoto. *In vivo retinal imaging by optical coherence tomography*. Optics letters, vol. 18, no. 21, pages 1864–1866, 1993.
- [Szkulmowski 05] M. Szkulmowski, M. Wojtkowski, T. Bajraszewski, I. Gorczyńska, P. Targowski, W. Wasilewski, A. Kowalczyk & C. Radzewicz. *Quality improvement for high resolution in*

- in vivo* images by spectral domain optical coherence tomography with supercontinuum source. *Optics Communications*, vol. 246, no. 4-6, pages 569–578, 2005.
- [Tang 21] E. M. Tang & Y. K. Tao. *Modeling and optimization of galvanometric point-scanning temporal dynamics*. *Biomedical Optics Express*, vol. 12, no. 11, page 6701, 2021.
- [Tanguy 20] Q. A. A. Tanguy, O. Gaiffe, N. Passilly, J.-M. Cote, G. Cabodevila, S. Bargiel, P. Lutz, H. Xie & C. Gorecki. *Real-time Lissajous imaging with a low-voltage 2-axis MEMS scanner based on electrothermal actuation*. *Optics Express*, vol. 28, no. 6, pages 8512–8527, 2020.
- [Tanner 01] S. Tanner, S. C. Lauxtermann, M. Wany, M. Willemin, N. Blanc, J. Grupp, R. Dinger, E. Doering, M. Ansorge, P. Seitz & F. Pellandini. *Low-power digital image sensor for still-picture image acquisition*. In *Proceedings of SPIE: Sensors and Camera Systems for Scientific, Industrial, and Digital Photography Applications II*, volume 4306, page 358, San Jose, CA, United States, 2001. SPIE.
- [Tao 10] Y. K. Tao, J. P. Ehlers, C. A. Toth & J. A. Izatt. *Intra-operative spectral domain optical coherence tomography for vitreoretinal surgery*. *Optics Letters*, vol. 35, no. 20, page 3315, 2010.
- [Tearney 97] G. J. Tearney, M. E. Brezinski, B. E. Bouma, S. A. Boppart, C. Pitris, J. F. Southern & J. G. Fujimoto. *In vivo endoscopic optical biopsy with optical coherence tomography*. *Science*, vol. 276, no. 5321, pages 2037–2039, 1997.
- [Temilola 19] D. O. Temilola, M. Wium, T. Herve Couliadiati, H. Ademola Adeola, G. Maria Carbone, C. Vittorio Catapano & L. Fernando Zerbini. *The prospect and challenges to the flow of liquid biopsy in africa*. *Cells*, vol. 8, no. 8, 2019.
- [Trout 23] R. M. Trout, C. Viehland, J. D. Li, W. Raynor, A.-H. Dhalla, L. Vajzovic, A. N. Kuo, C. A. Toth & J. A. Izatt. *Methods for real-time feature-guided image fusion of intra-surgical volumetric optical coherence tomography with digital microscopy*. *Biomedical Optics Express*, vol. 14, no. 7, pages 3308–3326, 2023.
- [Tsai 14] T.-H. Tsai, J. Fujimoto & H. Mashimo. *Endoscopic Optical Coherence Tomography for Clinical Gastroenterology*, 2014.
- [Tuma 12a] T. Tuma, J. Lygeros, V. Kartik, A. Sebastian & A. Pantazi. *High-speed multiresolution scanning probe microscopy based on Lissajous scan trajectories*. *Nanotechnology*, vol. 23, no. 18, 2012.

- [Tuma 12b] T. Tuma, J. Lygeros, A. Sebastian & A. Pantazi. *Optimal scan trajectories for high-speed scanning probe microscopy*. In Proceedings of the American Control Conference, pages 3791–3796, 2012.
- [Vakoc 09] B. J. Vakoc, R. M. Lanning, J. A. Tyrrell, T. P. Padera, L. A. Bartlett, T. Stylianopoulos, L. L. Munn, G. J. Tearney, D. Fukumura, R. K. Jain & B. E. Bouma. *Three-dimensional microscopy of the tumor microenvironment in vivo using optical frequency domain imaging*. Nature Medicine, vol. 15, no. 10, pages 1219–1223, 2009.
- [Vakoc 12] B. J. Vakoc, D. Fukumura, R. K. Jain & B. E. Bouma. *Cancer imaging by optical coherence tomography: Preclinical progress and clinical potential*. Nature Reviews Cancer, vol. 12, no. 5, pages 363–368, 2012.
- [Vienola 12] K. V. Vienola, B. Braaf, C. K. Sheehy, Q. Yang, P. Tiruveedhula, D. W. Arathorn, J. F. de Boer & A. Roorda. *Real-time eye motion compensation for OCT imaging with tracking SLO*. Biomedical Optics Express, vol. 3, no. 11, pages 2950–2963, 2012.
- [Walther 08] J. Walther, A. Krüger, M. Cuevas & E. Koch. *Effects of axial, transverse, and oblique sample motion in FD OCT in systems with global or rolling shutter line detector*. Journal of the Optical Society of America, vol. 25, no. 11, pages 2791–2802, 2008.
- [Wang 04] T. D. Wang & J. Van Dam. *Optical biopsy: a new frontier in endoscopic detection and diagnosis*. Clinical gastroenterology and hepatology, vol. 2, no. 9, pages 744–753, 2004.
- [Wang 15] C. Wang, X. Xia, B. Tian & S. Zhou. *Comparison of Fourier-Domain and Time-Domain Optical Coherence Tomography in the Measurement of Thinnest Corneal Thickness in Keratoconus*. Journal of Ophthalmology, vol. 2015, 2015.
- [Wang 17] J. Wang, Y. Xu & S. A. Boppart. *Review of optical coherence tomography in oncology*. Journal of Biomedical Optics, vol. 22, no. 12, page 1, 2017.
- [Wang 18] J. Wang, Y. Hu & J. Wu. *Three-dimensional endoscopic OCT using sparse sampling with a miniature magnetic-driven scanning probe*. Applied Optics, vol. 57, no. 34, pages 10056–10061, 2018.

- 
- [Welge 13] W. A. Welge & J. K. Barton. *Spiral-scanning, side-viewing optical coherence tomography endoscope for three-dimensional fully sampled in vivo imaging of the mouse colon*. Endoscopic Microscopy VIII, vol. 8575, page 85750R, 2013.
- [Yao 17] X. Yao, Y. Gan, E. Chang, H. Hibshoosh, F. Sheldon & C. Hendon. *Visualization and Tissue Classification of Human Breast Cancer Images Using Ultrahigh-resolution OCT*. Lasers Surg Med, vol. 49, no. 3, pages 258–269, 2017.
- [Yaqoob 05] Z. Yaqoob, J. Wu & C. Yang. *Spectral domain optical coherence tomography: a better OCT imaging strategy*. BioTechniques, vol. 39, no. 6, 2005.
- [Yong 12a] Y. K. Yong, A. Bazaei, S. O. Moheimani & F. Allgower. *Design and control of a novel non-raster scan pattern for fast scanning probe microscopy*. In IEEE/ASME International Conference on Advanced Intelligent Mechatronics, AIM, pages 456–461. IEEE, 2012.
- [Yong 12b] Y. K. Yong, S. O. Moheimani, B. Kenton & K. K. Leang. *Invited Review Article: High-speed flexure-guided nanopositioning: Mechanical design and control issues*. Review of Scientific Instruments, vol. 83, no. 12, 2012.
- [Yu 13] H. Yu, J.-H. Shen, K. M. Joos & N. Simaan. *Design, calibration and preliminary testing of a robotic telemanipulator for OCT guided retinal surgery*. In 2013 IEEE International Conference on Robotics and Automation (ICRA), pages 225–231, Germany, 2013.
- [Yu 15] H. Yu, J.-H. Shen, R. J. Shah, N. Simaan & K. M. Joos. *Evaluation of microsurgical tasks with OCT-guided and/or robot-assisted ophthalmic forceps*. Biomedical optics express, vol. 6, no. 2, pages 457–472, feb 2015.
- [Zawadzki 07] R. J. Zawadzki, A. R. Fuller, S. S. Choi, D. F. Wiley, B. Hamann & J. S. Werner. *Correction of motion artifacts and scanning beam distortions in 3D ophthalmic optical coherence tomography imaging*. In B. E. Stuck, M. B. M.D., F. Manns, P. G. Söderberg & A. Ho, editors, Ophthalmic Technologies XVII, volume 6426, page 642607. International Society for Optics and Photonics, SPIE, 2007.
- [Zeiss 14] Zeiss. *Zeiss Rescan 700 Technical Specifications*, 2014.
- [Zhang 04] F. Zhang, E. W. Justh & P. S. Krishnaprasad. *Boundary following using gyroscopic control*. In Proceedings of the IEEE Conference on Decision and Control, volume 5, pages 5204–5209, 2004.
-

- [Zhang 14] Y. Zhang, T. Pfeiffer, M. Weller, W. Wieser, R. Huber, J. Raczkowski, J. Schipper, H. Wörn & T. Klenzner. *Optical coherence tomography guided laser cochleostomy: towards the accuracy on tens of micrometer scale*. BioMed research international, vol. 2014, page 251814, 2014.
- [Zhang 15] K. Zhang, T. Hatano, T. Tien, G. Herrmann, C. Edwards, S. C. Burgess & M. Miles. *An adaptive non-raster scanning method in atomic force microscopy for simple sample shapes*. Measurement Science and Technology, vol. 26, no. 3, page 35401, 2015.
- [Zhang 21] Z. Zhang, B. Rosa, O. Caravaca-Mora, P. Zanne, M. J. Gora & F. Nageotte. *Image-Guided Control of an Endoscopic Robot for OCT Path Scanning*. IEEE Robotics and Automation Letters, vol. 6, no. 3, pages 5881–5888, 2021.
- [Zhu 18] J. Zhu, X. He & Z. Chen. *Perspective: Current challenges and solutions of Doppler optical coherence tomography and angiography for neuroimaging*. APL Photonics, vol. 3, no. 12, page 120902, 2018.
- [Zysk 06] A. M. Zysk & S. A. Boppart. *Computational methods for analysis of human breast tumor tissue in optical coherence tomography images*. Journal of biomedical optics, vol. 11, no. 5, page 54015, 2006.

**Titre :** Balayage adaptatif et compensation des artefacts de mouvement 3D en tomographie par cohérence optique

**Mots clefs:** OCT, trajectoires non Cartésiennes, prévisualisation rapide, acquisition séquentiel, biopsie optique, rapport exploitation-exploration

**Résumé :** La Tomographie par Cohérence Optique (OCT) est utile pour fournir des images/volumes haute résolution des tissus biologiques, révélant des informations micro-structurales. Sa pertinence est notamment prononcée en oncologie pour la détection précoce des tumeurs malignes et la biopsie optique. L'acquisition de données OCT implique un balayage mécanique du tissu par un faisceau lumineux, délivrant des informations interférométriques le long de la profondeur du tissu. En raison du balayage mécanique, la fréquence d'acquisition et la résolution spatiale sont antagonistes (augmenter la fréquence compromet la résolution spatiale, et vice versa). De plus, un mode d'acquisition séquentiel (rolling

shutter) est induit, provoquant des artefacts géométriques dans le volume OCT. Pour résoudre ces problèmes, les objectifs de recherche sont ; i) proposer l'acquisition de données OCT en utilisant des trajectoires non Cartésiennes, accompagnée d'un ensemble de critères d'évaluation ; ii) proposer une stratégie adaptative dans l'acquisition de données OCT, où les données sont sélectivement acquises dans des régions informatives du champ de vision, réduisant ainsi potentiellement le temps d'acquisition ; iii) proposer une méthodologie pour estimer le mouvement à partir de volumes OCT géométriquement déformés, abordant particulièrement le défi d'estimer la forme et le mouvement à partir d'un seul volume OCT.

**Title :** Adaptive scanning and 3D motion artefact compensation in optical coherence tomography

**Keywords :** OCT, Non-raster trajectories, Fast preview, Rolling shutter, Optical biopsy, Exploitation-exploration ratio

**Abstract :** Optical Coherence Tomography (OCT) is instrumental in providing high-resolution images/volumes of biological tissues, revealing micro-structural information. Its significance is particularly pronounced in oncology for the early detection of malignant tumours and optical biopsy. The acquisition of OCT data involves a mechanical scan of the tissue surface by a light beam, delivering interferometric information along the tissue depth. Due to the mechanical scan, the acquisition frequency and spatial resolution are antagonistic (increasing the acquisition frequency compromises spatial resolution, and vice versa). Additionally, a rolling shutter acquisition mode is induced, causing geometric artefacts in the OCT volume. In view of these issues,

the contributions in this thesis are threefold: i) propose OCT data acquisition using non-raster trajectories, accompanied by a set of criteria to assess both the scan trajectories and the resulting volumetric data. Experimental results demonstrated that non-raster trajectories were nearly twice as fast as the raster trajectory without a significant loss in quality. ii) propose an adaptive strategy in OCT data acquisition, where data is selectively acquired in informative regions of the field of view, optimising the scan process and potentially reducing the acquisition time. And iii) propose a methodology for estimating motion from geometrically distorted OCT volumes, particularly addressing the challenge of estimating shape and motion from only one OCT volume.